

Zhang, Kangyong (2025) *Mangrove biomass estimation through remote sensing and machine learning based approaches.* PhD thesis.

https://theses.gla.ac.uk/85530/

Copyright and moral rights for this work are retained by the author

A copy can be downloaded for personal non-commercial research or study, without prior permission or charge

This work cannot be reproduced or quoted extensively from without first obtaining permission from the author

The content must not be changed in any way or sold commercially in any format or medium without the formal permission of the author

When referring to this work, full bibliographic details including the author, title, awarding institution and date of the thesis must be given

Enlighten: Theses
https://theses.gla.ac.uk/
research-enlighten@glasgow.ac.uk

Mangrove Biomass Estimation through Remote Sensing and Machine Learning Based Approaches

Kangyong Zhang

SUBMITTED IN FULFILMENT OF THE REQUIREMENTS FOR THE DEGREE OF

Doctor of Philosophy

SCHOOL OF GEOGRAPHICAL AND EARTH SCIENCES

COLLEGE OF SCIENCE AND ENGINEERING

UNIVERSITY OF GLASGOW



Abstract

Mangroves play a crucial role in providing valuable ecosystem services, particularly as highly efficient carbon sinks that mitigate climate change impacts Understanding their contribution to the global carbon cycle requires accurate assessment of carbon stocks, which typically depends on the estimation of biomass, especially aboveground biomass (AGB). Existing studies on accurate estimation of mangrove AGB have been constrained by uncertainties in modelling efforts, limited field data and methodological challenges in integrating multisource remote sensing datasets. This research develops improved methodologies of mangrove AGB estimation by addressing these challenges. First, two local mangrove forests in Mexico were used to evaluate the feasibility and performance of open access global digital elevation models (NASADEM, ALOS DSM and Copernicus GLO-30 DEM) for AGB estimation. After calibration with spaceborne LiDAR (Light Detection and Ranging) datasets, the DEMs produced comparable and spatially consistent AGB estimates. For stands with a mean canopy height of 15 m, the standard error was ~30% of the estimated AGB. Second, an approach was developed to upscale localised field inventory to a continental level (the Americas), by incorporating spaceborne LiDAR data. Third, a novel data fusion framework was introduced using extensive spaceborne LiDAR derived AGB estimates to train high-resolution optical mosaics and rasterised environmental variables through a machine learning algorithm. This integration produced wall-to-wall mangrove AGB estimates across the Americas, achieving a validation accuracy of $R^2 = 0.72$ and root mean square error (RMSE) = 37.24 Mg/ha. Ultimately, applying the improved methodologies of mangrove AGB estimation to the Americas revealed not only high agreements in AGB estimates across country-level undisturbed mangrove forests but also 5.10 million Mg AGB gains in regrowing mangroves between 2000 and 2020. The findings underscore the resilience of mangroves and their capacity to recover as significant carbon sinks, which is particularly relevant to climate change adaptation and conservation efforts. Overall, this research provides improved methodologies in mangrove AGB estimation by integrating multisource datasets at a local and a continental scale, which is transferable and valuable to other tropical coastal ecosystems, offering researchers and practitioners an effective means to better integrate mangrove carbon dynamics into global climate mitigation frameworks. Additionally, spatially explicit mangrove AGB estimates derived from the improved methodologies can inform conservation priorities, restoration strategies and national carbon accounting efforts.

Acknowledgement

Looking back on the past four years, I am humbled by the transformative journey of my PhD. Completing a PhD is never easy, let alone during a global pandemic. The pandemic cast a long shadow over this period, particularly the beginning of my PhD, turning isolation into a daily reality and research into a solitary pursuit. Yet within these challenges, I discovered unexpected resilience—learning to troubleshoot experiments and find solace in data analysis via video calls with supervisors, and to celebrate even smallest breakthroughs with colleagues across screens.

My deepest gratitude goes to my primary supervisor, Professor Brian Barrett, for the extraordinary mentorship. He met my moments of self-doubt with clarity, my fragmented ideas with constructive critique, and my progress with genuine pride. He has transformed his intangible knowledge into actionable guidance in every in-person meeting, making my PhD study more productive and intellectually efficient. I am equally indebted to my secondary supervisors, Dr. Alejandra Vovides and Professor Thorsten Balke, for their invaluable expertise and profound insights in mangrove research, helping refine both my research approach and this thesis. Special thanks are due to Dr. Jorge López-Portillo from Instituto de Ecología, A.C. (INECOL) in Mexico for his generous financial support and essential field assistance, which enabled the successful completion of my mangrove fieldwork in Mexico. In the meanwhile, I am deeply grateful to the local communities for their strong assistance and warm hospitality during the fieldwork.

To my family—sincerely thank you for enduring my absences, for your unwavering support, and for reminding me that there is a world beyond the thesis. To my friends and colleagues—you are more than just companions in this academic journey. The constructive discussions over writing, shared frustrations on the PhD, and moments of get-togethers after work have created memories I will treasure and remember forever. No words can fully capture my gratitude to all of you for making my PhD years truly meaningful.

Last but not least, I gratefully acknowledge the financial support from China Scholarship Council (CSC) for funding my doctoral studies abroad, as well as the Mobility Funding from School of Geographical & Earth Sciences in University of Glasgow and Volkswagen foundation for financing my mangrove fieldwork in Mexico. This PhD was not solely an academic pursuit; it was a profound lesson in scholarly humility, interdisciplinary collaboration, and cross-cultural learning.

Declaration

I hereby declare that this thesis is entirely my own work, except where the explicit acknowledgment is made through appropriate references to the contributions of others. The content of this thesis is of my own composition and has not been submitted, either in whole or in part, for the award of any other degree at the University of Glasgow or any other institution.

Table of Contents

Abstract	i
Acknowledgement	ii
Declaration	iii
Table of Contents	iv
List of Tables	viii
List of Figures	X
Chapter 1 Introduction	1
1.1 Mangrove distribution and ecosystem services	1
1.2 Status of global mangroves	3
1.3 Remote sensing applied in mangrove research	5
1.4 Aim, objectives and research questions	5
1.5 Study area	6
1.6 Thesis structure	9
References	10
Chapter 2 Evolution of mangrove remote sensing	15
2.1 Introduction	15
2.2 Remote sensing data for monitoring mangroves	15
2.2.1 Spaceborne optical imagery	15
2.2.2 Spaceborne radar imagery	23
2.2.3 Spaceborne LiDAR data	25
2.2.4 Airborne datasets	27
2.3 Remote sensing approaches in mangrove research	28
2.3.1 Distribution mapping and species discrimination	28
2.3.2 Biophysical parameters retrieval	34
2.3.3 Mangrove resilience investigation	39
2.4 Future opportunities	41
2.5 Summary	42
References	43
Chapter 3 Mapping aboveground biomass using global DEMs for	the mangroves bordering the
lagoons of La Mancha and El Llano, Mexico	64
Abstract	65

3.1 Introduction	66
3.2 Materials and methods	68
3.2.1 Study sites	68
3.2.2 Field data collection	69
3.2.3 Mangrove extent maps	70
3.3 Digital Elevation Models (DEMs)	71
3.3.1 NASADEM	71
3.3.2 ALOS World 3D-30m	71
3.3.3 Copernicus GLO-30 DEM	71
3.4 ICESat-2 LiDAR data	72
3.5 DEM calibration	72
3.6 Field AGB estimation methods	74
3.7 Allometric modelling of plot-level b	iomass and canopy height75
3.8 Results	76
3.8.1 Field mean canopy height and	AGB estimates
3.8.2 Comparison between differen	t allometric equations77
3.8.3 Performance of DEM calibrat	ion against field measurements78
3.8.4 Mangrove AGB mapping bas	ed on calibrated DEMs79
3.8.5 Comparisons between AGB e	stimation maps81
3.9 Discussion	83
3.9.1 Uncertainty of mangrove AG	B estimation83
3.9.2 Discrepancies between local	and global AGB estimates84
3.9.3 Difference among allometric	equations for field AGB estimation84
3.9.4 Limitations of AGB estimation	n using DEMs85
3.10 Conclusions	86
References	88
Chantan 4 Abayaanayand bianaas astim	tion of managery forests agrees the Americas wine
•	ation of mangrove forests across the Americas using
	94
	95 96
	98
·	98
·	99
4.2.3 Flanet continental mosaics	99

	4.2.4 GEDI LiDAR data	101
	4.2.5 Field AGB estimation method	101
	4.2.6 Allometric modelling of plot-level biomass and canopy height	102
	4.2.7 Random Forests regression model	104
	4.2.8 Comparisons between mangrove AGB estimates based on remote sensing	106
	4.3 Results	107
	4.3.1 Determination of the optimal number of variables and hyperparameters	107
	4.3.2 RF model performance assessment	108
	4.3.3 Mangrove AGB estimation in 2020 over the Americas	109
	4.3.4 Inter-comparison of mangrove AGB estimates	111
	4.4 Discussion	112
	4.4.1 Variations of country-level mangrove AGB estimates	112
	4.4.2 Feature importance of environmental variables	113
	4.4.3 AGB estimation uncertainty	113
	4.4.4 Implications for mangrove management and policy	114
	4.5 Conclusions	115
	References.	117
~ 1		
	anton 5 Quantifying aboveguound biomass dynamics of manguous negroveth agrees the	A mariana
	napter 5 Quantifying aboveground biomass dynamics of mangrove regrowth across the	
		126
	Abstract	1 26
	Abstract	126127128
	Abstract	126 127 128 130
	Abstract	126127128130130
	Abstract	126 127 128 130 130
	Abstract	126127128130130131
	Abstract	126127128130130131
	Abstract	126127128130130131131
	Abstract	126127130130131131132
	Abstract	126127130130131131132132
	Abstract	126127128130130131131132132134
	Abstract	126127130130131131132132134136
	Abstract	126127130130131131132132134137
	Abstract	126127130130131131132132134137137

5.4.4 Research uncertainties and limitations	141
5.5 Conclusions	142
References	143
Chapter 6 Discussion	148
6.1 Methodological context and contributions	148
6.2 Transferability across regions and scales	149
6.3 Implications for conservation, restoration, and carbon accounting	150
6.4 Research limitations and recommendations	151
References	153
Chapter 7 Conclusions	156

List of Tables

Table 1-1. Regional, national and international ecosystem restoration actions specific or related to
mangrove forest
Table 2-1. The specifications of spaceborne optical sensors. 18
Table 2-2. The specifications of spaceborne radar sensors used in mangrove research. 23
Table 2-3. The specifications of spaceborne LiDAR sensors used in mangrove research. 26
Table 2-4. Remote sensing-based approaches for mangrove extent mapping and species discrimination.32
Table 2-5. Remote sensing-based approaches for mangrove biomass estimation.
Table 2-6. The approaches for mangrove resilience or health investigation. 40
Table 3-1. Summary of key characteristics of NASADEM, ALOS DSM, and Copernicus DEM72
Table 3-2. Calibration of DEMs using ICESat-2 ATL08 segments with regression equations and accuracy metrics, where <i>HNASADEM</i> , <i>HALOSDSM</i> , and <i>HCOPDEM</i> represent original elevation values of NASADEM, ALOS DSM and Copernicus GLO-30 DEM, respectively; <i>NASADEMHmean ALOSDSMHmean</i> , and <i>COPDEMHmean</i> are new datasets of mean canopy height estimation
Table 3-3. Allometric equation for estimating mangrove aboveground biomass of the study area, where ρ AGB, D, and H represents wood density (g/cm³), aboveground biomass (kg), diameter at breast height (cm and canopy height (m), respectively
Table 3-4. Regression equations developed by other studies. 74
Table 3-5. The summary statistics of field measurements based on mangrove species. 76
Table 3-6. Summary of mangrove tree data per plot $(n = 24)$.
Table 4-1. The filters to GEDI canopy height metrics for quality check and nighttime strong-beam data 101
Table 4-2. Allometric equation for mangrove AGB estimation, where ρ, AGB, D, and H represents wood
density (g/cm ³), AGB (kg), DBH (cm) and canopy height (m), respectively
Table 4-3. The formulae of spectral vegetation indices used in the RF regression model. 105

Table 4-4. Environment variables included in the RF regression model. 106
Table 4-5. Mangrove AGB estimates summarised by country. 111
Table 5-1. Mangrove area (ha) summarized by country in terms of mangrove transition status (i.e., Type I
regrowth, Type II regrowth and undisturbed) between 2000 and 2020, excluding Barbados, the United
States of America, Puerto Rico, British Virgin Islands, and Virgin Islands. Numbers in parentheses
represent areas falling into mangrove reserves
Table 5-2. Country-level mangrove AGB (Mg) in terms of Type I/II regrowth between 2000 and 2020,
excluding Barbados, the United States of America, Puerto Rico, British Virgin Islands, and Virgin Islands.
Table 5-3. Country-level mangrove AGB (Mg) over undisturbed mangrove areas between 2000 and 2020,
excluding Barbados, the United States of America, Puerto Rico, British Virgin Islands, and Virgin Islands.

List of Figures

country adapted from Spalding et al. (2010)
Figure 1-2. Ecosystem services provided by mangrove ecosystems (Source: Worthington et al., 2020)2
Figure 1-3. The distribution of mangrove forests across the Americas in 2020 derived from Jia et al. (2023)
and species counts by country adapted from Spalding et al. (2010)
Figure 1-4. Geographical location of mangrove forests bordering El Llano (top) and La Mancha (bottom)
lagoons (outlined in red) in Mexico8
Figure 1-5. Field photographs taken from the fieldwork in July 2022: (a) measurement of canopy height in the mangrove forest around El Llano lagoon by Alejandra Vovides and her assistant Alvaro Gonzalez Ruiz;
(b) measurement of the diameter of a large Rhizophora mangle tree in the mangrove forest on the
southeastern side of La Mancha lagoon by Kangyong Zhang8
Figure 2-1. Remote sensing datasets acquired for monitoring mangroves
Figure 2-2. The smoothed reflectance spectrum of four mangrove species in China and field photos of
corresponding mangrove species (Source: Xu et al. (2019))
Figure 2-3. Schematic diagram of different wavelengths of radar system penetrating through mangroves.
Figure 2-4. Schematic diagrams of the ground tracks of different spaceborne LiDAR datasets: a) ICESat-
2 ATL08, b) GEDI L2A. Note that the across-track distances are not shown to scale for clarity and compactness (Source: Liu et al. (2021))
Figure 2-5. Generalised methodological workflow of remote sensing approaches in mangrove research.28
Figure 2-6. Aerial photograph taken on 14 December 1964 by the Hong Kong Lands Department, used for
historical mangrove extent mapping. The Mai Po Nature Reserve is outlined in white, and land covers are
annotated as mangroves (M), mudflats (MF), and gei wai (GW) (Source: Liu et al., 2022)29
Figure 3-1. Location of the study sites on the east coast of Mexico, connecting with the Gulf of Mexico
(denoted with a red star) where red patches represent the mangrove forests bordering the lagoons of El
Llano (north) and La Mancha (south), respectively. The mangrove extent was delineated for the year of

Figure 1-1. Global mangrove distribution in 2020 retrieved from Jia et al. (2023) and species counts by

2020	obtained	from	CONABIO	geoportal
(http://www.	conabio.gob.mx/informac	ion/gis/?vns=gis_roo	t/biodiv/monmang/bimagdm	o/mx_man20gw).
The base map	p was rendered through Es	sri World Image		69
Figure 3-2. T	Γhe location and numberin	g of the plot centroid	ls in the mangrove forest arou	und the lagoons of
El Llano (A)	and La Mancha (B). Field	measurement plots a	re coloured for different perio	ods. The base map
is rendered th	nrough Esri World Image.			70
Figure 3-3. S	Scatter plot with fitted line	ear regression model	s (95% confidence intervals)) comparing mean
canopy heigh	nt within each 100 m ICES	Sat/ATLAS ATL08 s	egment against mean DEM	elevation values at
the correspor	nding segments over the st	udy area		73
Figure 3-4. S	Scatterplot and model-fit of	f aboveground bioma	ss as a function of mean cano	py height (Hmean
for the field p	olots. OLS linear regressio	n model with logarit	hmic transformation (left); Po	ower-law function
in arithmetic	unit transformed from lin	near regression mode	el in logarithmic unit includ	ing the correction
factor (right)				76
Figure 3-5.	Kernel density distribution	on of plot-level AG	B estimates derived from di	fferent allometric
equations for	the study area			78
Figure 3-6. I	Field canopy height and A	AGB measurements a	against the estimations derive	ed from calibrated
DEMs with 9	95% confidence intervals:	(a) plot-level mean c	anopy height and (b) AGB	78
Figure 3-7. P	Probability density function	n of mean canopy hei	ghts over the mangrove fores	ts around El Llano
and La Manc	cha lagoons from calibrate	d DEMs using Gauss	sian kernel density estimation	n. Dash lines from
bottom to top	denote the values at 25 th ,	50 th and 75 th percen	tile, respectively	79
Figure 3-8. A	AGB estimation based on	three calibrated DEM	Is of El Llano mangroves (le	ft column) and La
Mancha man	groves (right column). (a),	(b) for NASADEM;	(c), (d) for ALOS DSM, (e),	(f) for Copernicus
GLO-30 DE	M. The base map is render	ered through Esri W	orld Image. Note that a dia	gonal black stripe
situated in th	ne southwest of mangrove	e extent maps of La	Mancha lagoon is a physic	cal gap (pathway)
separating the	e mangrove forest			80
Figure 3-9. P	Probability density function	n of estimated AGB o	over the mangrove forests aro	und El Llano (<i>left</i>)
and La Manc	cha (right) lagoons using	Gaussian kernel dens	sity estimation. Dash lines fr	om bottom to top
denote the va	alues at 25^{th} , 50^{th} and 75^{th}	percentile, respective	ly	81
Figure 3-10.	Differences between many	grove AGB estimates	s of El Llano (left two columr	ıs) and La Mancha
(right two co	lumns) based on three cal	ibrated DEM. (a), (b) for ALOS DSM vs. NASA	DEM: (c), (d) for

Copernicus GLO-30 DEM vs. ALOS DSM; (e), (f) for Copernicus GLO-30 DEM vs. NASADEM. Lef
sub-subplot of each paired subplot is in the unit of Mg/ha, while the right one is in percentage terms. The
base map is rendered through Esri World Image82
Figure 3-11. Pairwise comparisons with linear regression lines between the AGB estimation results derived
from NASADEM, ALOS DSM, Copernicus GLO-30 DEM and Simard et al. (2019). Lower triangle plots
are colour coded density plots as colour changes from purple to yellow for increasing density of data points
Each diagonal plot demonstrates probability density function of the AGB estimation corresponding to x/y axis label.
Figure 4-1. Locations of field sites and mangrove distribution in the Americas. The parenthesised numbers
demonstrate the plot count at each corresponding site. Note that the small-scale basemap leads to closely
spaced field plots visually condensed into a point. Two plots without geographic coordinates are no
presented in this map98
Figure 4-2. Box plot of NDVI values across mangrove areas of the Americas from Planet NICFI mosaics
for 2020. Low outliers represent misclassified areas (e.g., water pixels or non-vegetated surfaces labelled
as mangroves) or residual cloud shadows, leading to NDVI < 0
Figure 4-3. Crossplot and model-fit of aboveground biomass as a function of maximum canopy heigh
(Hmax) for the field plots. OLS linear regression model with logarithmic transformation (left); Power-law
function in arithmetic unit transformed from linear model in logarithmic unit including the correction factor
(right)
Figure 4-4. RFE with 5-fold CV results. (a) the change in negative RMSE as the number of selected
predictor variables increases, where the red dash line indicates the lowest RMSE is obtained when the
number is 29; (b) the feature importance of selected 29 predictor variables of the best performance108
Figure 4-5. The results of Grid Search with 5-fold CV for RF regression hyperparameter tuning108
Figure 4-6. Validation of mangrove AGB estimated model. The density plot changes from purple to yellow
with increasing data point density
Figure 4-7. Spatial distribution of mangrove AGB across the Americas aggregated to 1° grid cells. Grid
cells are coloured with darker green indicating higher AGB aggregation. The histograms along the top and
right panels show the longitudinal and latitudinal distributions of AGB, respectively. Red boxes (A-D)
indicate regions that are enlarged in bottom figures to provide zoom-in views: A, Términos Lagoon, Mexico

B, Columbus Channel, Venezuela; C, Sanquianga National Natural Park, Colombia; and D, Tracuateua Marine Extractive Reserve, Brazil
Figure 4-8. Comparisons between the AGB estimation and ESA CCI biomass (left) as well as GEDI L4B gridded biomass (right) maps for 2020, respectively. The density plot is colour coded as colour changes from purple to yellow for increasing density of data points
Figure 4-9. Visualization of AGB estimation maps clipped to mangrove areas in Rio Limbo, Venezuela. A, this study; B, ESA CCI biomass map; C, GEDI L4B gridded biomass map
Figure 4-10. Estimated AGB maps and corresponding standard deviation from Random Forest regression algorithm for mangrove areas in (A-B) Términos Lagoon, Mexico, and (C-D) Rio Limon, Venezuela114
Figure 5-1. The distribution of mangrove forests across the Americas in 2020 derived from Jia et al. (2023).
Figure 5-2. Workflow diagram for estimating mangrove AGB across the Americas between 2000 and 2020.
Figure 5-3. Mangrove regrowth across the Americas. Regrowth areas aggregated to 1° grid for better visualization (Data source: EC JRC). Two sites exhibited significant mangrove regrowth were marked by red rectangles: (A) Laguna de Términos protected area, Mexico; (B) Caeté-Taperaçu marine extractive reserve, Brazil.
Figure 5-4. Country-level AGB estimates over undisturbed mangrove forests in 2020 versus 2000 (Tg).
Figure 5-5. Zoom-in on intensive mangrove regrowth areas highlighted with red rectangles in Figure 5-1. (A) Laguna de Términos protected area, Mexico; (B) Caeté-Taperaçu marine extractive reserve, Brazil.
Figure 5-6. Country-level AGB estimates across mangrove regrowth areas using the proposed approach versus (A) GEDI L4B gridded AGB estimates and (B) ESA CCI Biomass 2020 product140

Chapter 1 Introduction

1.1 Mangrove distribution and ecosystem services

Mangroves are trees or shrubs that typically grow in the intertidal zone on tropical and subtropical coastlines between about 30°N and 30°S. Mangrove species do not belong to a single taxonomic group; they comprise a vast diversity of halophytic plants that are categorized into true mangroves and mangrove associates (Wang et al., 2011; Woodroffe et al., 2015). According to the most recent United Nations Food and Agriculture Organization (UN FAO)'s report on the world's mangroves, the total area of global mangroves in 2020 was 14.8 million ha, with the majority of mangroves concentrated in South and Southeast Asia (6.48 million ha, 43.8%) followed by South America (2.14 million ha), West and Central Africa (2.09 million ha), North and Central America (1.85 million ha) and Oceania (1.46 million ha) (FAO, 2023). The Indo-West Pacific is known to have the highest diversity of mangrove plants in the world as all mangrove species are postulated to originate in this region (Ellison et al., 1999) (**Figure 1-1**).

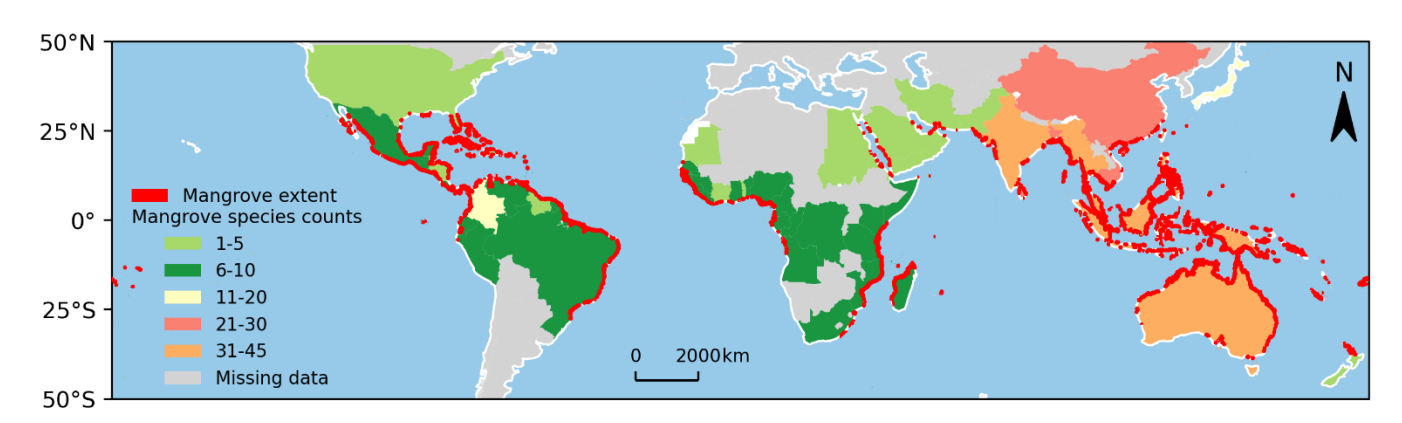


Figure 1-1. Global mangrove distribution in 2020 retrieved from Jia et al. (2023) and species counts by country adapted from Spalding et al. (2010).

As described in Worthington et al. (2020), major ecosystem services provided by mangroves include fisheries, coastal protection, timber and fuel provision, climate regulation, water purification and tourism (Figure 1-2). Located in the fringe of coastal zones, mangroves are considered a natural barrier for shoreline stabilization against coastal hazards such as storm surges, tsunamis, erosion and sea level rise (Cochard et al., 2008; McIvor et al., 2015; Spalding et al., 2014). Wave energy is attenuated when swelling waves pass through the dense aerial root systems and branches. Mangrove roots also contribute to increasing the soil volume through the sequestration of riverine and coastal sediment, preventing shoreline erosion and mitigating the impact of sea level rise. Large Tsunamis and extreme storm surges can overwhelm and even destroy mangroves, but a moderate reduction in inundation areas resulting from mangroves can help reduce both human and economic losses. Meanwhile, mangroves can catch the floating wrecks of buildings and

provide shelters and resources (timber and wood fuel) for disaster-affected communities in the secondary flooding and post-disaster reconstruction (Spalding et al., 2014).

Intricate roots of mangroves trap fine particles and nutrients from rivers and adjoining habitats, making mangroves an ideal nursery habitat that supports aquatic food chains (Hutchison et al., 2014), whereby marine fauna such as oysters, crabs and cockles can be collected from mangrove roots and mud, which birds, reptiles and mammals dwelling in the mangroves feed on (Cannicci et al., 2008; Nagelkerken et al., 2008). Fisheries in areas adjacent to mangrove forests benefit because many commercially important fish and shrimps use mangroves as nursery grounds before migrating to offshore habitats such as coral reefs (Brander et al., 2012; Carrasquilla-Henao and Juanes, 2017; Mumby et al., 2004). Also, mangroves can act as biological filters for water purification (Ouyang and Guo, 2016; Walters et al., 2008) and have great potential in recreational fishing and tourism (Spalding and Parrett, 2019).

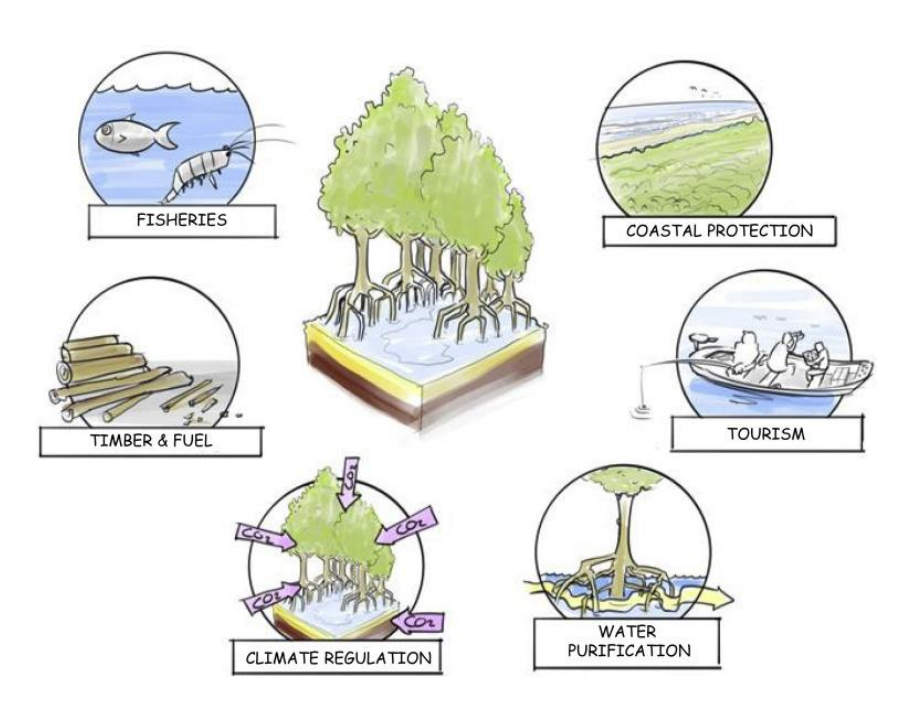


Figure 1-2. Ecosystem services provided by mangrove ecosystems (Source: Worthington et al., 2020)

Among these ecosystem services, the importance of mangroves for climate regulation has been receiving greater attention in the context of stronger climate change awareness. Mangroves are inundated by periodic flooding with saline water that leads to anoxic conditions of soil and slower decomposition of organic matter. Generally, mangroves are perceived as an efficient blue carbon sink which can contribute to mitigate climate change at national and global scales (Song et al., 2023; Taillardat et al., 2018; Uddin et al., 2023). As one of the most productive ecosystems, mangroves store an average of 738.9 Mg organic carbon per hectare, with an annual sequestration rate of 1.796 Mg/ha (Alongi, 2020). Organic carbon is distributed among aboveground biomass, belowground biomass, and soil. On average, belowground carbon accounts

for 85% of total mangrove carbon stocks (Kauffman, 2020), however, this can be quickly broken down with the clearance of mangroves and the drainage of soil (Worthington and Spalding, 2018).

1.2 Status of global mangroves

Coastal wetlands are currently faced with the "triple whammy" of threats, that is, growing industrialization and urbanization, a continuous decline in biological and physical resources (such as wading birds, fish, water, space and energy), and a weakened resilience to the impact of global warming and sea level rise (Waltham et al., 2020). Globally, there had been 677,000 ha of mangroves lost between 2000 and 2020 (FAO, 2023). The conversion of mangroves into economic commodity production accounted for the majority of the loss, such as the conversion to aquaculture ponds, rice paddies and oil palm plantations, especially in East and Southeast Asia (Bryan-Brown et al., 2020; FAO, 2023; Ma et al., 2019; Thomas et al., 2017). These conversions can be traced back to the 1900s and have often been backed by governmental incentives (Friess et al., 2016). For example, the Philippines officially prioritized the development of brackish water ponds in the 1970s, funded by the Central Bank and the Development Bank of the Philippines (Primavera, 2000). State governments in Malaysia, Penang and Selangor, neglected and repealed the federal guidelines for coastal buffer strips and permanent mangrove reserves to permit the construction of aquaculture ponds (Jusoff, 2013).

The removal of mangrove forests is alarming and explicit, but it should not be overlooked that mangrove forests may face degradation problems; changing environment such as sea level rise or alteration of rain patterns, can reduce fresh-water availability with increased salinity and further physiological changes that result in lower-stature trees and shrubs, or sometimes in obviously dieback with sparse forest coverage or even bare mudflats where mangroves once exhibited continuous growth (Chowdhury et al., 2019; Worthington and Spalding, 2018). For example, Rakhine mangroves in Myanmar exhibit sparse forest cover due to anthropogenic disturbances such as sea wall construction and aquaculture conversion, leading to the disruption of sea-freshwater exchange (Lee et al., 2021). Extreme weather events such as tropical cyclones and drought induced by climate change can also lead to mangrove degradations (Gilman et al., 2008; Lovelock et al., 2015; Mafi-Gholami et al., 2017). The mangrove forest in the Everglades National Park, USA is degraded with the loss of foliage and structural damage due to periodic hurricanes (Han et al., 2018; Lee et al., 2021). The tropical moist forest (TMF) dataset developed by Joint Research Centre (JRC) (Vancutsem et al., 2021) reported an estimated area of 271,500 ha of the world's mangroves classified as degraded during 2014-2022.

Recognising the importance of the ecosystem services provided by mangroves, different nations and international organizations have put forward various policies and actions against the loss and degradation

of mangroves (**Table 1-1**). In the last 20 years (2000-2020), the annual rate of global mangrove loss dropped from 0.12% in 2000-2010 to 0.07% in 2010-2020 with around half of total mangrove loss counteracted by mangrove afforestation (393,000 ha) (FAO, 2023). To ensure the effectiveness of mangrove restoration efforts, about 812,000 ha of global mangroves were identified as restorable areas in 2016, of which 303,710 ha were located in Southeast Asia (Worthington and Spalding, 2018), while China was estimated to have 16,800 ha of restorable mangrove area (Hu et al., 2020).

Table 1-1. Regional, national and international ecosystem restoration actions specific or related to mangrove forest.

Location	Actions	Organization/ Bureau in charge	Source
Global	To conserve and sustainably use the oceans, seas and marine resources for UN SDG 14: Life Below Water	UN Department of Economic and Social Affairs	Katila et al. (2019)
Global	Appeal a global effort to restore 150 million ha degraded and deforested lands by 2020 and 350 million ha by 2030.	Bonn Challenge led by IUCN and Global Partnership of Forest Landscape Restoration	Worthington and Spalding (2018)
Global	To prevent, halt and reverse the degradation of ecosystems worldwide by 2030	UN Environment Programme and FAO	Waltham et al. (2020)
Mainland China	To plant and restore mangrove forest to 9050 ha and 9750 ha by 2025, respectively	Ministry of Natural Resources and the National Forestry and Grassland Administration	http://english.www.gov.cn/st atecouncil/ministries/202008 /28/content_WS5f490ae4c6d 0f7257693b3cb.html
Philippines	To protect the remaining mangroves and restore lost forests, especially through fishpond reversion	Zoological Society of London	https://www.zsl.org/conserva tion/regions/asia/rehabilitatin g-mangroves-in-the- philippines
Mexico	To restore and conserve over 4,000 ha of mangroves across 10 sites	World Resources Institute	https://www.wri.org/mangro ve-guardians
Benin, Africa	By 2030, 15 million mangrove trees have been planted in the Ouémé MAB- UNESCO Reserve around Nokoué Lake	United Nations Environment Programme (UNEP)	https://www.bees-ong.org/
Guinea, Africa	To restore hydrology and soil conditions of 2,800 ha of abandoned lands to facilitate the natural recruitment of millions of seedlings	Wetlands International	https://www.wetlands.org/pu blications/conserving- biodiversity-cacheu- mangroves-national-park- guinea-bissau/

FAO: Food and Agriculture Organization; **IUCN**: International Union for Conservation of Nature; **SDG**: Sustainable Development Goal; **UN**: United Nations.

1.3 Remote sensing applied in mangrove research

Mangrove forests are generally remote and physically inaccessible with dense prop roots (e.g., *Rhizophora* genus) above muddy flats, making large-scale surveys time-consuming and laborious. Remote sensing has been used to investigate mangrove forests over the past decade (e.g., Jia et al., 2023; Lucas et al., 2020; Maurya et al., 2021; Pham et al., 2019; Wang et al., 2019). Remotely sensed data can be derived from airborne and spaceborne platforms, ranging from optical, microwave and LiDAR (Light Detection and Ranging) data, providing large amounts of multi-dimensional, spatially explicit and highly resolved observations for monitoring, mapping and characterizing mangrove forests.

Each source of remote sensing data has their own strengths and limitations. For instance, optical data enables spectral investigations over mangrove forests. However, due to cloud cover, spaceborne optical data can be limited in data availability, while longer wavelength microwaves from Synthetic Aperture Radar (SAR) can penetrate the cloud and be backscattered by ground objects, albeit not with spectral information as broad as multispectral and hyperspectral imagery. Different from two-dimensional observations, LiDAR data explicitly demonstrates forest vertical structures enabling the extraction of mangrove biophysical parameters, such as canopy height and crown diameter of whole forests. Additionally, owing to low flight altitude and mobility, the introduction of unmanned aerial vehicles (UAVs), facilitates very-high-resolution data acquisition such as hyperspectral and LiDAR data across inaccessible areas.

Mangrove research based on remote sensing can be technically categorized into extent and species identification, and biophysical parameters retrieval such as biomass, canopy height and leaf area index (LAI). For mangrove extent and species identification, remote sensing-based approaches comprise visual interpretation, object-based image analysis (OBIA), unsupervised classification and supervised classification (machine learning). For biophysical parameter retrieval, the approaches can be categorized into empirical, physical, and machine learning models that are particularly advantageous for both classification and regression tasks. Through characterising mangrove forests, these methods enable deeper investigation into the provision of ecosystem services and mangrove resilience under the scenarios of increasing anthropogenic interference and climate change impacts (e.g., Asbridge et al., 2018; Dahdouh-Guebas et al., 2004; Jia et al., 2014; Quoc Vo et al., 2015; Romer et al., 2012; Servino et al., 2018; Zhai et al., 2019).

1.4 Aim, objectives and research questions

Accurate quantity information on mangrove biomass is essential for carbon stock estimation and resilience determination. The importance of using remote sensing techniques has been highlighted due to the difficulty

in accessing these ecosystems (Worthington et al., 2020). Therefore, the aim of this research is to develop approaches for improved aboveground biomass (AGB) estimation of mangroves using multiple sources of remote sensing data and to quantify AGB dynamics of regrowing mangroves relevant to climate change adaptation and ongoing conservation efforts. The following objectives and specific research questions are:

Objective 1 – to develop the methodology of mangrove AGB estimation in the mangrove forests around La Mancha and El Llano lagoons in Mexico using freely accessible DEMs (digital elevation models) (Chapter 3)

- What is the relationship between plot-level mean canopy height and aboveground biomass?
- How can DEMs be calibrated to identical ground-based vertical datum and represent mangrove mean canopy height?
- How does the developed methodology perform in comparison to existing mangrove AGB products?

Objective 2 – to develop a novel approach for mangrove AGB estimation across the Americas using compiled field inventory data and multisource remote sensing data (Chapter 4)

- How are localised field inventory data introduced to realise mangrove AGB estimation at a continental scale?
- How can spaceborne LiDAR data be integrated with spaceborne optical imagery?
- How does mangrove AGB estimation benefit from high-resolution imagery?

Objective 3 – to quantify AGB dynamics of mangrove regrowth areas across the Americas between 2000 and 2020, reflecting mangrove resilience relevant to climate change adaptation and conservation efforts (Chapter 5)

- How is the mangrove regrowth identified and discriminated between 2000 and 2020?
- Are the approaches of mangrove AGB estimation for 2000 and 2020 consistent or comparable?
- How resilient were mangrove forests across the Americas in regrowing from disturbances during 2000-2020?

1.5 Study area

This research targets mangrove forests across the Americas (**Figure 1-3**). The mangroves in the Americas, including North and Central America, and South America, covered an estimated area of 3.99 million ha in

2020, making up 27% of worldwide mangroves (FAO, 2023). The Americas have the highest regional inclusion of mangroves within formal protected areas, with 72% of mangroves in South America and 67% of mangroves in North and Central America and the Caribbean under protection (Spalding and Leal, 2022). While the Indo-West Pacific region hosts a high diversity of mangrove species with 62 species identified, the Americas are home to only 13 native mangrove species (Spalding et al., 2010). In the Americas, the dominant genera of frontal mangroves include *Rhizophora*, *Avicennia*, *Laguncularia* and *Conocarpus* (Twomey and Lovelock, 2024).

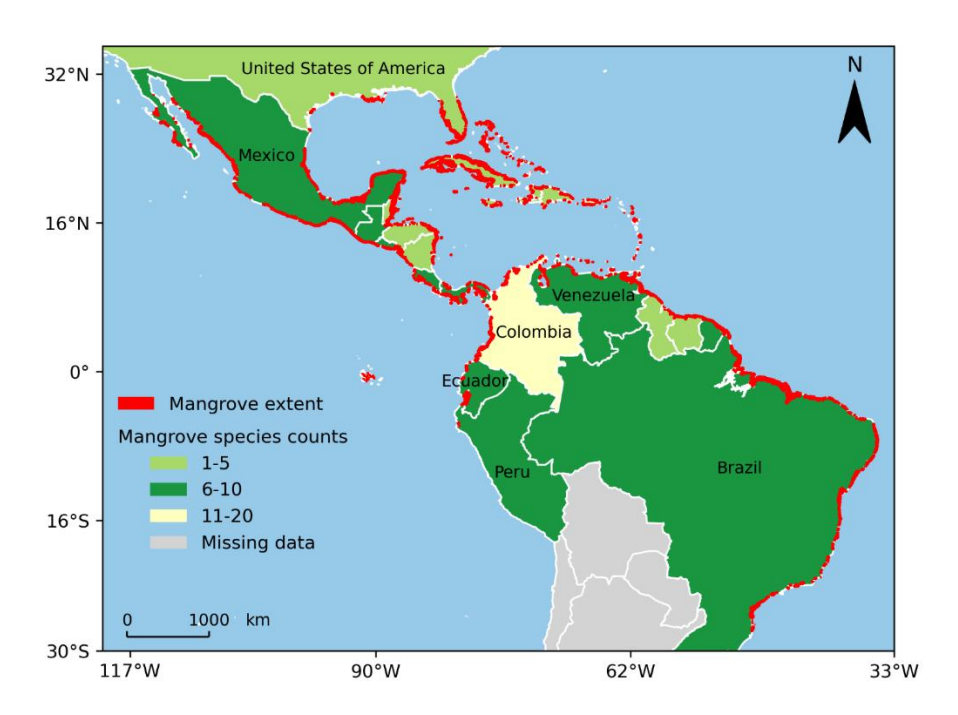


Figure 1-3. The distribution of mangrove forests across the Americas in 2020 derived from Jia et al. (2023) and species counts by country adapted from Spalding et al. (2010).

Regionally, this research focuses on mangrove forests bordering the lagoons of La Mancha (19°33′ – 19°36′ N, 96°22′ – 96°24′W) and El Llano (19°38′ – 19°40′N, 96°24′ – 96°25′W) in the state of Veracruz, Mexico (**Figure 1-4**). There are four mangrove species: *Avicennia germinans*, *Rhizophora mangle*, *Laguncularia racemosa* and *Conocarpus erectus*. The climate is classified as a sub-humid warm climate (Aw2), with annual precipitation ranging from 1,000 to 1,500 mm and an average annual temperature of around 24°C (RAMSAR, 2004). La Mancha lagoon and El Llano lagoon have surface areas of 135 ha and 226 ha, respectively (Chávez-López and Rocha-Ramírez, 2020; Vovides et al., 2021). La Mancha lagoon receives freshwater primarily from the Caño Gallegos River at its southern end of the lagoon and marine water from the Gulf of Mexico through an intermittently opened inlet in the northeastern end (Chacón Abarca et al., 2021; Chávez-Cerón et al., 2016; Harte Research Institute for Gulf of Mexico, 2021a). Salinity in the lagoon increases northward regardless of the season, influencing mangrove species zonation; *A. germinans* dominates the northern region with few *R. mangle*, while mixed forests of *A. germinans* with either *R. mangle* or *L. racemosa* is observed in the southern part of the lagoon (Méndez-Alonzo et al., 2012; Vovides

et al., 2018). *C. erectus* is less common, typically found in the eastern side of the area (Moreno-Casasola et al., 2009). Unlike La Mancha lagoon, the salinity of El Llano lagoon is regulated exclusively by marine water entering through an inlet in the northeastern part, which opens to the Gulf of Mexico only during rainfall. From November to January (dry season), a natural sandy bar forms, isolating the lagoon from the ocean. This separation leads to hyper-salinity in the lagoon during the low-water season (Chávez-López and Rocha-Ramírez, 2020; Harte Research Institute for Gulf of Mexico, 2021b). **Figure 1-5** provides supplementary context for the study area, showing field conditions and measurement activities carried out during the July 2022 field campaign.

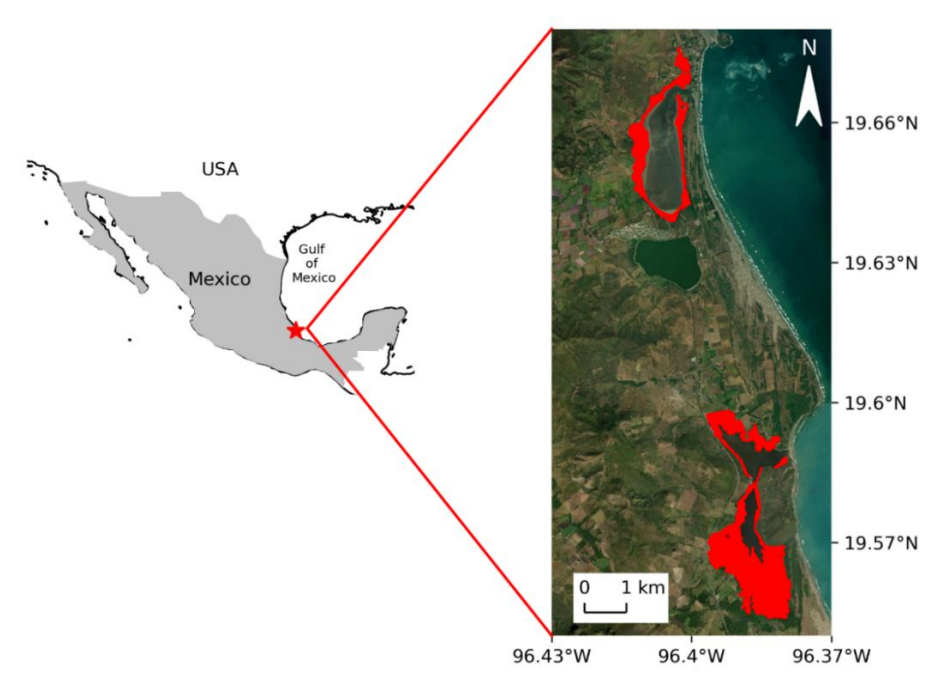


Figure 1-4. Geographical location of mangrove forests bordering El Llano (top) and La Mancha (bottom) lagoons (outlined in red) in Mexico.



Figure 1-5. Field photographs taken from the fieldwork in July 2022: (a) measurement of canopy height in the mangrove forest around El Llano lagoon by Alejandra Vovides and her assistant Alvaro Gonzalez Ruiz; (b) measurement of the diameter of a large *Rhizophora mangle* tree in the mangrove forest on the southeastern side of La Mancha lagoon by Kangyong Zhang.

1.6 Thesis structure

This thesis consists of seven chapters. Chapter 1 provides an introduction to the research and study areas, as well as outlining the aim, objectives and research questions. Chapter 2 is a literature review on how mangrove remote sensing has evolved, referring to remotely sensed data from spaceborne and airborne platforms and methodologies applied to mangrove research such as extent and species identification and biophysical parameter retrieval, as well as future opportunities. Chapter 3 proposes a methodology of mangrove AGB estimation across the mangrove forests around La Mancha and El Llano lagoon in Mexico. In this chapter, mangrove field data collected in 2022 was combined with historical field data for the development of plot-level biomass-height allometry. This allometry was subsequently applied to freely accessible DEMs calibrated with spaceborne LiDAR data to retrieve AGB estimation of mangroves in the study area. Chapter 4 proposes a methodology for mangrove AGB estimation across the Americas in 2020. A compilation of mangrove field data across the Americas was introduced to develop plot-level biomassheight allometry. Then, this allometry was applied to newer spaceborne LiDAR data from the mission of Global Ecosystem Dynamics Investigation (GEDI) for footprint-level AGB estimation. Due to the discrete nature of GEDI footprints, high-resolution spaceborne mosaics with environmental variables were employed with the help of Random Forests regression algorithm for wall-to-wall mangrove AGB retrieval at a continental level. Chapter 5 quantifies AGB dynamics of regrowing mangrove areas across the Americas over the last 20 years (2000-2020). This chapter defines the mangrove regrowth as regrowing mangroves in previously forested or non-forested areas, delineated using the annual tropical moist forest coverage dataset from Joint Research Centre (JRC). AGB estimates were derived for regrowing mangroves in 2000 and 2020 based on period-specific methodologies. Therefore, mangrove resilience was investigated by quantifying two-decade AGB dynamics in regrowth areas to discern post-disturbance recovery patterns. Chapter 6 synthesises the findings from the empirical chapters, providing further discussions on the methodological contributions, the transferability of the approaches and the implications for broader research. It also outlines the limitations of this research and key recommendations for future research. Finally, Chapter 7 concludes the thesis by reflecting on the challenges, insights and advances achieved in this research.

References

- Alongi, D.M., 2020. Global Significance of Mangrove Blue Carbon in Climate Change Mitigation. Sci 2, 67. https://doi.org/10.3390/sci2030067
- Asbridge, E., Lucas, R., Rogers, K., et al., 2018. The extent of mangrove change and potential for recovery following severe Tropical Cyclone Yasi, Hinchinbrook Island, Queensland, Australia. Ecology and Evolution 8, 10416–10434. https://doi.org/10.1002/ece3.4485
- Brander, L.M., Wagtendonk, A.J., Hussain, S.S., et al., 2012. Ecosystem service values for mangroves in Southeast Asia: A meta-analysis and value transfer application. Ecosystem Services 1, 62–69. https://doi.org/10.1016/j.ecoser.2012.06.003
- Bryan-Brown, D.N., Connolly, R.M., Richards, D.R., et al., 2020. Global trends in mangrove forest fragmentation. Scientific Reports 10. https://doi.org/10.1038/s41598-020-63880-1
- Cannicci, S., Burrows, D., Fratini, S., et al., 2008. Faunal impact on vegetation structure and ecosystem function in mangrove forests: A review. Aquatic Botany 89, 186–200. https://doi.org/10.1016/j.aquabot.2008.01.009
- Carrasquilla-Henao, M., Juanes, F., 2017. Mangroves enhance local fisheries catches: a global meta-analysis. Fish and Fisheries 18, 79–93. https://doi.org/10.1111/faf.12168
- Chacón Abarca, S., Chávez, V., Silva, R., et al., 2021. Understanding the Dynamics of a Coastal Lagoon:
 Drivers, Exchanges, State of the Environment, Consequences and Responses. Geosciences 11.
 https://doi.org/10.3390/geosciences11080301
- Chávez-Cerón, V., Mendoza-Baldwin, E., Ramírez-Méndez, E., et al., 2016. Response of Empirically Managed Sites to Winter Storms. Case Study: La Mancha, Veracruz, Mexico. Coastal Engineering Proceedings 15–15. https://doi.org/10.9753/icce.v35.management.15
- Chávez-López, R., Rocha-Ramírez, A., 2020. Composición de la comunidad de peces en el estuario ciego laguna El Llano, Veracruz, México. Revista Mexicana de Biodiversidad 91. https://doi.org/10.22201/ib.20078706e.2020.91.2494
- Chowdhury, R., Sutradhar, T., Begam, Mst.M., et al., 2019. Effects of nutrient limitation, salinity increase, and associated stressors on mangrove forest cover, structure, and zonation across Indian Sundarbans. Hydrobiologia 842, 191–217. https://doi.org/10.1007/s10750-019-04036-9
- Cochard, R., Ranamukhaarachchi, S.L., Shivakoti, G.P., et al., 2008. The 2004 tsunami in Aceh and Southern Thailand: A review on coastal ecosystems, wave hazards and vulnerability. Perspectives in Plant Ecology, Evolution and Systematics 10, 3–40. https://doi.org/10.1016/j.ppees.2007.11.001
- Dahdouh-Guebas, F., Van Pottelbergh, I., Kairo, J.G., et al., 2004. Human-impacted mangroves in Gazi (Kenya): Predicting future vegetation based on retrospective remote sensing, social surveys, and tree distribution. Marine Ecology Progress Series 272, 77–92. https://doi.org/10.3354/meps272077

- Ellison, A.M., Farnsworth, E.J., Merkt, R.E., 1999. Origins of mangrove ecosystems and the mangrove biodiversity anomaly. Global Ecology and Biogeography 8, 95–115. https://doi.org/10.1046/j.1466-822X.1999.00126.x
- FAO, 2023. The world's mangroves 2000–2020. FAO, Rome. https://doi.org/10.4060/cc7044en
- Friess, D.A., Thompson, B.S., Brown, B., et al., 2016. Policy challenges and approaches for the conservation of mangrove forests in Southeast Asia. Conservation Biology 30, 933–949. https://doi.org/10.1111/cobi.12784
- Gilman, E.L., Ellison, J., Duke, N.C., et al., 2008. Threats to mangroves from climate change and adaptation options: A review. Aquatic Botany 89, 237–250. https://doi.org/10.1016/j.aquabot.2007.12.009
- Han, X., Feng, L., Hu, C., et al., 2018. Hurricane-Induced Changes in the Everglades National Park Mangrove Forest: Landsat Observations Between 1985 and 2017. Journal of Geophysical Research: Biogeosciences 123, 3470–3488. https://doi.org/10.1029/2018jg004501
- Hu, W., Wang, Y., Zhang, D., et al., 2020. Mapping the potential of mangrove forest restoration based on species distribution models: A case study in China. Science of The Total Environment 748, 142321. https://doi.org/10.1016/j.scitotenv.2020.142321
- Hutchison, J., Spalding, M., zu Ermgassen, P., 2014. The role of mangroves in fisheries enhancement. The Nature Conservancy and Wetlands International 54.
- Jia, M., Wang, Z., Mao, D., et al., 2023. Mapping global distribution of mangrove forests at 10-m resolution. Science Bulletin 68, 1306–1316. https://doi.org/10.1016/j.scib.2023.05.004
- Jia, M.M., Zhang, Y.Z., Wang, Z.M., et al., 2014. Mapping the distribution of mangrove species in the Core Zone of Mai Po Marshes Nature Reserve, Hong Kong, using hyperspectral data and high-resolution data. Int. J. Appl. Earth Obs. Geoinf. 33, 226–231. https://doi.org/10.1016/j.jag.2014.06.006
- Jusoff, K., 2013. Malaysian Mangrove Forests and their Significance to the Coastal Marine Environment. Polish journal of environmental studies 22.
- Katila, P., Pierce Colfer, C.J., de Jong, W., et al., 2019. Sustainable Development Goals: Their Impacts on Forests and People. https://doi.org/10.1017/9781108765015
- Kauffman, J.B., Adame, M.F., Arifanti, V.B., et al., 2020. Total ecosystem carbon stocks of mangroves across broad global environmental and physical gradients. Ecological Monographs 90, e01405. https://doi.org/10.1002/ecm.1405
- Lee, C.K.F., Duncan, C., Nicholson, E., et al., 2021. Mapping the Extent of Mangrove Ecosystem Degradation by Integrating an Ecological Conceptual Model with Satellite Data. Remote Sensing 13, 2047. https://doi.org/10.3390/rs13112047
- Lovelock, C.E., Cahoon, D.R., Friess, D.A., et al., 2015. The vulnerability of Indo-Pacific mangrove forests to sea-level rise. Nature 526, 559–563. https://doi.org/10.1038/nature15538

- Lucas, R., Van De Kerchove, R., Otero, V., et al., 2020. Structural characterisation of mangrove forests achieved through combining multiple sources of remote sensing data. Remote Sensing of Environment 237. https://doi.org/10.1016/j.rse.2019.111543
- Ma, C., Ai, B., Zhao, J., et al., 2019. Change detection of mangrove forests in coastal Guangdong during the past three decades based on remote sensing data. Remote Sensing 11. https://doi.org/10.3390/rs11080962
- Mafi-Gholami, D., Mahmoudi, B., Zenner, E.K., 2017. An analysis of the relationship between drought events and mangrove changes along the northern coasts of the Persian Gulf and Oman Sea. Estuarine, Coastal and Shelf Science 199, 141–151. https://doi.org/10.1016/j.ecss.2017.10.008
- Maurya, K., Mahajan, S., Chaube, N., 2021. Remote sensing techniques: mapping and monitoring of mangrove ecosystem—a review. Complex Intell. Syst. 7, 2797–2818. https://doi.org/10.1007/s40747-021-00457-z
- McIvor, A., Spencer, T., Spalding, M., et al., 2015. Mangroves, Tropical Cyclones, and Coastal Hazard Risk Reduction, in: Coastal and Marine Hazards, Risks, and Disasters. Elsevier, pp. 403–429. https://doi.org/10.1016/b978-0-12-396483-0.00014-5
- Méndez-Alonzo, R., Hernández-Trejo, H., López-Portillo, J., 2012. Salinity constrains size inequality and allometry in two contrasting mangrove habitats in the Gulf of Mexico. Journal of Tropical Ecology 28, 171–179. https://doi.org/10.1017/S0266467412000016
- Moreno-Casasola, P., López Rosas, H., Infante Mata, D., et al., 2009. Environmental and anthropogenic factors associated with coastal wetland differentiation in La Mancha, Veracruz, Mexico. Plant Ecol 200, 37–52. https://doi.org/10.1007/s11258-008-9400-7
- Mumby, P.J., Edwards, A.J., Ernesto Arias-González, J., et al., 2004. Mangroves enhance the biomass of coral reef fish communities in the Caribbean. Nature 427, 533–536. https://doi.org/10.1038/nature02286
- Nagelkerken, I., Blaber, S.J.M., Bouillon, S., et al., 2008. The habitat function of mangroves for terrestrial and marine fauna: A review. Aquatic Botany 89, 155–185. https://doi.org/10.1016/j.aquabot.2007.12.007
- Ouyang, X., Guo, F., 2016. Paradigms of mangroves in treatment of anthropogenic wastewater pollution. Science of The Total Environment 544, 971–979. https://doi.org/10.1016/j.scitotenv.2015.12.013
- Pham, T.D., Yokoya, N., Bui, D.T., et al., 2019. Remote Sensing Approaches for Monitoring Mangrove Species, Structure, and Biomass: Opportunities and Challenges. Remote Sensing 11, 230. https://doi.org/10.3390/rs11030230
- Primavera, J.H., 2000. Development and conservation of Philippine mangroves: institutional issues. Ecological Economics 35, 91–106. https://doi.org/10.1016/s0921-8009(00)00170-1

- Quoc Vo, T., Kuenzer, C., Oppelt, N., 2015. How remote sensing supports mangrove ecosystem service valuation: A case study in Ca Mau province, Vietnam. Ecosystem Services 14, 67–75. https://doi.org/10.1016/j.ecoser.2015.04.007
- RAMSAR, 2004. La Mancha y El Llano: Ramsar sites information service. [WWW Document]. URL https://rsis.ramsar.org/ris/1336?language=en
- Romer, H., Jeewarongkakul, J., Kaiser, G., et al., 2012. Monitoring post-tsunami vegetation recovery in Phang-Nga province, Thailand, based on IKONOS imagery and field investigations a contribution to the analysis of tsunami vulnerability of coastal ecosystems. Int. J. Remote Sens. 33, 3090–3121. https://doi.org/10.1080/01431161.2011.628710
- Servino, R.N., Gomes, L.E.D.O., Bernardino, A.F., 2018. Extreme weather impacts on tropical mangrove forests in the Eastern Brazil Marine Ecoregion. Science of the Total Environment 628–629, 233–240. https://doi.org/10.1016/j.scitotenv.2018.02.068
- Song, S., Ding, Y., Li, W., et al., 2023. Mangrove reforestation provides greater blue carbon benefit than afforestation for mitigating global climate change. Nat Commun 14, 756. https://doi.org/10.1038/s41467-023-36477-1
- Spalding, M., Kainuma, M., Collins, L., 2010. World atlas of mangroves. Earthscan, London, Washington D.C.
- Spalding, M., McIvor, A., Tonneijck, F., et al., 2014. Mangroves for coastal defence. Guidelines for coastal managers and policy makers. Wetlands International and The Nature Conservancy 13–34.
- Spalding, M., Parrett, C.L., 2019. Global patterns in mangrove recreation and tourism. Marine Policy 110. https://doi.org/10.1016/j.marpol.2019.103540
- Spalding, M.D., Leal, M. (Eds.), 2022. The State of the World's Mangroves 2022. Global Mangrove Alliance.
- Taillardat, P., Friess, D.A., Lupascu, M., 2018. Mangrove blue carbon strategies for climate change mitigation are most effective at the national scale. Biology Letters 14, 20180251. https://doi.org/10.1098/rsbl.2018.0251
- Thomas, N., Lucas, R., Bunting, P., et al., 2017. Distribution and drivers of global mangrove forest change, 1996–2010. PLOS ONE 12, e0179302. https://doi.org/10.1371/journal.pone.0179302
- Twomey, A., Lovelock, C., 2024. Global spatial dataset of mangrove genus distribution in seaward and riverine margins. Sci Data 11, 306. https://doi.org/10.1038/s41597-024-03134-1
- Uddin, M.M., Abdul Aziz, A., Lovelock, C.E., 2023. Importance of mangrove plantations for climate change mitigation in Bangladesh. Global Change Biology 29, 3331–3346. https://doi.org/10.1111/gcb.16674
- Vancutsem, C., Achard, F., Pekel, J.-F., et al., 2021. Long-term (1990–2019) monitoring of forest cover changes in the humid tropics. Science Advances 7, eabe1603. https://doi.org/10.1126/sciadv.abe1603

- Vovides, A.G., Berger, U., Grueters, U., et al., 2018. Change in drivers of mangrove crown displacement along a salinity stress gradient. Functional Ecology 32, 2753–2765. https://doi.org/10.1111/1365-2435.13218
- Vovides, A.G., Wimmler, M.-C., Schrewe, F., et al., 2021. Cooperative root graft networks benefit mangrove trees under stress. Communications Biology 4. https://doi.org/10.1038/s42003-021-02044-x
- Walters, B.B., Rönnbäck, P., Kovacs, J.M., et al., 2008. Ethnobiology, socio-economics and management of mangrove forests: A review. Aquatic Botany 89, 220–236. https://doi.org/10.1016/j.aquabot.2008.02.009
- Waltham, N.J., Elliott, M., Lee, S.Y., et al., 2020. UN Decade on Ecosystem Restoration 2021–2030—What Chance for Success in Restoring Coastal Ecosystems? Frontiers in Marine Science 7. https://doi.org/10.3389/fmars.2020.00071
- Wang, L., Jia, M., Yin, D., et al., 2019. A review of remote sensing for mangrove forests: 1956–2018. Remote Sensing of Environment 231, 111223. https://doi.org/10.1016/j.rse.2019.111223
- Wang, L., Mu, M., Li, X., et al., 2011. Differentiation between true mangroves and mangrove associates based on leaf traits and salt contents. Journal of Plant Ecology 4, 292–301. https://doi.org/10.1093/jpe/rtq008
- Woodroffe, C.D., Lovelock, C.E., Rogers, K., 2015. Mangrove Shorelines, in: Masselink, G., Gehrels, R. (Eds.), Coastal Environments and Global Change. Wiley, New York, NY, USA, pp. 251–267.
- Worthington, T.A., Andradi-Brown, D.A., Bhargava, R., et al., 2020. Harnessing Big Data to Support the Conservation and Rehabilitation of Mangrove Forests Globally. One Earth 2, 429–443. https://doi.org/10.1016/j.oneear.2020.04.018
- Worthington, T., Spalding, M., 2018. Mangrove restoration potential: A global map highlighting a critical opportunity. https://doi.org/10.17863/CAM.39153
- Zhai, L., Zhang, B., Roy, S.S., et al., 2019. Remote sensing of unhelpful resilience to sea level rise caused by mangrove expansion: A case study of islands in Florida Bay, USA. Ecological Indicators 97, 51–58. https://doi.org/10.1016/j.ecolind.2018.09.063

Chapter 2 Evolution of mangrove remote sensing

2.1 Introduction

Remote sensing allows for large-scale surveys over mangrove forests, offering spatially explicit, highly resolved and temporally revisited observations to support mangrove research areas such as distribution mapping, species discrimination, and biophysical parameter retrieval. It leverages passive and active sensors on board satellites, aircrafts and UAVs to acquire multispectral and hyperspectral imagery, along with radar and LiDAR data. Remote sensing therefore facilitates the assessment of mangrove health, the monitoring of deforestation and restoration efforts, and the evaluation of their resilience in the context of anthropogenic activities and climate change through integrated data analyses. The approaches to the analysis of remotely sensed data include visual interpretation, object-oriented methods, empirical models and machine learning algorithms, which can be deployed independently or in combinations to meet varied research objectives. Recent trends suggest that data fusion and deep learning provide significant potentials in improved accuracy, greater reliability and comprehensive insights for high-resolution canopy height estimation and dynamic mangrove monitoring system.

2.2 Remote sensing data for monitoring mangroves

2.2.1 Spaceborne optical imagery

Remote sensing datasets can be obtained through satellites, aircrafts or UAVs with varied data coverage (**Figure 2-1**). Spaceborne optical remote sensing is a passive technique featuring sensors such as radiometers or spectroradiometers onboard satellites that capture radiation reflected and emitted from the earth's surfaces between the visible wavelengths (0.4-0.7 μm) to near infrared (NIR, 0.7-1.5 μm) and up to thermal infrared (TIR, 8-14 μm). Since the launch of the first Landsat satellite in 1972 on which the Multispectral Scanner (MSS) was mounted (NASA, 2021), the availability and capabilities of spaceborne optical remote sensing missions have improved, varying in spatial and spectral resolutions (see **Table 2-1**). These remote sensors support global observation of earth's surfaces at frequent time intervals, providing multispectral or hyperspectral information. Given spatially explicit spectrum-rich information and intensive revisit time, spaceborne optical remote sensing has therefore become one of the most appropriate candidates in ecosystem monitoring, although the strong interaction of the electromagnetic radiation at these frequencies with the atmosphere and the occurrence of clouds constrains from retrieving valid observations.

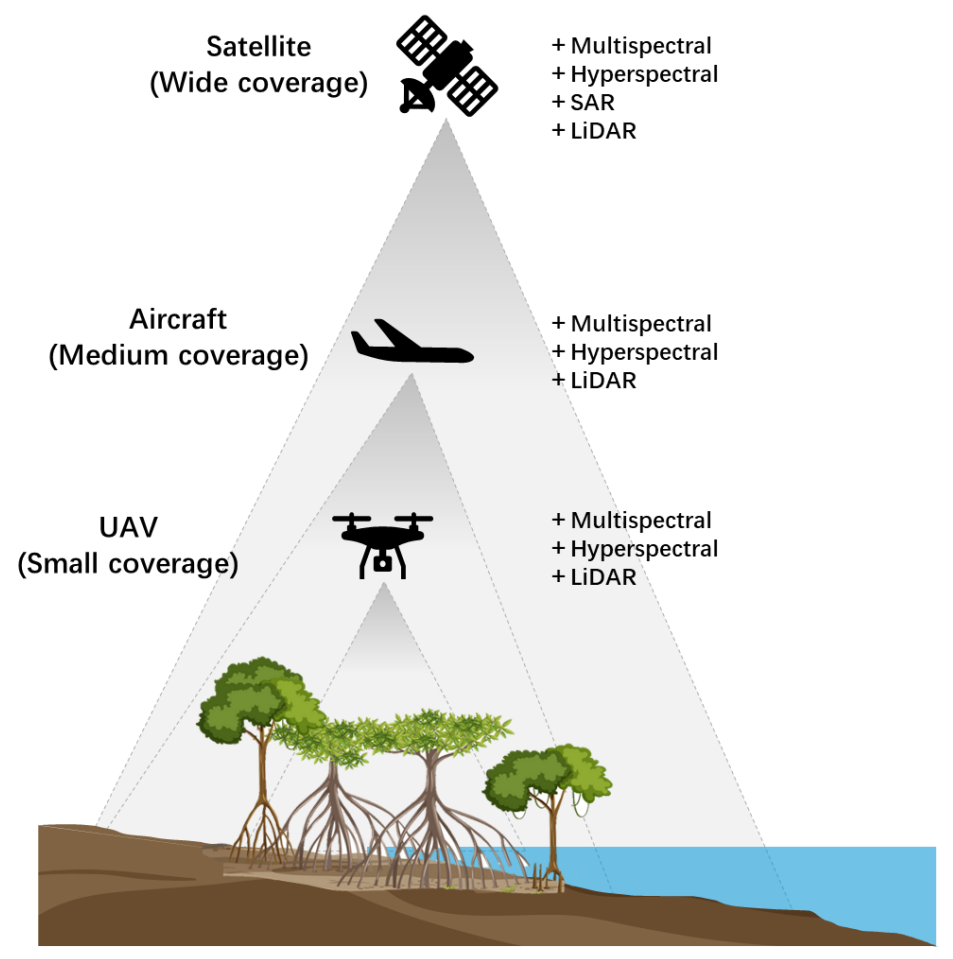


Figure 2-1. Remote sensing datasets acquired for monitoring mangroves.

Spaceborne optical imagery, capturing spectral and textural characteristics of mangrove canopies, delivers valuable data for advancing mangrove research (Wang et al., 2019). Landsat imagery is widely accepted as an appropriate spaceborne dataset for monitoring mangroves, due to its provision of global 30 m multispectral observations featuring long-term time-series and free access. These characteristics make Landsat images effective for mapping mangrove extent (e.g., Giri et al., 2011; Monsef and Smith, 2017; Rogers et al., 2017; Spalding et al., 2010; Wang et al., 2018), particularly for consistent mappings over time (FAO, 2023; Goldberg et al., 2020; Hamilton and Casey, 2016). However, it is challenging to outline mangrove patches smaller than moderate resolution images (~30 m), particularly in West Africa where mangroves are found as narrow riverine fringes (Liu et al., 2021). The delineation of mangrove distribution is finer using very high resolution (VHR) spaceborne imagery (<10 m) such as Gaofen-2, Pleiades and Ziyuan-3, providing finer textural information of canopies to detect scattered and small mangrove patches (e.g., Friess et al., 2016; Jia et al., 2023; Zhang et al., 2021a; Zhang et al., 2021b). Due to the trade-off between spectral and spatial resolution in spaceborne datasets, spaceborne VHR imagery typically includes only the blue, green, red and NIR bands (Table 2-1). Nevertheless, VHR imagery can capture finer textures of mangrove canopies, which helps avoid saturation in high biomass estimation (Proisy et al., 2007). Moreover, combining VHR imagery with spectral features can improve biomass estimation accuracy (Pham

and Brabyn, 2017), and the introduction of VHR imagery provides species discrimination performance comparable to that of hyperspectral imagery at similar fine resolutions (Jia et al., 2014; Lassalle et al., 2023).

Apart from the provision of finer textures, spaceborne optical imagery enables finer spectral investigation over mangroves, such as Gaofen-5, Hyperion, PRISMA, and DESIS (Jia et al., 2014; Kumar et al., 2019; Lassalle et al., 2023; Wan et al., 2020). In situ spectral reflectance measurements with portable spectroradiometers highlighted the detectability of hyperspectral signal for subtle spectral variations between mangrove species (Xu et al., 2019, **Figure 2-2**). The reflectance of mangrove leaves in NIR and shortwave infrared (SWIR) channels shows better spectral separability for species discrimination (Hoa et al., 2017; Kuenzer et al., 2011; Lassalle et al., 2023; Wang and Sousa, 2009; Zulfa et al., 2020). However, spaceborne hyperspectral imagery generally has a spatial resolution of 30 m, limiting the application in identifying mangrove species within highly mixed communities or small-patch (i.e., narrow) areas (Jia et al., 2014; Mondal et al., 2019). Since its launch in 2015, Sentinel-2 imagery, with high resolution (up to 10 m) and multispectral information including red edge and SWIR bands, has become another appropriate spaceborne optical dataset in mangrove research (e.g., Jia et al., 2023, 2024; Manna and Raychaudhuri, 2020; Maung and Sasaki, 2021; Navarro et al., 2019; Parida and Kumari, 2021; Zhang et al., 2023).

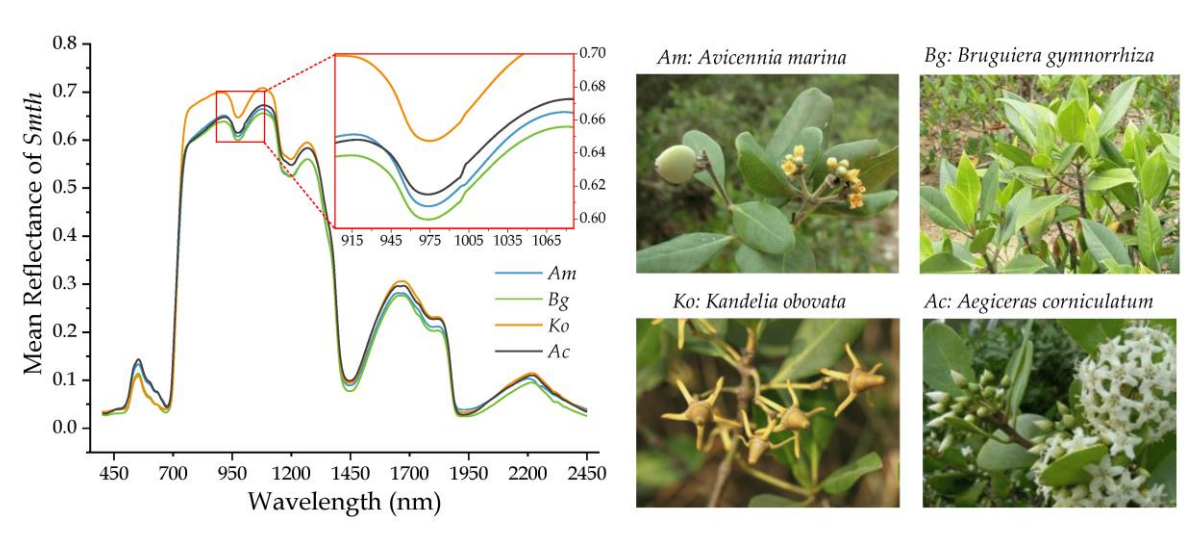


Figure 2-2. The smoothed reflectance spectrum of four mangrove species in China and field photos of corresponding mangrove species (Source: Xu et al. (2019)).

Table 2-1. The specifications of spaceborne optical sensors.

Satellite and Sensor	Band names with pixel size and wavelength (µm)	Revisit time	Operating period
Landsat 1-5 MSS	60 m Green: 0.5 – 0.6 60 m Red: 0.6 – 0.7 60 m NIR 1: 0.7 – 0.8 60 m NIR 2: 0.8 – 1.1	18 days for Landsat 1/2/3 16 days for Landsat 4/5	23/07/1972 – 06/01/1978 (Landsat 1) 22/01/1975 – 27/07/1983 (Landsat 2) 05/03/1978 – 07/09/1983 (Landsat 3)
Landsat 4/5 TM	30 m Blue: 0.45 – 0.52 30 m Green: 0.52 – 0.60 30 m Red: 0.63 – 0.69 30 m NIR: 0.76 – 0.90 30 m SWIR-1: 1.55 – 1.75 120 m TIR: 10.41 – 12.5 30 m SWIR-2: 2.08 – 2.35	16 days	16/07/1982 – 15/06/2001 (Landsat 4) 01/03/1984 – 19/06/2013 (Landsat 5)
Landsat 7 ETM+	30 m Blue: 0.441 – 0.514 30 m Green: 0.519 – 0.601 30 m Red: 0.631 – 0.692 30 m NIR: 0.772 – 0.898 30 m SWIR-1: 1.547 – 1.749 60 m TIR: 10.31 – 12.36 30 m SWIR-2: 2.064 - 2.345 15 m PAN: 0.515 – 0.896	16 days (when combined with Landsat 8, revisit time for data collection can be every 8 days)	15/04/1999 to present (Scan Line Corrector failure on 31/05/2003)
Landsat 8/9 OLI/OLI-2	30 m Coastal/Aerosol: 0.435 – 0.451 30 m Blue: 0.452 – 0.512 30 m Green: 0.533 – 0.590 30 m Red: 0.636 – 0.673 30 m NIR: 0.851 – 0.879 30 m SWIR-1: 1.566 – 1.651 30 m SWIR-2: 2.107 – 2.294 15 m PAN: 0.503 – 0.676 30 m Cirrus: 1.363 – 1.384 100 m TIR-1: 10.60 – 11.19 100 m TIR-2: 11.50 – 12.51	16 days (the combination of Landsat 8 and 9 can make revisit time for data collection every 8 days)	11/02/2013 to present (Landsat 8) 27/09/2021 to present (Landsat 9)

Table 2-1. Continued.

Satellite and Sensor	Band names with pixel size and wavelength (μm)	Revisit time	Operating period
Sentinel-2A/B MSI	Note: wavelengths here are central wavelength 60 m Coastal/Aerosol: 0.444 (S2A) / 0.442 (S2B) 10 m Blue: 0.497 (S2A) / 0.492 (S2B) 10 m Green: 0.560 (S2A) / 0.559 (S2B) 10 m Red: 0.664 (S2A) / 0.665 (S2B) 20 m Red Edge-1: 0.704 (S2A) / 0.704 (S2B) 20 m Red Edge-2: 0.740 (S2A) / 0.739 (S2B) 20 m Red Edge-3: 0.783 (S2A) / 0.780 (S2B) 10 m NIR: 0.835 (S2A) / 0.833 (S2B) 20 m Red Edge-4: 0.865 (S2A) / 0.864 (S2B) 60 m Water vapour: 0.945 (S2A) / 0.943 (S2B) 60 m Cirrus: 1.374 (S2A) / 1.377 (S2B) 20 m SWIR-1: 1.614 (S2A) / 1.610 (S2B) 20 m SWIR-2: 2.202 (S2A) / 2.186 (S2B)	10 days for each, 5 days for combined constellation	23/06/2015 to present (Sentinel-2A) 07/03/2017 to present (Sentinel-2B)
SPOT-1/2/3 HRV	20 m Green: 0.50 – 0.59 20 m Red: 0.61 – 0.68 20 m NIR: 0.79 – 0.89 10 m PAN: 0.51 – 0.73	About 1 to 4 days depending on the latitude due to oblique viewing capability	22/02/1986 – 17/11/2003 (SPOT 1) 22/01/1990 – 30/07/2009 (SPOT 2) 26/09/1993 – 14/11/1996 (SPOT 3)
SPOT-4 HRVIR/VGT	10 m Green: 0.50 – 0.59 10 m Red: 0.61 – 0.68 10 m NIR: 0.78 – 0.89 20 m SWIR: 1.58 – 1.75 10 m PAN: 0.61 – 0.71 (VGT) 1.15 km Blue: 0.437 - 0.480 (VGT) 1.15 km Red: 0.615 - 0.700 (VGT) 1.15 km NIR: 0.773 - 0.894 (VGT) 1.15 km SWIR: 1.603 - 1.695	About 1 to 4 days depending on the latitude due to oblique viewing capability (During February to end of May in 2013, repeat interval was changed to 5 days as the altitude of SPOT 4 had been lowered.)	24/03/1998 – 29/06/2013

Table 2-1. Continued.

Satellite and Sensor	Band names with pixel size and wavelength (μm)	Revisit time	Operating period
SPOT-5 HRG/HRS/VGT-2	20 m Green: 0.50 – 0.59 20 m Red: 0.61 – 0.68 20 m NIR: 0.79 – 0.89 20 m SWIR: 1.53 – 1.75 2.5/5 m PAN: 0.48 – 0.71 5/10 m PAN: 0.48 – 0.70 (for stereo pair images) (VGT-2) 1.15 km Blue: 0.439 - 0.476 (VGT-2) 1.15 km Red: 0.616 - 0.690 (VGT-2) 1.15 km NIR: 0.783 - 0.892 (VGT-2) 1.15 km SWIR: 1.584 - 1.685	About 2-3 days depending on latitude due to oblique viewing capability	04/05/2002 - 31/03/2015
SPOT-6/7 NAOMI SPOT-7 VGT-2 (Commercial)	6 m Blue: 0.45 – 0.52 6 m Green: 0.53 – 0.60 6 m Red: 0.62 – 0.69 6 m NIR: 0.76 – 0.89 1.5 m PAN: 0.45 – 0.75 (VGT-2) 1.15 km Blue: 0.439 - 0.476 (VGT-2) 1.15 km Red: 0.616 - 0.690 (VGT-2) 1.15 km NIR: 0.783 - 0.892 (VGT-2) 1.15 km SWIR: 1.584 - 1.685	1 day when SPOT 6 and 7 operate simultaneously, around 1 to 3 days when only one satellite does.	09/09/2012 to present (SPOT 6) 30/06/2014 to present (SPOT 7)
IKONOS OSA (Commercial)	4 m Blue: 0.45 – 0.53 4 m Green: 0.52 – 0.61 4 m Red: 0.64 – 0.72 4 m NIR: 0.76 – 0.86 1 m PAN: 0.45 – 0.90	Approximately 3 days at 40° latitude	24/09/1999 – 31/03/2015
RapidEye REIS (Commercial)	5 m Blue: 0.440 – 0.510 5 m Green: 0.520 – 0.590 5 m Red: 0.630 – 0.685 5 m Red Edge: 0.690 – 0.730 5 m NIR: 0.760 – 0.850	Daily revisit with body-pointing capability, 5.5 days at nadir over mid-latitude regions (\pm 84° latitude)	29/08/2008 – 31/03/2020 (constellation was deactivated)
QuickBird BGIS2000 (Commercial)	2.4 – 2.6 m Blue: 0.45 – 0.52 2.4 – 2.6 m Green: 0.52 – 0.60 2.4 – 2.6 m Red: 0.63 – 0.69 2.4 – 2.6 m NIR: 0.76 – 0.90 0.61 - 0.72 m PAN: 0.45 – 0.90	2.8 days at 1-metre GSD resolution 1.5 days at 1.5-metre GSD resolution (Both are at 20° latitude)	18/10/2001 — 27/01/2015

Table 2-1. Continued.

Satellite and Sensor	Band names with pixel size and wavelength (μm)	Revisit time	Operating period
WorldView-1 WV60 (Commercial)	0.50 - 0.55 m PAN: 0.45 – 0.90	1.7 days at 1 m GSD or less, 5.9 days at 20° off-nadir or less (0.51 m GSD)	18/09/2007 to present
WorldView-2 WV-110 (Commercial)	1.85 - 2.07 m Coastal Blue: 0.400 - 0.450 1.85 - 2.07 m Blue: 0.450 - 0.510 1.85 - 2.07 m Green: 0.510 - 0.580 1.85 - 2.07 m Yellow: 0.585 - 0.625 1.85 - 2.07 m Red: 0.630 - 0.690 1.85 - 2.07 m Red Edge: 0.705 - 0.745 1.85 - 2.07 m NIR-1: 0.770 - 0.895 1.85 - 2.07 m NIR-2: 0.860 - 1.040 0.46 - 0.52 m PAN: 0.45 - 0.80	1.1 days at 1 m GSD or less, 3.7 days at 20° off- nadir or less (0.52 m GSD)	08/10/2009 to present
WorldView-3 WV-110 (Commercial)	1.24 – 1.38 m Coastal Blue: 0.400 – 0.450 1.24 – 1.38 m Blue: 0.450 – 0.510 1.24 – 1.38 m Green: 0.510 – 0.580 1.24 – 1.38 m Yellow: 0.585 – 0.625 1.24 – 1.38 m Red: 0.630 – 0.690 1.24 – 1.38 m Red Edge: 0.705 – 0.745 1.24 – 1.38 m NIR-1: 0.770 – 0.895 1.24 – 1.38 m NIR-2: 0.860 – 1.040 0.31 - 0.34 m PAN: 0.45 – 0.80 3.70 – 4.10 m SWIR-1: 1.195 – 1.225 3.70 – 4.10 m SWIR-2: 1.550 – 1.590 3.70 – 4.10 m SWIR-3: 1.640 – 1.680 3.70 – 4.10 m SWIR-4: 1.710 – 1.750 3.70 – 4.10 m SWIR-5: 2.145 – 2.185 3.70 – 4.10 m SWIR-6: 2.185 – 2.225 3.70 – 4.10 m SWIR-7: 2.235 – 2.285 3.70 – 4.10 m SWIR-7: 2.235 – 2.285	About 1 day at 1 m GSD, 4.5 days at 20° off-nadir or less (0.59 m GSD)	13/08/2014 to present
WorldView-4 WV-110 (Commercial)	1.24/1.38/4 m Blue: 0.450 – 0.510 1.24/1.38/4 m Green: 0.510 – 0.580 1.24/1.38/4 m Red: 0.655 – 0.690 1.24/1.38/4 m NIR: 0.780 – 0.920 0.31/0.34/1 m PAN: 0.45 – 0.80	Less than 1.0 day at 1 m GSD (at 40° N latitude), more than 4.5 accesses per day for combined constellation	11/11/2016 – 07/01/2019

Table 2-1. Continued.

Satellite and Sensor	Band names with pixel size and wavelength (μm)	Revisit time	Operating period
Gaofen-2 PMC-2 (Chargeable)	3.24 m Blue: 0.45 - 0.52 3.24 m Green: 0.52 - 0.59 3.24 m Red: 0.63 - 0.69 3.24 m NIR: 0.77 - 0.89 0.81 m PAN: 0.45 - 0.90	5 days	19/08/2014 to present
Gaofen-5 AHSI/ VIMS (Commercial)	30 m spectral bands (from 0.4 to 2.5 μm) with the bandwidths of 5 nm for VNIR bands and 10 nm for SWIR bands (AHSI sensor) 20/40 m 12 spectral bands from 0.45 to 12.5 μm (VIMS sensor)	2 days	09/05/2018 to present
PlanetScope PSB.SD (Commercial)	3.7 - 4.2 m Coastal Blue: 0.431 – 0.452 3.7 - 4.2 m Blue: 0.465 – 0.515 3.7 - 4.2 m Green I: 0.513 – 0.549 3.7 - 4.2 m Green: 0.547 – 0.583 3.7 - 4.2 m Yellow: 0.600 – 0.620 3.7 - 4.2 m Red: 0.650 – 0.680 3.7 - 4.2 m Red Edge: 0.697 – 0.713 3.7 - 4.2 m NIR: 0.845 – 0.885	daily	Mid-Mach 2020 to present
EnMap	30 m 224 spectral bands with intervals of 6.5 nm and 10 nm in the VNIR (420 - 1000 nm) and SWIR (900 - 2450 nm) channels, respectively	27 days	01/04/2022 to present
EO-1 Hyperion	30 m 220 spectral bands (from 0.357 to 2.576 μ m) with a 10 nm bandwidth	16 days	21/11/2000 - 22/02/2017

OLI: Operational Land Imager; NIR: Near Infrared; SWIR: Shortwave Infrared; MSI: Multi-Spectral Instrument; SPOT: Système Pour l'Observation de la Terre; HRV: High-Resolution Visible; HRVIR: High-Resolution Visible and InfraRed; HRG: High-Resolution Geometric; HRS: High-Resolution Stereoscopic; NAOMI: New AstroSat Optical Modular Instrument; VGT: Vegetation Monitoring Instrument; OSA: Optical Sensor Assembly; REIS: RapidEye Earth-imaging System; BGIS2000: Ball Global Imagery System 2000; GSD: Ground Sample Distance; WV60: WorldView-60 camera; WV110: WorldView-110 camera; PMC-2: Panchromatic and Multispectral Camera Suite-2; AHSI: Advanced Hyper-Spectral Imager; VIMS: Visual and Infrared Multispectral Sensor; VNIR: Visible and Near Infrared; PSB.SD: PlanetScope Blue SuperDove; EnMap: Environmental Mapping and Analysis Program.

2.2.2 Spaceborne radar imagery

There is a fundamental challenge with spaceborne optical imagery as clouds have adverse impacts on the retrieval of spectral data from the ground, particularly in humid tropical areas, where cloud cover is frequent, persistent, and often dense. In contrast, synthetic aperture radar (SAR) data can be obtained independent of the weather conditions or time of day. SAR operates as an active sensor, generating and transmitting microwave signals and subsequently receives the returned or backscattered signals from the earth surface. The wavebands of spaceborne SAR data used in mangrove research include X-, C- and L-bands (see **Table 2-2**). Shorter wavelengths such as X-band (2.5-3.75 cm) and C-band (3.75-7.5 cm) strongly interact with the top of the canopy, while longer wavelengths such as L-band (15-30 cm) can penetrate through the canopy and interact with the larger tree structures such as trunks and larger branches (**Figure 2-3**). As SAR collects returned signals either horizontally or vertically, the type of SAR data consist of horizontal (HH), vertical (VV), and cross (HV or VH) polarization, which is a crucial parameter for understanding the interaction between electromagnetic waves and vegetation structures.

Table 2-2. The specifications of spaceborne radar sensors used in mangrove research.

			_	
Satellite and sensor	Waveband	Imaging mode and resolution (m)	Revisit time	Operating period
TanDEM-X	X	12 m (DEM product)	11 days	21/06/2010
Sentinel-1 A/B	С	Strip map: 3.5/10/40 Interferometric Wide swath: 10/40 Extra-Wide swath: 25/40 Wave: 25	6 - 12 days	03/04/2014 to present
RADARSAT	С	Extended High: 18 - 27 Extended Low: 30 ScanSAR Wide: 100 ScanSAR Narrow: 50 Wide: 30 Standard: 30 Fine: 8	24 days	04/11/1995 – 29/03/2013
RADARSAT-2	C	1 – 100 m depending on polarization and imaging modes	24 days	14/12/2007 to present
Envisat ASAR	C	Image: 30 Alternate Polarization: 30 Wide Swath: 150 Global Monitoring: 1000 Wave: 10	35 days	01/03/2002 - 08/04/2012
ERS-2 AMI	C	Image: 30 Wave: 30	35 days	21/04/1995 - 04/07/2011
JERS-1	L	18 m (range) x 18 m (azimuth, 3 looks)	44 days	11/02/1992 – 12/10/1998
ALOS PALSAR	L	Fine: 10/20 ScanSAR: 100 Polarimetric: 30	46 days	24/01/2006 - 12/05/2011

Table 2-2. Continued.

Satellite and sensor	Waveband	Imaging mode and resolution (m)	Revisit time	Operating period
ALOS-2 PALSAR-2	L	Strip map: 3/6/10 ScanSAR: 60/100 Spotlight: 1×3	24 days	24/05/2014 to present

ASAR: Advanced Synthetic Aperture Radar; **AMI**: Along-Track Scanning Radiometer; **JERS**: Japanese Earth Resources Satellite; **ALOS**: Advanced Land Observing Satellite; **PALSAR**: Phased Array L-band Synthetic Aperture Radar.

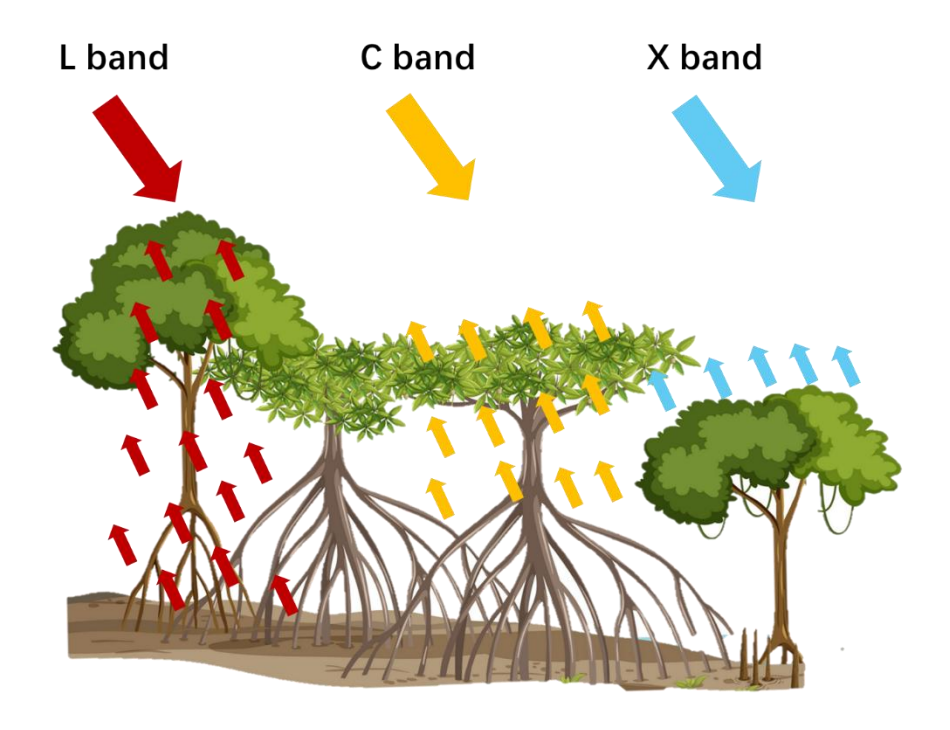


Figure 2-3. Schematic diagram of different wavelengths of radar system penetrating through mangroves.

Mangroves exhibit relatively higher backscattering coefficient on SAR data than the adjacent non-forest land covers. Applying thresholds on backscattering coefficient on spaceborne SAR imagery enables mangrove extent mapping (Bunting et al., 2022b; Kumar and Patnaik, 2013; Lucas et al., 2007). The sensitivity of SAR data relates to mangrove canopy cover, moisture content and vegetation volume, alongside physical parameters of SAR sensors such as baseline and radar wavelengths. Differences between mangroves and other forests are subtle when using L-band SAR data with shorter baseline (distance between antennas at 2 m) (Lucas et al., 2007). Meanwhile, intact mangrove forests with dense canopies and foliage strongly impact penetration of shorter radar wavelengths (Kumar and Patnaik, 2013). L-band SAR data with a larger baseline (several hundred meters) such as ALOS PALSAR facilitates improved mangrove discrimination (Lucas et al., 2007) and mangrove change monitoring (Bunting et al., 2022a), while C-band SAR data are found not to have significant relationships with mangrove biophysical parameters, i.e., stem density, basal area, and mean diameter at breast height (Kovacs et al., 2008). However, the performance using individual radar wavelength for mangrove extent and species discrimination is limited, since the thresholds are unlikely to be consistent across different study sites (Lucas et al., 2007; Bunting et al., 2022b).

The integration with spaceborne optical data such as Landsat, Sentinel-2 and Worldview-3 imagery enhanced the accuracy of mangrove extent and species discrimination (e.g., Bunting et al., 2022a; Huang et al., 2022; Wang et al., 2023; Zhang et al., 2018).

The relationships between backscattering coefficient and mangrove foliage and woody components are also employed to estimate mangrove leaf area index (LAI) and AGB (e.g., Fu et al., 2022, 2023; Kovacs et al., 2008; Lucas et al., 2020; Nedd et al., 2023). However, mangrove AGB estimation using backscattering coefficient faces challenges of saturation, due to an asymptotic relationship between these two variables (Pham et al., 2019). The level of saturation depends on the wavelength, polarizations and ground condition. At L-band, saturation typically occurs at AGB levels between 100 and 150 Mg/ha (Shugart et al., 2010). Not only electromagnetic but temporal characteristics does spaceborne SAR imagery provide. By differentiating two or more radar images of the same area acquired at different times from similar vantage points (Interferometric SAR; InSAR), mangrove canopy height models (CHMs) can be established (e.g., Berninger et al., 2019; Lee and Fatoyinbo, 2015; Suab et al., 2024). A variety of mangrove canopy height retrieval algorithms based on InSAR measurements have been developed and applied. These approaches differ in terms of model assumptions such as low-lying and flat growing environments of mangroves (Simard et al., 2006, 2008, 2019), number of baselines utilized (Lee et al., 2018) and wavelengths (Aslan and Aljahdali, 2022; Lee and Fatoyinbo, 2015). Since taller trees are considered to have higher proportion of AGB, deploying biomass-height regression analyses with CHMs provided significant potential to extrapolate higher AGB estimates of mangroves, mitigating the saturation of AGB estimation (e.g., Lucas et al., 2020; Pham et al., 2019; Simard et al., 2019; Tang et al., 2016).

2.2.3 Spaceborne LiDAR data

LiDAR is an active remote sensing technology that emits laser pulses towards the land and records the returned signals as laser pulses. When there is a vegetated surface, the returned signals, or waveforms, are a function of vertical distribution of vegetation and ground surfaces within the footprint (laser-illuminated area). Compared to optical and SAR sensors primarily providing two-dimensional representations of the earth's surface, LiDAR instruments enable three-dimensional investigations offering detailed vertical characteristics, particularly forest vertical structure. GLAS (Geoscience Laser Altimeter System) is the first spaceborne LiDAR instrument onboard NASA's Ice, Cloud, and Land Elevation Satellite (ICESat), collecting global coverage data from 2003 to August 2010 with a footprint of 70 m in diameter (Simard et al., 2008). Its successor, ICESat-2, has been equipped with the Advanced Topographic Laser Altimeter System (ATLAS) instrument, enabling denser and finer global observations since September 2018. Currently, there is first-ever spaceborne LiDAR mission in orbit aiming at global vegetation vertical

investigations, known as the Global Ecosystem Dynamics Investigation (GEDI), providing full-waveform observations of 25 m footprints (Duncanson et al., 2022; Markus et al., 2017) (**Table 2-3**). A schematic diagram of the ground tracks of ICESat-2 ATL08 and GEDI L2A products is provided in **Figure 2-4**. Similar to GEDI observations, ICESat also provides full-waveform observations where the distribution of returned energy is recorded, while ICESat-2 ATLAS employs photon counting LiDAR altimetry technique measuring the transit time of individual photons to determine surface height along track (Liu et al., 2021).

Satellite and sensor	Laser wavelength	Pulse Repetition Frequency (PRF)	Footprint resolution (in diameter)	Operating period
ICESat GLAS	1064 nm	40 Hz (170 m spacing)	70 m	12/01/2003 - 14/08/2010
ICESat-2 ATLAS	532 nm	10 kHz (0.7 m spacing)	17 m	15/09/2018 to present
GEDI	1064 nm	242 Hz (60 m spacing)	averaging 25 m	25/03/2019 - 17/03/2023

Table 2-3. The specifications of spaceborne LiDAR sensors used in mangrove research.

ICESat: Ice, Cloud, and Land Elevation Satellite; GLAS: Geoscience Laser Altimeter System; ATLAS: Advanced Topographic Laser Altimeter System; GEDI: Global Ecosystem Dynamics Investigation.

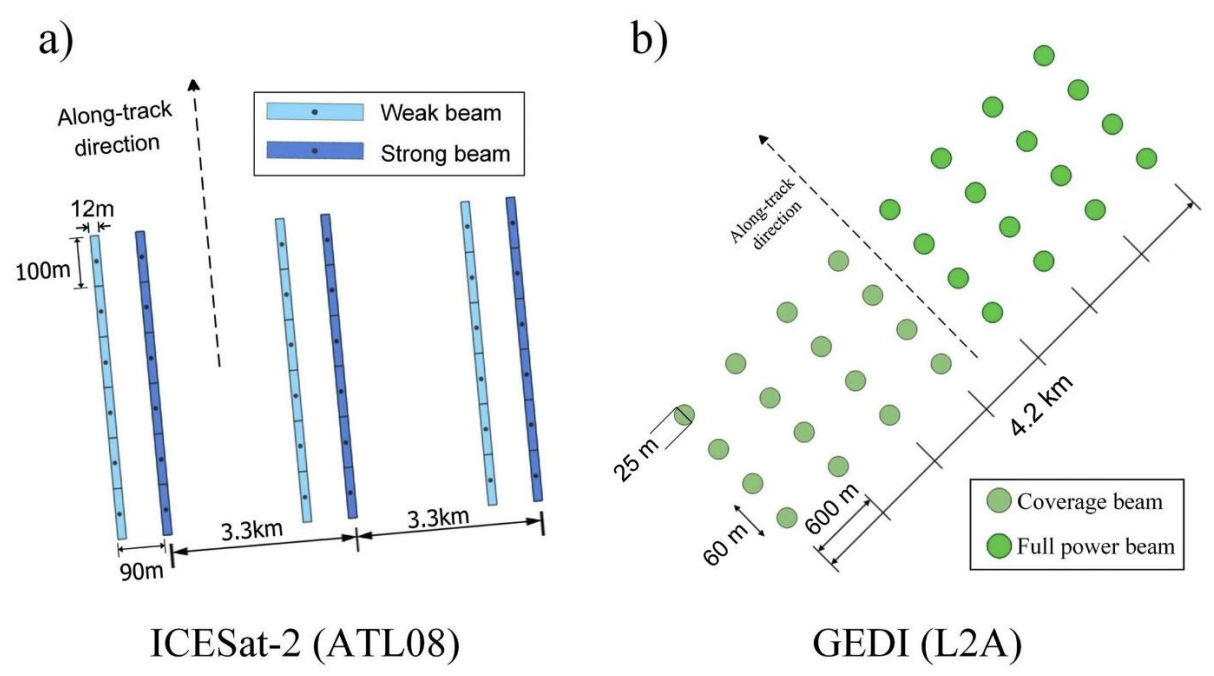


Figure 2-4. Schematic diagrams of the ground tracks of different spaceborne LiDAR datasets: a) ICESat-2 ATL08, b) GEDI L2A. Note that the across-track distances are not shown to scale for clarity and compactness (Source: Liu et al. (2021)).

Spaceborne LiDAR data have been used to estimate forest canopy height which can be determined through relative height (RH) metrics representing certain quantiles of returned energy relative to the ground or height values computed from identified canopy photons minus the interpolated ground surface. ICESat-2 and GEDI yield accurate canopy height estimates with root mean square error of 5.02 m and 3.56 m, respectively, as compared with locally calibrated airborne LiDAR products for USA territories (Liu et al., 2021). Given the importance of accurate canopy height estimation, spaceborne LiDAR data have been employed to link LiDAR-derived RH with field measurements of Lorey's mean canopy height (Saatchi et

al., 2011), plot-level canopy height at various quantiles (Baccini et al., 2012; Duncanson et al., 2022), and to calibrate medium resolution digital elevation models (DEMs) to pixel level canopy height estimates (Fatoyinbo and Simard, 2013; Simard et al., 2006, 2019). Canopy height is significantly correlated with AGB, making LiDAR observations a viable tool to estimate AGB with litter or even no saturation in high AGB estimation, while optical reflectance and SAR backscatter signals have been shown to saturate at relatively low AGB levels (Rodríguez-Veiga et al., 2019; Jagadish et al., 2024). However, unlike optical or radar sensors that provide wall-to-wall imagery, spaceborne LiDAR instruments (e.g., GLAS, GEDI, ATLAS) acquire data only along narrow tracks, resulting in discrete sampling footprints rather than continuous global coverage. For instance, GEDI was projected to acquire over 10 billion cloud-free observations, about 4% of the land surface, over a two-year nominal mission (Dubayah et al., 2020). Nonetheless, the LiDAR-derived canopy height estimates are a valuable resource for scaling limited field data, especially for typically remote and inaccessible mangrove forests in which it is physically difficult to conduct fieldwork at a large extent.

2.2.4 Airborne datasets

Before the prevailing application of satellite remote sensing, aerial photography was the primary source of remotely sensed data and the only means of assessing mangrove extent and health (Kuenzer et al., 2011; Liu et al., 2022). Given the mobility and low operation altitude of aircrafts, airborne remote sensing, with the advent of UAVs, offers time-sensitive and highly resolved geospatial data. Airborne remote sensing datasets primarily comprise hyperspectral and LiDAR data (Kuenzer et al., 2011; Pham et al., 2019; Wannasiri et al., 2013). Airborne hyperspectral data collected by sensors such as CASI (Compact Airborne Spectrographic Imager), AVIRIS (Airborne Visible/Infrared Imaging Spectrometer) and AISA (Airborne Imaging Spectrometer for Applications) have proven effective for regional-scale mangrove monitoring, offering detailed spectral information that improves the discrimination of mangrove species (e.g., Liu et al., 2019; Prakash Hati et al., 2020; Yang et al., 2009). Compared with spaceborne hyperspectral data Hyperion, and EnMap (Storch et al., 2023) with a spatial resolution of 30 m, airborne hyperspectral data record rich spectral information at higher resolution which can be up to sub-meter (0.5 m) depending on flight altitude (Lassalle et al., 2023). Airborne LiDAR data were found as 'gold standard' to have the best estimation of mangrove canopy height in Zambezi River (Lagomasino et al., 2016) and to have the best vertical accuracy of topography in Mexico when compared with geodetic benchmarks (Carrera-Hernández, 2021). However, the acquisition of airborne data is opportunistic with regards to data availability as the fight campaign is costly and weather-dependent, and more importantly, covering limited area of a specific region (Hancock et al., 2021; Kuenzer et al., 2011; Lagomasino et al., 2016).

2.3 Remote sensing approaches in mangrove research

2.3.1 Distribution mapping and species discrimination

A generalised methodological workflow of remote sensing approaches in mangrove research is presented in **Figure 2-5**. The schematic diagram synthesises common practices reported in the literature, covering data sources, analytical methods, outputs, and applications. Within this context, investigating mangrove distribution and species discrimination is beneficial to the effective management of mangrove forests. Remote sensing approaches for mangrove extent delineation and species discrimination are broadly categorized into traditional and machine learning based supervised methods (**Table 2-4**).

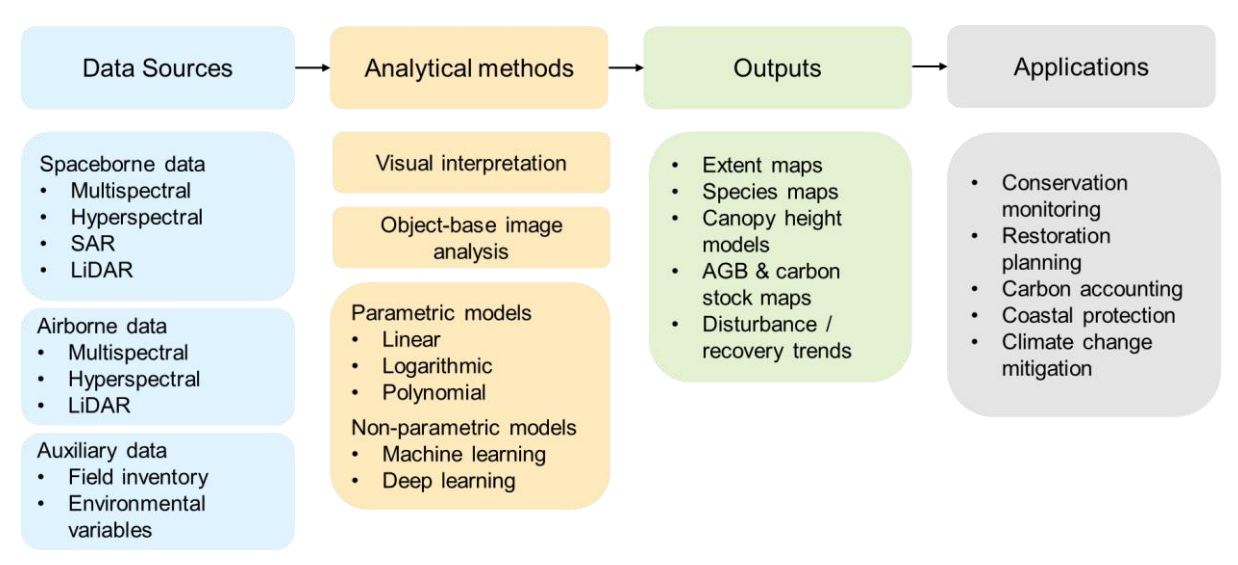


Figure 2-5. Generalised methodological workflow of remote sensing approaches in mangrove research.

Traditional methods comprise visual interpretation, object-based image analysis (OBIA) and unsupervised classification. Before the wider introduction of satellite images, mangrove extent and species identification relied on visual interpretation of aerial black and white photographs (Dahdouh-Guebas et al., 2002; Kuenzer et al., 2011; Liu et al., 2022). Figure 2-6 presents an aerial photograph captured in 1964 by the Hong Kong Lands Department, illustrating its application in historical mangrove extent mapping (Liu et al., 2022). High-resolution aerial photographs provide highly resolved and spatially explicit information for regional mangrove recognition at a finer scale with the image attributes of grey levels, texture, shape, shadows. Verheyden et al. (2002) employed these image attributes to visually interpret mangrove extent and species distribution in Sri Lanka and yielded overall satisfactory results of genus-level recognition. Since the spatial resolution of aerial photographs can be very high depending on flight height, the visual interpretation on archived aerial photographs aids in yielding high-resolution ground samples to train or validate the classification methods developed for lower-resolution satellite imagery (Hsu et al., 2020; Kamal et al., 2014;

Liu et al., 2022). However, visual interpretation on aerial interpretation requires expert knowledge on classified categories and is time-consuming for fragmented mangrove forests.



Figure 2-6. Aerial photograph taken on 14 December 1964 by the Hong Kong Lands Department, used for historical mangrove extent mapping. The Mai Po Nature Reserve is outlined in white, and land covers are annotated as mangroves (M), mudflats (MF), and gei wai (GW) (Source: Liu et al., 2022).

Considering rich spatially explicit information that high-resolution images (generally ≤10 m) deliver, OBIA has been deployed for effective mangrove extent mapping and species discrimination (e.g., Bihamta Toosi et al., 2020; Jia et al., 2023; Wang et al., 2004; Zhang et al., 2021; Zhang et al., 2021). OBIA includes two basic principles, segmentation and classification. Different from pixel-based methods, OBIA segments an image into representative vector shapes of different size and geometry of similar characteristics using the methods, such as watershed segmentation (Biswas et al., 2020) and multi-resolution (Zhang et al., 2023). Adjacent pixels are grouped in terms of image attributes, such as texture, shape and context (Blaschke, 2010). Subsequently, spectral, textural, and geometric features are extracted from these pixel groups for further classification. Zhang et al. (2021) found the incorporation of OBIA with random forest algorithm on 0.8 m Gaofen-2 imagery works successfully in detecting small mangrove patches. Mangrove species discrimination also benefits from OBIA using 0.5 m WorldView-2 image (Heenkenda et al., 2014) or 4 m airborne CASI-2 data (Kamal and Phinn, 2011).

Similar to OBIA, unsupervised classification methods such as iterative self-organizing data analysis techniques (ISODATA) and k-means clustering are grouping pixels of similar spectral properties into clusters which will be manually labelled (classified). However, these methods are pixel-based, not taking into account any of the information from neighbouring pixels, which leads to a 'salt and pepper' effect. For

mangrove extent mapping, when prior knowledge of field data or a well-trained interpreter is unavailable, remote sensing image pixels can be clustered into predefined classes on some statistical or mathematical relationship in unsupervised classification methods (Giri et al., 2011; Spalding et al., 2010). Usually, unsupervised classification methods are employed for preliminary analysis of data before conducting supervised classification (Maurya et al., 2021).

Supervised classification is significantly dependent on training samples derived from domain knowledge or the expertise of an analyst for the relationship between imagery and classes that can be established. Supervised machine learning algorithms such as maximum likelihood classification, artificial neural networks, random forests, support vector machine and Gradient Boosting Machine work well in mangrove extent mapping and species discrimination with the input data of optical (e.g., Bihamta Toosi et al., 2020; Kanniah et al., 2015; Liu et al., 2022; X. Liu et al., 2021; Peng et al., 2020; Wang et al., 2018, 2008), hyperspectral (e.g. Jia et al., 2014; Kumar et al., 2019; Lassalle et al., 2023; Wan et al., 2020) and SAR (e.g. Abdel-Hamid et al., 2018; Fu et al., 2023). Maximum likelihood classification (MLC) is a parametric model assuming a known form for the data distribution (i.e., normal distribution), while other machine learning algorithms are non-parametric models without the assumption of a specific distribution, relying on data-driven patterns. Non-parametric models yield satisfactory results in identifying mangrove extent and species with textural and spectral features (**Table 2-4**). The most commonly used of these models, support vector machines, random forests and artificial neural networks are explained further below.

Support vector machines (SVM) was introduced and developed by Vladimir Vapnik and his colleagues in the 1990s (Boser et al., 1992; Cortes and Vapnik, 1995) and has been widely applied to classification problems within machine learning domain, particularly in remote sensing application with limited training datasets (Mountrakis et al., 2011; Sheykhmousa et al., 2020). SVM can also be applied to regression tasks, where the relationships between predictor variables and output variables can be obtained. This type of SVM is referred to as support vector regression (SVR). SVM is a non-parametric statistical learning algorithm that is insensitive to training data distribution. Initially, SVM was designed to distinguish two classes by determining the optimal hyperplane which is the maximum margin between the closest data points of opposite classes. Then, a method called "kernel trick" (the use of kernel function) was applied to SVM for non-linearly separable data. The kernel functions such as polynomial kernels, radial basis function (RBF) kernels and sigmoid kernels are used to transform the data into a higher-dimensional space to enable linear separation, improving the separability between classes. Therefore, the performance of SVM largely depends on the suitable selection of a kernel function with correct kernel parameters. However, optimizing SVM parameters is very resource-intensive, and also, the classification over big data is always expensive

in computation, especially multiclass classification scenarios normally in remote sensing applications (Sheykhmousa et al., 2020).

Random forests (RF) use ensemble learning methods (i.e., Bagging, short for Bootstrap Aggregating) to solve classification or regression problems, making it much more robust against overfitting. The algorithm operates by constructing a number of decision trees at the training stage and producing the mean prediction for regression tasks and the mode prediction for classification tasks (Breiman, 2001). Given a training dataset with corresponding responses, RF repeatedly selects a random sample with replacement of the training dataset and fits trees to the samples. Different from general bagging method, RF selects a random subset of features at each candidate split when constructing decision trees. Consequently, RF performs well with high accuracy, robustness, and efficiency in dealing with high-dimensional data. Additionally, it is straightforward to train and tune RF to achieve satisfactory results. However, the procedure of constructing decision trees in RF is unknown, generally referred to as "black box" (Zhao et al., 2023). And, when it comes to regression, RF is not able to extrapolate from the training inputs as the predictions are the average of observed labels.

Artificial neural networks (ANN), inspired by biological nervous processing in the human brain, are interconnected neurons that aim to simulate neural processing and powerfully capable of nonlinear classification and regression tasks (Dey et al., 2023; Maung and Sasaki, 2021). ANN was first introduced by McCulloch and Pitts (1943) and proposed a simplified neuron model for logical operations. Multilayer perceptron (MLP) is the most widely recognized ANN, comprising an input and output layers in addition to one or more hidden layers. Thus, the capability of the MLP to discover the hidden relations between inputs and outputs heavily depends on the number of hidden layers. Initially, each node is connected with others and has randomly assigned weight. When there is the computed difference between actual values (classes) and predicted values (classes), weight values will be refined through a backpropagation algorithm iteratively. The backpropagation algorithm computes the gradient of loss function (e.g., mean squared error for regression tasks, cross-entropy for classification tasks), and then, updates the weight values using an optimization algorithm for the next iteration until the MLP model is well-trained with satisfactory results of the loss function (Hecht-nielsen, 1992). There are some drawbacks though that the MLP model is also resource-intensive for training big datasets, and prone to overfitting with small datasets. Also, the selection of model architecture and optimization of model hyperparameters can be complex and inefficient (Yuan et al., 2020).

Currently convolutional neural networks (CNNs), as a type of ANN, is gaining popularity in classification tasks in remote sensing (Kattenborn et al., 2021). CNN has an input and an output layer alongside stacked

units of convolutional, pooling and activation layers. The output layer is generally obtained with the same dimension as the input layer. In the convolutional layer, the input data is processed with convolution operation through local filters. And the pooling layer reduces the dimensions of the input data through operations like max-pooling and average-pooling. The activation layer introduces non-linearity into the CNN, enabling to learn complex patterns in the data. Similar to the MLP model, the weights of the CNN model are iteratively updated through backpropagation (Yuan et al., 2020). Due to the effectiveness of CNN models in capturing spatial patterns of remote sensing imagery, a broad spectrum of mangrove properties is able to be extracted, including mangrove extent, species, tree crowns and canopy gaps (e.g. Lassalle and de Souza Filho, 2022; Li et al., 2021; Lu and Wang, 2024; Tran et al., 2024; Wan et al., 2019).

Table 2-4. Remote sensing-based approaches for mangrove extent mapping and species discrimination.

Approach	Data source	Location and year	Performance	Reference
Visual interpretation	Aerial photographs	Pambala–Chilaw Lagoon complex in Sri Lanka, 1994	-	Dahdouh- Guebas et al. (2002)
ANN	IKONOS Geo- Bundle images	Caribbean coast of Panama, 2004	Kappa=0.93 (best)	Wang et al. (2008)
SAM LSU MSS	CASI-2 hyperspectral data	Brisbane River area in Australia, 2004	SAM: OA=69% Kappa=0.57 LSU: OA=56% Kappa=0.41 MSS: OA=76% Kappa=0.67	Kamal and Phinn (2011)
MSS Nearest neighbour	EO-1 Hyperion SPOT-5	Mai Po Marshes Nature Reserve in China, 2008	OA=88% Kappa=0.83	Jia et al. (2014)
MLC	Landsat imagery	Iskandar Malaysia, 1989-2014	OA: 73.10-94.07% Kappa: 0.67-0.94	Kanniah et al. (2015)
RF SVM CART	ALOS/PALSAR RapidEye Worldview-1	Red Sea coastline in Egypt, 2007	OA=92.15% Kappa=0.90 (RF works best with combined data)	Abdel-Hamid et al. (2018)
MRS RF	Landsat-8 Sentinel-2A Pleiades-1B	Dongzhaigang in China, 2014 and 2016	OA=91.89-96.52% Kappa=0.87-0.94	Wang et al. (2018)
Minimum Distance SAM SVM	EO-1 Hyperion	Indian Sundarbans, 2014	OA=99.08% Kappa=0.97 (SVM best)	Kumar et al. (2019)
CNN	WorldView-2	Shenzhen Mangrove Forest Nature Reserve and Mai Po Marshes Nature Reserve in China, 2010	OA=98.81% Kappa=0.986	Wan et al. (2019)
RF SVM	Gaofen-5 hyperspectral data	Mai Po Marshes Nature Reserve in China, 2018	OA=87.12% Kappa=0.835 (RF best)	Wan et al. (2020)

Table 2-4. Continued.

Approach	Data source	Location and year	Performance	Reference
MSS CART AdaBoost RF RoF	Gaofen-2 RapidEye-4	Qi'ao Island in China, 2016-2017	OA=92.01% Kappa=0.9016 (RoF works best with combined data)	Peng et al. (2020)
Upscaling approach RF	Sentinel-2 WorldView-2	Qeshm Island in Iran, 2017	OA=65.5% Kappa=0.63	Bihamta Toosi et al. (2020)
Visual interpretation	UAV RGB images	Baja California Sur (BCS) in Mexico, 2018 and 2019	OA= $98.3\% \pm 2.1\%$	Hsu et al. (2020)
MRS SVM	Gaofen-1 Ziyuan-3	China, 2018	OA=99.3% Kappa=0.985	Zhang et al. (2021)
RF SVM CNN	WorldView-3 Airborne hyperspectral and LiDAR data	Mai Po Marshes Nature Reserve in China, 2018	OA=89% Kappa=0.86 (CNN best with WV-3 PS and LiDAR)	Li et al. (2021)
Ensemble of RF, GBM, and ANN	SRTM Sentinel-1/2	West Africa, 2017	OA: 95-99% Kappa: 0.93-0.99	Liu et al. (2021)
Mask R-CNN	WorldView-3 WorldView-4	Four mangrove sites in Brazil, USA, Australia and Gabon, respectively, 2016-2019	OA=91.4% Kappa=0.89	Lassalle and de Souza Filho (2022)
Thresholding	L-band SAR from JAXA	Global, 1996-2020	OA=87.4% (95 th conf. int.)	Bunting et al. (2022)
RF Visual interpretation	Aerial photographs Landsat imagery	Greater Bay Area in China, 1924-2020	OA>99% Kappa > 0.99	Liu et al. (2022)
NGBoost CatBoost LightGBM	UAV RGB images Sentinel 1/2	Maowei Sea nature reserves in China, 2019	OA=93.18% (CatBoost best)	Fu et al. (2023)
MT-EDv3 NN	Spaceborne multi- and hyperspectral imagery Airborne hyperspectral images	Sao Paulo in Brazil, 2021	Airborne: OA=95% Kappa=0.93 Spaceborne: OA up to 97% Kappa up to 0.95	Lassalle et al. (2023)
U-Net	Sentinel-2A/B	southern coast of Vietnam, 2016-2023	OA= 94.53-96.89%	Tran et al. (2024)
Mask R–CNN	UAV LiDAR data	Dandou Sea coast in China, 2019	OA= 70.83%	Lu and Wang (2024)

OA: Overall Accuracy; ANN: Artificial Neural Network; SAM: Spectral Angle Mapper; LSU: Linear Spectral Unmixing; MLC: Maximum Likelihood Classification; GBM: Gradient Boosting Machine; MSS/MRS: Multi-scale (Multi-resolution) Segmentation; SVM: Support Vector Machine; RF: Random Forests; CNN: Convolutional Neural Network CART: Classification and Regression Trees; AdaBoost: Adaptive Boosting; RoF: Rotation Forest; JAXA: Japan Aerospace Exploration Agency; MT-EDv3: Multi-Task Encoder-Decoder; Mask R-CNN: Mask Region-based Convolutional Network.

2.3.2 Biophysical parameters retrieval

Biophysical parameters of mangrove forests are essential for assessing health condition, quantifying gross primary production (GPP) and carbon stock (Parida and Kumari, 2021). These biophysical parameters range from tree level to community level, such as canopy height, basal area, crown diameter, leaf area index (LAI), leaf chlorophyll concentration (LCC) and biomass. Remote sensing-based approaches for biophysical parameter retrieval are categorized in two ways through radiative transfer models (RTMs) or empirical models (Pham et al., 2019). RTMs are mathematical frameworks used to simulate the transfer of electromagnetic radiation through the atmosphere and the interacts with vegetation canopies, deployed to inverse forest biophysical parameters such as LAI and LCC (e.g., Miao et al., 2024; Zhao et al., 2023). Empirical models leverage spectral indices derived from remotely sensed multispectral and hyperspectral data to retrieve biophysical parameters using statistical regression equations (e.g., Díaz and Blackburn, 2003; Guo et al., 2021; Kovacs et al., 2004; Verrelst et al., 2015). Additionally, these models incorporate machine learning regression algorithms such as decision tress, ANN and SVR, which demonstrate flexibility in integrating prior knowledge from diverse datasets to analyse biophysical parameters (Verrelst et al., 2019)

2.3.2.1 Leaf area index

LAI is a significant indicator of mangrove health conditions, reflecting the characteristics of canopy structure and growth development (Luo et al., 2023; Manna and Raychaudhuri, 2020). As such, LAI inversion is one of the most common applications in remote sensing-based mangrove research (Pham et al., 2019; Wang et al., 2019). Many studies have employed regression analyses to estimate LAI, using spectral indices, backscattering coefficients or LiDAR observations (e.g., Guo et al., 2017; Kamal et al., 2016; Kovacs et al., 2004; Luo et al., 2023; Pu and Cheng, 2015).

For LAI estimation using RTMs, PROSAIL is one of the most popular RTMs combining PROSPECT (Leaf Optical Properties Model) and SAIL (Scattering by Arbitrarily Inclined Leaves) together (Bhadra et al., 2024). The PROSPECT model simulates the reflectance, transmittance and absorption of light by the leaves, while the SAIL model simulates the scattering of light in a plant canopy. By integrating these two models, PROSAIL can take several leaf and canopy level attributes as inputs such as LCC, Equivalent water thickness (EWT) and LAI, and then output a reflectance spectrum (400-2400 nm). Therefore, biophysical parameters can be inversed from remotely sensed multispectral data based on numerical optimization or look-up table (LUT) (Verrelst et al., 2019). Although PROSAIL shows reproducibility and generalization across various vegetation types, a plethora of input parameters are required to simulate canopy reflectance.

Recently, there has been an increasing use of hybrid regression, combining RTMs and machine learning algorithms, and thereby taking into account both the generalization of RTMs and computational efficiency of machine learning methods. This approach replaces ground truthing needed for training empirical models by setting RTM inputs. LUT-based RTMs generate a look-up table demonstrating a group of canopy realizations, and then a machine learning regression model employs all available data in this look-up table for training (Binh et al., 2022; Jia et al., 2024; Miao et al., 2024). Zhao et al. (2023) found spaceborne hyperspectral imagery (Zhuhai-1) outperformed other spaceborne multispectral imagery (Landsat-8, Sentinel-2 and Worldview-2) for mangrove LAI mapping using a hybrid approach combining the PROSAIL model and XGBoost. For mangrove forests, this is considered a promising approach to estimate LAI at regional or national scale due to the difficulty of collecting sufficient field data (Binh et al., 2022; Zhao et al., 2023).

2.3.2.2 Aboveground biomass

Mangrove biomass refers to the total mass of living organic matter of mangrove trees, divided into aboveground and belowground components (IPCC, 2003). Biomass estimation allows for the conversion into carbon stocks, forming the foundation for investigating the critical role mangroves play in carbon cycling (Alongi, 2020). Since belowground biomass is more challenging to investigate and less explicitly estimated through remote sensing observations, aboveground biomass has garnered greater research focus, where AGB estimation is conducive to monitoring mangrove health as healthy mangroves secure effective carbon sequestration. The remote sensing-based approaches for estimating AGB can be grouped into two main categories: (1) utilising the relationships between AGB and spectral information or radar backscattering coefficients, and (2) deriving tree structural parameters (i.e., canopy height) from remotely sensed data to estimate AGB using biomass-height allometric equations.

Since mangrove appearance is characterised by species composition, canopy cover and height distribution, the interaction between mangrove tree components and spectra or radar signals has been well investigated during field campaigns (e.g., Lucas et al., 2007; Mougin et al., 1999; Xu et al., 2019; Zulfa et al., 2020). Thus, spectral information and backscattering coefficient from spaceborne datasets have been introduced to mangrove biomass estimation in parametric or non-parametric regression models (**Table 2-5**). Parametric models normally include linear, logarithmic and polynomial models with assumptions of a specific relationship between AGB and selected surrogate variables such as reflectance in multispectral bands, vegetation indices and backscatter coefficient. For example, EVI (Enhanced Vegetation Index) and NDVI (Normalized Difference Vegetation Index) exhibit strong relationships with AGB estimates, which can be modelled using linear, logarithmic, or polynomial functions (Pandey et al., 2019), while reflectance in

multispectral bands and backscattering coefficient was used effectively in linear models for AGB estimation (Castillo et al., 2017; Friess et al., 2016; Pham and Yoshino, 2017). However, both spectral indices and backscattering coefficient are found to be saturated at low AGB level (Li et al., 2007; Shugart et al., 2010). Compared to parametric models, non-parametric models were deployed to yield more complex relationships between spaceborne variables and mangrove AGB, as they do not rely on the assumption of a predefined relationship. These models contain supervised machine learning models such as ANN, RF, SVR and XGBR, driven by input data with varied predictor variables. Predictor variables may include spaceborne, environmental, or a combination of both types. As the range of predictor variables expands, the models can harness more comprehensive information, enhancing their predictive capabilities (**Table 2-5**).

The introduction of canopy height models (CHMs) and biomass-height allometry is another remote sensingbased approach for mangrove AGB estimation. Canopy height has been seen as functionally related parameters to biomass estimation as taller trees dominate higher AGB (Duncanson et al., 2022). Mangrove CHMs can be derived from InSAR and LiDAR measurements, UAV overlapping images using Structure of Motion (SfM) photogrammetry, and stereo-pair or multiple-stereo aerial or spaceborne photographs (e.g., Dandois and Ellis, 2013; Hirschmugl et al., 2007; Lucas et al., 2000, 2020; St-Onge et al., 2008; Treuhaft et al., 2004; Wannasiri et al., 2013). The conversion from mangrove CHMs to AGB estimates generally employed parametric models that establish relationships between AGB and canopy height. These relationships are determined by correlating field plot level AGB with corresponding field plot level mean or maximum canopy height (Simard et al., 2006, 2019), height values derived from CHMs (Aslan et al., 2016), or relative height metrics obtained from LiDAR measurements (Duncanson et al., 2022). After AGB estimation, it is common practice to covert AGB into aboveground carbon stock with a multiplier between 0.46 to 0.5 when no region- or species-specific values exist (e.g., Harishma et al., 2020; Kauffman and Donato, 2012). As strong positive linear relationships are observed between the aboveground and belowground carbon stocks in mangroves, it is also viable to estimate belowground carbon stocks based on aboveground carbon stock estimates (e.g., Jachowski et al., 2013; Meng et al., 2021).

 Table 2-5. Remote sensing-based approaches for mangrove biomass estimation.

Approach	Data source	Location and year	Performance	Reference
Genetic model	Landsat TM images, Radarsat	Qi'ao Island, Zhuhai in China, 2004	R ² =0.769 RMSD=0.738 kg/m ²	Li et al. (2007)
MaxEnt	Field inventory data ICESat SRTM Global quick scatterometer (QSCAT) MODIS NDVI and LAI	Global, circa 2000 (not specific to mangroves)	Uncertainty at ±30% at a global scale	Saatchi et al. (2011)
RF	Field inventory data ICESat SRTM MODIS Land Surface Temperature MODIS reflectance bands	Global, 2000–2010 (not specific to mangroves)	R ² =0.83 RMSD=25 Mg C/ha	Baccini et al. (2012)
SVR	GeoEye-1, ASTER GDEM V2	Andaman Coast of Thailand, 2011	R ² =0.66 RMSD=53.4 Mg/ha	Jachowski et al. (2013)
BP ANN	Worldview-2	Qi'ao Island, Zhuhai in China, 2010	Average RMSE=40.15 Mg/ha (with species information as dummy variable)	Zhu et al. (2015)
GLMs	Pleiades imagery, SRTM, geographic distance variable	Singapore, April 2012 to August 2013	r=0.54 for AGB r=0.56 for BGB	Friess et al. (2016)
Empirical modelling	ALOS AVNIR-2	Karimunjawa Islands in Indonesia, 2010	R ² =0.688, SE=5.89 kg C m ⁻² for AGC R ² =0.567, SE=2.54 kg C m ⁻² for BGC	Wicaksono et al. (2016)
Spatially explicit analytical framework	SRTM	West Africa, 2000	-	Tang et al. (2016)
ESH	Mangrove field data Environmental drivers such as temperature and precipitation	Neotropics	adjusted R ² =0.19	Rovai et al. (2016)
NLQR	SRTM	Indonesian Papua, 2000	r=0.55	Aslan et al. (2016)
Linear regression, Machine Learning Algorithm	SRTM, Sentinel-1, Sentinel-2	Southern coast of Honda Bay in Philippines, 2015 and 2016	r=0.83 RMSE=27.75 Mg/ha	Castillo et al. (2017)
СНМ	Airborne LiDAR, TanDEM-X, WorldView-2	Everglades National Park in USA, 2012	R ² =0.82 Relative RMSE=37%	Feliciano et al. (2017)
RF	SPOT 4 SPOT 5	Cangio mangrove forest in Vietnam, 2000 and 2011	adjusted R ² =0.73	Pham and Brabyn (2017)

Table 2-5. Continued.

	Table 2-3. Continued.						
Approach	Data source	Location and year	Performance	Reference			
Stepwise multilinear regression models	ALOS-2 PALSAR-2	Hai Phong City in Vietnam, 2015	R ² =0.51, RMSE=35.5 Mg/ha for <i>S. caseolaris</i> R ² =0.64, RMSE=41.3 Mg/ha for <i>K. obovata</i>	Pham and Yoshino (2017)			
SVR	ALOS-2 PALSAR-2 and Sentinel-2A	Northern coast of Vietnam, 2015	R ² =0.596 RMSE=1.54 Mg/ha	Pham et al. (2018)			
SVR	UAV RGB images, Sentinel-1 and Sentinel-2 imagery	Sine Saloum and Casamance Deltas in Senegal, 2017	R ² =0.89 RMSE=2.35 Mg/ha	Navarro et al. (2019)			
Linear and non- linear regression models	EO-1 Hyperion	Bhitarkanika Forest Reserve in Odisha India, 2015	R ² =0.861(best result from polynomial model with EVI)	Pandey et al. (2019)			
СНМ	ICESat LiDAR SRTM	Global, 2000	R ² =0.55 RMSE=134.3 Mg/ha	Simard et al. (2019)			
СНМ	Landsat images, L-band SAR data, SRTM data, TanDEM-X-band and WorldView-2 stereo data	Matang Mangrove Forest Reserve in Peninsular Malaysia, 2000-2016	R ² =0.53 RMSE=79 Mg/ha	Lucas et al. (2020)			
UAV CHM	UAV RGB images	Southeastern coast of Australia, 2018	Adjusted R ² =0.932	Navarro et al. (2020)			
Linear regression	ALOS-2 PALSAR-2	Mahakam Delta, Indonesia, 2018	R ² =0.88 RMSE=24.05 Mg/ha	Nesha et al. (2020)			
ASO, ANFIS	Sentinel-1A, SPOT-6	Ca Mau coastal area in Vietnam, 2015	R ² =0.577 RMSE=70.882 Mg/ha	Pham et al. (2020)			
RF	UAV LiDAR, Sentinel-2	Northeast Hainan Island in China, 2018	R ² =0.62 RMSE=50.36 Mg/ha	Wang et al. (2020)			
RF	Worldview-2 UAV RGB images	Qi'ao Island, Zhuhai in China, 2010 and 2016	RMSE=50.99 Mg/ha Relative RMSE=30.48%	Zhu et al. (2020)			
ANN	Sentinel-1 A/B	Bhitarkanika Wildlife Sanctuary in India, 2018	R ² =0.45 RMSE=103.99 Mg/ha	Ghosh and Behera (2021)			
RF	Field plot data Environmental variables	Global, present	R ² =0.36 RMSE=108 Mg/ha	Rovai et al. (2021)			
PRVI	Sentinel 1A	Mundra Taluka in India, 2015-2018	R ² =0.56	Vaghela et al. (2021)			
UAV CHM XGBR	UAV RGB images	Beibu Gulf in China, 2019	R ² =0.83 RMSE=22.76 Mg/ha	Tian et al. (2021)			
UAV CHM	UAV RGB images	Lubuk Kertang in Indonesia, 2022	-	Basyuni et al. (2023)			

SVR: Support Vector Regression; **BP ANN**: Backpropagation – Artificial Neural Network; **GLMs**: Generalised Linear Models; **ESH**: Environmental Signature Hypothesis; **NLQR**: Nonlinear Quantile Regression; **RF**: Random Forests; **CHM**: Canopy

height model; **ASO**: Atom Search Algorithm; **ANFIS**: Adaptive Neuro-Fuzzy Inference System; **PRVI**: Polarimetric Radar Vegetation Index; **XGBR**: XGBoost regressor; **MaxEnt**: Maximum Entropy.

2.3.3 Mangrove resilience investigation

In the last two decades (2000-2020), mangroves have been threatened by anthropogenic activities such as aquaculture development and commercial crop conversion, and natural retraction induced by climate change and human activities (FAO, 2023). Due to increasing awareness of mangrove protection and restoration, the global loss of mangrove area has been 58% offset by afforestation and 42% of all the world's remaining mangroves have fallen within protected area status (FAO, 2023; Spalding and Leal, 2022). Since mangroves are still facing the impacts from anthropogenic activities and climate change (Friess et al., 2024), the investigation of mangrove resilience can shape mangrove management and restoration to be more scientific and effective (Dahdouh-Guebas et al., 2022; Ong and Ellison, 2021).

Resilience is traditionally defined as the capacity to withstand and recover from disturbances while maintaining structure, functions and identity, involving adaptive, absorptive, and transformative capacities (Ong and Ellison, 2021). Mangrove resilience is assessed through ecological and socioeconomic indicators, further classified into biotic, abiotic, social, economic and political factors (Day et al., 2018; McLeod and Salm, 2006). Biotic factors involve mangrove extent and biophysical parameters such as AGB, while abiotic factors refer to NDVI, sea level, tropical cyclone path, etc. Social, economic and political factors cover mangrove protection legislation, stakeholder involvement and local community well-being (Ong and Ellison, 2021). Generally, resilience investigation requires spatiotemporal analyses of these indicators. remote sensing primarily supports the estimation of ecological factors including mangrove extent delineation, AGB and NDVI, while socioeconomic indicator investigations predominantly depend on field surveys and literature review (Table 2-6). For example, as NDVI is highly correlated with LAI, species richness and AGB, the analyses of NDVI before and after extreme weather events from spaceborne datasets indicate mangrove damage or recovery levels (e.g., Adame et al., 2021; Amaral et al., 2023; Lagomasino et al., 2021; Taillie et al., 2020). The dynamics of AGB estimated from L-band SAR data are used to indicate mangrove's capacity to maintain functionality under sea level rise (Duncan et al., 2018).

Table 2-6. The approaches for mangrove resilience or health investigation.

Environmental drivers	Approaches	Datasets	Location and year	Reference
Extreme events	Visually interpreted vegetation coverage and related NDVI to extreme events	Climate and oceanographic data QuickBird Worldview-2	El Rosario Island in Columbia, 2002-2014	Galeano et al. (2017)
Sea level rise	Detected the change of mangrove extent and biomass	ALOS/PALSAR ENVISAT-MERIS SRTM Landsat-5/8	Four mangrove sites from West Africa to South Asia, 2007-2015	Duncan et al. (2018)
Sea level rise	Detected the change of mangrove extent and island area	historical aerial photographs Landsat images	Florida Bay in the USA, 1953-2014	Zhai et al. (2019)
Anthropogenic activities	Formulated a Mangrove Quality Index	Mangrove properties, soil, marine ecosystem, hydrology and socio- economic variables	Matang Mangrove Forest Reserve in Malaysia, 2015- 2016	Faridah-Hanum et al. (2019)
Sand deposition	Produced NDVI and Tasselled Cap transformation indices mapping	SPOT-6 WorldView-2	Tanjung Piai in Malaysia, 2015-2016	Razali et al. (2019)
Rainfall and salinity variation	Combined field campaign with remote sensing results to examine mangrove replantation and regrowth	Landsat-4/5/7/8	Saloum Delta in Senegal, 1979-2015	Andrieu et al. (2020)
Shrimp farm	Analysed spectral vegetation indices over time	Landsat-5/8 Sentinel-2A	Jazan Economic City in Saudi Arabia, 2016-2017	Arshad et al. (2020)
Anthropogenic activities	Applied PSR model to establish a mangrove ecosystem health evaluation system	Mangrove properties, environmental and socio-economic variables	Mangrove forest in Guangdong Province, China	Wang et al. (2021)
Anthropogenic activities	Developed mangrove health index to monitor mangrove health with spaceborne observations	SPOT satellite images	Mui Ca Mau mangroves in Vietnam, 1995-2017	Hai et al. (2022)
Tropical storms	Calculated changes in mangrove forest greenness through the NDVI	Mangrove extent maps Cyclones pathways Landsat imagery	Mangrove forests of the Caribbean and the Gulf of Mexico regions, 1996-2020	Amaral et al. (2023)
Restoration post- tsunami	Conducted participatory workshops	Transcripts from the recordings of the workshops	Koh Klang in Thailand, 2017	Elwin et al. (2024)

2.4 Future opportunities

As canopy height is a fundamental indicator of biomass and the associated carbon stock, canopy height has been ranked as a high-priority biodiversity variable from spaceborne observations (Skidmore et al., 2021). High-resolution CHMs better illustrate the heterogeneity of vegetation structure at a finer scale, showing significant potential in advancing the modelling of climate change impacts. As space-based observations continue to improve with higher spatial resolutions and enhanced capability for investigating forest structures, the integration of spaceborne LiDAR measurements with spaceborne optical imagery shows great potential for large-scale canopy height estimation. Potapov et al. (2021) incorporated Landsat imagery with GEDI-derived canopy height metrics to generate global 30 m canopy height map, while Lang et al. (2023) incorporated the same LiDAR measurements with Sentinel-2 images for global 10 m canopy height map. As deep learning exhibits great performance in high-resolution image interpretation, Tolan et al. (2024) deployed advanced deep learning algorithm to produce global 1 m canopy height estimation map with the integration of airborne LiDAR data and Maxar optical imagery. However, it should be noted that errors may be introduced by these modelled global products when applied in biodiversity models, as global datasets are designed to represent general vegetation patterns rather than specific species (Moudrý et al., 2024). Several global mangrove canopy height products have been developed with spatial resolutions of 30 m (Aslan and Aljahdali, 2022; Simard et al., 2019; Yu et al., 2024) and 12 m (Simard et al., 2025), but there is limited understanding of their consistency at a local scale or intercomparison between them (Stovall et al., 2021).

Since increasing mangrove conservation and restoration efforts have been being carried out, there is a need to establish effective mangrove monitoring systems (Eger et al., 2022; Lovelock et al., 2022). Worthington et al. (2020) illustrated a new platform for visualizing and disseminating global mangrove dataset to stakeholders, including scientific communities, non-governmental organizations, governmental agencies, and those involved in restoration efforts. Gatt et al. (2022) developed a framework of key metrics and indicators on mangrove forest restoration, aiming at evaluating restoration efforts for restoration practitioners and providing the baseline for future restoration. As big data and remote sensing approaches have developed rapidly, particularly in spatiotemporal resolutions, mangrove monitoring systems are anticipated to be more dynamic (i.e., near-term) and frequently updated through high-frequency spaceborne observations. This will enable the timely mobilization of on-the-ground resources to address emerging threats to mangroves, while also allowing iterative comparisons between predictions and new observations, ultimately enhancing adaptive mangrove management (Dietze et al., 2018).

2.5 Summary

This chapter summarizes various remote sensing data and approaches in mangrove research, including distribution mapping and species discrimination, LAI and AGB estimation, and resilience investigation. Each remote sensing data source exhibits distinct strengths and limitations. For example, optical imagery, with broader spectral range, enables more detailed mangrove species discrimination compared to SAR imagery; on the other hand, SAR imagery is less affected by cloud cover and time of acquisition than optical imagery. Spaceborne LiDAR measurements provide large scale three-dimensional information for mangrove vertical structure investigation but lack the provision of wall-to-wall data coverage. Based on these remote sensing data, the approaches in mangrove research are mainly grouped into parametric and non-parametric methods, alongside visual interpretation and object-oriented methods. These data and approaches can be introduced individually or combined for challenging research objectives. Furthermore, the advancement of deep learning with multisource data fusion shows significant potentials in high-resolution canopy height estimation and dynamic mangrove monitoring system, propelling mangrove research with more comprehensive insights.

References

- Abdel-Hamid, A., Dubovyk, O., El-Magd, I.A., et al., 2018. Mapping mangroves extents on the Red Sea coastline in Egypt using polarimetric SAR and high resolution optical remote sensing data. Sustainability (Switzerland) 10. https://doi.org/10.3390/su10030646
- Adame, M.F., Connolly, R.M., Turschwell, M.P., et al., 2021. Future carbon emissions from global mangrove forest loss. Global Change Biology 27, 2856–2866. https://doi.org/10.1111/gcb.15571
- Akram, H., Hussain, S., Mazumdar, P., et al., 2023. Mangrove Health: A Review of Functions, Threats, and Challenges Associated with Mangrove Management Practices. Forests 14, 1698. https://doi.org/10.3390/f14091698
- Alongi, D.M., 2020. Global Significance of Mangrove Blue Carbon in Climate Change Mitigation. Sci 2, 67. https://doi.org/10.3390/sci2030067
- Alongi, D.M., 2012. Carbon sequestration in mangrove forests. Carbon Management 3, 313–322. https://doi.org/10.4155/cmt.12.20
- Alongi, D.M., 2002. Present state and future of the world's mangrove forests. Environmental Conservation 29, 331–349. https://doi.org/10.1017/s0376892902000231
- Amaral, C., Poulter, B., Lagomasino, D., et al., 2023. Drivers of mangrove vulnerability and resilience to tropical cyclones in the North Atlantic Basin. Science of The Total Environment 898, 165413. https://doi.org/10.1016/j.scitotenv.2023.165413
- Andrieu, J., Lombard, F., Fall, A., et al., 2020. Botanical field-study and remote sensing to describe mangrove resilience in the Saloum Delta (Senegal) after 30 years of degradation narrative. Forest Ecology and Management 461, 117963. https://doi.org/10.1016/j.foreco.2020.117963
- Arshad, M., Eid, E.M., Hasan, M., 2020. Mangrove health along the hyper-arid southern Red Sea coast of Saudi Arabia. Environ Monit Assess 192, 189. https://doi.org/10.1007/s10661-020-8140-6
- Asbridge, E., Lucas, R., Rogers, K., et al., 2018. The extent of mangrove change and potential for recovery following severe Tropical Cyclone Yasi, Hinchinbrook Island, Queensland, Australia. Ecology and Evolution 8, 10416–10434. https://doi.org/10.1002/ece3.4485
- Aslan, A., Aljahdali, M.O., 2022. Characterizing Global Patterns of Mangrove Canopy Height and Aboveground Biomass Derived from SRTM Data. Forests 13, 1545. https://doi.org/10.3390/f13101545
- Aslan, A., Rahman, A.F., Warren, M.W., et al., 2016. Mapping spatial distribution and biomass of coastal wetland vegetation in Indonesian Papua by combining active and passive remotely sensed data. Remote Sensing of Environment 183, 65–81. https://doi.org/10.1016/j.rse.2016.04.026

- Baccini, A., Goetz, S.J., Walker, W.S., et al., 2012. Estimated carbon dioxide emissions from tropical deforestation improved by carbon-density maps. Nature Clim Change 2, 182–185. https://doi.org/10.1038/nclimate1354
- Baret, F., Vanderbilt, V.C., Steven, M.D., et al., 1994. Use of spectral analogy to evaluate canopy reflectance sensitivity to leaf optical properties. Remote Sensing of Environment 48, 253–260. https://doi.org/10.1016/0034-4257(94)90146-5
- Basyuni, M., Wirasatriya, A., Iryanthony, S.B., et al., 2023. Aboveground biomass and carbon stock estimation using UAV photogrammetry in Indonesian mangroves and other competing land uses. Ecological Informatics 77, 102227. https://doi.org/10.1016/j.ecoinf.2023.102227
- Bergen, K.M., Dobson, M.C., 1999. Integration of remotely sensed radar imagery in modeling and mapping of forest biomass and net primary production. Ecological Modelling 122, 257–274. https://doi.org/10.1016/s0304-3800(99)00141-6
- Berninger, A., Lohberger, S., Zhang, D., et al., 2019. Canopy Height and Above-Ground Biomass Retrieval in Tropical Forests Using Multi-Pass X- and C-Band Pol-InSAR Data. Remote Sensing 11, 2105. https://doi.org/10.3390/rs11182105
- Bhadra, S., Sagan, V., Sarkar, S., et al., 2024. PROSAIL-Net: A transfer learning-based dual stream neural network to estimate leaf chlorophyll and leaf angle of crops from UAV hyperspectral images. ISPRS Journal of Photogrammetry and Remote Sensing 210, 1–24. https://doi.org/10.1016/j.isprsjprs.2024.02.020
- Bihamta Toosi, N., Soffianian, A.R., Fakheran, S., et al., 2020. Land Cover Classification in Mangrove Ecosystems Based on VHR Satellite Data and Machine Learning—An Upscaling Approach. Remote Sensing 12, 2684. https://doi.org/10.3390/rs12172684
- Binh, N.A., Hauser, L.T., Viet Hoa, P., et al., 2022. Quantifying mangrove leaf area index from Sentinel-2 imagery using hybrid models and active learning. International Journal of Remote Sensing 43, 5636–5657. https://doi.org/10.1080/01431161.2021.2024912
- Biswas, H., Zhang, K., Ross, M.S., et al., 2020. Delineation of Tree Patches in a Mangrove-Marsh Transition Zone by Watershed Segmentation of Aerial Photographs. Remote Sensing 12, 2086. https://doi.org/10.3390/rs12132086
- Blaschke, T., 2010. Object based image analysis for remote sensing. ISPRS Journal of Photogrammetry and Remote Sensing 65, 2–16. https://doi.org/10.1016/j.isprsjprs.2009.06.004
- Boser, B.E., Guyon, I.M., Vapnik, V.N., 1992. A training algorithm for optimal margin classifiers, in: Proceedings of the Fifth Annual Workshop on Computational Learning Theory, COLT '92. Association for Computing Machinery, New York, NY, USA, pp. 144–152. https://doi.org/10.1145/130385.130401

- Brander, L.M., Wagtendonk, A.J., Hussain, S.S., et al., 2012. Ecosystem service values for mangroves in Southeast Asia: A meta-analysis and value transfer application. Ecosystem Services 1, 62–69. https://doi.org/10.1016/j.ecoser.2012.06.003
- Breiman, L., 2001. Random Forests. Machine Learning 45, 5–32. https://doi.org/10.1023/A:1010933404324
- Bryan-Brown, D.N., Connolly, R.M., Richards, D.R., et al., 2020. Global trends in mangrove forest fragmentation. Scientific Reports 10. https://doi.org/10.1038/s41598-020-63880-1
- Bunting, P., Rosenqvist, A., Hilarides, L., et al., 2022a. Global Mangrove Extent Change 1996–2020: Global Mangrove Watch Version 3.0. Remote Sensing 14, 3657. https://doi.org/10.3390/rs14153657
- Bunting, P., Rosenqvist, A., Hilarides, L., et al., 2022b. Global Mangrove Watch: Updated 2010 Mangrove Forest Extent (v2.5). Remote Sensing 14, 1034. https://doi.org/10.3390/rs14041034
- Cannicci, S., Burrows, D., Fratini, S., et al., 2008. Faunal impact on vegetation structure and ecosystem function in mangrove forests: A review. Aquatic Botany 89, 186–200. https://doi.org/10.1016/j.aquabot.2008.01.009
- Carrasquilla-Henao, M., Juanes, F., 2017. Mangroves enhance local fisheries catches: a global meta-analysis. Fish and Fisheries 18, 79–93. https://doi.org/10.1111/faf.12168
- Carrera-Hernández, J.J., 2021. Not all DEMs are equal: An evaluation of six globally available 30 m resolution DEMs with geodetic benchmarks and LiDAR in Mexico. Remote Sensing of Environment 261, 112474. https://doi.org/10.1016/j.rse.2021.112474
- Castillo, J.A.A., Apan, A.A., Maraseni, T.N., et al., 2017. Estimation and mapping of above-ground biomass of mangrove forests and their replacement land uses in the Philippines using Sentinel imagery. ISPRS Journal of Photogrammetry and Remote Sensing 134, 70–85. https://doi.org/10.1016/j.isprsjprs.2017.10.016
- Chave, J., Andalo, C., Brown, S., et al., 2005. Tree allometry and improved estimation of carbon stocks and balance in tropical forests. Oecologia 145, 87–99. https://doi.org/10.1007/s00442-005-0100-x
- Chowdhury, R., Sutradhar, T., Begam, Mst.M., et al., 2019. Effects of nutrient limitation, salinity increase, and associated stressors on mangrove forest cover, structure, and zonation across Indian Sundarbans. Hydrobiologia 842, 191–217. https://doi.org/10.1007/s10750-019-04036-9
- Cochard, R., Ranamukhaarachchi, S.L., Shivakoti, G.P., et al., 2008. The 2004 tsunami in Aceh and Southern Thailand: A review on coastal ecosystems, wave hazards and vulnerability. Perspectives in Plant Ecology, Evolution and Systematics 10, 3–40. https://doi.org/10.1016/j.ppees.2007.11.001
- Cortes, C., Vapnik, V., 1995. Support-vector networks. Mach Learn 20, 273–297. https://doi.org/10.1007/BF00994018

- Curnick, D.J., Pettorelli, N., Amir, A.A., et al., 2019. The value of small mangrove patches. Science 363, 239. https://doi.org/10.1126/science.aaw0809
- Dahdouh-Guebas, F., Friess, D.A., Lovelock, C.E., et al., 2022. Cross-cutting research themes for future mangrove forest research. Nat. Plants 8, 1131–1135. https://doi.org/10.1038/s41477-022-01245-4
- Dahdouh-Guebas, F., Van Pottelbergh, I., Kairo, J.G., et al., 2004. Human-impacted mangroves in Gazi (Kenya): Predicting future vegetation based on retrospective remote sensing, social surveys, and tree distribution. Marine Ecology Progress Series 272, 77–92. https://doi.org/10.3354/meps272077
- Dahdouh-Guebas, F., Zetterström, T., Rönnbäck, P., et al., 2002. Recent Changes in Land-Use in the Pambala–Chilaw Lagoon Complex (Sri Lanka) Investigated Using Remote Sensing and GIS: Conservation of Mangroves vs. Development of Shrimp Farming. Environment, Development and Sustainability 4, 185–200. https://doi.org/10.1023/A:1020854413866
- Dandois, J.P., Ellis, E.C., 2013. High spatial resolution three-dimensional mapping of vegetation spectral dynamics using computer vision. Remote Sensing of Environment 136, 259–276. https://doi.org/10.1016/j.rse.2013.04.005
- Day, R.H., Allen, S.T., Brenner, J., et al., 2018. Ecological resilience indicators for mangrove ecosystems 91–150.
- Dey, B., Ahmed, R., Ferdous, J., et al., 2023. Automated plant species identification from the stomata images using deep neural network: A study of selected mangrove and freshwater swamp forest tree species of Bangladesh. Ecological Informatics 75, 102128. https://doi.org/10.1016/j.ecoinf.2023.102128
- Díaz, B.M., Blackburn, G.A., 2003. Remote sensing of mangrove biophysical properties: Evidence from a laboratory simulation of the possible effects of background variation on spectral vegetation indices. International Journal of Remote Sensing 24, 53–73. https://doi.org/10.1080/01431160305012
- Dietze, M.C., Fox, A., Beck-Johnson, L.M., et al., 2018. Iterative near-term ecological forecasting: Needs, opportunities, and challenges. Proceedings of the National Academy of Sciences 115, 1424–1432. https://doi.org/10.1073/pnas.1710231115
- Donato, D.C., Kauffman, J.B., Murdiyarso, D., et al., 2011. Mangroves among the most carbon-rich forests in the tropics. Nature Geoscience 4, 293–297. https://doi.org/10.1038/ngeo1123
- Dubayah, R., Blair, J.B., Goetz, S., et al., 2020. The Global Ecosystem Dynamics Investigation: High-resolution laser ranging of the Earth's forests and topography. Science of Remote Sensing 1, 100002. https://doi.org/10.1016/j.srs.2020.100002
- Duncan, C., Owen, H.J.F., Thompson, J.R., et al., 2018. Satellite remote sensing to monitor mangrove forest resilience and resistance to sea level rise. Methods in Ecology and Evolution 9, 1837–1852. https://doi.org/10.1111/2041-210X.12923

- Duncanson, L., Kellner, J.R., Armston, J., et al., 2022. Aboveground biomass density models for NASA's Global Ecosystem Dynamics Investigation (GEDI) lidar mission. Remote Sensing of Environment 270, 112845. https://doi.org/10.1016/j.rse.2021.112845
- Eger, A.M., Earp, H.S., Friedman, K., et al., 2022. The need, opportunities, and challenges for creating a standardized framework for marine restoration monitoring and reporting. Biological Conservation 266, 109429. https://doi.org/10.1016/j.biocon.2021.109429
- Elwin, A., Robinson, E.J.Z., Feola, G., et al., 2024. How is mangrove ecosystem health defined? A local community perspective from coastal Thailand. Ocean & Coastal Management 251, 107037. https://doi.org/10.1016/j.ocecoaman.2024.107037
- FAO, 2023. The world's mangroves 2000–2020. FAO, Rome. https://doi.org/10.4060/cc7044en
- Faridah-Hanum, I., Yusoff, F.M., Fitrianto, A., et al., 2019. Development of a comprehensive mangrove quality index (MQI) in Matang Mangrove: Assessing mangrove ecosystem health. Ecological Indicators 102, 103–117. https://doi.org/10.1016/j.ecolind.2019.02.030
- Fatoyinbo, T.E., Simard, M., 2013. Height and biomass of mangroves in Africa from ICESat/GLAS and SRTM. International Journal of Remote Sensing 34, 668–681. https://doi.org/10.1080/01431161.2012.712224
- Feliciano, E.A., Wdowinski, S., Potts, M.D., et al., 2017. Estimating Mangrove Canopy Height and Above-Ground Biomass in the Everglades National Park with Airborne LiDAR and TanDEM-X Data. Remote Sensing 9, 702. https://doi.org/10.3390/rs9070702
- Friess, D.A., Adams, J., Andradi-Brown, D.A., et al., 2024. Mangrove forests: their status, threats, conservation and restoration, in: Reference Module in Earth Systems and Environmental Sciences. Elsevier, p. B9780323907989000317. https://doi.org/10.1016/B978-0-323-90798-9.00031-7
- Friess, D.A., Richards, D.R., Phang, V.X.H., 2016. Mangrove forests store high densities of carbon across the tropical urban landscape of Singapore. Urban Ecosystems 19, 795–810. https://doi.org/10.1007/s11252-015-0511-3
- Friess, D.A., Rogers, K., Lovelock, C.E., et al., 2019. The State of the World's Mangrove Forests: Past, Present, and Future. Annual Review of Environment and Resources 44, 89–115. https://doi.org/10.1146/annurev-environ-101718-033302
- Fu, B., Liang, Y., Lao, Z., et al., 2023. Quantifying scattering characteristics of mangrove species from Optuna-based optimal machine learning classification using multi-scale feature selection and SAR image time series. International Journal of Applied Earth Observation and Geoinformation 122, 103446. https://doi.org/10.1016/j.jag.2023.103446
- Fu, B., Sun, J., Wang, Y., et al., 2022. Evaluation of LAI Estimation of Mangrove Communities Using DLR and ELR Algorithms With UAV, Hyperspectral, and SAR Images. Front. Mar. Sci. 9. https://doi.org/10.3389/fmars.2022.944454

- Galeano, A., Urrego, L.E., Botero, V., et al., 2017. Mangrove resilience to climate extreme events in a Colombian Caribbean Island. Wetlands Ecol Manage 25, 743–760. https://doi.org/10.1007/s11273-017-9548-9
- Gatt, Y.M., Andradi-Brown, D.A., Ahmadia, G.N., et al., 2022. Quantifying the Reporting, Coverage and Consistency of Key Indicators in Mangrove Restoration Projects. Front. For. Glob. Change 5. https://doi.org/10.3389/ffgc.2022.720394
- Ghosh, S.M., Behera, M.D., 2021. Aboveground biomass estimates of tropical mangrove forest using Sentinel-1 SAR coherence data The superiority of deep learning over a semi-empirical model. Computers & Geosciences 150, 104737. https://doi.org/10.1016/j.cageo.2021.104737
- Gilman, E.L., Ellison, J., Duke, N.C., et al., 2008. Threats to mangroves from climate change and adaptation options: A review. Aquatic Botany 89, 237–250. https://doi.org/10.1016/j.aquabot.2007.12.009
- Giri, C., Ochieng, E., Tieszen, L.L., et al., 2011. Status and distribution of mangrove forests of the world using earth observation satellite data. Global Ecology and Biogeography 20, 154–159. https://doi.org/10.1111/j.1466-8238.2010.00584.x
- Guo, Q., Su, Y., Hu, T., et al., 2017. An integrated UAV-borne lidar system for 3D habitat mapping in three forest ecosystems across China. International Journal of Remote Sensing 38, 2954–2972. https://doi.org/10.1080/01431161.2017.1285083
- Guo, X., Wang, M., Jia, M., et al., 2021. Estimating mangrove leaf area index based on red-edge vegetation indices: A comparison among UAV, WorldView-2 and Sentinel-2 imagery. International Journal of Applied Earth Observation and Geoinformation 103, 102493. https://doi.org/10.1016/j.jag.2021.102493
- Hai, P.M., Tinh, P.H., Son, N.P., et al., 2022. Mangrove health assessment using spatial metrics and multi-temporal remote sensing data. PLOS ONE 17, e0275928. https://doi.org/10.1371/journal.pone.0275928
- Hamilton, S.E., Casey, D., 2016. Creation of a high spatio-temporal resolution global database of continuous mangrove forest cover for the 21st century (CGMFC-21). Global Ecology and Biogeography 25, 729–738. https://doi.org/10.1111/geb.12449
- Han, X., Feng, L., Hu, C., et al., 2018. Hurricane-Induced Changes in the Everglades National Park Mangrove Forest: Landsat Observations Between 1985 and 2017. Journal of Geophysical Research: Biogeosciences 123, 3470–3488. https://doi.org/10.1029/2018jg004501
- Hancock, S., McGrath, C., Lowe, C., et al., 2021. Requirements for a global lidar system: spaceborne lidar with wall-to-wall coverage. Royal Society Open Science 8, 211166. https://doi.org/10.1098/rsos.211166

- Harishma, K.M., Sandeep, S., Sreekumar, V.B., 2020. Biomass and carbon stocks in mangrove ecosystems of Kerala, southwest coast of India. Ecological Processes 9. https://doi.org/10.1186/s13717-020-00227-8
- Hecht-nielsen, R., 1992. Theory of the Backpropagation Neural Network*, in: Wechsler, H. (Ed.), Neural Networks for Perception. Academic Press, pp. 65–93. https://doi.org/10.1016/B978-0-12-741252-8.50010-8
- Heenkenda, M.K., Joyce, K.E., Maier, S.W., et al., 2014. Mangrove Species Identification: Comparing WorldView-2 with Aerial Photographs. Remote Sensing 6, 6064–6088. https://doi.org/10.3390/rs6076064
- Held, A., Ticehurst, C., Lymburner, L., et al., 2001. Hyperspectral mapping of rainforests and mangroves, in: IGARSS 2001: Scanning the Present and Resolving the Future, Vols 1-7, Proceedings, IEEE International Symposium on Geoscience and Remote Sensing (IGARSS). IEEE, New York, pp. 2787–2789.
- Hirschmugl, M., Ofner, M., Raggam, J., et al., 2007. Single tree detection in very high resolution remote sensing data. Remote Sensing of Environment 110, 533–544. https://doi.org/10.1016/j.rse.2007.02.029
- Hoa, P.V., Giang, N.V., Binh, N.A., et al., 2017. Mangrove species discrimination in southern Vietnam based on in-situ measured hyperspectral reflectance. International Journal of Geoinformatics 13, 25–35.
- Hsu, A.J., Kumagai, J., Favoretto, F., et al., 2020. Driven by Drones: Improving Mangrove Extent Maps Using High-Resolution Remote Sensing. Remote Sensing 12, 3986. https://doi.org/10.3390/rs12233986
- Hu, T., Zhang, Y., Su, Y., et al., 2020. Mapping the Global Mangrove Forest Aboveground Biomass Using Multisource Remote Sensing Data. Remote Sensing 12, 1690. https://doi.org/10.3390/rs12101690
- Hu, W., Wang, Y., Zhang, D., et al., 2020. Mapping the potential of mangrove forest restoration based on species distribution models: A case study in China. Science of The Total Environment 748, 142321. https://doi.org/10.1016/j.scitotenv.2020.142321
- Huang, K., Yang, G., Yuan, Y., et al., 2022. Optical and SAR images Combined Mangrove Index based on multi-feature fusion. Science of Remote Sensing 5, 100040. https://doi.org/10.1016/j.srs.2022.100040
- Hutchison, J., Spalding, M., zu Ermgassen, P., 2014. The role of mangroves in fisheries enhancement. The Nature Conservancy and Wetlands International 54.
- IPCC, 2003. Good Practice Guidance for Land Use, Land-Use Change and Forestry (GPG-LULUCF) Glossary.

- Jachowski, N.R.A., Quak, M.S.Y., Friess, D.A., et al., 2013. Mangrove biomass estimation in Southwest Thailand using machine learning. Applied Geography 45, 311–321. https://doi.org/10.1016/j.apgeog.2013.09.024
- Jagadish, B., Behera, M.D., Prakash, A.J., et al., 2024. Indicating Saturation Limits of Multi-sensor Satellite Data in Estimating Aboveground Biomass of a Mangrove Forest. J Indian Soc Remote Sens 52, 2483–2500. https://doi.org/10.1007/s12524-024-01968-1
- Ji, M.H., Wu, Y.M., Deng, Z.W., et al., 2008. Mapping mangroves from high-resolution multispectral imagery: using Beilun Estuary, Guangxi, China as a case study, in: Remote Sensing and Modeling of Ecosystems for Sustainability V, Proceedings of SPIE. Spie-Int Soc Optical Engineering, Bellingham.
- Jia, M., Guo, X., Zhang, L., et al., 2024. Mapping mangrove functional traits from Sentinel-2 imagery based on hybrid models coupled with active learning strategies. International Journal of Applied Earth Observation and Geoinformation 130, 103905. https://doi.org/10.1016/j.jag.2024.103905
- Jia, M., Wang, Z., Mao, D., et al., 2023. Mapping global distribution of mangrove forests at 10-m resolution. Science Bulletin 68, 1306–1316. https://doi.org/10.1016/j.scib.2023.05.004
- Jia, M.M., Zhang, Y.Z., Wang, Z.M., et al., 2014. Mapping the distribution of mangrove species in the Core Zone of Mai Po Marshes Nature Reserve, Hong Kong, using hyperspectral data and high-resolution data. Int. J. Appl. Earth Obs. Geoinf. 33, 226–231. https://doi.org/10.1016/j.jag.2014.06.006
- Jusoff, K., 2013. Malaysian Mangrove Forests and their Significance to the Coastal Marine Environment. Polish journal of environmental studies 22.
- Kamal, M., Phinn, S., 2011. Hyperspectral Data for Mangrove Species Mapping: A Comparison of Pixel-Based and Object-Based Approach. Remote Sensing 3, 2222–2242. https://doi.org/10.3390/rs3102222
- Kamal, M., Phinn, S., Johansen, K., 2014. Characterizing the Spatial Structure of Mangrove Features for Optimizing Image-Based Mangrove Mapping. Remote Sensing 6, 984–1006. https://doi.org/10.3390/rs6020984
- Kamal, M., Phinn, S., Johansen, K., 2016. Assessment of multi-resolution image data for mangrove leaf area index mapping. Remote Sensing of Environment 176, 242–254. https://doi.org/10.1016/j.rse.2016.02.013
- Kanniah, K.D., Sheikhi, A., Cracknell, A.P., et al., 2015. Satellite Images for Monitoring Mangrove Cover Changes in a Fast Growing Economic Region in Southern Peninsular Malaysia. Remote Sensing 7, 14360–14385. https://doi.org/10.3390/rs71114360
- Kattenborn, T., Leitloff, J., Schiefer, F., et al., 2021. Review on Convolutional Neural Networks (CNN) in vegetation remote sensing. ISPRS Journal of Photogrammetry and Remote Sensing 173, 24–49. https://doi.org/10.1016/j.isprsjprs.2020.12.010

- Kauffman, J.B., Donato, D.C., 2012. Protocols for the measurement, monitoring and reporting of structure, biomass, and carbon stocks in mangrove forests. Center for International Forestry Research, Bogor, Indonesia.
- Kovacs, J.M., Flores-Verdugo, F., Wang, J., et al., 2004. Estimating leaf area index of a degraded mangrove forest using high spatial resolution satellite data. Aquatic Botany 80, 13–22. https://doi.org/10.1016/j.aquabot.2004.06.001
- Kovacs, J.M., Vandenberg, C.V., Wang, J., et al., 2008. The Use of Multipolarized Spaceborne SAR Backscatter for Monitoring the Health of a Degraded Mangrove Forest. coas 2008, 248–254. https://doi.org/10.2112/06-0660.1
- Kuenzer, C., Bluemel, A., Gebhardt, S., et al., 2011. Remote Sensing of Mangrove Ecosystems: A Review. Remote Sensing 3, 878–928. https://doi.org/10.3390/rs3050878
- Kumar, T., Mandal, A., Dutta, D., et al., 2019. Discrimination and classification of mangrove forests using EO-1 Hyperion data: a case study of Indian Sundarbans. Geocarto International 34, 415–442. https://doi.org/10.1080/10106049.2017.1408699
- Kumar, T., Patnaik, C., 2013. Discrimination of mangrove forests and characterization of adjoining land cover classes using temporal C-band Synthetic Aperture Radar data: A case study of Sundarbans. International Journal of Applied Earth Observation and Geoinformation 23, 119–131. https://doi.org/10.1016/j.jag.2012.12.001
- Lagomasino, D., Fatoyinbo, T., Castañeda-Moya, E., et al., 2021. Storm surge and ponding explain mangrove dieback in southwest Florida following Hurricane Irma. Nat Commun 12, 4003. https://doi.org/10.1038/s41467-021-24253-y
- Lagomasino, D., Fatoyinbo, T., Lee, S., et al., 2016. A Comparison of Mangrove Canopy Height Using Multiple Independent Measurements from Land, Air, and Space. Remote Sensing 8, 327. https://doi.org/10.3390/rs8040327
- Lang, N., Jetz, W., Schindler, K., et al., 2023. A high-resolution canopy height model of the Earth. Nat Ecol Evol 7, 1778–1789. https://doi.org/10.1038/s41559-023-02206-6
- Lassalle, G., de Souza Filho, C.R., 2022. Tracking canopy gaps in mangroves remotely using deep learning. Remote Sensing in Ecology and Conservation 8, 890–903. https://doi.org/10.1002/rse2.289
- Lassalle, G., Ferreira, M.P., Cué La Rosa, L.E., et al., 2023. Advances in multi- and hyperspectral remote sensing of mangrove species: A synthesis and study case on airborne and multisource spaceborne imagery. ISPRS Journal of Photogrammetry and Remote Sensing 195, 298–312. https://doi.org/10.1016/j.isprsjprs.2022.12.003
- Lee, C.K.F., Duncan, C., Nicholson, E., et al., 2021. Mapping the Extent of Mangrove Ecosystem Degradation by Integrating an Ecological Conceptual Model with Satellite Data. Remote Sensing 13, 2047. https://doi.org/10.3390/rs13112047

- Lee, S.-K., Fatoyinbo, T.E., 2015. TanDEM-X Pol-InSAR Inversion for Mangrove Canopy Height Estimation. IEEE Journal of Selected Topics in Applied Earth Observations and Remote Sensing 8, 3608–3618. https://doi.org/10.1109/JSTARS.2015.2431646
- Lee, S.-K., Fatoyinbo, T.E., Lagomasino, D., et al., 2018. Multibaseline TanDEM-X Mangrove Height Estimation: The Selection of the Vertical Wavenumber. IEEE Journal of Selected Topics in Applied Earth Observations and Remote Sensing 11, 3434–3442. https://doi.org/10.1109/JSTARS.2018.2835647
- Lefsky, M.A., 2010. A global forest canopy height map from the Moderate Resolution Imaging Spectroradiometer and the Geoscience Laser Altimeter System. Geophysical Research Letters 37, n/a-n/a. https://doi.org/10.1029/2010gl043622
- Li, Q., Wong, F.K.K., Fung, T., 2021. Mapping multi-layered mangroves from multispectral, hyperspectral, and LiDAR data. Remote Sensing of Environment 258, 112403. https://doi.org/10.1016/j.rse.2021.112403
- Li, X., Gar-On Yeh, A., Wang, S., et al., 2007. Regression and analytical models for estimating mangrove wetland biomass in South China using Radarsat images. International Journal of Remote Sensing 28, 5567–5582. https://doi.org/10.1080/01431160701227638
- Liu, A., Cheng, X., Chen, Z., 2021. Performance evaluation of GEDI and ICESat-2 laser altimeter data for terrain and canopy height retrievals. Remote Sensing of Environment 264, 112571. https://doi.org/10.1016/j.rse.2021.112571
- Liu, C.C., Hsu, T.W., Wen, H.L., et al., 2019. Mapping pure mangrove patches in small corridors and sandbanks using airborne hyperspectral imagery. Remote Sensing 11. https://doi.org/10.3390/rs11050592
- Liu, M., Leung, F., Lee, S.-Y., 2022. Interpreting Mangrove Habitat and Coastal Land Cover Change in the Greater Bay Area, Southern China, from 1924 to 2020 Using Historical Aerial Photos and Multiple Sources of Satellite Data. Remote Sensing 14, 5163. https://doi.org/10.3390/rs14205163
- Liu, X., Fatoyinbo, T.E., Thomas, N.M., et al., 2021. Large-Scale High-Resolution Coastal Mangrove Forests Mapping Across West Africa With Machine Learning Ensemble and Satellite Big Data. Front. Earth Sci. 8. https://doi.org/10.3389/feart.2020.560933
- Lovelock, C.E., Barbier, E., Duarte, C.M., 2022. Tackling the mangrove restoration challenge. PLOS Biology 20, e3001836. https://doi.org/10.1371/journal.pbio.3001836
- Lovelock, C.E., Cahoon, D.R., Friess, D.A., et al., 2015. The vulnerability of Indo-Pacific mangrove forests to sea-level rise. Nature 526, 559–563. https://doi.org/10.1038/nature15538
- Lu, Y., Wang, L., 2024. Leveraging optimal UAV-lidar features for two CNN approaches to delineate mangrove tree crowns. Remote Sensing Applications: Society and Environment 35, 101260. https://doi.org/10.1016/j.rsase.2024.101260

- Lucas, R., Milne, A.K., Mitchell, A., et al., 2000. Use of stereo aerial photography for assessing changes in the extent and height of mangrove canopies in tropical Australia. Presented at the IGARSS 2000. IEEE 2000 International Geoscience and Remote Sensing Symposium. Taking the Pulse of the Planet: The Role of Remote Sensing in Managing the Environment. Proceedings (Cat. No.00CH37120), IEEE, Honolulu, HI, USA, pp. 1880–1882. https://doi.org/10.1109/igarss.2000.858154
- Lucas, R.M., Mitchell, A.L., Rosenqvist, A., et al., 2007. The potential of L-band SAR for quantifying mangrove characteristics and change: case studies from the tropics. Aquatic Conservation: Marine and Freshwater Ecosystems 17, 245–264. https://doi.org/10.1002/aqc.833
- Lucas, R., Rebelo, L.-M., Fatoyinbo, L., et al., 2014. Contribution of L-band SAR to systematic global mangrove monitoring. Mar. Freshwater Res. 65, 589. https://doi.org/10.1071/MF13177
- Lucas, R., Van De Kerchove, R., Otero, V., et al., 2020. Structural characterisation of mangrove forests achieved through combining multiple sources of remote sensing data. Remote Sensing of Environment 237. https://doi.org/10.1016/j.rse.2019.111543
- Luo, Q., Li, Z., Huang, Z., et al., 2023. Retrieval of Mangrove leaf area index and its response to typhoon based on WorldView-3 image. Remote Sensing Applications: Society and Environment 30, 100931. https://doi.org/10.1016/j.rsase.2023.100931
- Ma, C., Ai, B., Zhao, J., et al., 2019. Change detection of mangrove forests in coastal Guangdong during the past three decades based on remote sensing data. Remote Sensing 11. https://doi.org/10.3390/rs11080962
- Mafi-Gholami, D., Mahmoudi, B., Zenner, E.K., 2017. An analysis of the relationship between drought events and mangrove changes along the northern coasts of the Pe rsian Gulf and Oman Sea. Estuarine, Coastal and Shelf Science 199, 141–151. https://doi.org/10.1016/j.ecss.2017.10.008
- Manna, S., Raychaudhuri, B., 2020. Retrieval of Leaf area index and stress conditions for Sundarban mangroves using Sentinel-2 data. International Journal of Remote Sensing 41, 1019–1039. https://doi.org/10.1080/01431161.2019.1655174
- Markus, T., Neumann, T., Martino, A., et al., 2017. The Ice, Cloud, and land Elevation Satellite-2 (ICESat-2): Science requirements, concept, and implementation. Remote Sensing of Environment 190, 260–273. https://doi.org/10.1016/j.rse.2016.12.029
- Maung, W.S., Sasaki, J., 2021. Assessing the Natural Recovery of Mangroves after Human Disturbance Using Neural Network Classification and Sentinel-2 Imagery in Wunbaik Mangrove Forest, Myanmar. Remote Sensing 13, 52. https://doi.org/10.3390/rs13010052
- Maurya, K., Mahajan, S., Chaube, N., 2021. Remote sensing techniques: mapping and monitoring of mangrove ecosystem—a review. Complex Intell. Syst. 7, 2797–2818. https://doi.org/10.1007/s40747-021-00457-z

- McCarthy, M.J., Jessen, B., Barry, M.J., et al., 2020. Automated High-Resolution Time Series Mapping of Mangrove Forests Damaged by Hurricane Irma in Southwest Florida. Remote Sens. 12. https://doi.org/10.3390/rs12111740
- McCulloch, W.S., Pitts, W., 1943. A logical calculus of the ideas immanent in nervous activity. The Bulletin of Mathematical Biophysics 5, 115–133. https://doi.org/10.1007/BF02478259
- McIvor, A., Spencer, T., Spalding, M., et al., 2015. Mangroves, Tropical Cyclones, and Coastal Hazard Risk Reduction, in: Coastal and Marine Hazards, Risks, and Disasters. Elsevier, pp. 403–429. https://doi.org/10.1016/b978-0-12-396483-0.00014-5
- McLeod, E., Salm, R.V., 2006. Managing mangroves for resilience to climate change. International Union for the Conservation of Nature and Natural Resources, Gland, Switzerland.
- Meng, Y., Bai, J., Gou, R., et al., 2021. Relationships between above- and below-ground carbon stocks in mangrove forests facilitate better estimation of total mangrove blue carbon. Carbon Balance and Management 16. https://doi.org/10.1186/s13021-021-00172-9
- Miao, J., Wang, J., Zhao, D., et al., 2024. Modeling strategies and influencing factors in retrieving canopy equivalent water thickness of mangrove forest with Sentinel-2 image. Ecological Indicators 158, 111497. https://doi.org/10.1016/j.ecolind.2023.111497
- Mondal, B., Saha, A.K., Roy, A., 2019. Mapping mangroves using LISS-IV and Hyperion data in part of the Indian Sundarban. Int. J. Remote Sens. 40, 9380–9400. https://doi.org/10.1080/01431161.2019.1630784
- Monsef, H.A.-E., Smith, S.E., 2017. A new approach for estimating mangrove canopy cover using Landsat 8 imagery. Computers and Electronics in Agriculture 135, 183–194. https://doi.org/10.1016/j.compag.2017.02.007
- Mougin, E., Proisy, C., Marty, G., et al., 1999. Multifrequency and multipolarization radar backscattering from mangrove forests. IEEE Transactions on Geoscience and Remote Sensing 37, 94–102. https://doi.org/10.1109/36.739128
- Mountrakis, G., Im, J., Ogole, C., 2011. Support vector machines in remote sensing: A review. ISPRS Journal of Photogrammetry and Remote Sensing 66, 247–259. https://doi.org/10.1016/j.isprsjprs.2010.11.001
- Mumby, P.J., Edwards, A.J., Ernesto Arias-González, J., et al., 2004. Mangroves enhance the biomass of coral reef fish communities in the Caribbean. Nature 427, 533–536. https://doi.org/10.1038/nature02286
- Nagelkerken, I., Blaber, S.J.M., Bouillon, S., et al., 2008. The habitat function of mangroves for terrestrial and marine fauna: A review. Aquatic Botany 89, 155–185. https://doi.org/10.1016/j.aquabot.2007.12.007

- NASA, 2021. Landsat 1 | Landsat Science [WWW Document]. URL https://landsat.gsfc.nasa.gov/satellites/landsat-1/ (accessed 1.9.23).
- Navarro, A., Young, M., Allan, B., et al., 2020. The application of Unmanned Aerial Vehicles (UAVs) to estimate above-ground biomass of mangrove ecosystems. Remote Sensing of Environment 242, 111747. https://doi.org/10.1016/j.rse.2020.111747
- Navarro, J.A., Algeet, N., Fernández-Landa, A., et al., 2019. Integration of UAV, Sentinel-1, and Sentinel-2 Data for Mangrove Plantation Aboveground Biomass Monitoring in Senegal. Remote Sensing 11. https://doi.org/10.3390/rs11010077
- Nedd, G.A., Oyedotun, T.D.T., Simard, M., 2023. Evaluation of Spatio-Temporal Dynamics of Guyana's Mangroves Using SAR and GEE. Earth Syst Environ 7, 509–524. https://doi.org/10.1007/s41748-021-00277-8
- Nesha, M.K., Hussin, Y.A., Van Leeuwen, L.M., et al., 2020. Modeling and mapping aboveground biomass of the restored mangroves using ALOS-2 PALSAR-2 in East Kalimantan, Indonesia. International Journal of Applied Earth Observation and Geoinformation 91, 102158. https://doi.org/10.1016/j.jag.2020.102158
- Niu, C., Phinn, S., Roelfsema, C., 2021. Global Sensitivity Analysis for Canopy Reflectance and Vegetation Indices of Mangroves. Remote Sensing 13, 2617. https://doi.org/10.3390/rs13132617
- Ong, W.J., Ellison, J.C., 2021. Chapter 20 A framework for the quantitative assessment of mangrove resilience, in: Sidik, F., Friess, D.A. (Eds.), Dynamic Sedimentary Environments of Mangrove Coasts. Elsevier, pp. 513–538. https://doi.org/10.1016/B978-0-12-816437-2.00016-1
- Ouyang, X., Guo, F., 2016. Paradigms of mangroves in treatment of anthropogenic wastewater pollution. Science of The Total Environment 544, 971–979. https://doi.org/10.1016/j.scitotenv.2015.12.013
- Pandey, P.C., Anand, A., Srivastava, P.K., 2019. Spatial distribution of mangrove forest species and biomass assessment using field inventory and earth observation hyperspectral data. Biodiversity and Conservation 28, 2143–2162. https://doi.org/10.1007/s10531-019-01698-8
- Parida, B.R., Kumari, A., 2021. Mapping and modeling mangrove biophysical and biochemical parameters using Sentinel-2A satellite data in Bhitarkanika National Park, Odisha. Model. Earth Syst. Environ. 7, 2463–2474. https://doi.org/10.1007/s40808-020-01005-3
- Peng, L., Liu, K., Cao, J., et al., 2020. Combining GF-2 and RapidEye satellite data for mapping mangrove species using ensemble machine-learning methods. International Journal of Remote Sensing 41, 813–838. https://doi.org/10.1080/01431161.2019.1648907
- Pham, L.T.H., Brabyn, L., 2017. Monitoring mangrove biomass change in Vietnam using SPOT images and an object-based approach combined with machine learning algorithms. ISPRS Journal of Photogrammetry and Remote Sensing 128, 86–97. https://doi.org/10.1016/j.isprsjprs.2017.03.013

- Pham, M.H., Do, T.H., Pham, V.-M., et al., 2020. Mangrove forest classification and aboveground biomass estimation using an atom search algorithm and adaptive neuro-fuzzy inference system. PLOS ONE 15, e0233110. https://doi.org/10.1371/journal.pone.0233110
- Pham, T.D., Yokoya, N., Bui, D.T., et al., 2019. Remote Sensing Approaches for Monitoring Mangrove Species, Structure, and Biomass: Opportunities and Challenges. Remote Sensing 11, 230. https://doi.org/10.3390/rs11030230
- Pham, T.D., Yoshino, K., 2017. Aboveground biomass estimation of mangrove species using ALOS-2 PALSAR imagery in Hai Phong City, Vietnam. Journal of Applied Remote Sensing 11, 026010. https://doi.org/10.1117/1.JRS.11.026010
- Pham, T.D., Yoshino, K., Le, N.N., et al., 2018. Estimating aboveground biomass of a mangrove plantation on the Northern coast of Vietnam using machine learning techniques with an integration of ALOS-2 PALSAR-2 and Sentinel-2A data. International Journal of Remote Sensing 39, 7761–7788. https://doi.org/10.1080/01431161.2018.1471544
- Potapov, P., Li, X., Hernandez-Serna, A., et al., 2021. Mapping global forest canopy height through integration of GEDI and Landsat data. Remote Sensing of Environment 253, 112165. https://doi.org/10.1016/j.rse.2020.112165
- Prakash Hati, J., Samanta, S., Rani Chaube, N., et al., 2020. Mangrove classification using airborne hyperspectral AVIRIS-NG and comparing with other spaceborne hyperspectral and multispectral data. Egyptian Journal of Remote Sensing and Space Science. https://doi.org/10.1016/j.ejrs.2020.10.002
- Primavera, J.H., 2000. Development and conservation of Philippine mangroves: institutional issues. Ecological Economics 35, 91–106. https://doi.org/10.1016/s0921-8009(00)00170-1
- Proisy, C., Couteron, P., Fromard, F., 2007. Predicting and mapping mangrove biomass from canopy grain analysis using Fourier-based textural ordination of IKONOS images. Remote Sensing of Environment 109, 379–392. https://doi.org/10.1016/j.rse.2007.01.009
- Pu, R., Cheng, J., 2015. Mapping forest leaf area index using reflectance and textural information derived from WorldView-2 imagery in a mixed natural forest area in Florida, US. International Journal of Applied Earth Observation and Geoinformation 42, 11–23. https://doi.org/10.1016/j.jag.2015.05.004
- Quoc Vo, T., Kuenzer, C., Oppelt, N., 2015. How remote sensing supports mangrove ecosystem service valuation: A case study in Ca Mau province, Vietnam. Ecosystem Services 14, 67–75. https://doi.org/10.1016/j.ecoser.2015.04.007
- RAMSAR, 2004. La Mancha y El Llano: Ramsar sites information service. [WWW Document]. URL https://rsis.ramsar.org/ris/1336?language=en

- Razali, S.M., Nuruddin, A.A., Lion, M., 2019. Mangrove Vegetation Health Assessment Based on Remote Sensing Indices for Tanjung Piai, Malay Peninsular. Sciendo. https://doi.org/10.2478/jlecol-2019-0008
- Rodríguez-Veiga, P., Quegan, S., Carreiras, J., et al., 2019. Forest biomass retrieval approaches from earth observation in different biomes. International Journal of Applied Earth Observation and Geoinformation 77, 53–68. https://doi.org/10.1016/j.jag.2018.12.008
- Rogers, K., Lymburner, L., Salum, R., et al., 2017. Mapping of mangrove extent and zonation using high and low tide composites of Landsat data. Hydrobiologia 803, 49–68. https://doi.org/10.1007/s10750-017-3257-5
- Romer, H., Jeewarongkakul, J., Kaiser, G., et al., 2012. Monitoring post-tsunami vegetation recovery in Phang-Nga province, Thailand, based on IKONOS imagery and field investigations a contribution to the analysis of tsunami vulnerability of coastal ecosystems. Int. J. Remote Sens. 33, 3090–3121. https://doi.org/10.1080/01431161.2011.628710
- Rovai, A.S., Riul, P., Twilley, R.R., et al., 2016. Scaling mangrove aboveground biomass from site-level to continental-scale. Global Ecology and Biogeography 25, 286–298. https://doi.org/10.1111/geb.12409
- Rovai, A.S., Twilley, R.R., Castañeda-Moya, E., et al., 2021. Macroecological patterns of forest structure and allometric scaling in mangrove forests. Global Ecology and Biogeography 30, 1000–1013. https://doi.org/10.1111/geb.13268
- Saatchi, S.S., Harris, N.L., Brown, S., et al., 2011. Benchmark map of forest carbon stocks in tropical regions across three continents. Proceedings of the National Academy of Sciences 108, 9899–9904. https://doi.org/10.1073/pnas.1019576108
- Saenger, P., Ragavan, P., Sheue, C.-R., et al., 2019. Mangrove Biogeography of the Indo-Pacific, in: Gul, B., Böer, B., Khan, M.A., et al. (Eds.), Sabkha Ecosystems, Tasks for Vegetation Science. Springer International Publishing, Cham, pp. 379–400. https://doi.org/10.1007/978-3-030-04417-6 23
- Senger, D.F., Saavedra Hortua, D.A., Engel, S., et al., 2021. Impacts of wetland dieback on carbon dynamics: A comparison between intact and degraded mangroves. Science of the Total Environment 753. https://doi.org/10.1016/j.scitotenv.2020.141817
- Servino, R.N., Gomes, L.E.D.O., Bernardino, A.F., 2018. Extreme weather impacts on tropical mangrove forests in the Eastern Brazil Marine Ecoregion. Science of the Total Environment 628–629, 233–240. https://doi.org/10.1016/j.scitotenv.2018.02.068
- Sheykhmousa, M., Mahdianpari, M., Ghanbari, H., et al., 2020. Support Vector Machine Versus Random Forest for Remote Sensing Image Classification: A Meta-Analysis and Systematic Review. IEEE Journal of Selected Topics in Applied Earth Observations and Remote Sensing 13, 6308–6325. https://doi.org/10.1109/JSTARS.2020.3026724

- Shugart, H.H., Saatchi, S., Hall, F.G., 2010. Importance of structure and its measurement in quantifying function of forest ecosystems. Journal of Geophysical Research: Biogeosciences 115. https://doi.org/10.1029/2009JG000993
- Skidmore, A.K., Coops, N.C., Neinavaz, E., et al., 2021. Priority list of biodiversity metrics to observe from space. Nat Ecol Evol 5, 896–906. https://doi.org/10.1038/s41559-021-01451-x
- Simard, M., Fatoyinbo, L., Smetanka, C., et al., 2019. Mangrove canopy height globally related to precipitation, temperature and cyclone frequency. Nature Geoscience 12, 40–45. https://doi.org/10.1038/s41561-018-0279-1
- Simard, M., Fatoyinbo, L., Thomas, N.M., et al., 2025. A New Global Mangrove Height Map with a 12 meter spatial resolution. Sci Data 12, 15. https://doi.org/10.1038/s41597-024-04213-z
- Simard, M., Rivera-Monroy, V.H., Mancera-Pineda, J.E., et al., 2008. A systematic method for 3D mapping of mangrove forests based on Shuttle Radar Topography Mission elevation data, ICEsat/GLAS waveforms and field data: Application to Ciénaga Grande de Santa Marta, Colombia. Remote Sensing of Environment, Earth Observations for Terrestrial Biodiversity and Ecosystems Special Issue 112, 2131–2144. https://doi.org/10.1016/j.rse.2007.10.012
- Simard, M., Zhang, K., Rivera-Monroy, V.H., et al., 2006. Mapping height and biomass of mangrove forests in Everglades National Park with SRTM elevation data. Photogrammetric Engineering & Remote Sensing 72, 299–311.
- Song, S., Ding, Y., Li, W., et al., 2023. Mangrove reforestation provides greater blue carbon benefit than afforestation for mitigating global climate change. Nat Commun 14, 756. https://doi.org/10.1038/s41467-023-36477-1
- Spalding, M., Kainuma, M., Collins, L., 2010. World atlas of mangroves. Earthscan, London, Washington D.C.
- Spalding, M., McIvor, A., Tonneijck, F., et al., 2014. Mangroves for coastal defence. Guidelines for coastal managers and policy makers. Wetlands International and The Nature Conservancy 13–34.
- Spalding, M., Parrett, C.L., 2019. Global patterns in mangrove recreation and tourism. Marine Policy 110. https://doi.org/10.1016/j.marpol.2019.103540
- Spalding, M.D., Leal, M. (Eds.), 2022. The State of the World's Mangroves 2022. Global Mangrove Alliance.
- St-Onge, B., Hu, Y., Vega, C., 2008. Mapping the height and above-ground biomass of a mixed forest using LiDAR and stereo IKONOS images. International Journal of Remote Sensing 29, 1277–1294. https://doi.org/10.1080/01431160701736505

- Storch, T., Honold, H.-P., Chabrillat, S., et al., 2023. The EnMAP imaging spectroscopy mission towards operations. Remote Sensing of Environment 294, 113632. https://doi.org/10.1016/j.rse.2023.113632
- Stovall, A.E.L., Fatoyinbo, T., Thomas, N.M., et al., 2021. Comprehensive comparison of airborne and spaceborne SAR and LiDAR estimates of forest structure in the tallest mangrove forest on earth. Science of Remote Sensing 4, 100034. https://doi.org/10.1016/j.srs.2021.100034
- Suab, S.A., Supe, H., Louw, A.S., et al., 2024. Mapping of Temporally Dynamic Tropical Forest and Plantations Canopy Height in Borneo Utilizing TanDEM-X InSAR and Multi-sensor Remote Sensing Data. J Indian Soc Remote Sens. https://doi.org/10.1007/s12524-024-01820-6
- Sulong, I., Mohd-Lokman, H., Mohd-Tarmizi, K., et al., 2002. Mangrove mapping using Landsat imagery and aerial photographs: Kemaman District, Terengganu, Malaysia. Environment, Development and Sustainability 4, 135–152. https://doi.org/10.1023/A:1020844620215
- Taillardat, P., Friess, D.A., Lupascu, M., 2018. Mangrove blue carbon strategies for climate change mitigation are most effective at the national scale. Biology Letters 14, 20180251. https://doi.org/10.1098/rsbl.2018.0251
- Taillie, P.J., Roman-Cuesta, R., Lagomasino, D., et al., 2020. Widespread mangrove damage resulting from the 2017 Atlantic mega hurricane season. Environ. Res. Lett. 15, 064010. https://doi.org/10.1088/1748-9326/ab82cf
- Tang, W., Feng, W., Jia, M., et al., 2016. The assessment of mangrove biomass and carbon in West Africa: a spatially explicit analytical framework. Wetlands Ecology and Management 24, 153–171. https://doi.org/10.1007/s11273-015-9474-7
- Thomas, N., Lucas, R., Bunting, P., et al., 2017. Distribution and drivers of global mangrove forest change, 1996–2010. PLOS ONE 12, e0179302. https://doi.org/10.1371/journal.pone.0179302
- Tian, Y., Huang, H., Zhou, G., et al., 2021. Aboveground mangrove biomass estimation in Beibu Gulf using machine learning and UAV remote sensing. Science of The Total Environment 781, 146816. https://doi.org/10.1016/j.scitotenv.2021.146816
- Tolan, J., Yang, H.-I., Nosarzewski, B., et al., 2024. Very high resolution canopy height maps from RGB imagery using self-supervised vision transformer and convolutional decoder trained on aerial lidar. Remote Sensing of Environment 300, 113888. https://doi.org/10.1016/j.rse.2023.113888
- Tran, T.V., Reef, R., Zhu, X., et al., 2024. Characterising the distribution of mangroves along the southern coast of Vietnam using multi-spectral indices and a deep learning model. Science of The Total Environment 923, 171367. https://doi.org/10.1016/j.scitotenv.2024.171367
- Treuhaft, R.N., Law, B.E., Asner, G.P., 2004. Forest Attributes from Radar Interferometric Structure and Its Fusion with Optical Remote Sensing. BioScience 54, 561. https://doi.org/10.1641/0006-3568(2004)054[0561:fafris]2.0.co;2

- Twomey, A., Lovelock, C., 2024. Global spatial dataset of mangrove genus distribution in seaward and riverine margins. Sci Data 11, 306. https://doi.org/10.1038/s41597-024-03134-1
- Uddin, M.M., Abdul Aziz, A., Lovelock, C.E., 2023. Importance of mangrove plantations for climate change mitigation in Bangladesh. Global Change Biology 29, 3331–3346. https://doi.org/10.1111/gcb.16674
- Vaghela, B., Chirakkal, S., Putrevu, D., et al., 2021. Modelling above ground biomass of Indian mangrove forest using dual-pol SAR data. Remote Sensing Applications: Society and Environment 21, 100457. https://doi.org/10.1016/j.rsase.2020.100457
- Veettil, B.K., 2022. Current status of mangrove vegetation in Batticaloa Lagoon, Sri Lanka, using high-resolution satellite imagery. J Coast Conserv 26, 74. https://doi.org/10.1007/s11852-022-00923-x
- Verheyden, A., Dahdouh-Guebas, F., Thomaes, K., et al., 2002. High-Resolution Vegetation Data for Mangrove Research as Obtained From Aerial Photography. Environment, Development and Sustainability 4, 113–133. https://doi.org/10.1023/A:1020887510357
- Verrelst, J., Camps-Valls, G., Muñoz-Marí, J., et al., 2015. Optical remote sensing and the retrieval of terrestrial vegetation bio-geophysical properties A review. ISPRS Journal of Photogrammetry and Remote Sensing 108, 273–290. https://doi.org/10.1016/j.isprsjprs.2015.05.005
- Verrelst, J., Malenovský, Z., Van Der Tol, C., et al., 2019. Quantifying Vegetation Biophysical Variables from Imaging Spectroscopy Data: A Review on Retrieval Methods. Surv Geophys 40, 589–629. https://doi.org/10.1007/s10712-018-9478-y
- Walters, B.B., Rönnbäck, P., Kovacs, J.M., et al., 2008. Ethnobiology, socio-economics and management of mangrove forests: A review. Aquatic Botany 89, 220–236. https://doi.org/10.1016/j.aquabot.2008.02.009
- Waltham, N.J., Elliott, M., Lee, S.Y., et al., 2020. UN Decade on Ecosystem Restoration 2021–2030—What Chance for Success in Restoring Coastal Ecosystems? Frontiers in Marine Science 7. https://doi.org/10.3389/fmars.2020.00071
- Wan, L., Lin, Y., Zhang, H., et al., 2020. GF-5 Hyperspectral data for species mapping of mangrove in Mai Po, Hong Kong. Remote Sensing 12. https://doi.org/10.3390/rs12040656
- Wan, L., Zhang, H., Lin, G., et al., 2019. A small-patched convolutional neural network for mangrove mapping at species level using high-resolution remote-sensing image. Annals of GIS 25, 45–55. https://doi.org/10.1080/19475683.2018.1564791
- Wang, D., Wan, B., Liu, J., et al., 2020. Estimating aboveground biomass of the mangrove forests on northeast Hainan Island in China using an upscaling method from field plots, UAV-LiDAR data and Sentinel-2 imagery. International Journal of Applied Earth Observation and Geoinformation 85, 101986. https://doi.org/10.1016/j.jag.2019.101986

- Wang, D., Wan, B., Qiu, P., et al., 2018. Evaluating the Performance of Sentinel-2, Landsat 8 and Pléiades-1 in Mapping Mangrove Extent and Species. Remote Sensing 10, 1468. https://doi.org/10.3390/rs10091468
- Wang, L., Jia, M., Yin, D., et al., 2019. A review of remote sensing for mangrove forests: 1956–2018. Remote Sensing of Environment 231, 111223. https://doi.org/10.1016/j.rse.2019.111223
- Wang, L., Mu, M., Li, X., et al., 2011. Differentiation between true mangroves and mangrove associates based on leaf traits and salt contents. Journal of Plant Ecology 4, 292–301. https://doi.org/10.1093/jpe/rtq008
- Wang, L., Silván-Cárdenas, J.L., Sousa, W.P., 2008. Neural Network Classification of Mangrove Species from Multi-seasonal Ikonos Imagery. Photogrammetric Engineering & Remote Sensing 74, 921– 927. https://doi.org/10.14358/PERS.74.7.921
- Wang, L., Sousa, W.P., 2009. Distinguishing mangrove species with laboratory measurements of hyperspectral leaf reflectance. Int. J. Remote Sens. 30, 1267–1281. https://doi.org/10.1080/01431160802474014
- Wang, L., Sousa, W.P., Gong, P., 2004. Integration of object-based and pixel-based classification for mapping mangroves with IKONOS imagery. Int. J. Remote Sens. 25, 5655–5668. https://doi.org/10.1080/014311602331291215
- Wang, X., Tan, L., Fan, J., 2023. Performance Evaluation of Mangrove Species Classification Based on Multi-Source Remote Sensing Data Using Extremely Randomized Trees in Fucheng Town, Leizhou City, Guangdong Province. Remote Sensing 15, 1386. https://doi.org/10.3390/rs15051386
- Wang, Y.-T., Wang, Y.-S., Wu, M.-L., et al., 2021. Assessing ecological health of mangrove ecosystems along South China Coast by the pressure–state–response (PSR) model. Ecotoxicology 30, 622–631. https://doi.org/10.1007/s10646-021-02399-1
- Wannasiri, W., Nagai, M., Honda, K., et al., 2013. Extraction of Mangrove Biophysical Parameters Using Airborne LiDAR. Remote Sensing 5, 1787–1808. https://doi.org/10.3390/rs5041787
- Wicaksono, P., Danoedoro, P., Hartono, et al., 2016. Mangrove biomass carbon stock mapping of the Karimunjawa Islands using multispectral remote sensing. International Journal of Remote Sensing 37, 26–52. https://doi.org/10.1080/01431161.2015.1117679
- Woodhouse, I.H., Mitchard, E.T.A., Brolly, M., et al., 2012. Radar backscatter is not a "direct measure" of forest biomass. Nature Climate Change 2, 556–557. https://doi.org/10.1038/nclimate1601
- Woodroffe, C.D., Lovelock, C.E., Rogers, K., 2015. Mangrove Shorelines, in: Masselink, G., Gehrels, R. (Eds.), Coastal Environments and Global Change. Wiley, New York, NY, USA, pp. 251–267.
- Worthington, T.A., Andradi-Brown, D.A., Bhargava, R., et al., 2020. Harnessing Big Data to Support the Conservation and Rehabilitation of Mangrove Forests Globally. One Earth 2, 429–443. https://doi.org/10.1016/j.oneear.2020.04.018

- Worthington, T., Spalding, M., 2018. Mangrove restoration potential: A global map highlighting a critical opportunity. https://doi.org/10.17863/CAM.39153
- Xu, Y., Wang, J., Xia, A., et al., 2019. Continuous Wavelet Analysis of Leaf Reflectance Improves Classification Accuracy of Mangrove Species. Remote Sensing 11, 254. https://doi.org/10.3390/rs11030254
- Yang, C., Everitt, J.H., Fletcher, R.S., et al., 2009. Evaluating AISA+ Hyperspectral Imagery for Mapping Black Mangrove along the South Texas Gulf Coast. Photogrammetric Engineering and Remote Sensing 75, 425–435. https://doi.org/10.14358/PERS.75.4.425
- Yu, J., Nie, S., Liu, W., et al., 2024. Mapping global mangrove canopy height by integrating Ice, Cloud, and Land Elevation Satellite-2 photon-counting LiDAR data with multi-source images. Science of The Total Environment 939, 173487. https://doi.org/10.1016/j.scitotenv.2024.173487
- Yuan, Q., Shen, H., Li, T., et al., 2020. Deep learning in environmental remote sensing: Achievements and challenges. Remote Sensing of Environment 241, 111716. https://doi.org/10.1016/j.rse.2020.111716
- Zhai, L., Zhang, B., Roy, S.S., et al., 2019. Remote sensing of unhelpful resilience to sea level rise caused by mangrove expansion: A case study of islands in Florida Bay, USA. Ecological Indicators 97, 51–58. https://doi.org/10.1016/j.ecolind.2018.09.063
- Zhang, H., Wang, T., Liu, M., et al., 2018. Potential of Combining Optical and Dual Polarimetric SAR Data for Improving Mangrove Species Discrimination Using Rotation Forest. Remote Sensing 10, 467. https://doi.org/10.3390/rs10030467
- Zhang, H., Xia, Q., Dai, S., et al., 2023. Mangrove forest mapping from object-oriented multi-feature ensemble classification using Sentinel-2 images. Front. Mar. Sci. 10. https://doi.org/10.3389/fmars.2023.1243116
- Zhang, R., Jia, M., Wang, Z., et al., 2021a. A comparison of Gaofen-2 and Sentinel-2 imagery for mapping mangrove forests using object-oriented analysis and random forest. IEEE Journal of Selected Topics in Applied Earth Observations and Remote Sensing. https://doi.org/10.1109/JSTARS.2021.3070810
- Zhang, T., Hu, S., He, Y., et al., 2021b. A Fine-Scale Mangrove Map of China Derived from 2-Meter Resolution Satellite Observations and Field Data. ISPRS International Journal of Geo-Information 10, 92. https://doi.org/10.3390/ijgi10020092
- Zhao, C., Jia, M., Wang, Z., et al., 2023. Identifying mangroves through knowledge extracted from trained random forest models: An interpretable mangrove mapping approach (IMMA). ISPRS Journal of Photogrammetry and Remote Sensing 201, 209–225. https://doi.org/10.1016/j.isprsjprs.2023.05.025

- Zhao, D., Zhen, J., Zhang, Y., et al., 2023. Mapping mangrove leaf area index (LAI) by combining remote sensing images with PROSAIL-D and XGBoost methods. Remote Sens Ecol Conserv 9, 370–389. https://doi.org/10.1002/rse2.315
- Zhen, J., Jiang, X., Xu, Y., et al., 2021. Mapping leaf chlorophyll content of mangrove forests with Sentinel-2 images of four periods. International Journal of Applied Earth Observation and Geoinformation 102, 102387. https://doi.org/10.1016/j.jag.2021.102387
- Zhila, H., Mahmood, H., Rozainah, M.Z., 2014. Biodiversity and biomass of a natural and degraded mangrove forest of Peninsular Malaysia. Environmental Earth Sciences 71, 4629–4635. https://doi.org/10.1007/s12665-013-2853-6
- Zhu, Y., Liu, K., Liu, L., et al., 2020. Estimating and Mapping Mangrove Biomass Dynamic Change Using WorldView-2 Images and Digital Surface Models. IEEE Journal of Selected Topics in Applied Earth Observations and Remote Sensing 13, 2123–2134. https://doi.org/10.1109/jstars.2020.2989500
- Zhu, Y., Liu, K., Liu, L., et al., 2015. Retrieval of Mangrove Aboveground Biomass at the Individual Species Level with WorldView-2 Images. Remote Sensing 7, 12192–12214. https://doi.org/10.3390/rs70912192
- Zulfa, A.W., Norizah, K., Hamdan, O., et al., 2020. Discriminating trees species from the relationship between spectral reflectance and chlorophyll contents of mangrove forest in Malaysia. Ecological Indicators 111, 106024. https://doi.org/10.1016/j.ecolind.2019.106024

Chapter 3 Mapping aboveground biomass using global DEMs for the mangroves bordering the lagoons of La Mancha and El Llano, Mexico

Abstract

Estimation of mangrove aboveground biomass (AGB) is important for investigating mangrove health, succession and carbon storage. Canopy height is one of the best performing explanatory factors of AGB. As mangroves are normally located in low-lying and flat coastal regions, earth surface models can be used for canopy height investigation with the assumption of negligible topographic impacts. However, there is limited knowledge of the performance of using earth surface models for determining canopy height and AGB estimation at a local scale. In this study, three freely accessible Digital Elevation Models (DEMs), i.e., NASADEM, ALOS DSM and Copernicus GLO-30 DEM, were used to estimate mean canopy height and AGB for two mangrove forests of the central coast of the Gulf of Mexico (El Llano and La Mancha) by applying a power law equation for plot level aboveground biomass and mean canopy height. Even though the introduced DEMs represent different nominal time periods, plot-level mean canopy heights show high agreement with the DEMs as intact and well-established mangrove forests exhibit canopy height changes at finer resolution, where the DEMs with 30 m resolution suffice to demonstrate the distribution of mean canopy height. An ordinary least squares regression using field plot measurements achieved an R² of 0.61 between plot-level mean canopy height and AGB. Fixed 100 m ICESat-2 ATL08 segments were used to calibrate the DEMs for reducing the bias introduced from different DEM generation methods. Mangrove AGB of El Llano lagoon was predicted to in the range of 35.22 – 211.56 Mg/ha through NASADEM, 50.02 - 237.00 Mg/ha through ALOS DSM and 49.26 - 238.41 Mg/ha through Copernicus GLO-30 DEM at the 5th and 95th percentile. Mangroves around La Mancha lagoon were predicted to have AGB in the range of 106.75 – 468.78 Mg/ha through NASADEM, 92.91 – 438.49 Mg/ha through ALOS DSM and 67.61 – 435.69 Mg/ha through Copernicus GLO-30 DEM at the 5th and 95th percentile. Error propagation for mangrove AGB estimation involved regression coefficient error and mean canopy height estimation error, resulting in the standard error σ_{AGB} varying between \pm 151.78 - 154.95 Mg/ha (~30% of the estimated AGB) for stands with estimated mean canopy height $H_{mean} = 15$ m. The results of this study show comparable AGB estimates of the study area and the feasibility of using freely accessible DEMs for mean canopy height and AGB estimation of mangrove forests, providing further opportunities in the validation of global biomass estimations of mangroves.

Keywords: Mangrove aboveground biomass estimation; Digital elevation models; Spaceborne LiDAR data; La Mancha and El Llano lagoons, Mexico

3.1 Introduction

Mangroves occupy the transition between land and sea in tropical and sub-tropical regions, providing critical ecosystem services, including feeding and breeding habitats (e.g. Arceo-Carranza et al., 2021), protecting coastlines (e.g. Zhang et al., 2022), and sequestering carbon (e.g. Rosa et al., 2022). As one of the most productive ecosystems, mangroves store organic carbon per unit area with a mean value of 738.9 \pm 27.9Mg/ha where the sequestration rate is 1.796 Mg/ha per year (Alongi, 2020). Mangroves are therefore perceived as efficient blue carbon sinks that help mitigate climate change at national and global scales (Song et al., 2023; Taillardat et al., 2018; Uddin et al., 2023). However, confronted with human activities and climate change, there had been 284,000 ha of mangrove net loss between 2000 and 2020, though about half of the total loss was counteracted by mangrove afforestation (3,930 km²) (FAO, 2023). As aboveground biomass (AGB) is a proxy for above ground carbon stock and ecosystem resilience, quantifying AGB is important, not only to better understand the role of mangroves in the global carbon cycle, but also to quantify mangrove ecosystem dynamics (Duncan et al., 2018; Harishma et al., 2020; Jones et al., 2020; Tang et al., 2018; Worthington et al., 2020).

AGB, also referred to as aboveground biomass density, is the total amount of living plant material (biomass) found above the ground surface in a particular area or ecosystem. It is accurately calculated from harvested or felled trees using laboratory weighing (Kauffman and Donato, 2012; Smith and Whelan, 2006). However, this destructive approach can be time consuming and often challenging to perform in areas that are difficult to access (Komiyama et al., 2005, 2008). To simplify AGB quantification, allometric equations can be developed using single measurements, i.e., diameter at breast height (DBH) or canopy height. For a given individual tree, the allometric equations are formulated as power-law functions, such as $M = \alpha X^{\beta}$, where M represents tree mass (dry weight), X represents DBH or canopy height, and α and β are the model's fitted parameters. These equations are developed by felling trees to measure their heights and DBH, and then samples of their stems, branches and leaves are oven dried to determine dry weight (Chave et al., 2005; Day et al., 1987; Fromard et al., 1998; Komiyama et al., 2005; Smith and Whelan, 2006). After the allometric equations are determined, they are applied to all the individual trees in plots (defined areas) of whole forests. The total AGB of a plot equals the sum of the individual masses expressed in tonnes dry weight per hectare (Mg/ha).

There are however considerable limitations associated with fieldwork in mangrove forests, such as restricted access and limited opportunities for height measurements under dense canopies. Remote sensing enables consistent large area surveys and has been utilised in the retrieval of mangrove cover and vegetation structure data (e.g., Maurya et al., 2021; Tran et al., 2022; Wang et al., 2019; Worthington et al., 2020).

This facilitates local, regional, or even global AGB mapping in areas with limited field data using the relationships between mangrove AGB and predictor variables derived from remotely sensed data (Pham et al., 2019).

Canopy height is considered a key biophysical parameter to estimate aboveground biomass (Chave et al., 2005, 2014). The availability of Digital Elevation Models (DEMs) allows for the estimation of mangrove canopy height with an assumption that mangroves exist in low-lying and flat coastal regions at sea level resulting in minimal impact from topography (Simard et al., 2006, 2019). Since the first near-global Shuttle Radar Topography Mission (SRTM) DEM was released in 2003, more advanced DEMs with a similar spatial resolution of approximately 30 meters, such as the ASTER GDEM, Copernicus GLO-30 DEM and ALOS DSM (Digital Surface Model) have become available. These DEMs were generated using data sources mainly acquired in a specific time period but remain stable over time with a medium resolution of 30 m representing canopy height distribution in mature, intact mangrove forests as finer changes in the mangrove forests do not disturb the measurements (Lagomasino et al., 2016). This characteristic makes it feasible to investigate canopy height distribution of mangroves and facilitate AGB estimation with canopy height-based allometric equations. Various studies have been carried out at a continental or global scale (Aslan and Aljahdali, 2022; Fatoyinbo and Simard, 2013; Simard et al., 2008, 2019; Tang et al., 2018), but there is limited knowledge of the performance of these DEMs for the estimation of mangrove canopy height and AGB at a local scale.

Mangrove forests around La Mancha and El Llano lagoons in Mexico are Ramsar sites of international ecological importance (Ramsar, 2004), however there is a lack of local AGB estimation of the area. This study aims to quantify mangrove AGB of these areas based on canopy height estimation, and to examine and compare the performance of DEMs for canopy height and AGB estimation at the forest scale. A comparison was conducted among mangrove AGB estimates derived from canopy height-based allometric equations in which canopy height was retrieved from different DEMs. Three freely accessible 30 m DEMs were analysed: 1) NASADEM, 2) ALOS DSM and 3) Copernicus GLO-30 DEM, which represent global vegetation surfaces. Due to the sensitivities of sensors, different vertical datum and time frames, there are discrepancies between DEMs. As LiDAR measurements have the best vertical accuracy aligned to geodetic benchmarks (Carrera-Hernández, 2021) and come with larger footprints than forest plot sizes, the DEMs, processed to the same datum, were calibrated with spaceborne ICESat-2 LiDAR data. Google Earth Engine (GEE) was used in this study for data processing and analysis. This study illustrates the performance of freely accessible DEMs for estimating mangrove mean canopy height and AGB, permitting enhanced validation and comparison of global biomass data and above ground carbon stock investigation.

3.2 Materials and methods

3.2.1 Study sites

The study area incorporates the lagoons of La Mancha (19°33′ - 19°36′ N, 96°22′ - 96°24′ W) and El Llano (19°38′ - 19°40′ N, 96°24′ - 96°25′ W) in the state of Veracruz, Mexico, along the central coast of the Gulf of Mexico (Figure 3-1). Four mangrove species are found at the study area: Avicennia germinans, Rhizophora mangle, Laguncularia racemosa, and Conocarpus erectus. The climate is recognized as subhumid warm climate (Aw2) with annual precipitation fluctuating between 1000 and 1500 mm and the mean annual temperature of approximately 24°C (Méndez-Alonzo et al., 2012). The extent of the waterbody of La Mancha and El Llano lagoons is 135 ha and 226 ha, respectively (Chávez-López and Rocha-Ramírez, 2020; Vovides et al., 2021). La Mancha lagoon receives fresh water mainly from a river (Caño Gallegos) in the southern end, and marine water through an intermittently opened inlet in the north-eastern to the Gulf of Mexico (Chacón Abarca et al., 2021; Chávez-Cerón et al., 2016; Harte Research Institute for Gulf of Mexico, 2021a). This geomorphologic arrangement, irrespective of season, results in a salinity gradient that increases northwards, influencing the mangrove species zonation. The northernmost side is dominated by A. germinans with few R. mangle, while A. germinans and R. mangle or A. germinans and L. racemosa codominate towards the south of the lagoon (Méndez-Alonzo et al., 2012; Vovides et al., 2018). C. erectus accounts for a small number of trees, normally situated in the eastern side of the area (Moreno-Casasola et al., 2009).

In contrast to La Mancha lagoon, the salinity of El Llano lagoon is mostly regulated by marine water through an inlet in the north-eastern part which only opens up to the Gulf of Mexico during rainfall. Spanning from November to January every year (dry season), a sandy bar naturally emerges separating the lagoon from the ocean. This occurrence results in the lagoon experiencing hyper-salinity during the lowwater season (Chávez-López and Rocha-Ramírez, 2020; Harte Research Institute for Gulf of Mexico, 2021b). Oysters, clams and shrimp are fished regularly in both lagoons (Ramsar, 2004). The Instituto de Ecología, A.C. (INECOL) is located on the site, supporting ongoing research activities and developing community management plans.

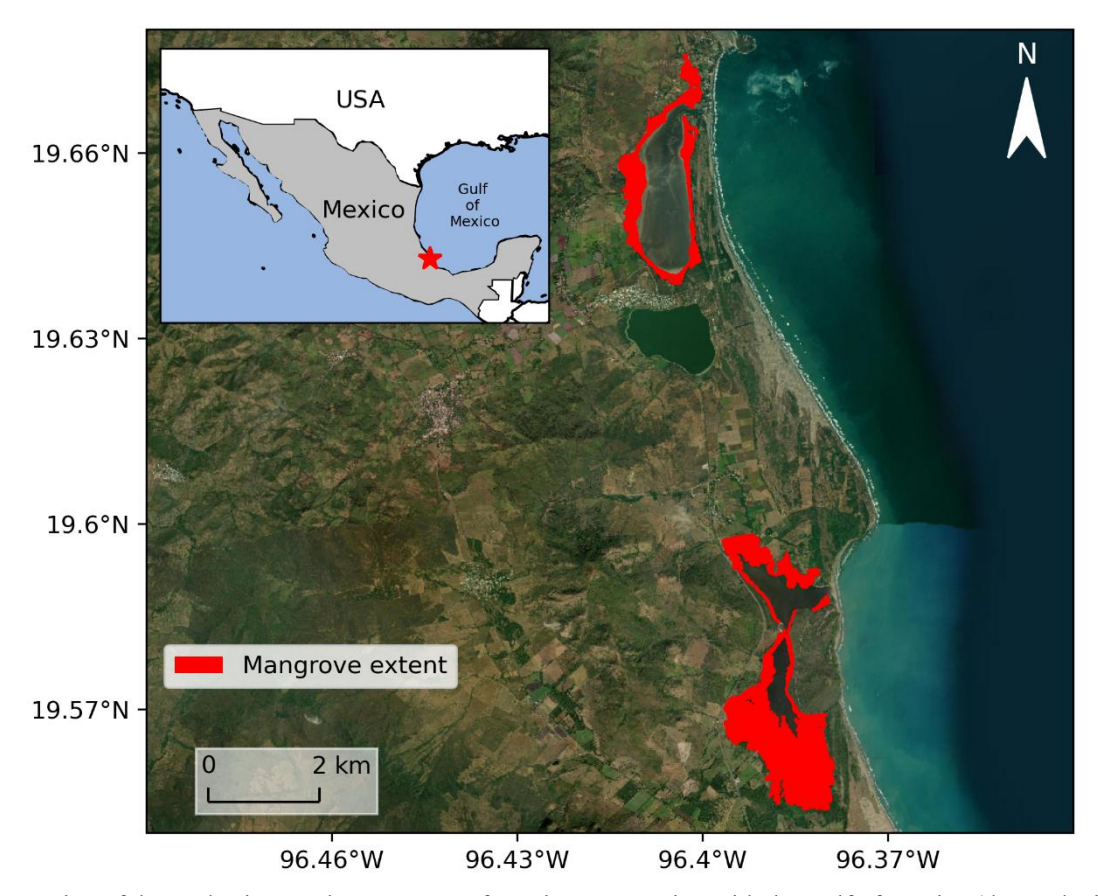


Figure 3-1. Location of the study sites on the east coast of Mexico, connecting with the Gulf of Mexico (denoted with a red star) where red patches represent the mangrove forests bordering the lagoons of El Llano (north) and La Mancha (south), respectively. The mangrove extent was delineated for the year of 2020 obtained from CONABIO geoportal (http://www.conabio.gob.mx/informacion/gis/?vns=gis_root/biodiv/monmang/bimagdmo/mx_man20gw). The base map was rendered through Esri World Image.

3.2.2 Field data collection

Permanent monitoring plots were established in the mangrove forests surrounding the lagoons of La Mancha and El Llano in 2010 and 2017. In 2010, 12 permanent plots (10 with 30 \times 30 m, and two with 20 \times 20 m) were analysed, where trees with stem diameters >2.5 cm were tagged and measured (Vovides et al., 2018). A follow-up visit in 2017 established a new plot with 30 \times 30 m (Vovides et al., 2021). Between 27 June and 13 July 2022, a total of 11 field plots were investigated, where six plots were located at El Llano lagoon, and five at La Mancha lagoon. Plot size varied in relation to stand density. Around the lagoon of El Llano, three plots of 10×10 m were delimited in the west of the lagoon and three plots of the same size on the east, neighbouring a system of stabilized dunes. Around La Mancha lagoon, two 10×10 m plots and two 15×15 m subplots within existing 30×30 m permanent plots were established on the northern side, while a 20×20 m plot, specifically intended for large *R. mangle* trees, was sampled on the southeastern side of the lagoon. Species id, stem diameter (cm) at 1.3 m from ground surface, and tree height (m) were recorded within each plot. Additionally, trunk diameter at lowest living branch, canopy

width and length in the case of shrubs or young trees, and diameter above the highest prop root in the case of *R. mangle* were also recorded. The coordinates of all four corners of each plot were recorded using a Geode multi-GNSS receiver GNS2 which has a horizontal accuracy of 60 cm at 95% – 98% precision (2DRMS, twice the distance root mean square). In total, 24 field plot measurements were used for this study, comprising 6 plots at El Llano and 18 plots at La Mancha (**Figure 3-2**).

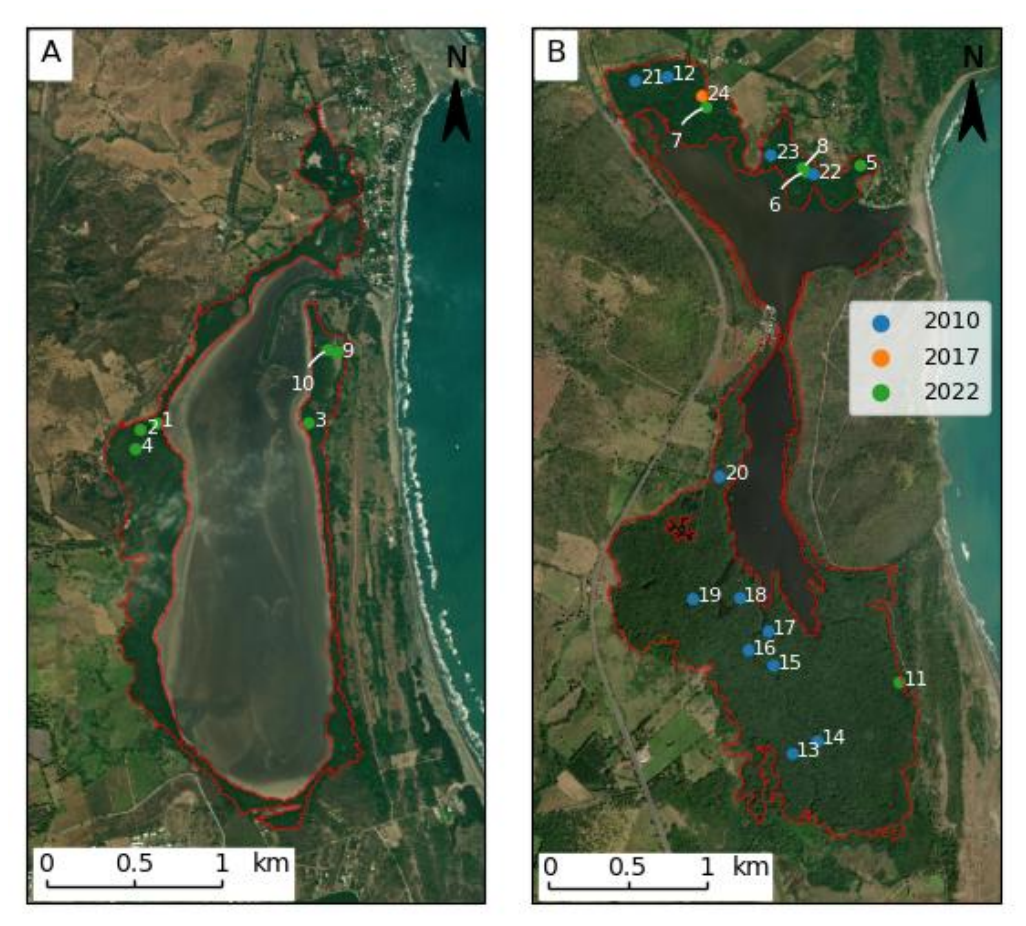


Figure 3-2. The location and numbering of the plot centroids in the mangrove forest around the lagoons of El Llano (A) and La Mancha (B). Field measurement plots are coloured for different periods. The base map is rendered through Esri World Image.

3.2.3 Mangrove extent maps

Mexico's Mangrove Monitoring System (SMMM, acronym in Spanish), mandated with cartographic information retrieval of mangroves through remote sensing technology, has generated national mangrove extent maps of Mexico for five time points: one composite map for the 1970-1980 period, and subsequent maps for 2005, 2010, 2015, and 2020 (Rodríguez-Zúñiga et al., 2022). The maps of 2005, 2010 and 2015 represent the distribution of mangroves using SPOT 5 satellite images with a spatial resolution of 10 m (Valderrama-Landeros et al., 2020). These datasets were coordinated and delivered by the National Commission for the Knowledge and Use of Biodiversity (CONABIO) which is a Mexican inter-ministerial commission created in 1992 to form and develop the National System of Information on Biodiversity, Mexico (CONABIO, 2023a, 2023b). In this study, 2005, 2010 and 2015 mangrove extent maps of the study

area were downloaded and used to delineate mangrove boundaries, corresponding to the nominal years of the DEMs.

3.3 Digital Elevation Models (DEMs)

3.3.1 NASADEM

The Shuttle Radar Topography Mission (SRTM) deployed two Synthetic Aperture Radars (C and X bands) mounted on the space shuttle Endeavor to capture the topography of the Earth in February 2000 and generated the near-global digital elevation model (Farr et al., 2007). Since its original release, the SRTM DEM has been improved (Grohman et al., 2006; NASA JPL, 2013). This study used the latest version of the SRTM DEM, NASADEM, with a resolution of 1 arc-second (approximately 30m). This dataset has been produced by reprocessing the original SRTM radar data and reducing voids with improved interferometric unwrapping algorithms, using ICESat data for better vertical control (Crippen et al., 2016).

3.3.2 ALOS World 3D-30m

ALOS World 3D-30m (AW3D30) is a global DSM dataset with a spatial resolution of approximately 30 m. This dataset was resampled from 5 m ALOS World 3D (AW3D) DSM produced from millions of satellite stereoscopic images from 2006 to 2011 acquired by ALOS PRISM (Advanced Land Observing Satellite Panchromatic Remote-sensing Instrument for Stereo Mapping) (Tadono et al., 2014; Takaku et al., 2014).

3.3.3 Copernicus GLO-30 DEM

The Copernicus DEM, derived from an edited global DSM named WorldDEM, is provided in three instances: EEA-10 (European coverage), GLO-30 and GLO-90 (global coverage) with the resolutions of approximately 10 m, 30 m and 90 m, respectively (ESA, 2022). The WorldDEM with a resolution of 12 m is based on the Synthetic Aperture Radar data (X band) acquired during the TanDEM-X Mission spanning from 2011 to 2015, which is funded by a Public Private Partnership between the German Aerospace Centre (DLR) and Airbus Defence and Space (Riegler et al., 2015). Significant terrain and hydrological corrections have been made to the Copernicus DEM, such as water body flattening, river consistency, water lines and implausible terrain structures editing (AIRBUS, 2022). To enable comparison with the other two DEMs, Copernicus GLO-30 DEM was used to extract elevation values over the study area. Since Copernicus DEM deploys EGM2008 as a vertical datum, prior to the quantitative assessment, the vertical reference system

of Copernicus DEM is transformed from EGM2008 to EGM96 to provide a consistent comparison. The orthometric height (elevation data of DEM) conversion between EMG96 and EGM2008 was carried out using the MSP GEOTRANS 3.9 datum transformation tool (**Table 3-1**).

Table 3-1. Summary of key characteristics of NASADEM, ALOS DSM, and Copernicus DEM.

Data product	Pixel spacing	Time span	Vertical datum	Absolute vertical accuracy
NASADEM		2000	EGM96	< 9 m (90% linear error)
ALOS DSM	Approx. 30 m	2006-2011	EGM96	4.40 m (Root mean square error)
Copernicus DEM		2011-2015	EGM2008	< 4 m (90% linear error)

3.4 ICESat-2 LiDAR data

ICESat-2 (Ice, Cloud, and land Elevation Satellite 2) is the successor to the ICESat mission, launched in 2018. The spacecraft carries a single instrument onboard, the Advanced Topographic Laser Altimeter System (ATLAS), and operates in a near-polar orbit with a 91-day exact repeat cycle. The ATLAS is a photon counting lidar altimeter that transmits visible laser pulses with a wavelength of 532 nm (green), measuring the travel time of laser photons from ICESat-2 to earth and back. Six beams are coupled in three pairs and generate nominal 14 m footprints sampling every 0.7 m along track. Each pair is separated by 3.3 km and the beams in each pair are spaced about 90 m apart comprising one strong beam and one weak beam at an energy ratio of 4:1 (Neumann et al., 2019). The land and vegetation height product (ATL08) was adopted in this study, which contains along-track heights for the ground and canopy surfaces. The product is processed in fixed 100 m segments (14 × 100 m), typically including more than 100 signal photons. As the geophysical boundary of the study area was set, 84 segments of ATL08 data (version 006) from 30 September 2019 to 16 July 2024 were returned and downloaded (in units of meters) from the NASA Earthdata Search website (https://search.earthdata.nasa.gov/search).

3.5 DEM calibration

In this study, DSM and DEM are interchangeable as the introduced topographic models represent vegetation surface on the earth. However, different from ALOS DSM, NASADEM and Copernicus GLO-30 DEM are derived from interferometric Synthetic Aperture Radar (SAR) data, whereby NASADEM, derived from SRTM C-band microwave data, does not record the top of vegetation canopy but the interferometric scattering phase centre of the canopy. Thus, to reduce the elevation bias introduced by different DEM generation methods, ICESat-2 ATL08 segment data was utilised to calibrate DEMs as the segments are larger than the field plots and better for representing natural height variability. Since the segments are not square along the track, the centroids of the first and last segments were used to calculate

the track inclination, and then, generated a rectangular buffer of 100×14 m around the centroids of the segments. The elevation values of DEMs were averaged over overlapping segment areas and compared with mean canopy height ('h_mean_canopy') in the corresponding segments. The mean canopy height information is relative to the ground and therefore independent from the vertical datum.

Linear regression models with OLS were fitted to relate ATL08 mean canopy height to DEM elevation values (**Figure 3-3**). The resulting calibration equations (**Table 3-2**) were subsequently applied to generate DEM-based mean canopy heights across the study area.

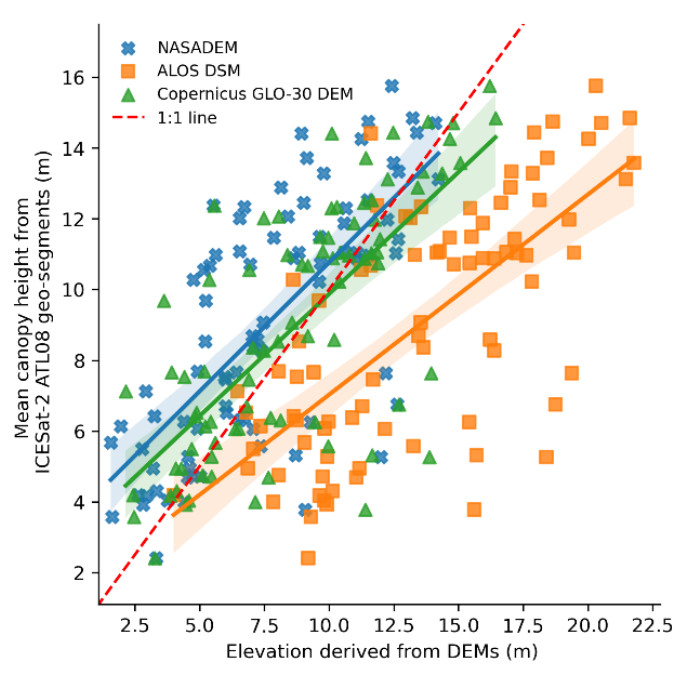


Figure 3-3. Scatter plot with fitted linear regression models (95% confidence intervals) comparing mean canopy height within each 100 m ICESat/ATLAS ATL08 segment against mean DEM elevation values at the corresponding segments over the study area.

Table 3-2. Calibration of DEMs using ICESat-2 ATL08 segments with regression equations and accuracy metrics, where $H_{NASADEM}$, $H_{ALOSDSM}$, and H_{COPDEM} represent original elevation values of NASADEM, ALOS DSM and Copernicus GLO-30 DEM, respectively; $NASADEMH_{mean}$, $ALOSDSMH_{mean}$, and $COPDEMH_{mean}$ are new datasets of mean canopy height estimation.

DEM calibration equations	\mathbb{R}^2	RMSE (m)
$NASADEMH_{mean} = 0.73 \times H_{NASADEM} + 3.48$	0.50	2.45
$ALOSDSMH_{mean} = 0.57 \times H_{ALOSDSM} + 1.37$	0.49	2.49
$COPDEMH_{mean} = 0.69 \times H_{COPDEM} + 2.97$	0.51	2.43

3.6 Field AGB estimation methods

As there are no site-specific allometric equations for the study area, a generalised allometric equation developed for pantropical forests of the world (Chave et al., 2014) was employed in this study. This equation integrates tree diameter, height and species-specific wood density as covariates, developed with more field inventory data, thereby reducing bias across tropical forest types compared to earlier models (Chave et al., 2005). Considering the demonstrated applicability and frequent application in mangrove studies (Simard et al., 2019), this allometric equation provides a reliable basis for AGB estimation in the absence of locally developed models. Wood density of different mangrove species was retrieved from the Global Wood Density Database (Zanne et al., 2009). The generalised allometric equation and wood density for each mangrove species are presented in **Table 3-3**.

Table 3-3. Allometric equation for estimating mangrove aboveground biomass of the study area, where ρ , AGB, D, and H represents wood density (g/cm³), aboveground biomass (kg), diameter at breast height (cm) and canopy height (m), respectively.

Species	Equation	Region	Reference	Wood density (g/cm ³)
A. germinans R. mangle	$AGB = 0.0673 \times (\rho D^2 H)^{0.976}$	Pantropical	Chave et al.	0.67 0.84
L. racemosa C. erectus	1102 010070 X (p2 11)		(2014)	0.6 0.69

Additionally, to assess the sensitivity of AGB estimation to allometric model selection, AGB was also calculated using allometric equations developed for American mangrove species in Laguna de Términos, Mexico (Day et al., 1987), French Guyana (Fromard et al., 1998) and the Everglades, Florida, USA (Smith & Whelan, 2006) (**Table 3-4**). These allometric equations are specific to mangrove species that are the same as the ones in the study area, except for *C. erectus*. Following Castañeda-Moya et al. (2013) and Simard et al. (2006), the allometric equation of *L. racemosa* was applied to *C. erectus* due to similar growth forms.

Table 3-4. Regression equations developed by other studies.

Species	DBH range (cm)	Equation	Reference
A. germinans	1-10	$\ln AGB = 2.3023 \times \ln DBH - 1.5852$	
L. racemosa	1-10	$\ln AGB = 2.1924 \times \ln DBH - 1.5919$	Day et al. (1987)
R. mangle	1-10	$\ln AGB = 2.5072 \times \ln DBH - 1.5605$	
A. germinans	1-42	$AGB = 0.140 \times DBH^{2.4}$	
L. racemosa	1-10	$AGB = 0.102 \times DBH^{2.5}$	Fromard et al. (1998)
R. mangle	1-32	$AGB = 0.128 \times DBH^{2.6}$	
A. germinans	0.7-21.5	$\log_{10} AGB = 1.934 \times \log_{10} DBH - 0.395$	
L. racemosa	0.5-18	$\log_{10} AGB = 1.930 \times \log_{10} DBH - 0.441$	Smith & Whelan (2006)
R. mangle	0.5-20	$\log_{10} AGB = 1.731 \times \log_{10} DBH - 0.112$	

3.7 Allometric modelling of plot-level biomass and canopy height

A power-law function of $M = \alpha X^{\beta}$ was used to yield the relationship between plot level AGB and mean canopy height, where M and X denote plot level AGB and plot level mean canopy height, respectively, α and β are the fitted parameters using field inventory measurements. The power-law function was linearized as $\ln AGB = a + \beta \ln H_{mean}$, where $a = \ln \alpha$, H_{mean} represents the mean canopy height of each plot. Ordinary Least Squares (OLS) was used to fit this log-linear regression model by minimizing the sum of the squares of the differences between $\ln AGB$ and $\ln \widehat{AGB}$ (estimated from the linear regression equation). However, there is a systematic bias resulting in the biomass underestimation in the original unit when log-transformation was applied to the input data (Baskerville, 1972). Thus, for the unbiased estimation, Baskerville (1972) introduced a correction factor (CF) to the conversion of logarithmic estimates to arithmetic units; $CF = exp\left(\frac{\sigma^2}{2}\right)$, where σ^2 stands for sample variance of the logarithmic equation. The unbiased estimate for σ^2 is $\widehat{\sigma}^2 = \frac{RSS}{m}$, where RSS stands for the sum of squared residuals and m is residual degree of freedom (Clifford et al., 2013). CF should be multiplied to the AGB estimates; that is, $\widehat{AGB} = exp\left(\widehat{\alpha} + \widehat{\beta} \ln H_{mean} + \frac{RSS}{2 \cdot m}\right)$ where for a given H_{mean} , \widehat{AGB} is the unbiased estimates in the arithmetic unit (Mg/ha) for the given mean canopy height H_{mean} with the regressed constant \widehat{a} and coefficient $\widehat{\beta}$.

Applying this method to the plot-level AGB estimates in the study area, derived from field inventory data using the allometric equation in **Table 3-3**, the regression model was obtained as

$$\ln AGB = 1.23 + 1.82 \times \ln H_{mean}$$
 (R² = 0.92, p < 0.001) (Equation 3.1)

where intercept a = 1.23 with standard error $\sigma_a = 0.26$ and slope $\beta = 1.82$ with standard error $\sigma_{\beta} = 0.12$. After incorporating the correction factor, the power-law function was yielded as:

$$AGB = 3.64 \times H_{mean}^{1.82}$$
 (Equation 3.2)

with an R² of 0.61 and an RMSE at 87.25 Mg/ha. This equation was then applied to the calibrated DEMs elevation values for DEM-based AGB estimation (**Figure 3-4**).

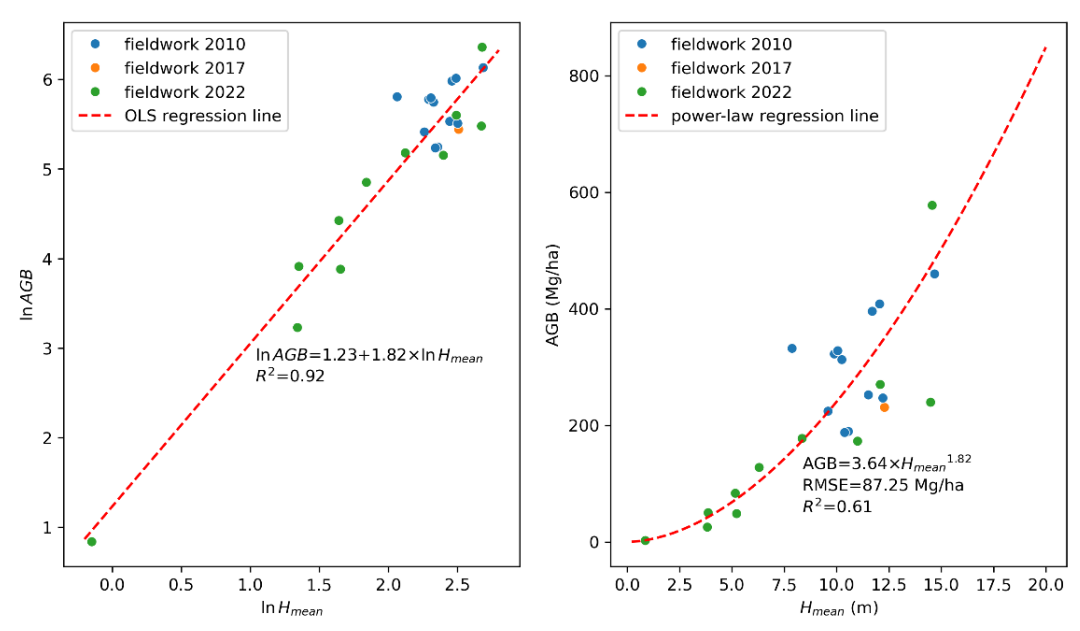


Figure 3-4. Scatterplot and model-fit of aboveground biomass as a function of mean canopy height (H_{mean}) for the field plots. OLS linear regression model with logarithmic transformation (left); Power-law function in arithmetic unit transformed from linear regression model in logarithmic unit including the correction factor (right).

3.8 Results

3.8.1 Field mean canopy height and AGB estimates

Based on the field measurements of the study area, the summary statistics for each mangrove species demonstrate a wide range of tree measurements (**Table 3-5**). The plot-level AGB estimates therefore vary from 2.31 to 577.43 Mg/ha (**Table 3-6**). Compared with the mangrove forest around El Llano lagoon, higher AGB with higher mean canopy height was investigated in the mangrove forest around La Mancha (172.78-577.43 Mg/ha; 7.87-14.68 m). In this study, most of field inventory data fall within the DBH range (5-103.4 cm) except for Plot 9 which is situated to the east of El Llano lagoon with a young *A. germinans* stand and was not previously defined as mangrove (**Figure 3-2**). To incorporate AGB estimates across the entire range of mangrove canopy heights, the field AGB estimation of Plot 9 is included in the development of the proposed regression equation.

Table 3-5. The summary statistics of field measurements based on mangrove species.

Species	DBH (cm)			Canopy height (m)		
Species	Min	Max	Mean	Min	Max	Mean
A. germinans	0.5	103.4	17.5	0.2	31	9.2
R. mangle	0.7	82.7	8.7	1.2	25.2	8.1
L. racemosa	1.8	54.8	27.8	2.7	32.2	17.5
C. erectus	2.3	19.5	6.8	1.5	7.5	3.6

Table 3-6. Summary of mangrove tree data per plot (n = 24).

Plot	Region	Year	Number of trees	Plot size (m ²)	Dominant species	Mean canopy height (m)	AGB (Mg/ha)
1	El Llano	2022	12	100	A. germinans	5.23	48.43
2	El Llano	2022	9	100	A. germinans	6.30	127.71
3	El Llano	2022	73	100	A. germinans	5.16	83.41
4	El Llano	2022	27	100	A. germinans	3.87	49.96
5	La Mancha	2022	11	100	L. racemosa	14.57	577.43
6	La Mancha	2022	14	225	R. mangle	12.09	270.02
7	La Mancha	2022	11	225	A. germinans	11.01	172.78
8	La Mancha	2022	17	100	R. mangle	8.35	177.45
9	El Llano	2022	43	100	A. germinans	0.86	2.31
10	El Llano	2022	17	100	C. erectus	3.83	25.26
11	La Mancha	2022	15	400	R. mangle	14.49	239.49
12	La Mancha	2010	58	400	A. germinans	11.71	395.62
13	La Mancha	2010	58	900	R. mangle	14.68	459.66
14	La Mancha	2010	123	900	R. mangle	9.89	322.38
15	La Mancha	2010	83	900	A. germinans	10.25	312.67
16	La Mancha	2010	47	900	A. germinans	11.52	252.14
17	La Mancha	2010	54	900	A. germinans	10.56	189.44
18	La Mancha	2010	38	900	A. germinans	10.38	187.57
19	La Mancha	2010	27	900	A. germinans	9.59	224.22
20	La Mancha	2010	56	400	A. germinans	7.87	331.95
21	La Mancha	2010	43	900	A. germinans	12.21	246.78
22	La Mancha	2010	77	900	A. germinans	12.06	408.16
23	La Mancha	2010	80	900	A. germinans	10.06	327.94
24	La Mancha	2017	58	900	A. germinans	12.29	230.76

3.8.2 Comparison between different allometric equations

Plot-level AGB estimates derived from the pantropical equation (Chave et al., 2014) exhibited a broader range than those obtained from localised allometric equations developed in Mexico, French Guiana, and the Everglades (**Figure 3-5**). Kernel density distributions show that Smith & Whelan (2006) generated significantly constrained values while central tendencies are generally consistent. The allometric equations of Day et al. (1987) and Fromard et al. (1998) produced similar estimates, but both of them were limited to derive AGB values higher than 500 Mg/ha.

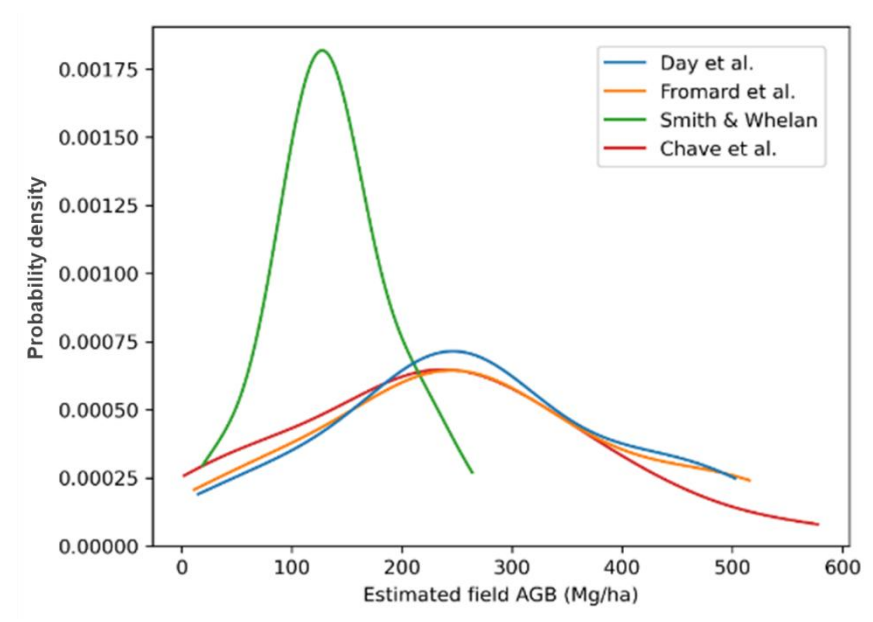


Figure 3-5. Kernel density distribution of plot-level AGB estimates derived from different allometric equations for the study area.

3.8.3 Performance of DEM calibration against field measurements

The calibrated Copernicus GLO-30 DEM was found to have the highest agreement with plot-level mean canopy heights over the study area with an R² of 0.82 and an RMSE of 1.51 m, followed by the calibrated NASADEM (R²: 0.76, RMSE: 1.76 m) and ALOS DSM (R²: 0.73, RMSE: 1.88 m) (**Figure 3-6a**). Also, the AGB estimates derived from the calibrated Copernicus GLO-30 DEM using Equation (3.2) agreed the most with plot-level AGB with the R² of 0.66 and the RMSE of 81.93 Mg/ha, while using the calibrated ALOS DSM (R²: 0.54, RMSE: 95.09 Mg/ha) yielded a slightly better agreement than the calibrated NASADEM (R²: 0.49, RMSE: 99.91 Mg/ha) (**Figure 3-6b**).

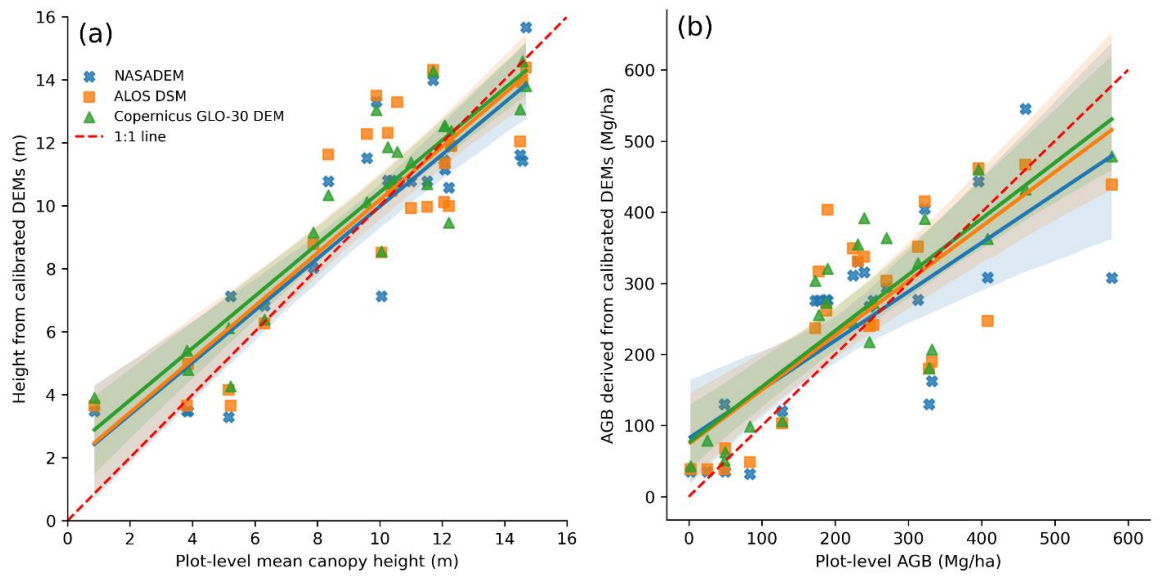


Figure 3-6. Field canopy height and AGB measurements against the estimations derived from calibrated DEMs with 95% confidence intervals: (a) plot-level mean canopy height and (b) AGB.

3.8.4 Mangrove AGB mapping based on calibrated DEMs

Compared to mean canopy height distribution of calibrated DEMs over mangroves in El Llano, the values over La Mancha mangroves ranged up to ~16 m (**Figure 3-7**). However, unexpectedly high values of NASADEM and Copernicus GLO-30 DEM were observed for El Llano mangroves, leading to anomalously high AGB estimates in a small southeastern area (**Figure 3-8**, **Figure 3-9**). Generally, all the calibrated DEMs demonstrate comparable quartiles of height estimates over mangroves for each area. Due to data sources of different time periods for DEM generation, calibrated ALOS DSM and Copernicus GLO-30 DEM demonstrated an increase in the distribution of higher height values as mangroves might have increased in height. For instance, mean canopy heights of La Mancha mangrove forests were distributed more at higher values in Copernicus GLO-30 DEM (10.34 m at 50th) than NASADEM (10.05 m at 50th).

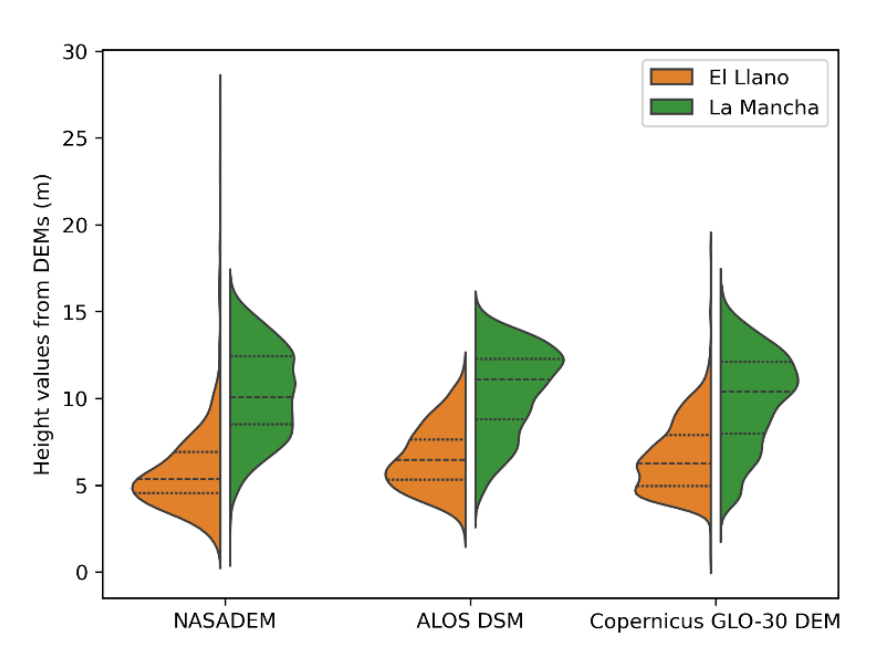


Figure 3-7. Probability density function of mean canopy heights over the mangrove forests around El Llano and La Mancha lagoons from calibrated DEMs using Gaussian kernel density estimation. Dash lines from bottom to top denote the values at 25th, 50th and 75th percentile, respectively.

Equation (3.2) was applied to calibrated DEMs for mangrove AGB estimation (**Figure 3-8**). Consistent with height estimates, mangroves on the south of La Mancha lagoon were predicted to have higher AGB, while El Llano mangroves had lower AGB distributed in the range of 35.22 – 211.56 Mg/ha using NASADEM, 50.02 – 237.00 Mg/ha using ALOS DSM and 49.26 – 238.41 Mg/ha using Copernicus GLO-30 DEM at the 5th and 95th percentile. La Mancha mangrove forests were predicted to have AGB distributed in the range of 106.75 – 468.78 Mg/ha using NASADEM, 92.91 – 438.49 Mg/ha using ALOS DSM and 67.61 – 435.69 Mg/ha using Copernicus GLO-30 DEM at the 5th and 95th percentile (**Figure 3-9**). The distribution of AGB estimates exhibits similar patterns to mean canopy height estimates from calibrated DEMs.

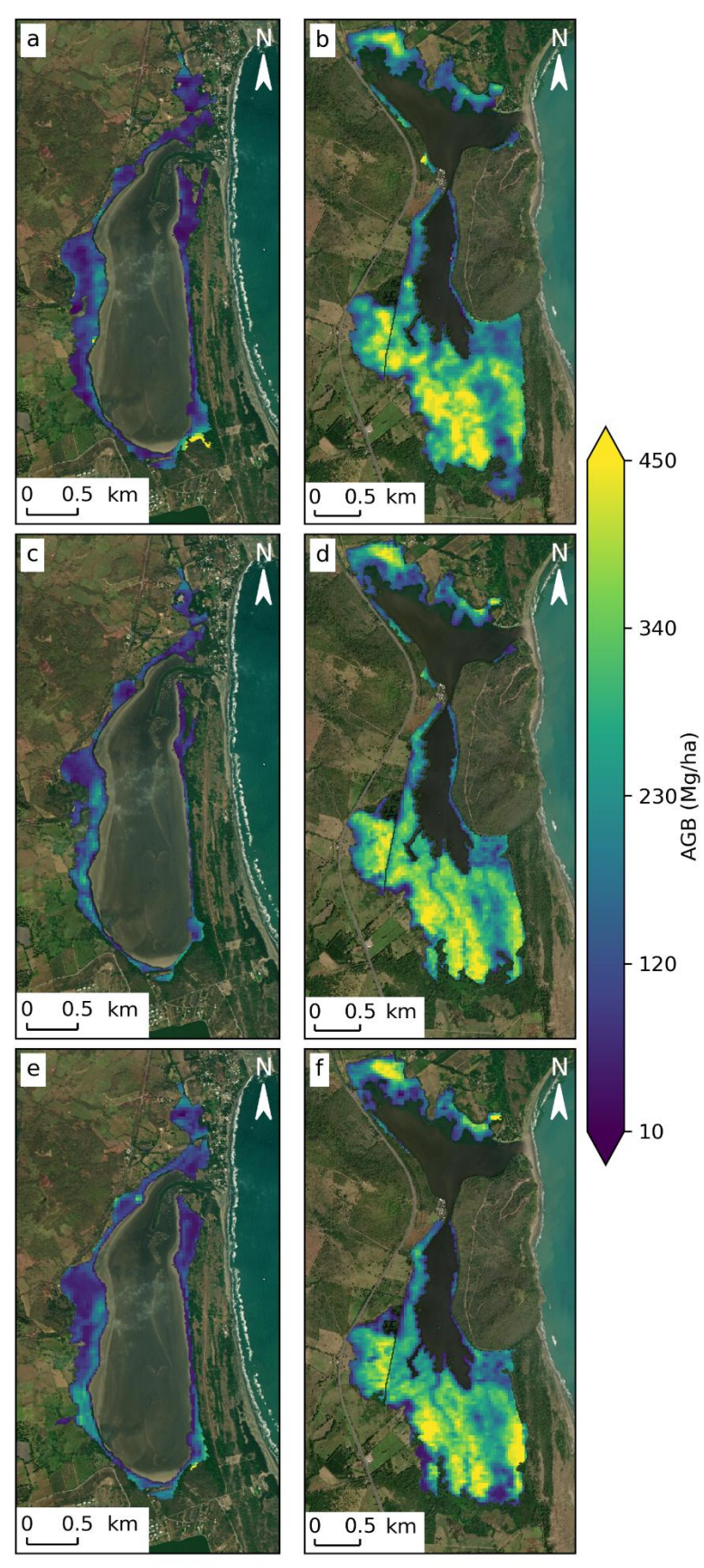


Figure 3-8. AGB estimation based on three calibrated DEMs of El Llano mangroves (left column) and La Mancha mangroves (right column). (a), (b) for NASADEM; (c), (d) for ALOS DSM, (e), (f) for Copernicus GLO-30 DEM. The base map is rendered through Esri World Image. Note that a diagonal black stripe situated in the southwest of mangrove extent maps of La Mancha lagoon is a physical gap (pathway) separating the mangrove forest.

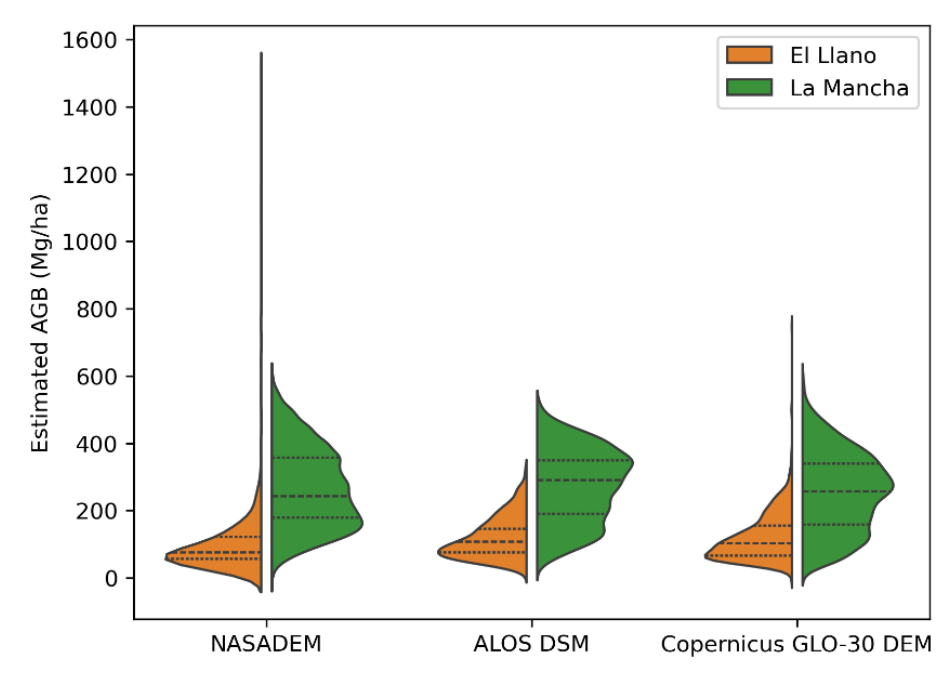


Figure 3-9. Probability density function of estimated AGB over the mangrove forests around El Llano (*left*) and La Mancha (*right*) lagoons using Gaussian kernel density estimation. Dash lines from bottom to top denote the values at 25th, 50th and 75th percentile, respectively.

3.8.5 Comparisons between AGB estimation maps

The spatiotemporal variation of the AGB results was investigated over the study area for El Llano mangroves and La Mancha mangroves using difference percentage (i.e., $Diff\% = \frac{AGB_i - AGB_j}{AGB_j} \times 100\%$). For El Llano mangroves, the AGB estimation results of ALOS DSM and Copernicus GLO-30 DEM are nearly 30% higher than NASADEM. Considering NASADEM sourced from the data in 2000 and natural growth of mangroves, NASADEM captured lower canopy heights of that time resulting in lower AGB

nearly 30% higher than NASADEM. Considering NASADEM sourced from the data in 2000 and natural growth of mangroves, NASADEM captured lower canopy heights of that time resulting in lower AGB estimation (**Figure 3-10a, b**). The reported AGB accumulation rates for mangroves average 3.3 Mg/ha/yr (95% CI: 3.1 - 3.5) in tropical dry areas (IPCC, 2014), which also characterises the climatic conditions of the study area. It is a similar situation for the landward and seaward edges of La Mancha mangroves (**Figure 3-10b, f**), where mangroves may experience significant changes, such as establishment and harvesting. AGB estimations of the south of La Mancha mangroves derived from ALOS DSM and Copernicus GLO-30 DEM were in higher agreement between \pm 12% difference (**Figure 3-10d**). Additionally, the mangrove AGB maps ($AGB_{NASADEM}$, AGB_{COPDEM}) of this study show comparable R² values (0.74 for $AGB_{NASADEM}$ vs. AGB_{COPDEM} vs. AGB_{COPDEM} and 0.78 for $AGB_{ALOSDSM}$ vs. AGB_{COPDEM}) and the RMSE of around 60 Mg/ha (**Figure 3-11**).

The 30m global mangrove AGB estimation map from Simard et al. (2019) was introduced for intercomparisons. This map was generated by applying the field-measured biomass-height allometry to

SRTM estimates of basal area weighted canopy height across the global mangrove extent. Simard's map predicts a lower AGB over the mangrove forests in the study area, where the corresponding R^2 values are -0.90, -1.23 and -1.16 for $AGB_{NASADEM}$, $AGB_{ALOSDSM}$, AGB_{COPDEM} vs. AGB_{Simard} , while showing apparent linear relationships with the AGB estimation results (**Figure 3-11**).

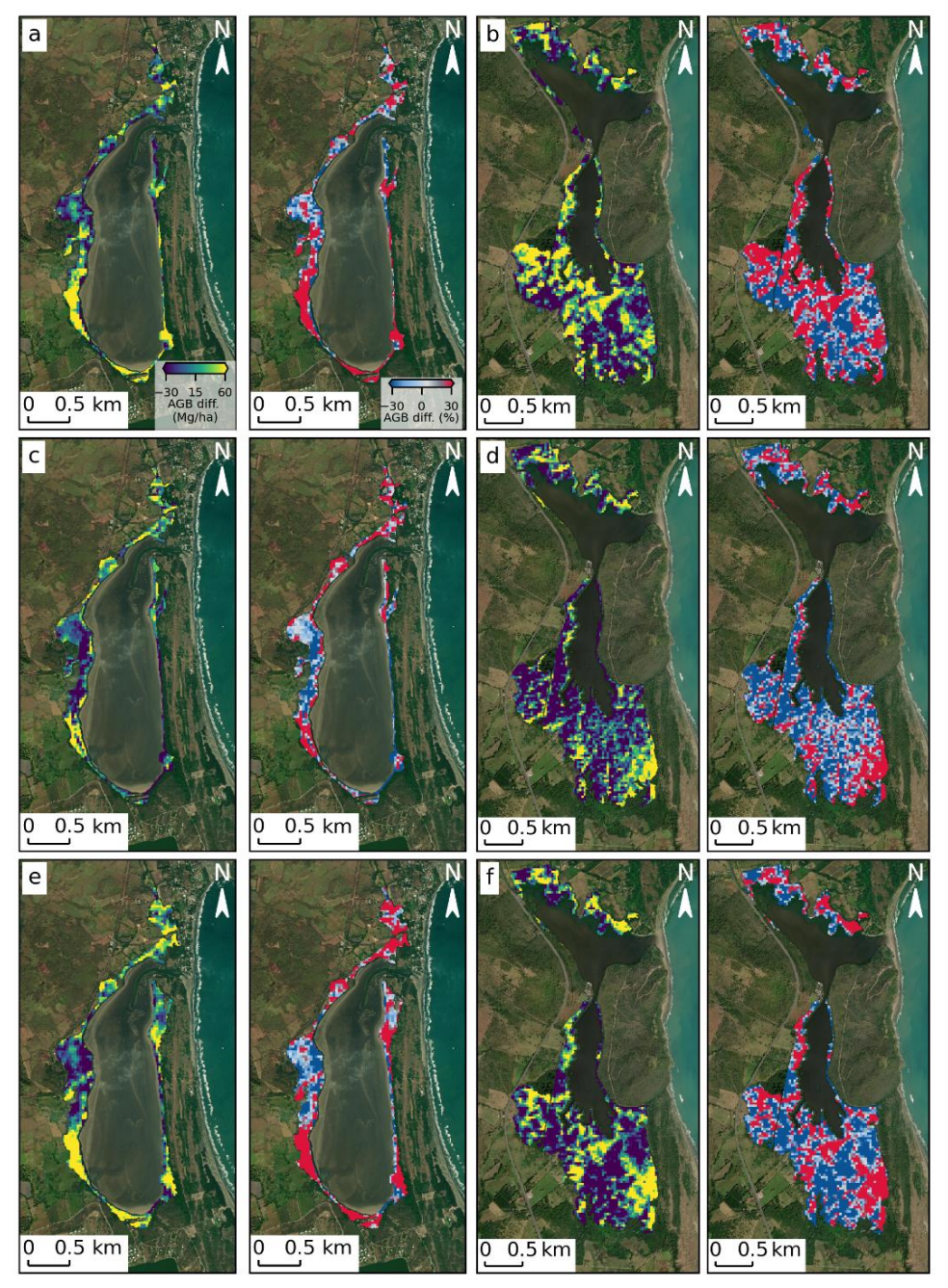


Figure 3-10. Differences between mangrove AGB estimates of El Llano (left two columns) and La Mancha (right two columns) based on three calibrated DEM. (a), (b) for ALOS DSM vs. NASADEM; (c), (d) for Copernicus GLO-30 DEM vs. ALOS DSM; (e), (f) for Copernicus GLO-30 DEM vs. NASADEM. Left sub-subplot of each paired subplot is in the unit of Mg/ha, while the right one is in percentage terms. The base map is rendered through Esri World Image.

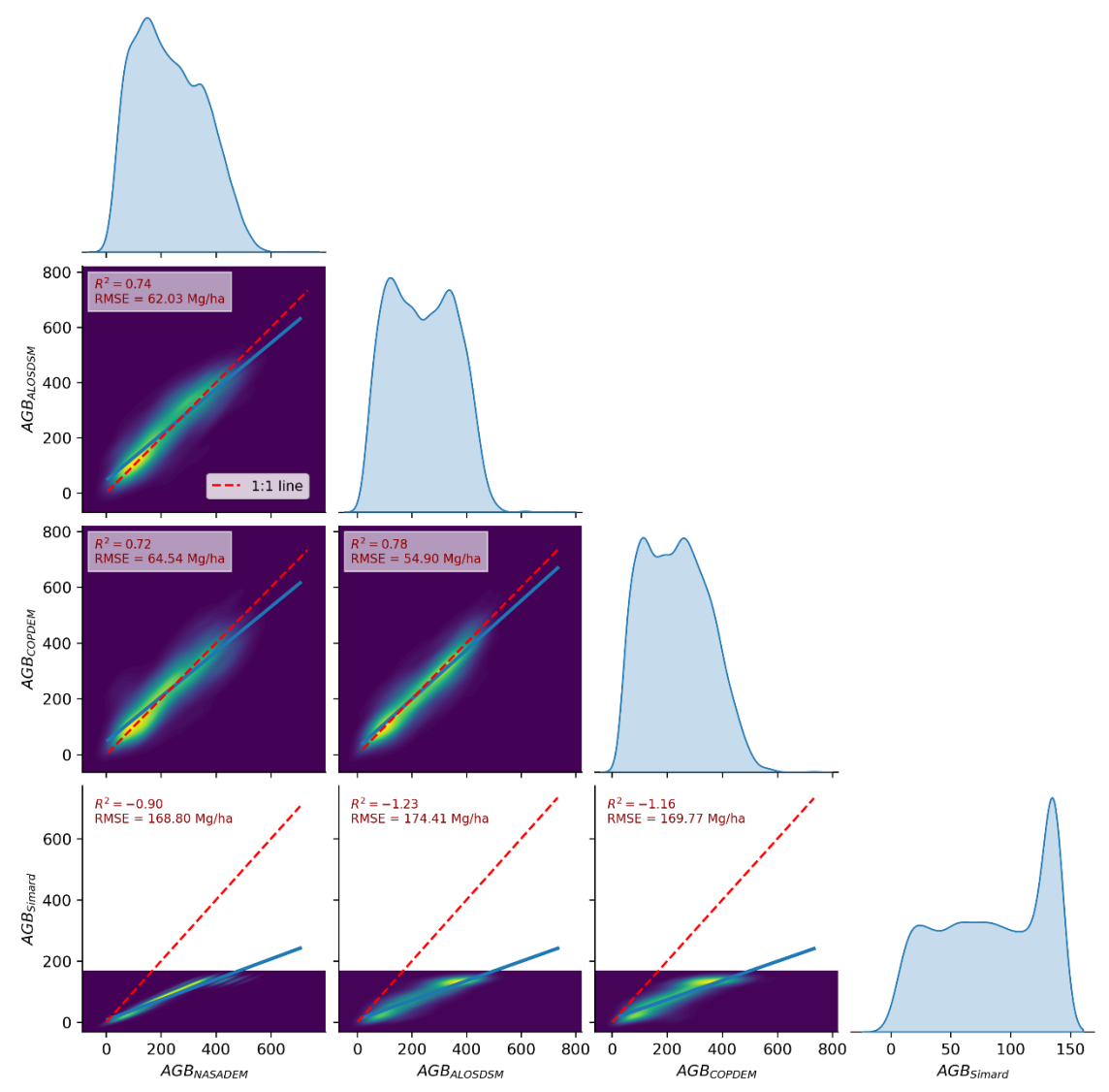


Figure 3-11. Pairwise comparisons with linear regression lines between the AGB estimation results derived from NASADEM, ALOS DSM, Copernicus GLO-30 DEM and Simard et al. (2019). Lower triangle plots are colour coded density plots as colour changes from purple to yellow for increasing density of data points. Each diagonal plot demonstrates probability density function of the AGB estimation corresponding to x/y axis label.

3.9 Discussion

3.9.1 Uncertainty of mangrove AGB estimation

This study demonstrates the feasibility of using global DEMs for estimating the AGB of two local mangrove forests in Mexico. The main sources of uncertainty result from errors in DEM-derived mean canopy height estimation and errors in plot-level biomass-height model. Field measurement errors and spaceborne LiDAR measurement errors are not considered here as ICESat-2 LiDAR metrics have low errors for mangrove canopy height estimation (Yu et al., 2022) and are deemed as canopy height reference to calibrate DEMs while field data were acquired through averaging repeated measurements. Thus, the uncertainty of the

proposed methodology for mangrove AGB estimation was computed as standard errors by propagating mean canopy height errors into plot-level AGB estimation errors. This was expressed as:

$$\sigma_{AGB} = \sqrt{\left(\frac{\partial AGB}{\partial H_{mean}}\right)^2 \sigma_{H_{mean}}^2 + \left(\frac{\partial AGB}{\partial a}\right)^2 \sigma_a^2 + \left(\frac{\partial AGB}{\partial \beta}\right)^2 \sigma_\beta^2 + 2\left(\frac{\partial AGB}{\partial a}\frac{\partial AGB}{\partial \beta}\right) \sigma_{a\beta}^2} \quad \text{(Equation 3.3)}$$

where $\sigma_{H_{mean}}$ represents standard errors of mean canopy height estimation from DEMs and $\sigma_{a\beta}^2$ is the covariance between the fitted parameters a and β . The standard errors (RMSE) of mean canopy height estimation using NASADEM, ALOS DESM and Copernicus GLO-30 DEM are shown summarised shown in **Table 3-2**. Therefore, the standard errors of mangrove AGB estimation (σ_{AGB}) computed through Equation 3.3 are varying between \pm 15.16 – 15.53 Mg/ha for stands with a mean canopy height $H_{mean} = 1$ m, and \pm 151.78 – 154.95 Mg/ha for $H_{mean} = 15$ m. Generally, the uncertainty is expected to be reduced when more field measurements are included for biomass-height allometry development.

3.9.2 Discrepancies between local and global AGB estimates

The AGB estimates obtained in this study are consistently higher than those reported by the global mangrove AGB map of Simard et al. (2019) (**Figure 3-11**). These discrepancies primarily stem from the differences in how biomass-height allometry was developed. As we developed biomass-height allometry using field measurements of the study area, the structural characteristics of local mangrove forests were captured. Conversely, Simard's estimates relied on a global mangrove field inventory, from which a generalised biomass-height relationship was derived. While the global model provides a valuable baseline for global-scale assessments, its transferability to specific regions is limited. The global allometry captures the overall trend but systematically underestimates the values of mangrove AGB in the study area.

3.9.3 Difference among allometric equations for field AGB estimation

The differences in the kernel density distribution of AGB estimates highlight the influence of model calibration datasets and diameter ranges. The allometric equations from Smith & Whelan (2006) reflect the limited DBH range of harvested trees used in model development (**Table 3-4**). Similarly, the equations of Day et al. (1987) and Fromard et al. (1998) produced more realistic estimates but were developed from trees with smaller DBH ranges, meaning that many field measurements in this study (0.5–103.4 cm DBH; **Table 3-5**) fell outside their validity domains.

In contrast, the pantropical model of Chave et al. (2014) covers a broad DBH range (5–212 cm) that overlaps with most field observations in this study, making it more reliable and widely applicable. Although a small number of mangroves had DBH < 5 cm, Chave's allometric equation was still applied given the lack of species-specific models for small individuals in the study area. Despite the availability of several allometric equations, the broader applicability and better alignment with field measurements justify the selection of Chave et al. (2014) for mangrove AGB estimation for this study.

3.9.4 Limitations of AGB estimation using DEMs

In this study, DEMs were used to estimate mangrove mean canopy height and AGB based on plot-level biomass-height allometry. This approach relies on the assumption that mangroves are situated in low-lying and flat coastal areas where topographic impacts are negligible, which does not compromise DEM-derived canopy height estimation. In reality, however, coastal topography invariably slopes upward out of the intertidal areas, leading to systematically higher canopy height estimation at the landward margin of mangrove forests. Nonetheless, mangroves rarely establish on steep slopes, meaning that DEMs remain broadly reliable for canopy height retrieval. Cannon et al. (2020) found that hydrodynamic habitat has shaped the mangrove distribution around a microtidal estuarine lagoon, with more than 90% of mangrove presence occurring where intertidal slopes were <0.5 and 80th percentile wave heights were <2.5 cm. Therefore, the impacts of increased slopes will cause significant overestimation of canopy height over a small number of mangroves and should be explicitly accounted for when higher-resolution or site-specific analyses are required.

As intact and well-established mangrove forests normally exhibit canopy height changes at finer resolution, 30 m DEMs are sufficient over time to demonstrate mean canopy height and its distribution (Lagomasino et al., 2016). Additionally, as the mangrove forest around El Llano lagoon is facing higher hydrological stress, i.e., high salinity regulated by seawater, it indicates that the growth of large mangrove trees is suppressed whilst small trees contribute to mangrove growth in high salinity areas (Ahmed et al., 2023). Though La Mancha lagoon receives freshwater in the south leading to low salinity, mangrove canopy heights response inversely to increasing salinity as there is a salinity gradient in the La Mancha lagoon (Vovides et al., 2014). All the factors make the introduced DEMs feasible and reliable to estimate mangrove canopy height over time across the study area. But the time lag of two decades should be carefully taken into account when the proposed methodology is applied to *Sonneratia* species mangroves that can exhibit significant natural canopy growth in several years (Wang et al., 2021).

Compared to the limited plot size and number in this study, fixed 100 m segments of ICESat-2 ATL08 were used to calibrate DEMs in mean canopy height estimation. However, because ICESat-2 data did not overlap with the established field plots, its accuracy relative to field measurements could not be directly validated in this study. Despite this limitation, ICESat-2 ATL08 data are widely considered reliable ground truths for canopy height, as these spaceborne LiDAR measurements provide high accuracy aligned with geodetic benchmarks (Carrera-Hernández, 2021). Copernicus GLO-30 DEM works the best in mean canopy height and AGB estimation, as it was produced using data sources temporally closer to the field plot measurements capturing small mangrove tree growth, especially where mangroves do not exist when the data was required for the generation of NASADEM and ALOS DSM (**Figure 3-7**). Calibrated ALOS DSM and NASADEM work similarly for the estimation of mean canopy height and AGB.

3.10 Conclusions

This study presents an approach for using DEMs to estimate AGB for the mangrove forests bordering the lagoons of La Mancha and El Llano in Mexico and examines the performance of using DEMs for mean canopy height and AGB estimation. With an assumption that the underlying environment of mangroves is flat and low-lying at sea level, DEMs can be sufficiently utilized to estimate canopy height. The metric of mean canopy relative height from ICESat-2 was used to calibrate DEM height measurements though there is a time lag between these datasets, since well-established mangrove forests have witnessed few significant canopy changes and high salinity limits mangrove tree growth. A power-law model $AGB = \alpha H_{mean}^{\beta}$ was introduced for the relationship between plot-level AGB estimation and mean canopy height, which was regressed by OLS using field plot measurements. The standard errors of mean canopy height estimation are 2.45 m, 2.49 m and 2.43 m for NASADEM, ALOS DESM and Copernicus GLO-30 DEM, respectively. Therefore, the uncertainty was computed through error propagation of mean canopy height estimation errors and regression coefficient errors of biomass-height allometry, resulting in σ_{AGB} varying between \pm 15.16 - 15.53 Mg/ha for stands with mean canopy height $H_{mean} = 1$ m. Mangrove AGB of El Llano and La Mancha lagoons was estimated to be 212 – 239 Mg/ha and 436 – 469 Mg/ha at the 95th percentile, respectively. The intercomparisons of DEM-derived AGB estimates show comparable results with the R² ranging from 0.72 to 0.78 and RMSE ranging from 54.90 to 64.54 Mg/ha, while the comparisons with a global mangrove AGB estimation map from Simard et al. (2019) show significant discrepancies with negative R² as the global biomass-height allometry is limited to capture the structural characteristics at a local scale.

Overall, this study generated local AGB estimation of mangroves bordering the lagoons of La Mancha and El Llano in Mexico which can be used for future carbon stock assessments and mangrove health and

resilience investigations. Additionally, this study shows comparable mean canopy height and AGB estimation using calibrated DEMs, however, more contemporary DEM was recommended to be used for the investigation of small mangrove tree growth, i.e., Copernicus GLO-30 DEM. As there are about 79.4% (11,905 km²) of global lagoonal mangroves across North and Central America and the Caribbean region (Worthington et al., 2020), the proposed methodology is potentially transferable for AGB estimation in these areas.

References

- Ahmed, S., Sarker, S.K., Friess, D.A., et al., 2023. Mangrove tree growth is size-dependent across a large-scale salinity gradient. For. Ecol. and Manage. 537, 120954. https://doi.org/10.1016/j.foreco.2023.120954
- AIRBUS, 2022. Copernicus Digital Elevation Model Product Handbook (Version 4.0).
- Alongi, D.M., 2020. Global Significance of Mangrove Blue Carbon in Climate Change Mitigation. Sci 2 (3), 67. https://doi.org/10.3390/sci2030067
- Arceo-Carranza, D., Chiappa-Carrara, X., Chávez López, R., et al., 2021. Mangroves as Feeding and Breeding Grounds, in: Rastogi, R.P., Phulwaria, M., Gupta, D.K. (Eds.), Mangroves: Ecology, Biodiversity and Management. Springer, Singapore, pp. 63–95. https://doi.org/10.1007/978-981-16-2494-0_3
- Aslan, A., Aljahdali, M.O., 2022. Characterizing Global Patterns of Mangrove Canopy Height and Aboveground Biomass Derived from SRTM Data. Forests 13 (10), 1545. https://doi.org/10.3390/f13101545
- Baskerville, G.L., 1972. Use of Logarithmic Regression in the Estimation of Plant Biomass. Can. J. For. Res. 2 (1), 49–53. https://doi.org/10.1139/x72-009
- Cannon, D., Kibler, K., Donnelly, M., et al., 2020. Hydrodynamic habitat thresholds for mangrove vegetation on the shorelines of a microtidal estuarine lagoon. Ecol. Eng. 158, 106070. https://doi.org/10.1016/j.ecoleng.2020.106070
- Carrera-Hernández, J.J., 2021. Not all DEMs are equal: An evaluation of six globally available 30 m resolution DEMs with geodetic benchmarks and LiDAR in Mexico. Remote Sens. Environ. 261, 112474. https://doi.org/10.1016/j.rse.2021.112474
- Castañeda-Moya, E., Twilley, R.R., Rivera-Monroy, V.H., 2013. Allocation of biomass and net primary productivity of mangrove forests along environmental gradients in the Florida Coastal Everglades, USA. For. Ecol. Manag. 307, 226–241. https://doi.org/10.1016/j.foreco.2013.07.011
- Chacón Abarca, S., Chávez, V., Silva, R., et al., 2021. Understanding the Dynamics of a Coastal Lagoon:

 Drivers, Exchanges, State of the Environment, Consequences and Responses. Geosciences 11.

 https://doi.org/10.3390/geosciences11080301
- Chave, J., Andalo, C., Brown, S., et al., 2005. Tree allometry and improved estimation of carbon stocks and balance in tropical forests. Oecologia 145, 87–99. https://doi.org/10.1007/s00442-005-0100-x
- Chave, J., Condit, R., Aguilar, S., et al., 2004. Error propagation and scaling for tropical forest biomass estimates. Phil. Trans. R. Soc. Lond. B 359, 409–420. https://doi.org/10.1098/rstb.2003.1425

- Chave, J., Réjou-Méchain, M., Búrquez, A., et al., 2014. Improved allometric models to estimate the aboveground biomass of tropical trees. Glob. Change Biol. 20, 3177–3190. https://doi.org/10.1111/gcb.12629
- Chávez-Cerón, V., Mendoza-Baldwin, E., Ramírez-Méndez, E., et al., 2016. Response of Empirically Managed Sites to Winter Storms. Case Study: La Mancha, Veracruz, Mexico. Coast. Eng. Proc. 1(35), p. management.15. https://doi.org/10.9753/icce.v35.management.15
- Chávez-López, R., Rocha-Ramírez, A., 2020. Composición de la comunidad de peces en el estuario ciego laguna El Llano, Veracruz, México. Rev. Mex. Biodivers. 91. https://doi.org/10.22201/ib.20078706e.2020.91.2494
- Clifford, D., Cressie, N., England, J.R., et al., 2013. Correction factors for unbiased, efficient estimation and prediction of biomass from log-log allometric models. For. Ecol. Manag. 310, 375–381. https://doi.org/10.1016/j.foreco.2013.08.041
- CONABIO, 2023a. Portal de Información Geográfica CONABIO. http://www.conabio.gob.mx/informacion/gis/?vns=gis_root/biodiv/monmang/bimagdmo/mexman 2005gw (accessed 8 January 2023).
- CONABIO, 2023b. Portal de Información Geográfica CONABIO. http://www.conabio.gob.mx/informacion/gis/?vns=gis_root/biodiv/monmang/bimagdmo/mexman 2010gw (accessed 8 January 2023).
- Crippen, R., Buckley, S., Agram, P., et al., 2016. NASADEM GLOBAL ELEVATION MODEL: METHODS AND PROGRESS. Int. Arch. Photogramm. Remote Sens. Spatial Inf. Sci. XLI-B4, 125–128. https://doi.org/10.5194/isprs-archives-XLI-B4-125-2016
- Day, J.W., Conner, W.H., Ley-Lou, F., et al., 1987. The productivity and composition of mangrove forests, Laguna de Términos, Mexico. Aquat. Bot. 27, 267–284. https://doi.org/10.1016/0304-3770(87)90046-5
- Duncan, C., Owen, H.J.F., Thompson, J.R., et al., 2018. Satellite remote sensing to monitor mangrove forest resilience and resistance to sea level rise. Methods Ecol. Evol. 9, 1837–1852. https://doi.org/10.1111/2041-210X.12923
- ESA, 2022. Copernicus DEM Global and European Digital Elevation Model (COP-DEM). https://doi.org/10.5270/ESA-c5d3d65
- FAO, 2023. The world's mangroves 2000–2020. FAO, Rome. https://doi.org/10.4060/cc7044en
- Farr, T.G., Rosen, P.A., Caro, E., et al., 2007. The Shuttle Radar Topography Mission. Rev. Geophys. 45. https://doi.org/10.1029/2005RG000183
- Fatoyinbo, T.E., Simard, M., 2013. Height and biomass of mangroves in Africa from ICESat/GLAS and SRTM. Int. J. Remote Sens. 34, 668–681. https://doi.org/10.1080/01431161.2012.712224

- Fromard, F., Puig, H., Mougin, E., et al., 1998. Structure, above-ground biomass and dynamics of mangrove ecosystems: new data from French Guiana. Oecologia 115, 39–53. https://doi.org/10.1007/s004420050489
- Grohman, G., Kroenung, G., Strebeck, J., 2006. Filling SRTM Voids: The Delta Surface Fill Method. Photogramm. Eng. Remote Sens. 72, 213–216.
- Harishma, K.M., Sandeep, S., Sreekumar, V.B., 2020. Biomass and carbon stocks in mangrove ecosystems of Kerala, southwest coast of India. Ecol. Process. 9. https://doi.org/10.1186/s13717-020-00227-8
- Harte Research Institute for Gulf of Mexico, 2021a. Gulfbase: Laguna La Mancha. https://www.gulfbase.org/geological-feature/laguna-la-mancha (accessed 8 January 2023).
- Harte Research Institute for Gulf of Mexico, 2021b. Gulfbase: Laguna El Llano. https://www.gulfbase.org/geological-feature/laguna-el-llano (accessed 8 January 2023).
- IPCC, 2014. 2013 supplement to the 2006 IPCC guidelines for national greenhouse gas inventories: Wetlands, Hiraishi, T., Krug, T., Tanabe, K., et al. (Eds.). IPCC, Switzerland.
- Jones, A.R., Raja Segaran, R., Clarke, K.D., et al., 2020. Estimating mangrove tree biomass and carbon content: A comparison of forest inventory techniques and drone imagery. Front. Mar. Sci. 6. https://doi.org/10.3389/fmars.2019.00784
- Kauffman, J.B., Donato, D.C., 2012. Protocols for the measurement, monitoring and reporting of structure, biomass, and carbon stocks in mangrove forests. Center for International Forestry Research, Bogor, Indonesia.
- Komiyama, A., Ong, J.E., Poungparn, S., 2008. Allometry, biomass, and productivity of mangrove forests: A review. Aquat. Bot. 89 (2), 128–137. https://doi.org/10.1016/j.aquabot.2007.12.006
- Komiyama, A., Poungparn, S., Kato, S., 2005. Common allometric equations for estimating the tree weight of mangroves. J. Trop. Ecol. 21, 471–477. https://doi.org/10.1017/S0266467405002476
- Lagomasino, D., Fatoyinbo, T., Lee, S., et al., 2016. A Comparison of Mangrove Canopy Height Using Multiple Independent Measurements from Land, Air, and Space. Remote Sens. 8, 327. https://doi.org/10.3390/rs8040327
- Maurya, K., Mahajan, S., Chaube, N., 2021. Remote sensing techniques: mapping and monitoring of mangrove ecosystem—a review. Complex Intell. Syst. 7, 2797–2818. https://doi.org/10.1007/s40747-021-00457-z
- Méndez-Alonzo, R., Hernández-Trejo, H., López-Portillo, J., 2012. Salinity constrains size inequality and allometry in two contrasting mangrove habitats in the Gulf of Mexico. J. Trop. Ecol. 28, 171–179. https://doi.org/10.1017/S0266467412000016
- Moreno-Casasola, P., López Rosas, H., Infante Mata, D., et al., 2009. Environmental and anthropogenic factors associated with coastal wetland differentiation in La Mancha, Veracruz, Mexico. Plant Ecol. 200, 37–52. https://doi.org/10.1007/s11258-008-9400-7

- NASA JPL, 2013. NASA Shuttle Radar Topography Mission Global 1 arc second. https://doi.org/10.5067/MEaSUREs/SRTM/SRTMGL1.003
- Neumann, T.A., Martino, A.J., Markus, T., et al., 2019. The Ice, Cloud, and Land Elevation Satellite 2 mission: A global geolocated photon product derived from the Advanced Topographic Laser Altimeter System. Remote Sens. Environ. 233, 111325. https://doi.org/10.1016/j.rse.2019.111325
- Pham, T.D., Yokoya, N., Bui, D.T., et al., 2019. Remote Sensing Approaches for Monitoring Mangrove Species, Structure, and Biomass: Opportunities and Challenges. Remote Sens. 11, 230. https://doi.org/10.3390/rs11030230
- Ramsar, 2004. La Mancha y El Llano: Ramsar sites information service. https://rsis.ramsar.org/ris/1336 (accessed 8 January 2023).
- Riegler, G., Hennig, S.D., Weber, M., 2015. WORLDDEM A NOVEL GLOBAL FOUNDATION LAYER. Int. Arch. Photogramm. Remote Sens. Spatial Inf. Sci. XL-3/W2, 183–187. https://doi.org/10.5194/isprsarchives-XL-3-W2-183-2015
- Rodríguez-Zúñiga, M.T., Troche-Souza, C., Cruz-López, M.I., et al., 2022. Development and Structural Organization of Mexico's Mangrove Monitoring System (SMMM) as a Foundation for Conservation and Restoration Initiatives: A Hierarchical Approach. Forests 13, 621. https://doi.org/10.3390/f13040621
- Rosa, L.N., Duarte de Paula Costa, M., de Freitas, D.M., 2022. Modelling spatial-temporal changes in carbon sequestration by mangroves in an urban coastal landscape. Estuar. Coast. Shelf Sci. 276. https://doi.org/10.1016/j.ecss.2022.108031
- Simard, M., Fatoyinbo, L., Smetanka, C., et al., 2019. Mangrove canopy height globally related to precipitation, temperature and cyclone frequency. Nat. Geosci. 12, 40–45. https://doi.org/10.1038/s41561-018-0279-1
- Simard, M., Rivera-Monroy, V.H., Mancera-Pineda, J.E., et al., 2008. A systematic method for 3D mapping of mangrove forests based on Shuttle Radar Topography Mission elevation data, ICESat/GLAS waveforms and field data: Application to Ciénaga Grande de Santa Marta, Colombia. Remote Sens. Environ. 112 (5), 2131–2144. https://doi.org/10.1016/j.rse.2007.10.012
- Simard, M., Zhang, K., Rivera-Monroy, V.H., et al., 2006. Mapping height and biomass of mangrove forests in Everglades National Park with SRTM elevation data. Photogramm. Eng. Remote Sens. 72, 299–311.
- Smith, T.J., Whelan, K.R.T., 2006. Development of allometric relations for three mangrove species in South Florida for use in the Greater Everglades Ecosystem restoration. Wetl. Ecol. Manag. 14, 409–419. https://doi.org/10.1007/s11273-005-6243-z

- Song, S., Ding, Y., Li, W., et al., 2023. Mangrove reforestation provides greater blue carbon benefit than afforestation for mitigating global climate change. Nat. Commun. 14, 756. https://doi.org/10.1038/s41467-023-36477-1
- Tadono, T., Ishida, H., Oda, F., et al., 2014. Precise Global DEM Generation by ALOS PRISM. ISPRS Ann. Photogramm. Remote Sens. Spat. Inf. Sci. II–4, 71–76. https://doi.org/10.5194/isprsannals-II-4-71-2014
- Taillardat, P., Friess, D.A., Lupascu, M., 2018. Mangrove blue carbon strategies for climate change mitigation are most effective at the national scale. Biol. Lett. 14, 20180251. https://doi.org/10.1098/rsbl.2018.0251
- Takaku, J., Tadono, T., Tsutsui, K., 2014. Generation of High Resolution Global DSM from ALOS PRISM.
 Int. Arch. Photogramm. Remote Sens. Spatial Inf. Sci. XL–4, 243–248.
 https://doi.org/10.5194/isprsarchives-XL-4-243-2014
- Tang, W., Zheng, M., Zhao, X., et al., 2018. Big Geospatial Data Analytics for Global Mangrove Biomass and Carbon Estimation. Sustainability 10, 472. https://doi.org/10.3390/su10020472
- Tran, T.V., Reef, R., Zhu, X., 2022. A Review of Spectral Indices for Mangrove Remote Sensing. Remote Sens. 14, 4868. https://doi.org/10.3390/rs14194868
- Uddin, M.M., Abdul Aziz, A., Lovelock, C.E., 2023. Importance of mangrove plantations for climate change mitigation in Bangladesh. Glob. Change Biol. 29, 3331–3346. https://doi.org/10.1111/gcb.16674
- Valderrama-Landeros, L.H., López-Portillo, J., Velázquez-Salazar, S., et al., 2020. Regional Distribution and Change Dynamics of Mangroves in México between 1970/80 and 2015. Wetlands 40, 1295–1305. https://doi.org/10.1007/s13157-020-01299-0
- Vovides, A.G., Vogt, J., Kollert, A., et al., 2014. Morphological plasticity in mangrove trees: salinity-related changes in the allometry of Avicennia germinans. Trees 28, 1413–1425. https://doi.org/10.1007/s00468-014-1044-8
- Vovides, A.G., Berger, U., Grueters, U., et al., 2018. Change in drivers of mangrove crown displacement along a salinity stress gradient. Funct. Ecol. 32, 2753–2765. https://doi.org/10.1111/1365-2435.13218
- Vovides, A.G., Wimmler, M.-C., Schrewe, F., et al., 2021. Cooperative root graft networks benefit mangrove trees under stress. Commun. Biol. 4. https://doi.org/10.1038/s42003-021-02044-x
- Wang, G., Zhang, Y., Guan, D., et al., 2021. The potential of mature Sonneratia apetala plantations to enhance carbon stocks in the Zhanjiang Mangrove National Nature Reserve. Ecol. Indic. 133, 108415. https://doi.org/10.1016/j.ecolind.2021.108415
- Wang, L., Jia, M., Yin, D., et al., 2019. A review of remote sensing for mangrove forests: 1956–2018. Remote Sens. Environ. 231, 111223. https://doi.org/10.1016/j.rse.2019.111223

- Worthington, T. A., Andradi-Brown, D.A., Bhargava, R., et al., 2020. Harnessing Big Data to Support the Conservation and Rehabilitation of Mangrove Forests Globally. One Earth 2, 429–443. https://doi.org/10.1016/j.oneear.2020.04.018
- Worthington, Thomas A., zu Ermgassen, P.S.E., Friess, D.A., et al., 2020. A global biophysical typology of mangroves and its relevance for ecosystem structure and deforestation. Sci. Rep. 10, 14652. https://doi.org/10.1038/s41598-020-71194-5
- Yu, J., Nie, S., Liu, W., et al., 2022. Accuracy Assessment of ICESat-2 Ground Elevation and Canopy Height Estimates in Mangroves. IEEE Geosci. Remote Sens. Lett. 19, 1–5. https://doi.org/10.1109/LGRS.2021.3107440
- Zanne, A.E., Lopez-Gonzalez, G., Coomes, D.A., et al., 2009. Data from: Towards a worldwide wood economics spectrum. https://doi.org/10.5061/DRYAD.234
- Zhang, X., Lin, P., Chen, X., 2022. Coastal Protection by Planted Mangrove Forest during Typhoon Mangkhut. J. Mar. Sci. Eng. 10(9), 1288. https://doi.org/10.3390/jmse10091288

Chapter 4 Aboveground biomass estimation of mangrove forests across the Americas using multisource remote sensing data

Abstract

The estimation of aboveground biomass (AGB) of mangroves serves as an important indicator for carbon stocks. Since well-established and mature mangrove forests exhibit changes at a finer scale, an accurate and high-resolution mangrove AGB estimation can facilitate spatially explicit delineation of mangrove carbon inventory. However, few studies have estimated and mapped finer-scale mangrove AGB (<10 m) at a continental level due to limited availability of high-resolution remote sensing datasets. This study proposes a novel approach for high-resolution mangrove AGB estimation that combines plot-level biomassheight allometry and Random Forests (RF) regression model with sparse canopy height data from the Global Ecosystem Dynamics Investigation (GEDI) spaceborne LiDAR mission and continental cloudless mosaics from Planet NICFI Satellite Data Program. The large amount of GEDI data bridges the gap between limited field measurements and continental AGB estimation and mapping for the training of RF model. The results showed a plot level biomass-height allometry with an R² of 0.36 and a root mean square error (RMSE) of 92.86 Mg/ha, while the RF model showed an R² of 0.72 with the RMSE of 37.24 Mg/ha. A total of 362 Tg AGB was found in the mangrove forests across the Americas in 2020, with approximately 31% distributed in Brazil. Compared with other AGB estimation maps, a higher agreement was found across the low AGB areas (<50 Mg/ha), showing the resulting map is consistent in mangrove AGB estimation at a finer scale. Overall, the approach can serve ongoing efforts for finer resolution investigation of mangroves and their management at continental or global levels and has the potential to provide highly resolved information for climate and carbon modelling.

Keywords: Mangroves; Aboveground biomass; Planet NICFI imagery; GEDI LiDAR data; Random Forests

4.1 Introduction

Mangroves are globally acknowledged as tropical ecosystems highly abundant in carbon and vital to various essential ecosystem services to surrounding coastal communities (Alongi, 2020; Uddin et al., 2023). They have historically been undervalued, particularly with large scale conversion to aquaculture and are being threatened by extreme weather events associated to changing climate (Friess et al., 2019; Goldberg et al., 2020). As mangroves have become recognized as an important ecosystem that makes crucial contributions to many objectives outlined in the Sustainable Development Goals of the 2030 Agenda, mangrove restoration and protection strategies have been put forward locally, nationally and internationally (e.g., FAO, 2023; Friess et al., 2024, 2016; Slobodian and Vidal, 2023). Aboveground biomass (AGB) estimation of mangroves is key for carbon stocks estimation and to understand mangrove carbon dynamics and its role in climate change mitigation. To facilitate the global community's efforts in further restoring and protecting mangroves, it is crucial to know the amount of biomass stored in mangroves and monitor its change over time.

Mangrove AGB refers to the total amount of living organic matter contained in the aboveground parts of mangrove trees within a specific area (generally expressed in megagram, Mg; 1 Mg = 10⁶ g). As such, normally AGB also refers to AGB density (AGBD, in the unit of Mg/ha). Traditional AGB measurement requires field-based destructive tree sampling, which is further utilized to develop allometric equations, facilitating the inference of AGB based on single trait field measurements, i.e., diameter at breast height (DBH) or canopy height (Kauffman and Donato, 2012; Komiyama et al., 2008). But the environment of mangrove forests is generally muddy, remote and inaccessible, which poses difficulties to large-scale mangrove forest biomass inventories. Remote sensing enables large-area surveys providing spatially explicit information relying on passive (e.g., multispectral and hyperspectral) or active (Synthetic Aperture Radar (SAR) and Light Detection and Ranging (LiDAR)) sensors. These types of spaceborne data show practical capability in estimating mangrove AGB at regional, national and global scales (e.g., Hu et al., 2020; Lucas et al., 2020; Prakash et al., 2022; Simard et al., 2019; Wang et al., 2020).

National or global seamless AGB mapping relies on spaceborne optical and SAR imagery, such as tropical forest AGB mapping over Peru (Csillik et al., 2019) and European Space Agency (ESA) Climate Change Initiative (CCI) global biomass maps (Santoro and Cartus, 2023). Compared to medium resolution spaceborne imagery (e.g., 30 m Landsat images), high resolution imagery such as Sentinel-2 and SPOT-5 delineates more detailed spectral and textural information across mangrove forests leading to AGB estimation at a 10 m scale (Pham and Brabyn, 2017; Pham et al., 2019). However, the high cost and limited coverage of very high resolution (VHR; spatial resolution <10 m) spaceborne images constrain the

application for mangrove AGB estimation at finer scales (Hojas Gascón et al., 2019). Planet, cooperating with Norway's International Climate and Forest Initiative (NICFI) has provided biannual and monthly high-resolution satellite mosaics with 4.77 m pixel spacing since 2015 and 2020, respectively. These mosaics are generated from PlanetScope satellite data to create cloudless and seamless datasets across the tropical Americas, Asia and Africa, normalised and harmonised with Landsat surface reflectance images (Pandey et al., 2023).

The bio-physical relationship between spectral signatures and forest vertical structure are complex, with a lack of in-depth understanding due to limited availability of field inventory data (Rodríguez-Veiga et al., 2017; Wang et al., 2019), resulting in challenging forest characteristics estimation such as canopy height or AGB from optical imagery (Lang et al., 2023). Therefore, fusing multisource remotely sensed data enables more comprehensive mapping of forest characteristics with complementary spatially explicit information (Hu et al., 2020; Lang et al., 2023; Shendryk, 2022; Wang et al., 2020). LiDAR measurements are considered a significant data source to advance AGB estimation in multisource data fusion as canopy height, a key parameter to estimate AGB, can be reliably obtained (Fatoyinbo et al., 2018; Salum et al., 2020; Tian et al., 2022; Wang et al., 2020). The Global Ecosystem Dynamics Investigation (GEDI) spaceborne mission collected full-waveform LiDAR data for the purpose of measuring global forest vertical characteristics between approximately 51.6 °N and 51.6 °S (Duncanson et al., 2022). The GEDI fullwaveform observations show high capabilities to retrieve forest canopy height, which represents a certain quantile of returned energy relative to the ground. Also, the GEDI observations are considered circular footprints of 25 m in diameter, capable of more comprehensive vegetation structure mapping than ICESat GLAS data due to smaller footprint size and denser data coverage. Given the vast amount of GEDI observations spanning from April 2019 to March 2023, the gap between limited field data and global optical imagery can be bridged by exploiting biomass-height allometry to yield GEDI-based AGB estimates for supervised machine learning.

This study aims to develop a novel approach for seamless VHR AGB estimation at a continental scale by incorporating transcontinental field data, spaceborne LiDAR data and high-resolution spaceborne imagery as well as various environmental variables. A three-steps approach was adopted: (i) obtaining plot-level biomass-height allometry based on field data across the Americas, (ii) applying the allometry to GEDI observations of relative canopy height for AGB estimates; (iii) splitting the vast amount of GEDI-based AGB estimates to train and validate the Random Forests regression model with spectral and environmental variables. This study estimates and maps mangrove AGB distribution at a finer scale over the Americas in 2020 and evaluate the agreement between other AGB estimation products (i.e., ESA CCI biomass and GEDI L4B gridded biomass maps). The resultant continental AGB map over the Americas is made publicly

available to support conservation efforts and science in disciplines such as climate, carbon and biodiversity modelling at a finer scale. Specifically, as small mangrove patches provide significant ecosystem services for vulnerable communities in the low-lying coastal areas (Curnick et al., 2019), this study is also expected to reveal the AGB distribution of small-scale mangroves from a continental perspective.

4.2 Material and methods

4.2.1 Study area

The study area of mangrove forests spanned the Americas. According to the report from UN FAO's (United Nations Food and Agriculture Organization), a total of 3.99 million hectares mangrove forests were distributed across the Americas (including North and Central America, and South America) in 2020 accounting for 27% of worldwide mangroves (FAO, 2023). While mangrove species richness is highest in the Indo-West Pacific region (62 species found), only 13 native mangrove species are recognized for the Americas (Spalding et al., 2010), at which the frontal mangrove genus mainly comprises *Rhizophora*, *Avicennia*, *Laguncularia* and *Conocarpus* (Twomey and Lovelock, 2024). A 10 m global mangrove extent map derived from Sentinel-2 imagery was used to delineate the mangrove distribution across the Americas (**Figure 4-1**). It has an overall accuracy of 93.6% (91.4-95.7%, 95% confidence interval) (Jia et al., 2023), delimited by the geographic regions defined by the Statistics Division of the United Nations, where the subregions of Americas comprise Northern America, South America, Central America, and the Caribbean (UNSD, 1999).

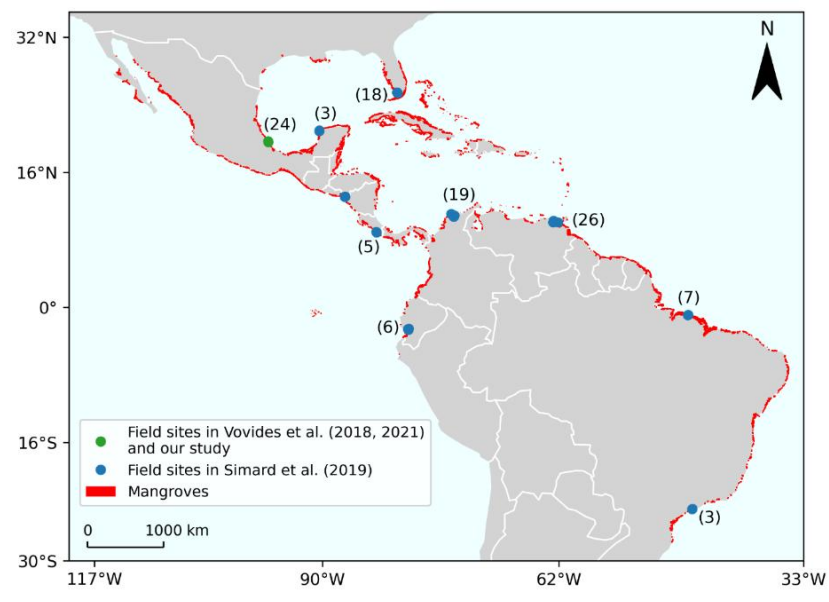


Figure 4-1. Locations of field sites and mangrove distribution in the Americas. The parenthesised numbers demonstrate the plot count at each corresponding site. Note that the small-scale basemap leads to closely spaced field plots visually condensed into a point. Two plots without geographic coordinates are not presented in this map.

4.2.2 Field inventory data

The fieldwork was carried out in the mangrove forests bordering La Mancha and El Llano lagoons in Mexico in June and July 2022 with a total of 11 field plots. Individual tree measurements in each plot were carried out including canopy height and DBH (diameter at breast height) with mangrove species recorded. Here, the field measurements in the mangrove forest bordering La Mancha from 2010 and 2017 (13 plots) (Vovides et al., 2018, 2021) were also adopted as well as mangrove inventory data across the Americas within a nearly 10-year period from 02 November 2004 to 22 May 2014 (125 plots) (Simard et al., 2019). Therefore, the recorded mangrove species consists of *Avicennia germinans*, *Rhizophora mangle*, *Laguncularia racemosa*, *Conocarpus erectus* and *Pelliciera rhizophorae*.

Field measurements were mainly collected within fixed size plots, but 64 plots of Simard's field data have variable radii. Variable-radius plots sampling is a flexible sampling practice, also referred to as angle count sampling, point sampling or prism cruising, based on the idea that trees are to be sampled with probability proportional to size (Kershaw et al., 2017). In practice, an angle device (e.g., prism or angel gauge) is used to tally trees in a full-circled rotation around the point centre. The trees are sampled when the subtended angle is larger than the reference angle, whereby a group of concentric plots with varied sizes are obtained depending on every tree size. The angle gauge coming with a basal area factor (BAF, m²/ha or ft²/acre) estimates the amount of basal area represented by each sampled tree across 1 hectare/acre area. Therefore, tree density per hectare/acre at each site is calculated by multiplying the number of sampled trees and specific BAF (Kershaw et al., 2017). In Simard's dataset, mangrove species, DBH, canopy height, and survival status (whether the tree is alive) were measured and recorded for each tallied tree at sites. Since these mangrove field data were collected from different sources under varied protocols, quality-control filters were used to acquire qualified tree measurements: (1) 'use for allometry' = 1, which represents the tree was used for allometry (Simard et al., 2019); (2) canopy height was properly measured; and (3) the most trees within the plot were not severely inclined. Thus, 89 plots in the Americas were selected from Simard's dataset, representing about 27% of the 331 global in situ plots. Together with 24 plots from the field campaigns in the mangrove forest in Mexico, a total of 113 plots were introduced in this study to develop plot level biomass-height allometry (see Figure 4-1).

4.2.3 Planet continental mosaics

Planet, cooperating with Norway's International Climate and Forest Initiative (NICFI) has provided biannual and monthly high-resolution cloudless satellite mosaics with 4.77 m pixel spacing since 2015 and 2020, respectively. These mosaics come with four multispectral bands (i.e., blue, green, red, and near

infrared) and cover the tropics of Americas between 30° N and 30° S, excluding the extent of the United States of America, Puerto Rico, British Virgin Islands, and Virgin Islands. Between December 2015 and August 2020, Planet had produced the mosaics biannually; but since September 2020, the mosaics has been being produced monthly.

In this study, a representative mosaic of 2020 was acquired for the mangrove forests across the Americas. Specifically, the images acquired in 2020 were used, including two biannual mosaics (December 2019 – May 2020 and June – August 2020) and four monthly mosaics (September – December 2020). To evaluate a compositing strategy that can minimises temporal differences, the NDVI (normalized difference vegetation index) of the 2020 mangrove extent in each mosaic was computed, given that NDVI is a positive indicator correlated with vegetation biomass (Ruan et al., 2022). The distributions of mangrove NDVI across mosaics showed only subtle variation with comparable median values (**Figure 4-2**), suggesting overall temporal consistency. Negative NDVI values observed in all mosaics largely correspond to non-vegetated surfaces (e.g., open water, residual cloud shadows), which persist due to misclassification in the 10 m mangrove extent map when overlaid with the 4.77m mosaics. Therefore, in order to mitigate the impacts of extreme pixel values, this study generated a median composite from all mosaics in 2020, which provides a more stable and representative mosaic of mangrove forests for subsequent AGB estimation and mapping.

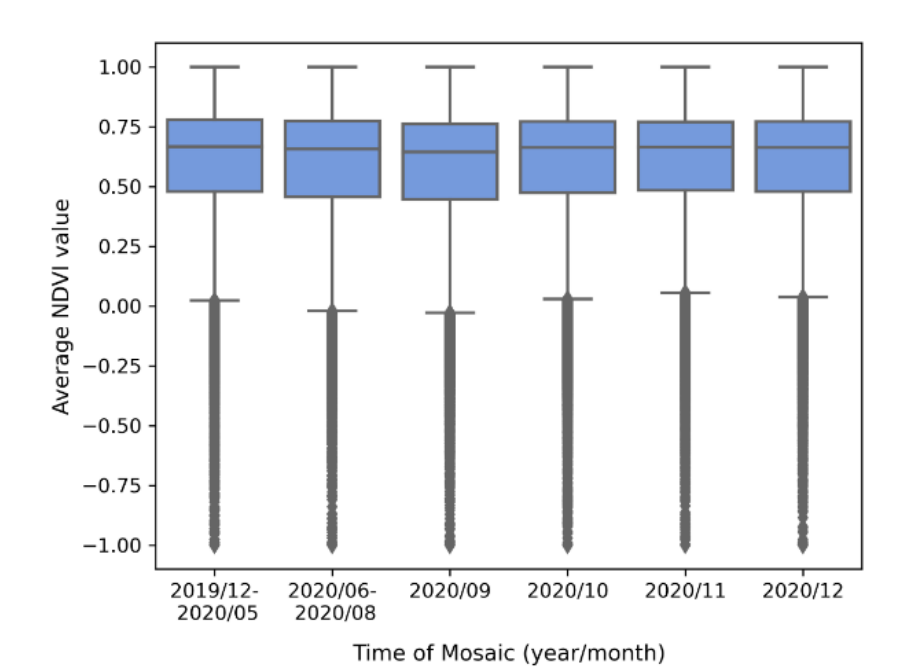


Figure 4-2. Box plot of NDVI values across mangrove areas of the Americas from Planet NICFI mosaics for 2020. Low outliers represent misclassified areas (e.g., water pixels or non-vegetated surfaces labelled as mangroves) or residual cloud shadows, leading to NDVI < 0.

4.2.4 GEDI LIDAR data

Launched on December 5, 2018, the GEDI instrument produces laser ranging observations of global 3D structure between 51.6° N and 51.6° S at the most highly resolved and densest sampling of any LiDAR instrument in orbit to date (Duncanson et al., 2022). There are three lasers within the instrument emitting eight beam ground transects (full power and coverage beams), whereby the beam transects are spaced approximately 600 m apart on the Earth's surface in the across-track direction and ~25 m footprint samples are spaced nearly every 60 m along-track (Dubayah et al., 2020). The return energy of each LiDAR footprint is contributed by a group of trees equal to a cylinder with a diameter of 25 m. On Google Earth Engine, GEDI LiDAR data were compiled and rasterized into monthly composites spanning from April 2019 to March 2023.

In this study, GEDI footprints were delimited within mangrove area across the Americas using the 10 m global mangrove extent from Jia et al. (2023) as each GEDI footprint was considered as a circular plot investigating canopy height profile over the mangrove areas. However, GEDI footprint centres are expected to have a geolocation error of 10m (Roy et al., 2021), the footprints that fall less than 40 m away from mangrove forest edge were masked out to exclude potential mixed or non-mangrove footprints (Stovall et al., 2021). Additional filters were applied to the GEDI footprints for the quality check and better performance, where GEDI nighttime strong-beam observations are recommended for canopy height retrieval (Liu et al., 2021) (**Table 4-1**). In total, 139,904 GEDI footprints were obtained as the median values were extracted for repeated observations over 2020 demonstrating canopy height profile across mangrove forests in the Americas.

Table 4-1. The filters to GEDI canopy height metrics for quality check and nighttime strong-beam data.

Property	Description	Value used for filtering	
quality_flag	Flag indicating waveform validity	= 1 (valid)	
degrade_flag	Flag indicating pointing and/or positioning degradation	= 0 (undegraded)	
beam	Beam flag identifying full power beam (strong) and coverage beam (weak)	>= 5	
solar_elevation	olar_elevation The elevation of the sun position vector from the laser bounce point position is positive up.		
sensitivity	Maximum canopy cover that can be penetrated	> 0 and $<= 1$	

4.2.5 Field AGB estimation method

The AGB of each single tree was calculated for each plot with an improved allometric equation developed for pantropical forests through a larger trunk diameter range (5-212 cm) from more tree harvest data including the data from South America (Chave et al., 2014). As wood density is a significant variable

introduced in this allometric equation, the wood density of the mangrove species in the field data was retrieved from the Global Wood Density Database (Zanne et al., 2009) (**Table 4-2**). However, the wood density of *Pelliciera rhizophorae* is missing in the database, this parameter was retrieved from the study of Southwell and Bultman (1971).

The AGB of fixed radius plots is the summation of the AGB of each single tree normalized by plot area, converted to the unit of megagram per hectare (Mg/ha). But, in variable radius plots sampling where there is no fixed plot area, concentric plot area is determined as a function of the DBH of each tallied tree, whereby the tree density represented by a single tallied tree can be estimated through normalizing corresponding plot area by hectares. The concentric plot area was first calculated through the equation: Plot area (m²) = $\pi \times \left(\frac{DBH}{100 \times CA}\right)^2$, where CA stands for the cruising angle of 0.02249719 as the BAF is 5 in Simard's dataset (Simard et al., 2019). Then, the AGB of individual tree was scaled up at a hectare scale, multiplied by corresponding tree density. Finally, the scaled AGB of single trees was summed at that site to yield plot-level AGB.

Table 4-2. Allometric equation for mangrove AGB estimation, where ρ , AGB, D, and H represents wood density (g/cm³), AGB (kg), DBH (cm) and canopy height (m), respectively.

Species	Equation	Region	Reference	Wood density (g/cm³)
A. germinans R. mangle L. racemosa C. erectus P. rhizophorae	$AGB = 0.0673 \times (\rho D^2 H)^{0.976}$	Pantropical	Chave et al. (2014)	0.67 0.84 0.6 0.69 0.75

4.2.6 Allometric modelling of plot-level biomass and canopy height

The relationship of plot level AGB against canopy height is determined by a power-law function of $M = \alpha X^{\beta}$, where M and X denote plot level AGB and canopy height, respectively, and α , β are the fitted parameters using field measurements. Plot level canopy height can be mean, maximum and crown size or basal area weighted mean height (Simard et al., 2019; Simard et al., 2006, 2008). This study introduced maximum plot canopy height into plot level biomass-height allometry as maximum canopy height is a strong predictor of AGB where larger trees contribute a greater proportion of the AGB within the plots (Duncanson et al., 2022).

The power-law function was linearized as $\ln AGB = a + \beta \ln H_{max}$, where $a = \ln \alpha$, H_{max} is maximum canopy height in each plot. Ordinary Least Squares (OLS) was used to fit this regression model by

minimizing the sum of squared residuals. However, there is a systematic bias leading to the AGB underestimation when log-transformation is converted back to original units (Baskerville, 1972). Hence, Baskerville (1972) introduced a correction factor (CF) to the conversion of logarithmic estimates to unbiased arithmetic estimation; $CF = exp\left(\frac{\sigma^2}{2}\right)$, where σ^2 is sample variance of the logarithmic regression equation. The unbiased σ^2 estimate is $\widehat{\sigma}^2 = \frac{RSS}{m}$, where RSS stands for the sum of squared residuals and m is residual degree of freedom (Clifford et al., 2013). The CF was applied to the AGB estimation in this study. Therefore, the unbiased AGB estimation is $\widehat{AGB} = exp\left(\widehat{\ln \alpha} + \widehat{\beta} \ln H_{max} + \frac{RSS}{2 \cdot m}\right)$, where \widehat{AGB} is in the arithmetic unit (Mg/ha) for a given H_{max} with the regressed constant $\widehat{\ln \alpha}$ and coefficient $\widehat{\beta}$.

Applying this method to the plot-level AGB estimates across the Americas, derived from field inventory data using the allometric equation in **Table 4-2**, the regression model was obtained as:

$$\ln AGB = 0.33 + 1.49 \times \ln H_{max} \quad (R^2 = 0.67, p < 0.001)$$
 (Equation 4.1)

which, after incorporating the correction factor, yields the power-law function:

$$AGB = 1.65 \times H_{max}^{1.49}$$
 (Equation 4.2)

with a root mean squared error (RMSE) of 92.86 Mg/ha and an R² of 0.36. This equation was subsequently applied to GEDI canopy height observations for footprint-based AGB estimates (**Figure 4-3**).

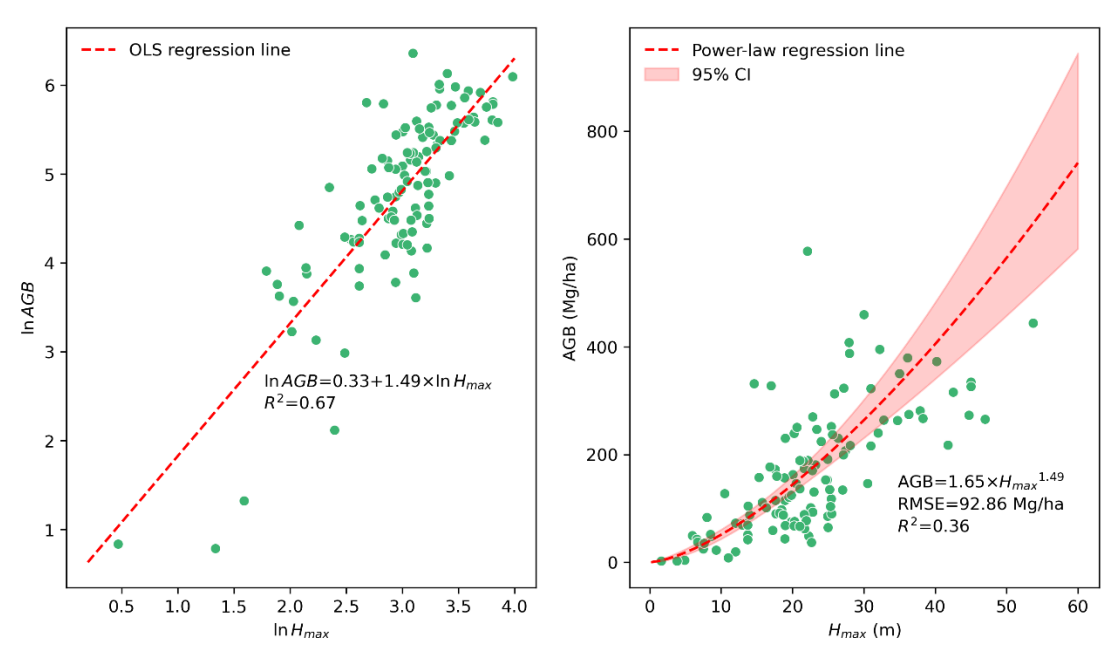


Figure 4-3. Crossplot and model-fit of aboveground biomass as a function of maximum canopy height (H_{max}) for the field plots. OLS linear regression model with logarithmic transformation (*left*); Power-law function in arithmetic unit transformed from linear model in logarithmic unit including the correction factor (*right*).

4.2.7 Random Forests regression model

Random Forests (RF) is a type of supervised machine learning which uses ensemble learning methods (i.e., Bagging, short for Bootstrap Aggregating) to solve classification or regression problems. The model runs by constructing a number of decision trees at the training stage and outputting the mean or mode of prediction of the individual trees for regression or classification tasks (Breiman, 2001). Random forests perform well with high accuracy, robustness, and efficiency in dealing with high-dimensional data. However, RF is not able to extrapolate from the training inputs as the predictions are the average of observed labels (Simard et al., 2019).

Random Forests has proved practical and efficient in mangrove AGB estimation (e.g., Ghosh et al., 2021; Hu et al., 2020; Prakash et al., 2022; Zhu et al., 2020) and was used in this study to estimate the AGB of the study area, implemented using Google Earth Engine (GEE). The median composite of Planet's NICFI mosaics across the Americas in 2020 was used as the input to estimate and map mangrove AGB. As such, four original bands (i.e., blue, green, red and near infrared) of Planet's NICFI mosaics and 17 derived vegetation spectral indices were considered as predictor variables in RF regression model (**Table 4-3**). These spectral indices are correlated with vegetation structure, coverage and health status, used in mangrove research (Gupta et al., 2018; Tran et al., 2022). Additionally, 20 environment variables that can influence mangrove AGB (Rovai et al., 2021; Simard et al., 2019) were also considered as predictor variables (**Table 4-4**). Since these environment variables are 1 km rasterized datasets containing gaps, the neighbouring two pixels in all directions were averaged to interpolate the gaps.

First, the biomass-height allometry was also applied to all the filtered GEDI observations of RH98 (relative height at the 98th percentile), which is considered a more reliable metric for maximum canopy height, for GEDI footprint-based AGB estimates. 119,175 out of 139,904 GEDI footprints were divided into 'train' (80%) and a hold-out 'test' (20%) dataset after the elimination of null data. This was done in a stratified manner by binning footprint-based AGB estimates into four 25th percentile bins. Then, apart from four original bands of Planet NICFI mosaic, the predictor variables include 17 derived vegetation spectral indices correlated with vegetation structure, coverage and health status used in mangrove research (Gupta et al., 2018; Tran et al., 2022), and 20 bioclimatic variables considered as environmental factors to influence mangrove AGB (Rovai et al., 2021; Simard et al., 2019). Recursive Feature Elimination (RFE) and Grid Search with a 5-fold cross-validation were carried out for the determination of optimal predictor variables and hyperparameters that yielded the most accurate RF regression model. Within the 5-fold cross-validation, the 'train' dataset was further divided into training and validation in the ratio of 4:1 in terms of the estimated AGB. Finally, the hold-out 'test' dataset was used to assess the performance of RF regression model.

Table 4-3. The formulae of spectral vegetation indices used in the RF regression model.

Acronym	Vegetation index	Formula	Reference
NDVI	Normalized Difference	NIR - RED	Rouse et al.
NDVI	Vegetation Index	$\overline{NIR + RED}$	(1973)
	Triangular Vegetation		Broge and
TVI	Index	$0.5 \times [120 \times (NIR - G) - 200 \times (R - G)]$	Leblanc
			(2001)
NDWI	Normalized Difference	$\underline{GREEN-NIR}$	Gao (1996)
	Water Index	$\overline{GREEN + NIR}$	` ,
CMRI	Combined Mangrove	NDVI - NDWI	Gupta et al.
	Recognition Index	NID CDEEN	(2018)
GNDVI	Green NDVI	NIR - GREEN	Gitelson et
	T 1 137 4 4	NIR + GREEN	al. (1996)
EVI	Enhanced Vegetation	$2.5 \times \frac{NIR - RED}{NIR + 6 \times RED - 7.5 \times BLUE + 1}$	Huete et al.
	Index	$NIR + 6 \times RED - 7.5 \times BLUE + 1$	(2002)
MTMO	Modified Triangular	1.5 × (NIK - GREEN) - 2.5 × (RED - GREEN)	Haboudane
MTVI2	Vegetation Index 2	$1.5 \times \frac{1.2 \times (NIR - GREEN) - 2.5 \times (RED - GREEN)}{\sqrt{(2 \times NIR + 1)^2 - (6 \times NIR - 5 \times \sqrt{RED}) - 0.5)}}$	et al. (2004)
		N NIR	Jordan
SR1	Simple Ratio 1	RED	(1969)
CD 2	C' I D ' A	NIR	()
SR2	Simple Ratio 2	\overline{GREEN}	-
SR3	Simple Ratio 3	NIR	_
SKJ	Simple Ratio 5	\overline{BLUE}	_
	M-4:6:-4 C:1- D-4:-	$\frac{NIR}{DED} - 1$	
MSR	Modified Simple Ratio	NID	Chen (1996)
	(MSR)	$rac{NIR}{RED} - 1 \ \sqrt{rac{NIR}{RED}} + 1$	
CATH	Soil Adjusted Vegetation		II (1000)
SAVI	Index (SAVI)	$\frac{NIR - RED}{NIR + RED + L} \times (1 + L), L = 0.5$	Huete (1988)
GARI	Green Atmospherically	$NIR - [GREEN - 1.7 \times (BLUE - RED)]$	Gitelson et
UAKI	Resistant Index	$\overline{NIR + [GREEN - 1.7 \times (BLUE - RED)]}$	al. (1996)
OSAVI	Optimized Soil Adjusted	NIR-RED	Rondeaux et
	Vegetation Index	$\overline{NIR + RED + 0.16}$	al. (1996)
CVI	Chlorophyll Vegetation	$NIR \times RED$	Vincini et al.
CVI	Index	GREEN ²	(2007)
ARVI	Atmospherically Resistant	$NIR - 2 \times RED + BLUE$	Kaufman and
AICVI	Vegetation Index	$\overline{NIR + 2 \times RED - BLUE}$	Tanre (1992)
TDVI	Transformed Difference	$1.5 \times \frac{NIR - RED}{}$	Bannari et al.
1011	Vegetation Index	$1.5 \times \frac{1.5 \times \sqrt{NIR^2 + RED + 0.5}}{\sqrt{NIR^2 + RED + 0.5}}$	(2002)

Table 4-4. Environment variables included in the RF regression model.

Alias	Variable	Units	Period	Resolution	Source
Bio-1	Annual Mean Temperature	°C	1970-2000	~1x1 km	Fick and Hijmans (2017)
Bio-2	Mean Diurnal Range (Mean of monthly (max temp - min temp))	$^{\circ}\mathrm{C}$	1970-2000	~1x1 km	Fick and Hijmans (2017)
Bio-3	Isothermality (Var2/Var7) (×100)	-	1970-2000	~1x1 km	Fick and Hijmans (2017)
Bio-4	Temperature Seasonality (standard deviation ×100)	°C	1970-2000	~1x1 km	Fick and Hijmans (2017)
Bio-5	Max Temperature of Warmest Month	$^{\circ}\mathrm{C}$	1970-2000	~1x1 km	Fick and Hijmans (2017)
Bio-6	Min Temperature of Coldest Month	°C	1970-2000	~1x1 km	Fick and Hijmans (2017)
Bio-7	Temperature Annual Range (Var5 - Var6)	$^{\circ}\mathrm{C}$	1970-2000	~1x1 km	Fick and Hijmans (2017)
Bio-8	Mean Temperature of Wettest Quarter	°C	1970-2000	~1x1 km	Fick and Hijmans (2017)
Bio-9	Mean Temperature of Driest Quarter	°C	1970-2000	~1x1 km	Fick and Hijmans (2017)
Bio-10	Mean Temperature of Warmest Quarter	$^{\circ}\mathrm{C}$	1970-2000	~1x1 km	Fick and Hijmans (2017)
Bio-11	Mean Temperature of Coldest Quarter	$^{\circ}\mathrm{C}$	1970-2000	~1x1 km	Fick and Hijmans (2017)
Bio-12	Annual Precipitation	mm	1970-2000	~1x1 km	Fick and Hijmans (2017)
Bio-13	Precipitation of Wettest Month	mm	1970-2000	~1x1 km	Fick and Hijmans (2017)
Bio-14	Precipitation of Driest Month	mm	1970-2000	~1x1 km	Fick and Hijmans (2017)
Bio-15	Precipitation Seasonality (Coefficient of Variation)	mm	1970-2000	~1x1 km	Fick and Hijmans (2017)
Bio-16	Precipitation of Wettest Quarter	mm	1970-2000	~1x1 km	Fick and Hijmans (2017)
Bio-17	Precipitation of Driest Quarter	mm	1970-2000	~1x1 km	Fick and Hijmans (2017)
Bio-18	Precipitation of Warmest Quarter	mm	1970-2000	~1x1 km	Fick and Hijmans (2017)
Bio-19	Precipitation of Coldest Quarter	mm	1970-2000	~1x1 km	Fick and Hijmans (2017)
ET	Annual Evapotranspiration	mm	2020	~1x1 km	Senay et al. (2020)

4.2.8 Comparisons between mangrove AGB estimates based on remote sensing

The most recently available global AGB product developed by the European Space Agency (ESA) Climate Change Initiative (CCI) for 2020 at 100 m resolution, Version 4 (Santoro and Cartus, 2023) as well as GEDI L4B Version 2 product for 2019 – 2021 at 1 km resolution (Duncanson et al., 2022) were used for inter-comparisons. Both biomass products are not specific to mangroves but have a global coverage. The

ESA CCI biomass map was generated using spaceborne SAR (Synthetic Aperture Radar) data, i.e., Sentinel 1A/B and ALOS-2 PALSAR-2 (Advanced Land Observing Satellite-2 Phased Array type L-band Synthetic Aperture Radar-2) in addition to GEDI data. A globally consistent biomass retrieval framework for ESA's GlobBiomass Project was deployed to develop the CCI AGB retrieval algorithm—CORE, merging the biomass estimates from BIOMASAR-C and -L algorithms resampled at 100 m (Santoro et al., 2023). The GEDI L4B product is gridded data that represents mean AGBD within the borders of each 1 km cell, where AGB was predicted by applying 13 pretrained allometric models over global categorized strata for GEDI RH metrics (Healey et al., 2023). In order to align the pixel resolution, the resulting AGB prediction map was resampled to average pixel values at 100 m and 1 km, whereby nearly 50,000 and 25,000 pixel values were sampled for inter-comparisons with ESA CCI biomass and GEDI L4B biomass maps, respectively.

4.3 Results

4.3.1 Determination of the optimal number of variables and hyperparameters

When the number of selected variables reached 20 or more based on the results of RFE with 5-fold CV, the RMSE only exhibited subtle changes as the curve turned to be flat. 29 out of 41 variables were identified as the optimal predictor variables (**Figure 4-4a**). Among these variables, Temperature Seasonality showed the highest importance to the model performance, followed by GARI and green band (G) (**Figure 4-4b**). When the selected 29 variables were used in the Grid Search with 5-fold CV, a higher 'number of trees' and a smaller 'minimum leaf population' resulted in a higher R² (**Figure 4-5**). As a large number of decision trees grow and develop with numerous 'leaf nodes' individually, the increase in R² becomes more computation-intensive without significantly optimizing the regression coefficient. Considering the trade-off between R² and training time, the hyperparameters of 'number of trees' and 'minimum leaf population' were set to 100 and 4, respectively.

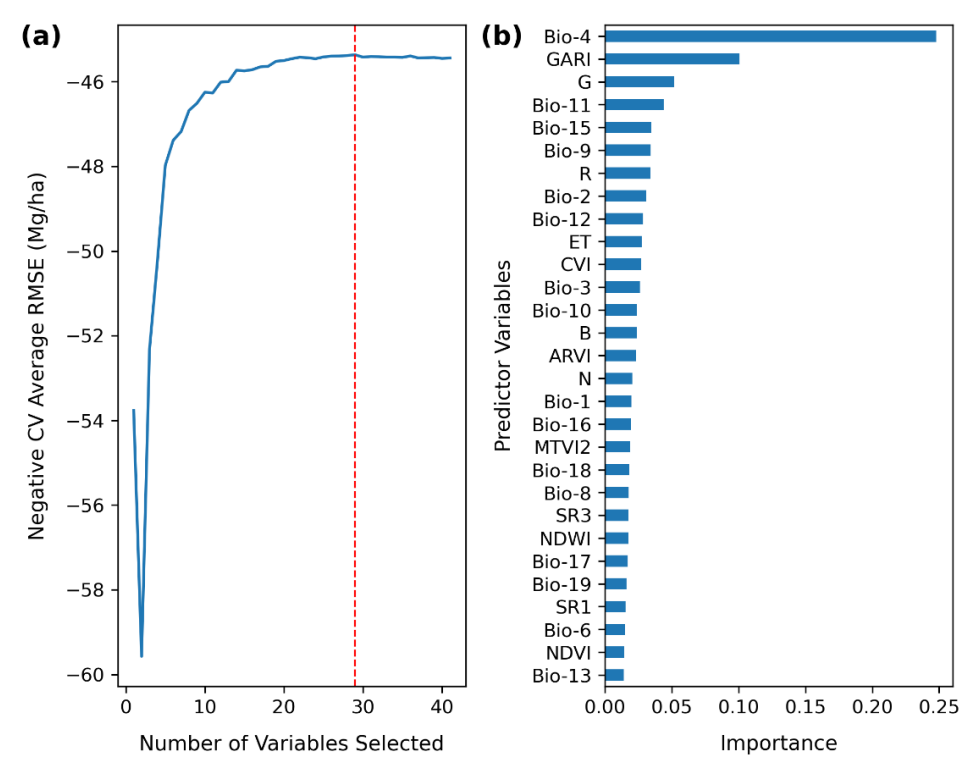


Figure 4-4. RFE with 5-fold CV results. (a) the change in negative RMSE as the number of selected predictor variables increases, where the red dash line indicates the lowest RMSE is obtained when the number is 29; (b) the feature importance of selected 29 predictor variables of the best performance.

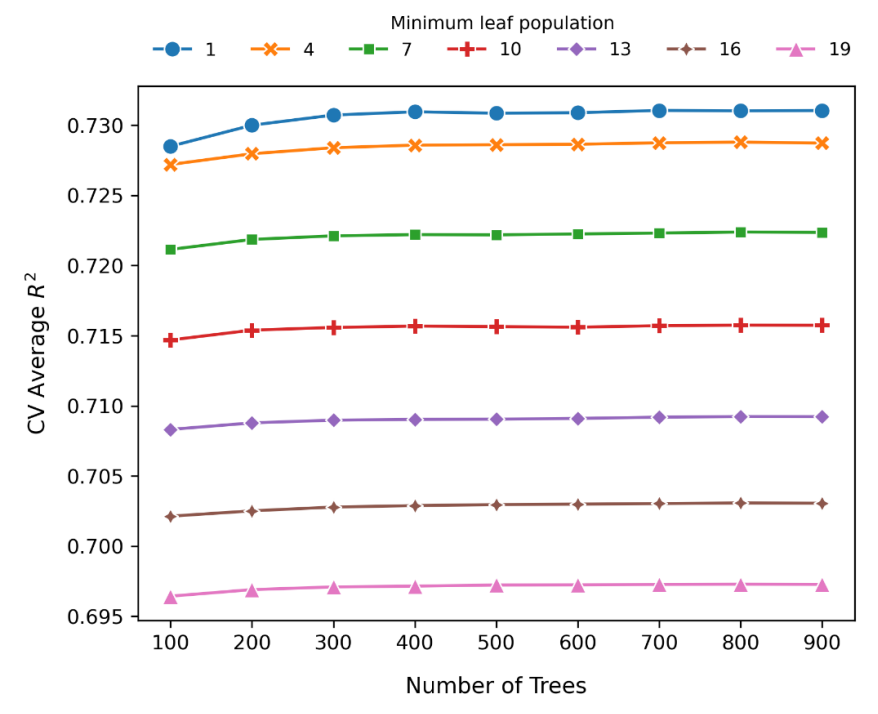


Figure 4-5. The results of Grid Search with 5-fold CV for RF regression hyperparameter tuning.

4.3.2 RF model performance assessment

The remaining 20% of GEDI footprint-based AGB estimates were used to validate the proposed approach for mangrove AGB estimation in 2020. The R^2 between predicted and observed AGB was 0.72 with the

RMSE of 37.24 Mg/ha. The proposed AGB estimation approach underestimated mangrove AGB at high values (>100 Mg/ha) and overestimated AGB densities at low values (<100 Mg/ha). However, there was high agreement in low mangrove AGB (<50 Mg/ha) (**Figure 4-6**).

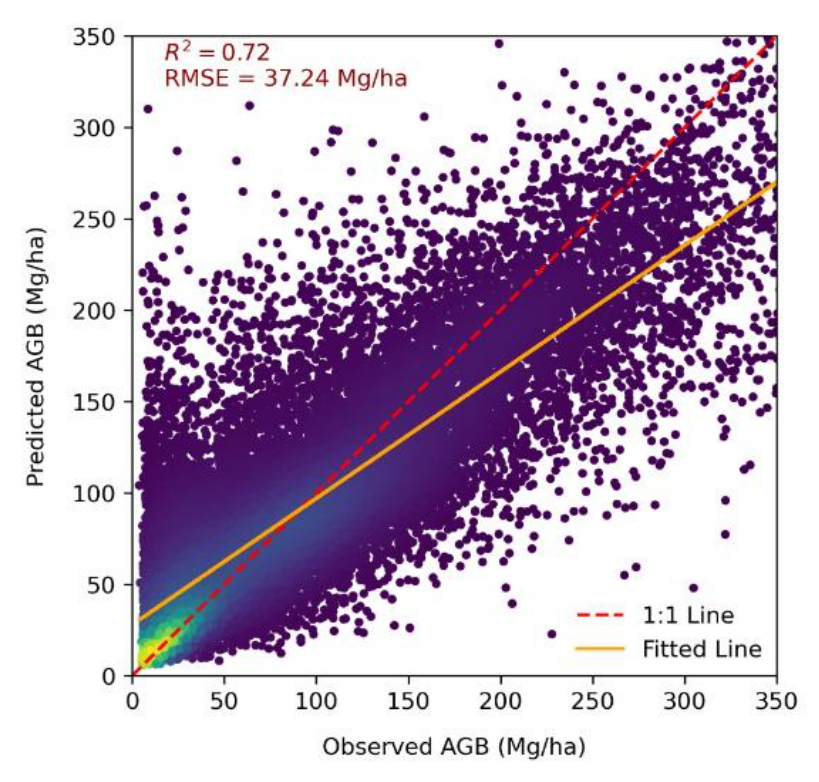


Figure 4-6. Validation of mangrove AGB estimated model. The density plot changes from purple to yellow with increasing data point density.

4.3.3 Mangrove AGB estimation in 2020 over the Americas

Mangrove AGB estimates in 2020 totalled 362 Tg (1 Tg = 10^6 Mg). When aggregated to 1° grid cells, the maximum was 19.10 Tg and the mean AGB was 0.97 Tg. Most AGB was distributed latitudinally across the areas between 2° S and 11° N, and longitudinally between 44° W and 62° W as well as 77° W and 83° W. Four regions with high AGB distribution were further investigated at a resolution of 4.77 m, showing pixel-level mangrove AGB estimation (**Figure 4-7**).

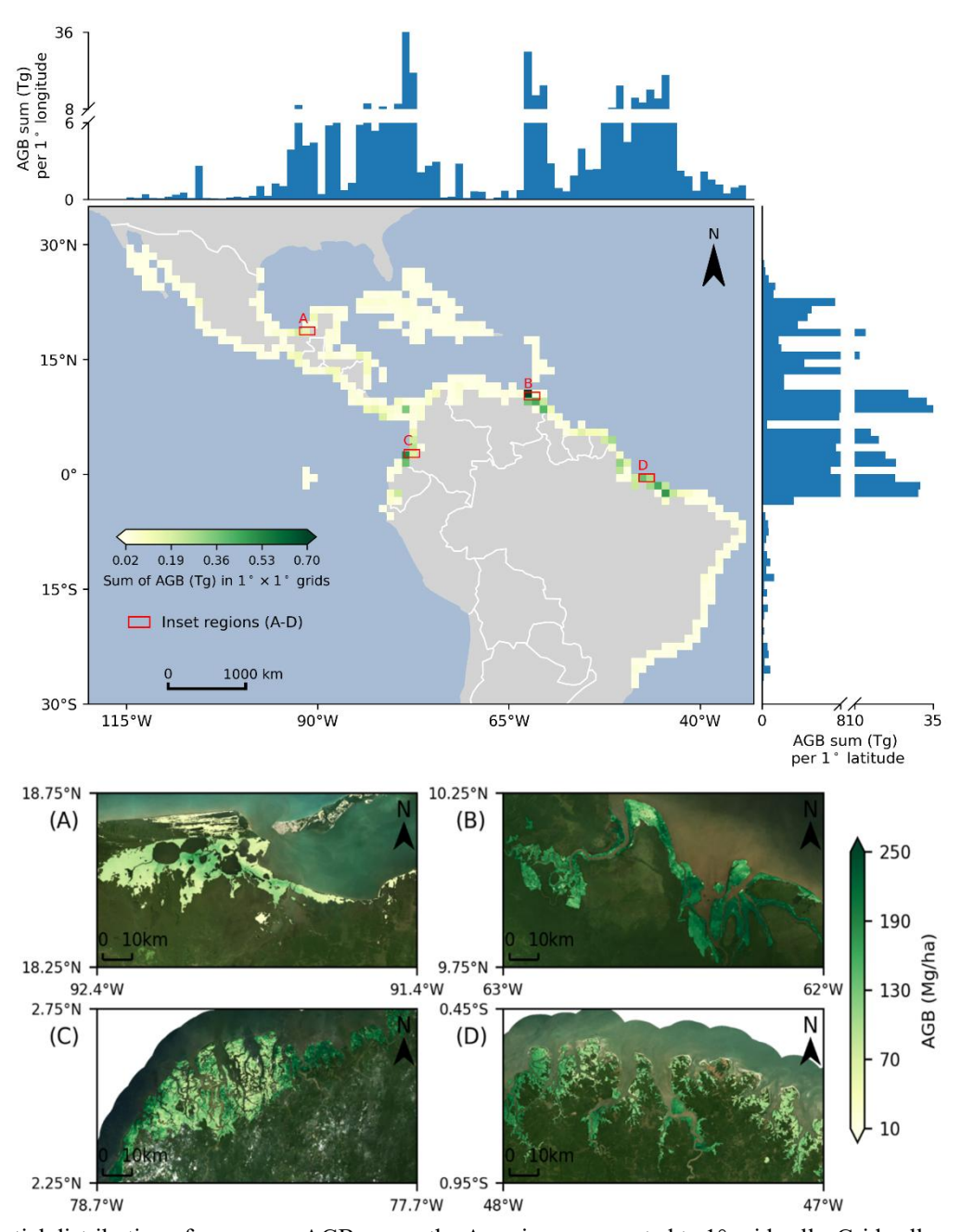


Figure 4-7. Spatial distribution of mangrove AGB across the Americas aggregated to 1° grid cells. Grid cells are coloured with darker green indicating higher AGB aggregation. The histograms along the top and right panels show the longitudinal and latitudinal distributions of AGB, respectively. Red boxes (A–D) indicate regions that are enlarged in bottom figures to provide zoom-in views: A, Términos Lagoon, Mexico; B, Columbus Channel, Venezuela; C, Sanquianga National Natural Park, Colombia; and D, Tracuateua Marine Extractive Reserve, Brazil.

Total AGB of mangroves across the Americas (excluding United States of America, Puerto Rico, British Virgin Islands, and Virgin Islands) was 362 Tg. Brazil, with the largest mangrove coverage, accounted for the highest total AGB representing about 31%, almost double Venezuela's contribution. In contrast, although Mexico's mangrove area was nearly twice that of Venezuela, its total AGB was only half of Venezuela's (**Table 4-5**).

		υ		,	
Country	Mangrove Area (ha)	Total AGB (Tg)	Country	Mangrove Area (ha)	Total AGB (Tg)
Brazil	1,214,880	113.4111	The Bahamas	87,485	0.8816
				,	
Venezuela	363,048	62.5112	Cayman Is.	11,590	0.7722
Colombia	311,561	46.1180	Trinidad & Tobago	6,900	0.7400
Mexico	775,477	32.2186	Haiti	20,408	0.5500
Panama	169,964	26.1182	Jamaica	7,980	0.4356
French Guiana	88,000	13.3155	Turks & Caicos Is.	20,195	0.2484
Ecuador	154,400	13.0905	Guadeloupe	3,152	0.1903
Cuba	369,516	9.7232	Martinique	1,698	0.1885
Suriname	72,178	8.2765	Peru	3,295	0.1524
Honduras	87,285	7.4332	Netherlands Antilles	2,697	0.1008
Nicaragua	94,123	6.5970	Antigua & Barbuda	1,301	0.0694
Costa Rica	41,284	5.2722	St. Lucia	158	0.0166
Guatemala	31,953	3.4938	Grenada	134	0.0144
El Salvador	37,835	3.4046	Aruba	116	0.0039
Guyana	21,436	3.1462	St. Vincent & the Grenadines	43	0.0036
Belize	33,648	1.2477	St. Kitts & Nevis	65	0.0027
Dominican Republic	11,540	0.8900	Barbados	12	0.0012

Table 4-5. Mangrove AGB estimates summarised by country.

4.3.4 Inter-comparison of mangrove AGB estimates

Comparisons between the AGB estimates and ESA CCI biomass and GEDI L4B gridded biomass maps for 2020 show good consistency in low AGB (<50 Mg/ha), although observed R² is less than 0.5 from both comparisons (**Figure 4-8**). Compared to ESA CCI biomass estimates, GEDI L4B biomass estimation exhibits better alignment and consistency with the estimated mangrove biomass. However, the proposed methodology tends to underestimate mangrove AGB for high AGB areas.

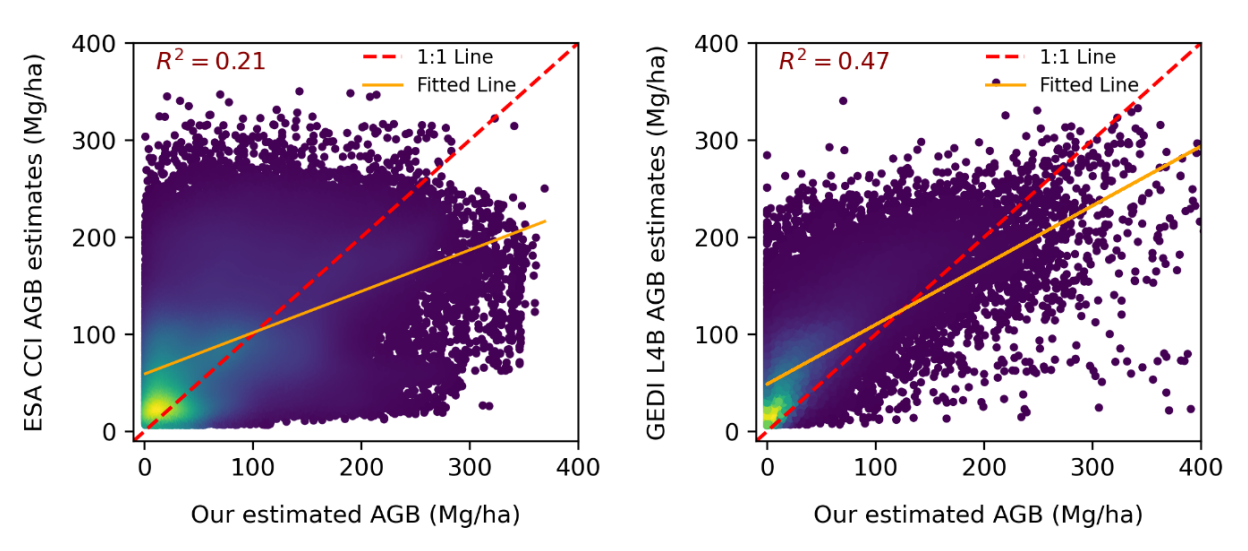


Figure 4-8. Comparisons between the AGB estimation and ESA CCI biomass (left) as well as GEDI L4B gridded biomass (right) maps for 2020, respectively. The density plot is colour coded as colour changes from purple to yellow for increasing density of data points.

4.4 Discussion

4.4.1 Variations of country-level mangrove AGB estimates

In this study, high-resolution (4.77 m) mangrove AGB estimates across the Americas were generated using Planet NICFI mosaics, providing one of the first continental-scale assessments at such a fine resolution. The results reveal total mangrove AGB of 362 Tg in the Americas, but this spatially explicit mapping highlights the strong spatial heterogeneity of mangrove AGB between countries (**Table 4-5**).

The significant variation in country-level mangrove AGB across the Americas reflects the interplay of multiple drivers. Brazil dominates the continental AGB stock with 113.41 Tg accounting for 31% of the total, due to its extensive mangrove extent (1.21 million ha) and the high productivity of the Amazon-influenced coast. Mangrove forests along Amazon Microtidal Mangrove Coast (AMMC) receive abundant rainfall and nutrient-rich river discharge, characterised by the tallest and most carbon-rich mangroves (Kauffman et al., 2018a). Total AGB and carbon accumulation reach their maximum values along the AMMC and show a steady decline with increasing latitude (de Lacerda et al., 2022). Previous studies reported maximum AGB values ranging from 290 to 451 Mg/ha for these mangrove forests (de Lacerda et al., 2022), while this study yielded maximum estimates of 318 Mg/ha, broadly consistent with the lower end of this range. In northeastern Brazil, climatic factors strongly constrain semiarid mangroves, with mean aboveground carbon biomass measured at 70 Mg C/ha (Kauffman et al., 2018b).

Mexico represents the second largest contributor to continental mangrove AGB but exhibits a strong west-east gradient. Mangrove forests along the Gulf of Mexico and Yucatán Peninsula benefit from humid conditions and freshwater inflows, sustaining tall stands, whereas mangroves on the drier Pacific coast are stunted and biomass-poor due to cold temperature and aridity (Ávila-Acosta et al., 2024; Ezcurra et al., 2016; Guerra-Santos et al., 2014; Hutchison et al., 2014). Additionally, recurrent hurricanes in the northern Pacific region limit long-term biomass accumulation by repeatedly resetting canopy structure (Vizcaya-Martínez et al., 2022).

While climate and geomorphology explain much of the large-scale variation, disturbance regimes and governance account for many of the country-level differences. The Caribbean and Pacific coasts are repeatedly affected by hurricanes and tropical storms, which limit long-term biomass accumulation (Krauss and Osland, 2020). Also, where effective protection policies are implemented, such as in Trinidad & Tobago, where two of the largest mangrove areas are officially protected (Juman and Hassanali, 2013), AGB per hectare can reach 107 Mg/ha despite the country's relatively small mangrove extent.

4.4.2 Feature importance of environmental variables

Initially, 41 predictor variables were identified as correlated with mangrove AGB distribution, including 21 spectral variables and 20 environmental variables. Among these, 29 variables were selected through RFE with a 5-fold cross validation, where nearly all the environmental variables were included except for Max Temperature of Warmest Month (Bio-5), Temperature Annual Range (Bio-7) and Precipitation of Driest Month (Bio-14). From the included variables, Temperature Seasonality (Bio-4) contributed most to the RF regression model. The feature importance of environmental variables here agrees with Rovai et al. (2021) and Simard et al. (2019), who found temperature, precipitation and evapotranspiration to significantly impact the variation of mangrove AGB. Although the bioclimatic variables are reanalysed climate data spanning 1970 to 2000, long-term climatic impacts still influence the environmental settings of mangrove forests. Across the Americas, the extent of mangrove forests between 2000 and 2020 has been primarily driven by natural expansion and retraction (FAO, 2023). However, as mangrove forests can be suppressed by high salinity and low nutrient and sediment deposition which tides largely regulate (Balke and Friess, 2016; Vovides et al., 2018), tidal amplitude and duration are recognized as important factors controlling global mangrove AGB (Rovai et al. 2021) and expected to be included in future studies.

4.4.3 AGB estimation uncertainty

The primary advantage of the proposed approach for AGB estimation is to generate finer-scale mangrove AGB maps using VHR imagery. Compared with existing products for the same period (i.e., ESA CCI for 2020 and GEDI L4B for 2019 – 2021), this study demonstrates an improved capability to capture local-scale AGB variation (**Figure 4-9**). However, a tendency to underestimate AGB was observed in dense vegetation areas where single tree crowns may exceed the 4.77m pixel size, while higher agreement among products was achieved in low-AGB regions (**Figure 4-8**).

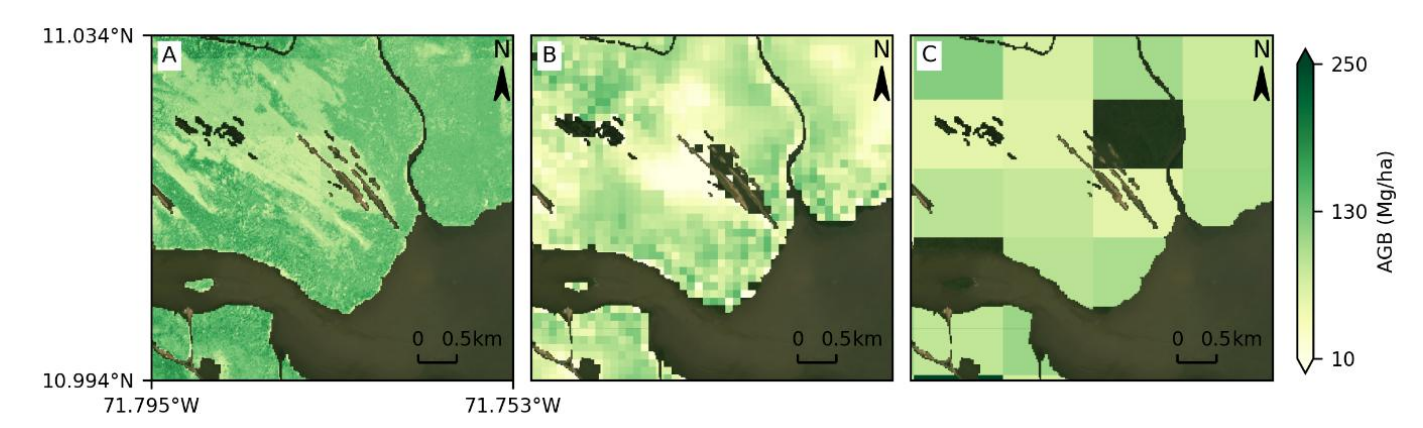


Figure 4-9. Visualization of AGB estimation maps clipped to mangrove areas in Rio Limbo, Venezuela. A, this study; B, ESA CCI biomass map; C, GEDI L4B gridded biomass map.

AGB estimation derived from the RF regression algorithm are the values averaged over an ensemble of decision trees, while the standard deviation (SD) of these results shows the uncertainty (Figure 4-10). Several sources of uncertainty were identified: (i) the error associated with the power-law function relating plot-level AGB to maximum canopy height, (ii) errors in GEDI L2A canopy height observations, and (iii) RF regression error. Importantly, errors from the power-law function and GEDI measurements were not propagated to per-pixel uncertainty of the AGB estimation. Field inventory data compiled from Simard et al. (2019), including plots in Mexico, were incorporated into developing the power-law function relating plot-level AGB to maximum canopy height, and an RMSE of 92.86 Mg/ha was obtained. However, this relationship is not fully representative of mangrove stands across the Americas due to limited availability of inventory data. Additionally, the GEDI Level 2A product is reported to have an uncertainty (i.e., RMSE) of 4.4 m and an underestimation bias of 1.0 m (mean error) (Lang et al., 2022). RH98 was used instead of RH100 as the maximum height metric, since RH98 has been shown to be more stable and reliable (Blair and Hofton, 1999) and is widely recognised as a significant predictor in AGB estimation (Duncanson et al., 2022). Given that mangrove forests are normally dense and exhibit zonal distribution with relatively uniform canopy heights, RH98 was considered a reliable and representative metric for this study.

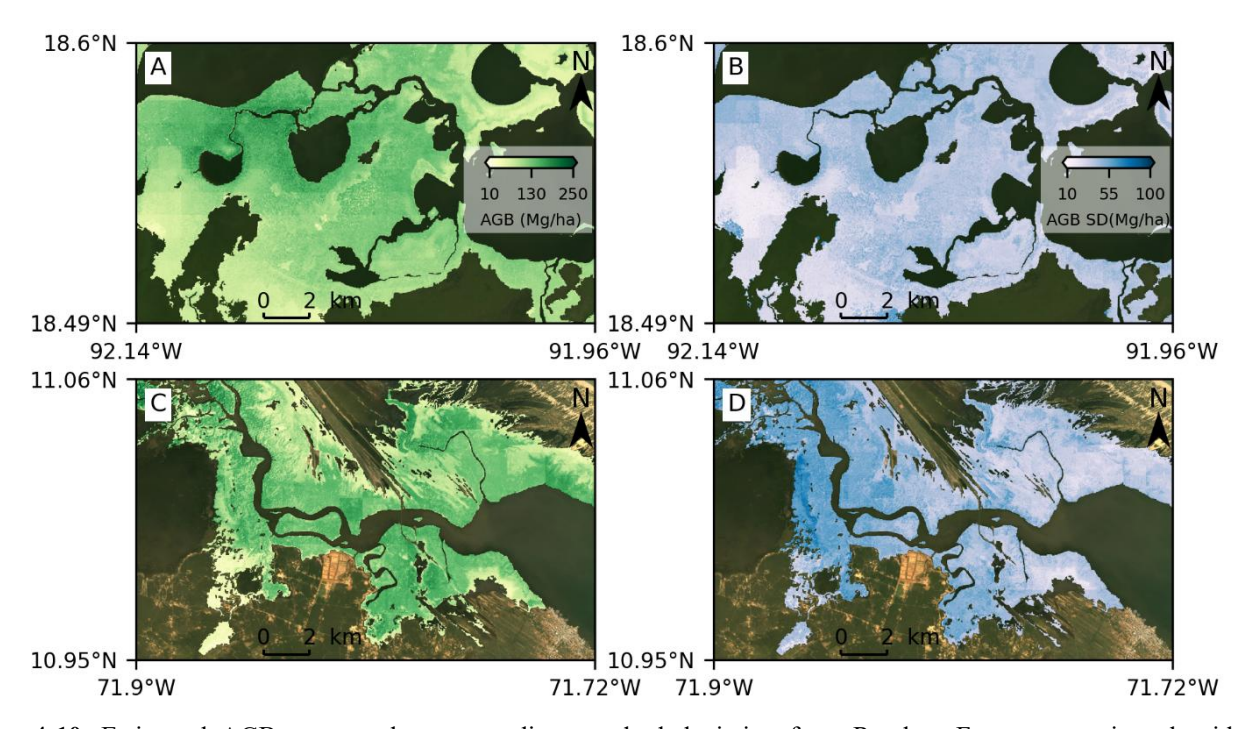


Figure 4-10. Estimated AGB maps and corresponding standard deviation from Random Forest regression algorithm for mangrove areas in (A-B) Términos Lagoon, Mexico, and (C-D) Rio Limon, Venezuela.

4.4.4 Implications for mangrove management and policy

This study generates high-resolution AGB estimation map, improving the understanding of mangrove carbon dynamics and providing actionable insights for management and policy. In the context of the

imperative need to protect mangroves as critical blue carbon ecosystems, the ability to capture spatial heterogeneity in biomass distribution has several implications. First, carbon accounting and climate policy can be enhanced by incorporating fine-scale biomass estimates into national greenhouse gas inventories and climate mitigation strategies. Many countries in the Americas are engaged in initiatives such as REDD+ and nationally determined contributions (NDCs) under the Paris Agreement, where accurate and spatially explicit carbon data are essential for reporting and verification (Alongi, 2020; Taillardat et al., 2018). In particular, this study offers a transferable methodology that can improve transparency and consistency in carbon stock estimation.

Second, conservation planning and land management can benefit from recognising high AGB hotspots that justify prioritisation for protection. Meanwhile, areas with lower biomass or evidence of degradation can be targeted for restoration, especially where mangroves provide coastal protection services against storms and sea-level rise (Spalding et al., 2014; Worthington and Spalding, 2018). These insights can support mangrove area management at both national and local levels, ensuring that limited resources are allocated effectively.

Finally, ecosystem service assessments of mangroves can be improved. High-resolution AGB maps can be integrated with hydrological, geomorphological, and socioeconomic data to quantify the co-benefits of mangrove ecosystems, including biodiversity conservation, sediment stabilisation, and fisheries support (Friess et al., 2019; Sanderman et al., 2018). Therefore, decision-makers can be informed about trade-offs and synergies between development and conservation.

4.5 Conclusions

This study developed a novel methodology that deploys plot level biomass-height allometry and Random Forests regression algorithm with field inventory measurements, GEDI spaceborne LiDAR data, high-resolution Planet NICFI satellite mosaics and environmental variables for high spatial resolution mangrove AGB estimation and mapping over the Americas. In this methodology, the plot-level biomass-height allometry was fitted by OLS with field inventory data across the Americas and applied to GEDI canopy height observations as GEDI data footprints were considered 25 m circular plots. Then, GEDI-based AGB estimates were used to train and validate RF regression model with the spectral and environmental variables. The most efficient RF model was identified using Recursive Feature Elimination and Grid Search both with a 5-fold cross-validation. It was found that 29 out of 41 variables were selected as the optimal feature combination, where temperature seasonality contributed most for the model performance. Compared with other AGB products in 2020, i.e., ESA CCI biomass and GEDI L4B gridded biomass maps, the resulting

map shows the capacity of finer AGB estimation as there is a higher agreement in low mangrove AGB (<50 Mg/ha). Overall, the proposed methodology of high-resolution mangrove AGB mapping shows the feasibility of the finer mangrove investigation and has the potential to advance highly resolved carbon modelling. Additionally, this study highlights that high-resolution AGB mapping is a scientific advance and also a practical tool to guide climate mitigation, conservation, and sustainable management of mangroves in the Americas and beyond.

References

- Akbar, M.R., Arisanto, P.A.A., Sukirno, B.A., et al., 2020. Mangrove vegetation health index analysis by implementing NDVI (normalized difference vegetation index) classification method on sentinel-2 image data case study: Segara Anakan, Kabupaten Cilacap. IOP Conf. Ser.: Earth Environ. Sci. 584, 012069. https://doi.org/10.1088/1755-1315/584/1/012069
- Alongi, D.M., 2020. Global Significance of Mangrove Blue Carbon in Climate Change Mitigation. Sci 2, 67. https://doi.org/10.3390/sci2030067
- Ávila-Acosta, C.R., Domínguez-Domínguez, M., Vázquez-Navarrete, C.J., et al., 2024. Aboveground Biomass and Carbon Storage in Mangrove Forests in Southeastern Mexico. Resources 13, 41. https://doi.org/10.3390/resources13030041
- Baccini, A., Goetz, S.J., Walker, W.S., et al., 2012. Estimated carbon dioxide emissions from tropical deforestation improved by carbon-density maps. Nature Clim Change 2, 182–185. https://doi.org/10.1038/nclimate1354
- Balke, T., Friess, D.A., 2016. Geomorphic knowledge for mangrove restoration: a pan-tropical categorization. Earth Surface Processes and Landforms 41, 231–239. https://doi.org/10.1002/esp.3841
- Bannari, A. et al., 2002. Transformed difference vegetation index (TDVI) for vegetation cover mapping, in: IEEE International Geoscience and Remote Sensing Symposium. Presented at the IEEE International Geoscience and Remote Sensing Symposium, pp. 3053–3055 vol.5. https://doi.org/10.1109/IGARSS.2002.1026867
- Baskerville, G.L., 1972. Use of Logarithmic Regression in the Estimation of Plant Biomass. Can. J. For. Res. 2, 49–53. https://doi.org/10.1139/x72-009
- Blair, J.B., Hofton, M.A., 1999. Modeling laser altimeter return waveforms over complex vegetation using high-resolution elevation data. Geophysical Research Letters 26, 2509–2512. https://doi.org/10.1029/1999GL010484
- Breiman, L., 2001. Random Forests. Machine Learning 45, 5–32. https://doi.org/10.1023/A:1010933404324
- Broge, N.H., Leblanc, E., 2001. Comparing prediction power and stability of broadband and hyperspectral vegetation indices for estimation of green leaf area index and canopy chlorophyll density. Remote Sensing of Environment 76, 156–172. https://doi.org/10.1016/S0034-4257(00)00197-8
- Chave, J., Andalo, C., Brown, S., et al., 2005. Tree allometry and improved estimation of carbon stocks and balance in tropical forests. Oecologia 145, 87–99. https://doi.org/10.1007/s00442-005-0100-x

- Chave, J., Réjou-Méchain, M., Búrquez, A., et al., 2014. Improved allometric models to estimate the aboveground biomass of tropical trees. Global Change Biology 20, 3177–3190. https://doi.org/10.1111/gcb.12629
- Chen, J.M., 1996. Evaluation of Vegetation Indices and a Modified Simple Ratio for Boreal Applications.

 Canadian Journal of Remote Sensing 22, 229–242.

 https://doi.org/10.1080/07038992.1996.10855178
- Clifford, D., Cressie, N., England, J.R., et al., 2013. Correction factors for unbiased, efficient estimation and prediction of biomass from log-log allometric models. Forest Ecology and Management 310, 375–381. https://doi.org/10.1016/j.foreco.2013.08.041
- Csillik, O., Kumar, P., Mascaro, J., et al., 2019. Monitoring tropical forest carbon stocks and emissions using Planet satellite data. Sci Rep 9, 17831. https://doi.org/10.1038/s41598-019-54386-6
- Curnick, D.J., Pettorelli, N., Amir, A.A., et al., 2019. The value of small mangrove patches. Science 363, 239. https://doi.org/10.1126/science.aaw0809
- de Lacerda, L.D., Ferreira, A.C., Borges, R., Ward, R., 2022. Mangroves of Brazil, in: Das, S.C., Pullaiah, Ashton, E.C. (Eds.), Mangroves: Biodiversity, Livelihoods and Conservation. Springer, Singapore. https://doi.org/10.1007/978-981-19-0519-3 20
- Dubayah, R., Blair, J.B., Goetz, S., et al., 2020. The Global Ecosystem Dynamics Investigation: High-resolution laser ranging of the Earth's forests and topography. Science of Remote Sensing 1, 100002. https://doi.org/10.1016/j.srs.2020.100002
- Duncanson, L., Kellner, J.R., Armston, J., et al., 2022. Aboveground biomass density models for NASA's Global Ecosystem Dynamics Investigation (GEDI) lidar mission. Remote Sensing of Environment 270, 112845. https://doi.org/10.1016/j.rse.2021.112845
- Ezcurra, P., Ezcurra, E., Garcillán, P.P., et al., 2016. Coastal landforms and accumulation of mangrove peat increase carbon sequestration and storage. Proceedings of the National Academy of Sciences 113, 4404–4409. https://doi.org/10.1073/pnas.1519774113
- FAO, 2023. The world's mangroves 2000–2020. FAO, Rome. https://doi.org/10.4060/cc7044en
- Fatoyinbo, T., Feliciano, E.A., Lagomasino, D., et al., 2018. Estimating mangrove aboveground biomass from airborne LiDAR data: a case study from the Zambezi River delta. Environ. Res. Lett. 13, 025012. https://doi.org/10.1088/1748-9326/aa9f03
- Fick, S.E., Hijmans, R.J., 2017. WorldClim 2: new 1-km spatial resolution climate surfaces for global land areas. International Journal of Climatology 37, 4302–4315. https://doi.org/10.1002/joc.5086
- Friess, D.A., Adams, J., Andradi-Brown, D.A., et al., 2024. Mangrove forests: their status, threats, conservation and restoration, in: Reference Module in Earth Systems and Environmental Sciences. Elsevier, p. B9780323907989000317. https://doi.org/10.1016/B978-0-323-90798-9.00031-7

- Friess, D.A., Rogers, K., Lovelock, C.E., et al., 2019. The State of the World's Mangrove Forests: Past, Present, and Future. Annual Review of Environment and Resources 44, 89–115. https://doi.org/10.1146/annurev-environ-101718-033302
- Friess, D.A., Thompson, B.S., Brown, B., et al., 2016. Policy challenges and approaches for the conservation of mangrove forests in Southeast Asia. Conservation Biology 30, 933–949. https://doi.org/10.1111/cobi.12784
- Gao, B., 1996. NDWI—A normalized difference water index for remote sensing of vegetation liquid water from space. Remote Sensing of Environment 58, 257–266. https://doi.org/10.1016/S0034-4257(96)00067-3
- Ghosh, S.M., Behera, M.D., Jagadish, B., et al., 2021. A novel approach for estimation of aboveground biomass of a carbon-rich mangrove site in India. Journal of Environmental Management 292, 112816. https://doi.org/10.1016/j.jenvman.2021.112816
- Gitelson, A.A., Gritz †, Y., Merzlyak, M.N., 2003. Relationships between leaf chlorophyll content and spectral reflectance and algorithms for non-destructive chlorophyll assessment in higher plant leaves. Journal of Plant Physiology 160, 271–282. https://doi.org/10.1078/0176-1617-00887
- Gitelson, A.A., Kaufman, Y.J., Merzlyak, M.N., 1996. Use of a green channel in remote sensing of global vegetation from EOS-MODIS. Remote Sensing of Environment 58, 289–298. https://doi.org/10.1016/S0034-4257(96)00072-7
- Goldberg, L., Lagomasino, D., Thomas, N., et al., 2020. Global declines in human-driven mangrove loss. Global Change Biology 26, 5844–5855. https://doi.org/10.1111/gcb.15275
- Guerra-Santos, J.J., Cerón-Bretón, R.M., Cerón-Bretón, J.G., et al., 2014. Estimation of the carbon pool in soil and above-ground biomass within mangrove forests in Southeast Mexico using allometric equations. Journal of Forestry Research 25, 129–134. https://doi.org/10.1007/s11676-014-0437-2
- Gupta, K., Mukhopadhyay, A., Giri, S., et al., 2018. An index for discrimination of mangroves from non-mangroves using LANDSAT 8 OLI imagery. MethodsX 5, 1129–1139. https://doi.org/10.1016/j.mex.2018.09.011
- Haboudane, D., Miller, J.R., Pattey, E., et al., 2004. Hyperspectral vegetation indices and novel algorithms for predicting green LAI of crop canopies: Modeling and validation in the context of precision agriculture. Remote Sensing of Environment 90, 337–352. https://doi.org/10.1016/j.rse.2003.12.013
- Healey, S.P., Patterson, P.L., Armston, J., 2023. Algorithm Theoretical Basis Document (ATBD) for GEDI Level-4B (L4B) Gridded Aboveground Biomass Density (Version 2.0).
- Hojas Gascón, L., Ceccherini, G., García Haro, F.J., et al., 2019. The Potential of High Resolution (5 m) RapidEye Optical Data to Estimate Above Ground Biomass at the National Level over Tanzania. Forests 10, 107. https://doi.org/10.3390/f10020107

- Hu, T., Zhang, Y., Su, Y., et al., 2020. Mapping the Global Mangrove Forest Aboveground Biomass Using Multisource Remote Sensing Data. Remote Sensing 12, 1690. https://doi.org/10.3390/rs12101690
- Huete, A., Didan, K., Miura, T., et al., 2002. Overview of the radiometric and biophysical performance of the MODIS vegetation indices. Remote Sensing of Environment, The Moderate Resolution Imaging Spectroradiometer (MODIS): a new generation of Land Surface Monitoring 83, 195–213. https://doi.org/10.1016/S0034-4257(02)00096-2
- Huete, A.R., 1988. A soil-adjusted vegetation index (SAVI). Remote Sensing of Environment 25, 295–309. https://doi.org/10.1016/0034-4257(88)90106-X
- Hutchison, J., Manica, A., Swetnam, R., et al., 2014. Predicting Global Patterns in Mangrove Forest Biomass. Conservation Letters 7, 233–240. https://doi.org/10.1111/conl.12060
- Jia, M., Wang, Z., Mao, D., et al., 2023. Mapping global distribution of mangrove forests at 10-m resolution. Science Bulletin 68, 1306–1316. https://doi.org/10.1016/j.scib.2023.05.004
- Jordan, C.F., 1969. Derivation of Leaf-Area Index from Quality of Light on the Forest Floor. Ecology 50, 663–666. https://doi.org/10.2307/1936256
- Juman, R.A., Hassanali, K., 2013. Mangrove Conservation in Trinidad and Tobago, West Indies, in: Gerard Gleason, Thomas R. Victor (Eds.), Mangrove Ecosystems. Nova Science Publishers, Inc.
- Kauffman, J.B., Bernardino, A.F., Ferreira, T.O., et al., 2018a. Carbon stocks of mangroves and salt marshes of the Amazon region, Brazil. Biology Letters. https://doi.org/10.1098/rsbl.2018.0208
- Kauffman, J.B., Bernardino, A.F., Ferreira, T.O., et al., 2018b. Shrimp ponds lead to massive loss of soil carbon and greenhouse gas emissions in northeastern Brazilian mangroves. Ecology and Evolution 8, 5530–5540. https://doi.org/10.1002/ece3.4079
- Kauffman, J.B., Donato, D.C., 2012. Protocols for the measurement, monitoring and reporting of structure, biomass, and carbon stocks in mangrove forests. Center for International Forestry Research, Bogor, Indonesia.
- Kaufman, Y.J., Tanre, D., 1992. Atmospherically resistant vegetation index (ARVI) for EOS-MODIS.
 IEEE Transactions on Geoscience and Remote Sensing 30, 261–270.
 https://doi.org/10.1109/36.134076
- Kershaw, J.A., Ducey, M.J., Beers, T.W., et al., 2017. Sampling Units For Estimating Parameters, in: Forest Mensuration. John Wiley & Sons, Ltd, Chichester, UK, pp. 273–304. https://doi.org/10.1002/9781118902028
- Komiyama, A., Ong, J.E., Poungparn, S., 2008. Allometry, biomass, and productivity of mangrove forests:

 A review. Aquatic Botany, Mangrove Ecology Applications in Forestry and Coastal Zone
 Management 89, 128–137. https://doi.org/10.1016/j.aquabot.2007.12.006

- Krauss, K.W., Osland, M.J., 2020. Tropical cyclones and the organization of mangrove forests: a review. Ann Bot 125, 213–234. https://doi.org/10.1093/aob/mcz161Lagomasino, D., Fatoyinbo, T., Lee, S., et al., 2016. A Comparison of Mangrove Canopy Height Using Multiple Independent Measurements from Land, Air, and Space. Remote Sensing 8, 327. https://doi.org/10.3390/rs8040327
- Lang, N., Jetz, W., Schindler, K., et al., 2023. A high-resolution canopy height model of the Earth. Nat Ecol Evol 7, 1778–1789. https://doi.org/10.1038/s41559-023-02206-6
- Lang, N., Kalischek, N., Armston, J., et al., 2022. Global canopy height regression and uncertainty estimation from GEDI LIDAR waveforms with deep ensembles. Remote Sensing of Environment 268, 112760. https://doi.org/10.1016/j.rse.2021.112760
- Li, Q., Wong, F.K.K., Fung, T., 2021. Mapping multi-layered mangroves from multispectral, hyperspectral, and LiDAR data. Remote Sensing of Environment 258, 112403. https://doi.org/10.1016/j.rse.2021.112403
- Liu, A. et al., 2021. Performance evaluation of GEDI and ICESat-2 laser altimeter data for terrain and canopy height retrievals. Remote Sensing of Environment 264, 112571. https://doi.org/10.1016/j.rse.2021.112571
- Lucas, R., Van De Kerchove, R., Otero, V., et al., 2020. Structural characterisation of mangrove forests achieved through combining multiple sources of remote sensing data. Remote Sensing of Environment 237. https://doi.org/10.1016/j.rse.2019.111543
- Pandey, P., Kington, J., Kanwar, A., et al., 2023. Planet Basemaps for NICFI Data Program--Addendum to Basemaps Product Specification (Version 2).
- Pham, L.T.H., Brabyn, L., 2017. Monitoring mangrove biomass change in Vietnam using SPOT images and an object-based approach combined with machine learning algorithms. ISPRS Journal of Photogrammetry and Remote Sensing 128, 86–97. https://doi.org/10.1016/j.isprsjprs.2017.03.013
- Pham, T.D., Yokoya, N., Bui, D.T., et al., 2019. Remote Sensing Approaches for Monitoring Mangrove Species, Structure, and Biomass: Opportunities and Challenges. Remote Sensing 11, 230. https://doi.org/10.3390/rs11030230
- Prakash, A.J., Behera, M.D., Ghosh, S.M., et al., 2022. A new synergistic approach for Sentinel-1 and PALSAR-2 in a machine learning framework to predict aboveground biomass of a dense mangrove forest. Ecological Informatics 72, 101900. https://doi.org/10.1016/j.ecoinf.2022.101900
- Rahman, M.S., Donoghue, D.N.M., Bracken, L.J., et al., 2021. Biomass estimation in mangrove forests: a comparison of allometric models incorporating species and structural information. Environ. Res. Lett. 16, 124002. https://doi.org/10.1088/1748-9326/ac31ee
- Rodríguez-Veiga, P., Wheeler, J., Louis, V., et al., 2017. Quantifying Forest Biomass Carbon Stocks from Space. Curr Forestry Rep 3, 1–18. https://doi.org/10.1007/s40725-017-0052-5

- Rondeaux, G. et al., 1996. Optimization of soil-adjusted vegetation indices. Remote Sensing of Environment 55, 95–107. https://doi.org/10.1016/0034-4257(95)00186-7
- Rouse, J.W., Jr., Haas, R.H., Schell, J.A., et al., 1973. Monitoring Vegetation Systems in the Great Plains with ERTS, in: Proceedings of 3rd Earth Resources Technology Satellite Symposium. Greenbelt, pp. 309–317.
- Rovai, A.S., Twilley, R.R., Castañeda-Moya, E., et al., 2021. Macroecological patterns of forest structure and allometric scaling in mangrove forests. Global Ecology and Biogeography 30, 1000–1013. https://doi.org/10.1111/geb.13268
- Roy, D.P. et al., 2021. The impact of geolocation uncertainty on GEDI tropical forest canopy height estimation and change monitoring. Science of Remote Sensing 4, 100024. https://doi.org/10.1016/j.srs.2021.100024
- Ruan, L., Yan, M., Zhang, L., et al., 2022. Spatial-temporal NDVI pattern of global mangroves: A growing trend during 2000–2018. Science of The Total Environment 844, 157075. https://doi.org/10.1016/j.scitotenv.2022.157075
- Saatchi, S.S., Harris, N.L., Brown, S., et al., 2011. Benchmark map of forest carbon stocks in tropical regions across three continents. Proceedings of the National Academy of Sciences 108, 9899–9904. https://doi.org/10.1073/pnas.1019576108
- Saenger, P., Ragavan, P., Sheue, C.-R., et al., 2019. Mangrove Biogeography of the Indo-Pacific, in: Gul,
 B., Böer, B., Khan, M.A., et al. (Eds.), Sabkha Ecosystems, Tasks for Vegetation Science. Springer
 International Publishing, Cham, pp. 379–400. https://doi.org/10.1007/978-3-030-04417-6
- Saliu, I.S., Satyanarayana, B., Bin Fisol, M.A., et al., 2021. An accuracy analysis of mangrove tree height mensuration using forestry techniques, hypsometers and UAVs. Estuarine, Coastal and Shelf Science, Mangroves and People: Impacts and Interactions 248, 106971. https://doi.org/10.1016/j.ecss.2020.106971
- Salum, R.B., Souza-Filho, P.W.M., Simard, M., et al., 2020. Improving mangrove above-ground biomass estimates using LiDAR. Estuarine, Coastal and Shelf Science 236, 106585. https://doi.org/10.1016/j.ecss.2020.106585
- Sanderman, J., Hengl, T., Fiske, G., et al., 2018. A global map of mangrove forest soil carbon at 30 m spatial resolution. Environmental Research Letters 13, 055002.
- Santoro, M., Cartus, O., 2023. ESA Biomass Climate Change Initiative (Biomass_cci): Global datasets of forest above-ground biomass for the years 2010, 2017, 2018, 2019 and 2020, v4. https://doi.org/10.5285/af60720c1e404a9e9d2c145d2b2ead4e
- Santoro, M., Cartus, O., Richard, L., et al., 2023. CCI BIOMASS Algorithm theoretical basis document (version 4.0).

- Senay, G.B. et al., 2020. Operational Global Actual Evapotranspiration: Development, Evaluation, and Dissemination. Sensors 20, 1915. https://doi.org/10.3390/s20071915
- Shendryk, Y., 2022. Fusing GEDI with earth observation data for large area aboveground biomass mapping.

 International Journal of Applied Earth Observation and Geoinformation 115, 103108.

 https://doi.org/10.1016/j.jag.2022.103108
- Simard, M., Fatoyinbo, L., Smetanka, C., et al., 2019. Mangrove canopy height globally related to precipitation, temperature and cyclone frequency. Nature Geoscience 12, 40–45. https://doi.org/10.1038/s41561-018-0279-1
- Simard, M., Rivera-Monroy, V.H., Mancera-Pineda, J.E., et al., 2008. A systematic method for 3D mapping of mangrove forests based on Shuttle Radar Topography Mission elevation data, ICEsat/GLAS waveforms and field data: Application to Ciénaga Grande de Santa Marta, Colombia. Remote Sensing of Environment, Earth Observations for Terrestrial Biodiversity and Ecosystems Special Issue 112, 2131–2144. https://doi.org/10.1016/j.rse.2007.10.012
- Simard, M., Zhang, K., Rivera-Monroy, V.H., et al., 2006. Mapping height and biomass of mangrove forests in Everglades National Park with SRTM elevation data. Photogrammetric Engineering & Remote Sensing 72, 299–311.
- Slobodian, L., Vidal, A., 2023. Mangrove Law and Policy. Global Mangrove Alliance.
- Southwell, C.R., Bultman, J.D., 1971. Marine Borer Resistance of Untreated Woods Over Long Periods of Immersion in Tropical Waters. Biotropica 3, 81–107. https://doi.org/10.2307/2989709
- Spalding, M., Kainuma, M., Collins, L., 2010. World atlas of mangroves. Earthscan, London, Washington D.C.
- Spalding, M.D., Leal, M. (Eds.), 2022. The State of the World's Mangroves 2022. Global Mangrove Alliance.
- Spalding, M., McIvor, A., Tonneijck, F., et al., 2014. Mangroves for coastal defence. Guidelines for coastal managers and policy makers. Wetlands International and The Nature Conservancy 13–34.
- Stovall, A.E.L., Fatoyinbo, T., Thomas, N.M., et al., 2021. Comprehensive comparison of airborne and spaceborne SAR and LiDAR estimates of forest structure in the tallest mangrove forest on earth. Science of Remote Sensing 4, 100034. https://doi.org/10.1016/j.srs.2021.100034
- Suwa, R., Rollon, R., Sharma, S., et al., 2021. Mangrove biomass estimation using canopy height and wood density in the South East and East Asian regions. Estuarine, Coastal and Shelf Science, Mangroves and People: Impacts and Interactions 248, 106937. https://doi.org/10.1016/j.ecss.2020.106937
- Taillardat, P., Friess, D.A., Lupascu, M., 2018. Mangrove blue carbon strategies for climate change mitigation are most effective at the national scale. Biology Letters 14, 20180251. https://doi.org/10.1098/rsbl.2018.0251

- Tian, Y., Zhang, Q., Huang, H., et al., 2022. Aboveground biomass of typical invasive mangroves and its distribution patterns using UAV-LiDAR data in a subtropical estuary: Maoling River estuary, Guangxi, China. Ecological Indicators 136, 108694. https://doi.org/10.1016/j.ecolind.2022.108694
- Tran, T.V. et al., 2022. A Review of Spectral Indices for Mangrove Remote Sensing. Remote Sensing 14, 4868. https://doi.org/10.3390/rs14194868
- Twomey, A., Lovelock, C., 2024. Global spatial dataset of mangrove genus distribution in seaward and riverine margins. Sci Data 11, 306. https://doi.org/10.1038/s41597-024-03134-1
- Uddin, M.M., Abdul Aziz, A., Lovelock, C.E., 2023. Importance of mangrove plantations for climate change mitigation in Bangladesh. Global Change Biology 29, 3331–3346. https://doi.org/10.1111/gcb.16674
- UNSD, 1999. Standard country or area codes for statistical use (M49) [WWW Document]. URL https://unstats.un.org/unsd/methodology/m49/ (accessed 12.18.23).
- Vincini, M. et al., 2007. Comparison of narrow-band and broad-band vegetation indices for canopy chlorophyll density estimation in sugar beet. Brill. https://doi.org/10.3920/9789086866038 022
- Vizcaya-Martínez, D.A., Flores-de-Santiago, F., Valderrama-Landeros, L., et al., 2022. Monitoring detailed mangrove hurricane damage and early recovery using multisource remote sensing data. J Environ Manage 320, 115830. https://doi.org/10.1016/j.jenvman.2022.115830
- Vovides, A.G., Berger, U., Grueters, U., et al., 2018. Change in drivers of mangrove crown displacement along a salinity stress gradient. Functional Ecology 32, 2753–2765. https://doi.org/10.1111/1365-2435.13218
- Vovides, A.G., Wimmler, M.-C., Schrewe, F., et al., 2021. Cooperative root graft networks benefit mangrove trees under stress. Communications Biology 4. https://doi.org/10.1038/s42003-021-02044-x
- Wang, D., Wan, B., Liu, J., et al., 2020. Estimating aboveground biomass of the mangrove forests on northeast Hainan Island in China using an upscaling method from field plots, UAV-LiDAR data and Sentinel-2 imagery. International Journal of Applied Earth Observation and Geoinformation 85, 101986. https://doi.org/10.1016/j.jag.2019.101986
- Wang, L., Jia, M., Yin, D., et al., 2019. A review of remote sensing for mangrove forests: 1956–2018. Remote Sensing of Environment 231, 111223. https://doi.org/10.1016/j.rse.2019.111223
- Worthington, T., Spalding, M., 2018. Mangrove restoration potential: A global map highlighting a critical opportunity. https://doi.org/10.17863/CAM.39153
- Yu, J., Nie, S., Liu, W., et al., 2022. Accuracy Assessment of ICESat-2 Ground Elevation and Canopy Height Estimates in Mangroves. IEEE Geoscience and Remote Sensing Letters 19, 1–5. https://doi.org/10.1109/LGRS.2021.3107440

Zanne, A.E., Lopez-Gonzalez, G., Coomes, D.A., et al., 2009. Data from: Towards a worldwide wood economics spectrum. https://doi.org/10.5061/DRYAD.234

Chapter 5 Quantifying aboveground biomass dynamics of mangrove regrowth across the Americas

Abstract

Mangroves are well-recognised for their importance in climate change mitigation through carbon sequestration and storage but historically have been underappreciated and largely deforested for timber harvesting, aquaculture and coastal development. Currently, increased recognition of their role in coastal protection and fishery productivity has shifted the tide for mangroves, incentivising people to carry out restoration and conservation efforts globally. However, little is known about mangrove resilience relevant to climate change adaptation and conservation efforts. In this study, aboveground biomass (AGB) dynamics were investigated over regrowing mangrove areas in the past two decades (2000-2020). This study targeted mangrove forests across the Americas as relatively strong conservation efforts have been implemented in this region. First, the tropical moist forest (TMF) annual coverage dataset from the Joint Research Centre (JRC) was used to determine the areas of mangrove regrowth through the analysis of land cover change between 2000 and 2020. Then, given the availability of data sources throughout the period, the periodspecific methodologies were proposed to estimate mangrove AGB for 2000 and 2020. The results found that 0.17 million ha (Mha) of mangrove forests across the Americas were regrowing from previous mangrove areas (Type I regrowth) and 0.05 Mha were from previous non-forest areas during 2000-2020 (Type II regrowth), while 2.52 Mha remained undisturbed. Both kinds of mangrove regrowth contributed to AGB gains of 2.71 Tg and 2.39 Tg, respectively. As normalized by their respective areas, Type II regrowth contributed 52 Mg/ha AGB, while Type I regrowth resulted in an AGB gain of 16 Mg/ha. These findings revealed that mangroves are actively colonising previously non-forested areas, resulting in significant AGB gains and indicating an expansion of suitable habitat. This study offers an insight into AGB dynamics related to mangrove regrowth, expected to serve as the first comprehensive investigation into mangrove resilience across the Americas for the first twenty years in the 21st century (2000-2020).

Keywords: Mangrove resilience; Aboveground biomass dynamics; Mangrove regrowth; Remote sensing; Americas

5.1 Introduction

Mangrove forests are of great importance in providing essential ecosystem services, including coastal protection, fisheries, and climate regulation through carbon sequestration and storage (Worthington et al., 2020). Historically, the social and ecological significance of mangroves were underappreciated; an estimated 35% of the world's mangrove area was lost in the 1980s and 1990s at an annual loss rate of 1-2.1% (Friess et al., 2024). Since the 2000s, growing awareness around mangroves socioecological well-being has led to global efforts on mangrove conservation and restoration, with annual loss rates declining to 0.1% and the establishment of 393,000 ha between 2000 and 2020 (FAO, 2023). However, less is known about how mangrove forest regrowth has contributed to carbon stocks during 2000-2020. Restoration typically refers to silviculture, including reforestation and afforestation. Reforestation is restoring forests in areas where forests previously existed but were deforested or degraded due to human activities or natural disasters, while afforestation is establishing forests in areas where there were no previous forests (Ellison, 2000). Mangrove forest regrowth can also be accredited to natural expansion.

Carbon stocks in mangroves are often inferred from aboveground biomass (AGB) estimations. AGB refers to the total amount of living organic matter contained in the aboveground parts of mangrove trees in area (normally using megagram per hectare, Mg/ha). Traditionally, AGB measurement requires field-based destructive sampling further used to develop allometric equations based on tree attributes such as diameter at breast height (DBH) and canopy height (Kauffman and Donato, 2012; Komiyama et al., 2008). However, as mangrove forests are characterised by closed canopies and dense stems in remote and muddy regions, this limited accessibility makes large-scale inventory efforts both labour-intensive and time-consuming. Remote sensing enables large-scale surveys by delivering spatially explicit information through passive sensors, such as multispectral and hyperspectral systems, or active sensors like Synthetic Aperture Radar (SAR) and Light Detection and Ranging (LiDAR). These remotely sensed data have proven effective for estimating mangrove AGB at regional, national, or global scales (e.g., Simard et al., 2019; Hu et al., 2020; Lucas et al., 2020; Wang et al., 2020; Zhu et al., 2020; Prakash et al., 2022). Consistency in mangrove AGB estimation approaches is essential through different years to ensure reliable estimates. However, varying acquisition periods lead to gaps in data availability between observed years when the same approach for mangrove AGB estimation is applied.

The scarcity of mangrove field inventory data presents challenges in deciphering the intricate bio-physical relationship between spectral signatures and forest vertical structure (Rodríguez-Veiga et al., 2017; Wang et al., 2019). This limitation complicates the estimation of mangrove AGB using optical imagery (Lang et al., 2023). But the advancement of SAR and LiDAR sensors has greatly enhanced the ability to estimate

canopy height, a key biophysical parameter for AGB estimation; these technologies enable more accurate and reliable measurements of vertical forest structure, thereby improving the estimation of mangrove AGB (Fatoyinbo et al., 2018; Lang et al., 2023; Shendryk, 2022; Wang et al., 2020). Canopy height can simplify the process of estimating AGB, working as the dependent variable in linear regression equations (Baccini et al., 2012; Basyuni et al., 2023; Duncanson et al., 2022; Simard et al., 2019; Simard et al., 2006, 2008).

The Shuttle Radar Topography Mission (SRTM), flown in February 2000, provided the first near-global topography including vegetation cover (Farr et al., 2007). The SRTM elevation product enabled the investigation of mangrove canopy height distribution across the world with the assumption that mangroves are generally located in low-lying and flat coastal regions with negligible topographic impacts (Simard et al., 2006, 2008). Simard et al. (2019) estimated the AGB of world's mangroves with the SRTM DEM (digital elevation model) calibrated by ICESat LiDAR data which allows for comprehensive and accurate canopy height mapping. The first-ever spaceborne LiDAR mission specifically designed for vegetation structure investigation in orbit, Global Ecosystem Dynamics Investigation (GEDI), provides full-waveform LiDAR data between approximately 51.6 °N and 51.6 °S spanning from 2019 to 2023 (Duncanson et al., 2022). The GEDI observations show high capabilities to retrieve forest canopy height which represents a certain quantile of returned energy relative to the ground within circular footprints of 25 m in diameter. However, GEDI LiDAR data are not wall-to-wall with significant coverage gaps, especially at the equator (Dubayah et al., 2020). Given the vast amount of GEDI observations, wall-to-wall mangrove AGB estimation can be realized with the introduction of optical imagery by exploiting biomass-height allometry to yield GEDI-based AGB estimates for supervised machine learning.

Focusing on the mangrove forests across the Americas, this study aims to investigate the contribution of mangrove regrowth (new colonisation included) to AGB dynamics between 2000 and 2020. AGB losses (e.g., conversion or dieback) are not quantified here and are discussed as a limitation in the Discussion section. Mangrove forests over the Americas are characterized by the highest inclusion of protected mangrove areas, providing a unique setting for the investigation of the contribution of mangrove regrowth with less anthropogenic disruptions (e.g., logging and conversion to coastal land use). The European Commission Joint Research Centre (JRC) holds a dataset of tropical moist forest (TMF) cover over the past three decades (1990-2023) at a spatial resolution of 30 m. It provides annual wall-to-wall mapping of the TMF extent (including mangroves) and other land covers, demonstrating the feasibility of detecting mangrove regrowth extent during 2000 - 2020 (Vancutsem et al., 2021). This study is anticipated to serve as the first comprehensive investigation into mangrove regrowth with AGB gains across the Americas for the first twenty years in the 21st century. It further reveals the mangrove resilience relevant to climate

change adaptation and conservation efforts, helping shape the understanding the effective management of mangroves.

5.2 Material and methods

5.2.1 Study area

This study focuses on the mangrove forests across the Americas and introduced the 10 m global mangrove extent map of 2020 to identify the mangrove areas (**Figure 5-1**). The global mangrove extent map is geographically delineated by both country boundaries and reserve divisions. Detailed description is provided in Section 4.2.1.



Figure 5-1. The distribution of mangrove forests across the Americas in 2020 derived from Jia et al. (2023).

5.2.2 JRC TMF data

The JRC TMF dataset was initially developed for a long-term monitoring of tropical moist forests from 1990 to 2019, comprising annual change collections where the extent of TMF was identified as undisturbed, degraded, deforested and regrowth, along with the identification of permanent and seasonal water and other land cover (Vancutsem et al., 2021). This dataset has been recently updated to 2023 and reprocessed using 30m Landsat Collection-2 imagery for better quality input data and a larger number of valid observations, freely accessible in the Google Earth Engine platform (JRC, 2023a). Within the JRC TMF dataset,

deforestation refers to a permanent conversion from forest to non-forested land, starting at the latest the current year, and observed over 2.5 years with no detected vegetation regrowing. Degradation denotes a temporary disturbance, such as trunk harvesting, wildfires, or extreme weather events, lasting at most 2.5 years in a forest and starting no later than the current year. Regrowth refers to the transition of vegetative regrowth on deforested lands which previously were TMF, as well as on other land cover, with a minimum duration of three years to avoid confusion with agriculture.

5.2.3 Mangrove regrowth area determination between 2000 and 2020

This study focuses on mangrove regrowth areas in the last 20 years (2000-2020) as most of AGB gains induced by regrowing mangroves occur in a 20-year period (Bourgeois et al., 2024). Across JRC TMF annual coverage products, TMF status has been reported as undisturbed, degraded, deforested and regrowing (JRC, 2023b). Here, the mangrove regrowth was determined as (1) forest regrowth from the undisturbed, degraded forests or deforested lands (Type I regrowth) and (2) forest regrowth from water or other land cover (Type II regrowth). The global mangrove extent map in 2020 was utilized to geographically delimit the mangrove forests based on country boundaries and reserve divisions across the Americas.

5.2.4 Mangrove AGB estimation between 2000 and 2020

The methodology of AGB estimation described in Chapter 3 was adopted to estimate mangrove AGB for 2000, which was adapted here with the introduction of SRTM Version 3 DEM data (SRTMGL1 v003), void-filled with open-source data (i.e. ASTER GDEM2, GMTED2010 and NED), and the biomass-height allometry developed in Chapter 4 incorporating maximum canopy height as an independent variable. The SRTM DEM represents vegetated areas and reports elevations situated at the radar scattering phase height centre instead of the top of canopy (Lagomasino et al., 2016; Simard et al., 2008) (a detailed description of the SRTM is provided in Section 3.3.1). The approach developed in Simard et al. (2019) was deployed to estimate the distribution of mangrove canopy height in 2000, where a total of ~58,000 selected ICESat/GLAS LiDAR waveforms spanning 2003-2009 were related to SRTM DEM values over global mangrove areas. A regression model without an intercept was obtained between the relative height at the 100th percentile (maximum canopy height) from GLAS waveforms and SRTM elevation measurements:

$$SRTMH_{max} = 1.697 \times H_{SRTM}$$
 (intercept = 0) (Equation 5.1)

where H_{SRTM} represents the original SRTM DEM values, and $SRTMH_{max}$ is the derived maximum canopy height dataset. The SRTM values of 0 m over mangrove areas were assigned 0.5 m in which scrub or sparse

mangroves were not probably detected by SRTM. Additionally, maximum $SRTMH_{max}$ in each country was capped at the 95th percentile of the values in the corresponding country to mitigate the impact of errors in canopy height of potential misclassified mangrove pixels (Simard et al., 2019).

However, as there is no open-access 2020-epoch global canopy-sensitive DSM comparable to SRTM, the SRTM/GLAS-based height proxy used for year 2000 cannot be validly applied to 2020. Therefore, AGB for 2000 and 2020 was estimated using period-specific models: an SRTM-based height proxy for 2000 (Equation 5.1) and a maximum-height model using recent spaceborne LiDAR/imagery for 2020 (Chapter 4) (**Figure 5-2**).

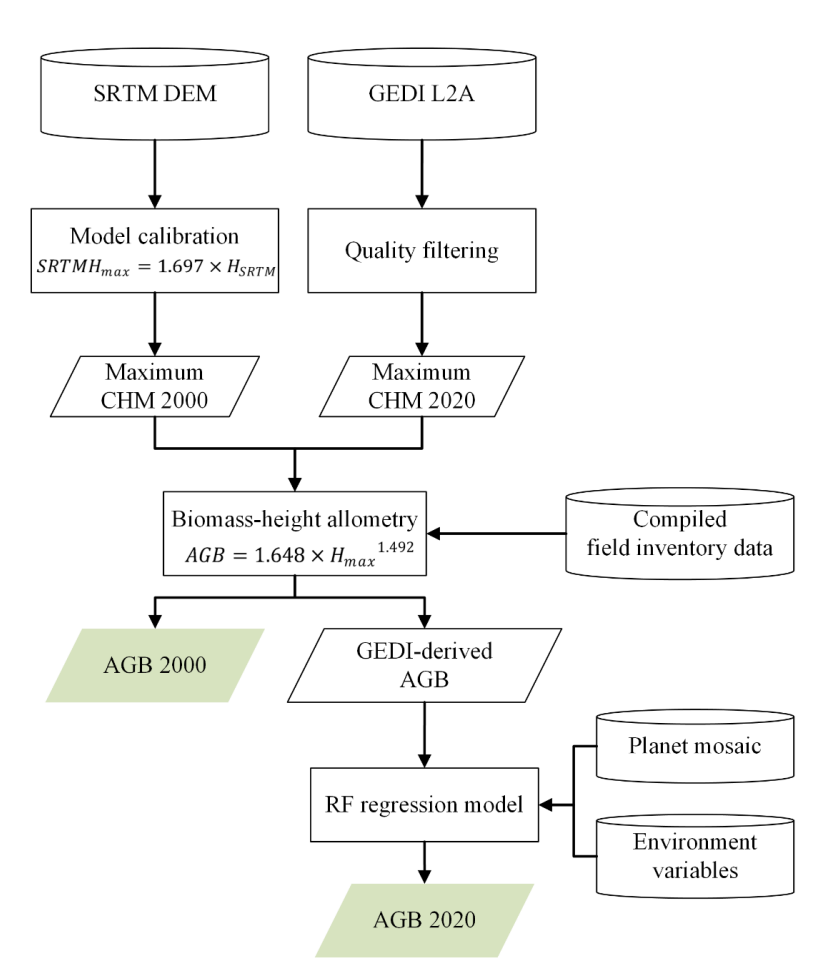


Figure 5-2. Workflow diagram for estimating mangrove AGB across the Americas between 2000 and 2020.

5.3 Results

5.3.1 Mangrove regrowth area between 2000 and 2020

Between 2000 and 2020, 0.17 million ha (Mha) of mangrove forests across the Americas were regrown from deforested land which used to be degraded or undisturbed mangroves (Type I regrowth), and 0.05

Mha were regrown on previous non-forest land (Type II regrowth), while 2.52 Mha remained undisturbed. Most mangrove regrowth areas were predominantly distributed around latitude 19° N with a total area of 0.03 Mha, and along longitude 87° W accounting for a total area of 0.02 Mha (**Figure 5-3**). Generally, mangroves were more likely to regrow from previous forest areas than non-forest areas in almost all countries across the Americas, except for Aruba, St. Vincent & the Grenadines, French Guiana, Panama, and Peru. On average, the areas of Type I regrowth accounted for 68.2% of country-level mangrove regrowth, while Type II regrowth made up 31.8%. The top three countries with the largest mangrove regrowth area are Mexico (85,652 ha), Brazil (44,128 ha) and Cuba (37,673 ha). Meanwhile, undisturbed mangrove forests in these countries account for a significant proportion (53%) of total undisturbed mangrove coverage over the Americas.

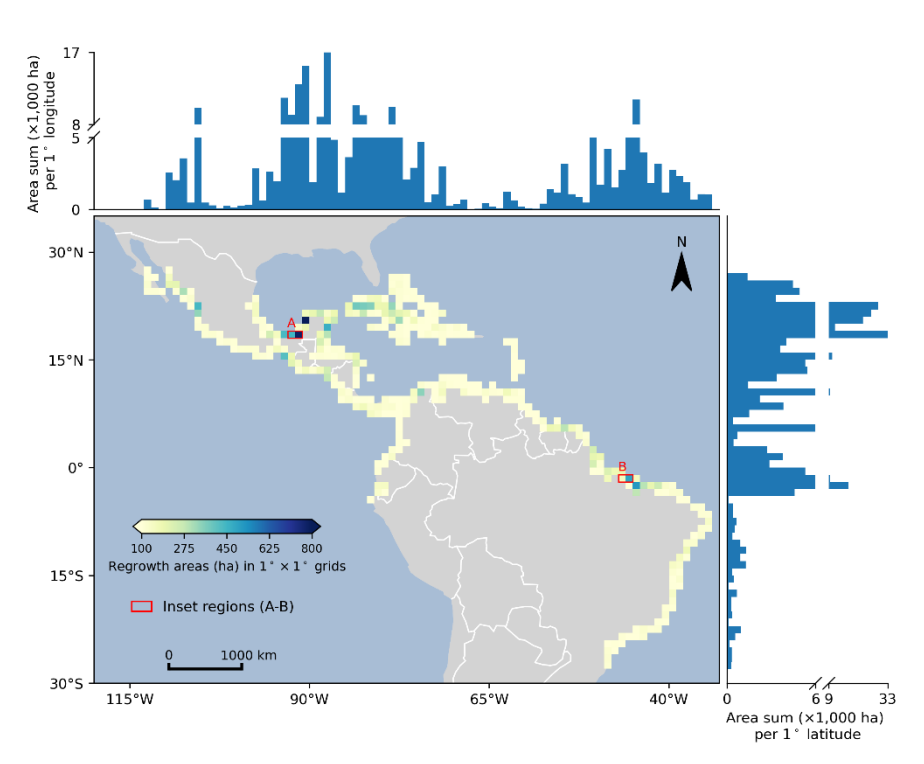


Figure 5-3. Mangrove regrowth across the Americas. Regrowth areas aggregated to 1° grid for better visualization (Data source: EC JRC). Two sites exhibited significant mangrove regrowth were marked by red rectangles: (A) Laguna de Términos protected area, Mexico; (B) Caeté-Taperaçu marine extractive reserve, Brazil.

From the perspective of protected area inclusion, 70% of mangrove regrowth areas and 63% of undisturbed mangrove forests fell into reserve divisions, where mangrove reserves benefited from 72% of Type I regrowth and 62% of Type II regrowth (**Table 5-1**). A large proportion of mangrove regrowth occurred within protected areas in Mexico, Brazil and Cuba. Notably, Cuba exhibited 84% of Type I regrowth and 79% of Type II regrowth situated within designated mangrove reserves. Furthermore, entire regrowth areas were found within mangrove reserves in several countries, including Aruba, Martinique, the Turks and Caicos Islands, El Salvador, the Cayman Islands, Peru, and Guadeloupe.

Table 5-1. Mangrove area (ha) summarized by country in terms of mangrove transition status (i.e., Type I regrowth, Type II regrowth and undisturbed) between 2000 and 2020, excluding Barbados, the United States of America, Puerto Rico, British Virgin Islands, and Virgin Islands. Numbers in parentheses represent areas falling into mangrove reserves.

Country	Type I regrowth	Type II regrowth	Undisturbed	
Antigua & Barbuda	26 (22)	15 (6)	252 (137)	
Aruba	2 (2)	6 (6)	19 (19)	
Belize	2,960 (1,536)	666 (337)	13,574 (4,595)	
Brazil	27,492 (16,722)	16,636 (8,909)	917,887 (564,784)	
Cayman Is.	417 (417)	159 (159)	1,963 (1,963)	
Colombia	4,316 (3,361)	1,571 (1,209)	254,223 (237,253)	
Costa Rica	809 (594)	654 (414)	33,890 (25,551)	
Cuba	31,326 (26,366)	6,347 (5,038)	149,566 (113,487)	
Dominican Republic	493 (209)	118 (42)	7,079 (3,373)	
Ecuador	1,109 (929)	849 (647)	129,229 (116,410)	
El Salvador	1,053 (1,053)	397 (397)	29,026 (29,026)	
French Guiana	772 (589)	938 (672)	65,947 (53,979)	
Grenada	6 (4)	1 (0.35)	62 (19)	
Guadeloupe	50 (50)	13 (13)	1,630 (1,630)	
Guatemala	1,950 (909)	540 (102)	19,548 (13,675)	
Guyana	249	150	16,384	
Haiti	1,244 (72)	190 (4)	11,413 (1,453)	
Honduras	3,112 (2,171)	1,209 (610)	59,583 (40,696)	
Jamaica	479 (431)	168 (160)	2,973 (2,690)	
Martinique	16 (16)	4 (4)	1,208 (1,208)	
Mexico	77,715 (59,834)	7,937 (5,429)	269,935 (201,363)	
Netherlands Antilles	20 (19)	15 (12)	1,499 (1,481)	
Nicaragua	3,578 (2,755)	1,912 (1,622)	44,215 (25,587)	
Panama	1,647 (580)	1,733 (515)	145,771 (78,772)	
Peru	41 (41)	43 (43)	2,146 (2,146)	
St. Kitts & Nevis	5	2	13	
St. Lucia	2(1)	0.45 (0.28)	105 (85)	
St. Vincent & the Grenadines	1	3	7	
Suriname	3,491 (653)	1,532 (1,180)	42,516 (29,334)	
The Bahamas	1,519 (5)	518 (13)	5,658 (312)	
Trinidad & Tobago	201 (189)	44 (26)	4,827 (4,649)	
Turks & Caicos Islands	582 (582)	56 (56)	2,851 (2,851)	
Venezuela	2,102 (940)	1,761 (878)	288,906 (18,227)	
Total	168,785 (121,400)	46,187 (28,648)	2,523,907 (1,583,373)	

5.3.2 Mangrove AGB estimation on regrowth areas

In 2020, the estimation of AGB for mangrove regrowth areas across the Americas totalled 11 Tg (1 Tg = 10^6 Mg). This included contributions of 8 Tg from Type I regrowth and 3 Tg from Type II regrowth. Compared to whole AGB estimates in 2000, Type I regrowth led to an increase in AGB estimates from 5.29 to 8 Tg (51%), and AGB led by Type II regrowth rose dramatically from 0.59 to 2.98 Tg (> 400% increase).

Table 5-2. Country-level mangrove AGB (Mg) in terms of Type I/II regrowth between 2000 and 2020, excluding Barbados, the United States of America, Puerto Rico, British Virgin Islands, and Virgin Islands.

	Type I r	egrowth	Type II	Type II regrowth	
Country	AGB 2000	AGB 2020	AGB 2000	AGB 2020	
	(Mg)	(MG)	(Mg)	(Mg)	
Antigua & Barbuda	865	1,314	260	702	
Aruba	57	87	55	178	
Belize	43,420	95,623	4,749	25,772	
Brazil	919,774	1,912,514	193,795	1,306,313	
Cayman Is.	13,982	18,229	3,238	10,037	
Colombia	94,745	345,272	13,786	122,653	
Costa Rica	34,313	88,110	14,474	77,747	
Cuba	1,386,597	825,738	123,046	162,318	
Dominican Republic	7,654	35,437	941	8,283	
Ecuador	18,843	81,944	4,822	54,411	
El Salvador	60,137	70,603	11,730	31,918	
French Guiana	28,087	105,547	17,010	135,301	
Grenada	703	656	6	80	
Guadeloupe	666	2,141	137	515	
Guatemala	155,519	204,533	24,398	41,007	
Guyana	4,570	22,668	317	12,164	
Haiti	32,394	32,916	1,730	5,127	
Honduras	43,993	190,659	5,730	76,702	
Jamaica	14,899	24,488	1,979	10,026	
Martinique	637	1,403	13	418	
Mexico	1,859,079	2,925,547	92,079	297,655	
Netherlands Antilles	291	548	110	438	
Nicaragua	103,971	180,184	12,310	81,429	
Panama	66,663	204,113	30,226	203,221	
Peru	606	1,605	339	1,610	
St. Kitts & Nevis	103	244	112	77	
St. Lucia	89	148	0	43	
St. Vincent & the Grenadines	384	93	327	240	
Suriname	256,768	375,485	8,083	153,306	
The Bahamas	39,578	23,280	10,289	9,775	
Trinidad & Tobago	16,920	19,149	1,308	5,142	
Turks & Caicos Islands	14,758	7,416	1,508	711	
Venezuela	67,112	199,403	10,485	143,376	
Total	5,288,176	7,997,097	589,393	2,978,698	

Almost every country shows an increase in AGB over mangrove regrowth areas (**Table 5-2**). Brazil exhibited the highest AGB increases of 2.11 Tg, followed by Mexico (1.27 Tg) and Colombia (0.36 Tg). Together, the AGB increases in these three countries accounted for 73% of the total AGB gains observed in 2020. Different from Type I regrowth, Type II regrowth, indicative of mangrove regrowth in previous

non-forest areas, exhibited the most dramatic relative AGB increases. For example, AGB of Type II regrowth in Panama surged from 30,226 to 203,221 Mg, representing a roughly 7-fold gain; both Honduras and Venezuela experienced more than 13-fold increases in AGB due to Type II regrowth. When considering AGB dynamics per unit regrowth area across the Americas, mangrove regrowth resulted in AGB gains of 24 Mg/ha, with Type I regrowth and Type II regrowth contributing to AGB gains of 16 Mg/ha and 52 Mg/ha, respectively. Specifically, French Guiana exhibited the highest AGB increase of 114 Mg/ha, followed by Panama (92 Mg/ha), Costa Rico (80 Mg/ha) and Guyana (75 Mg/ha). However, the increase in AGB per hectare was 48 Mg/ha in Brazil, while Mexico reported an increase of 15 Mg/ha.

5.3.3 Mangrove AGB estimation over undisturbed areas

AGB estimates over undisturbed mangrove areas were summarised by country for 2000 and 2020 (**Table 5-3**). At the continental scale, totals decreased from 338.37 Tg (2000) to 282.88 Tg (2020), a difference of -55.49 Tg (-16.4%).

Table 5-3. Country-level mangrove AGB (Mg) over undisturbed mangrove areas between 2000 and 2020, excluding Barbados, the United States of America, Puerto Rico, British Virgin Islands, and Virgin Islands.

	Undisturbed			Undisturbed	
Country	AGB 2000	AGB 2020	Country	AGB 2000	AGB 2020
	(Mg)	(Mg)		(Mg)	(Mg)
Antigua & Barbuda	2,133	13,975	Honduras	5,688,497	5,415,713
Aruba	1,049	804	Jamaica	147,187	153,087
Belize	436,233	561,760	Martinique	63,820	136,496
Brazil	118,075,350	93,794,702	Mexico	21,799,665	16,019,246
Cayman Is.	91,064	162,789	Netherlands Antilles	71,325	62,436
Colombia	36,710,704	40,503,656	Nicaragua	3,664,682	3,075,830
Costa Rica	6,339,821	4,381,803	Panama	31,748,738	23,235,700
Cuba	7,709,478	4,120,524	Peru	131,946	103,398
Dominican Republic	493,401	548,666	St. Kitts & Nevis	316	578
Ecuador	17,664,103	11,275,612	St. Lucia	11,441	11,116
El Salvador	3,801,594	2,780,545	St. Vincent & the Grenadines	418	518
French Guiana	11,419,199	10,619,049	Suriname	4,540,407	5,193,877
Grenada	4,879	6,425	The Bahamas	113,028	92,774
Guadeloupe	85,285	96,856	Trinidad & Tobago	618,824	546,347
Guatemala	4,009,057	2,337,049	Turks & Caicos Islands	71,410	53,227
Guyana	2,445,473	2,610,279	Venezuela	59,863,379	54,651,910
Haiti	547,550	316,300	Total	338,371,454	282,883,049

Country-level estimates remain broadly comparable between 2000 and 2020 for many countries, with notable absolute decreases in Brazil (-20.6%), Panama (-26.8%), Ecuador (-36.1%) and Mexico (-26.5%). Increases are observed in Colombia (+10.3%) and Suriname (+14.3%). Several small-island states show

relatively large percentage shifts on small absolute baselines (e.g., Antigua & Barbuda, Cayman Islands, Martinique), whereas most mid- to large-AGB countries exhibit smaller percentage deviations.

Country-level AGB in 2020 plotted against 2000 for the undisturbed areas shows a near-linear relationship (**Figure 5-4**). The fitted line y = 0.83*x + 0.10 with $R^2 = 0.93$ and RMSE% = 38.21%, and most countries plot below the 1:1 line, indicating that 2020 estimates are generally lower than 2000 by roughly 15–20% on average. The relative ranking of countries is largely unchanged, although the largest absolute difference occurs in Brazil.

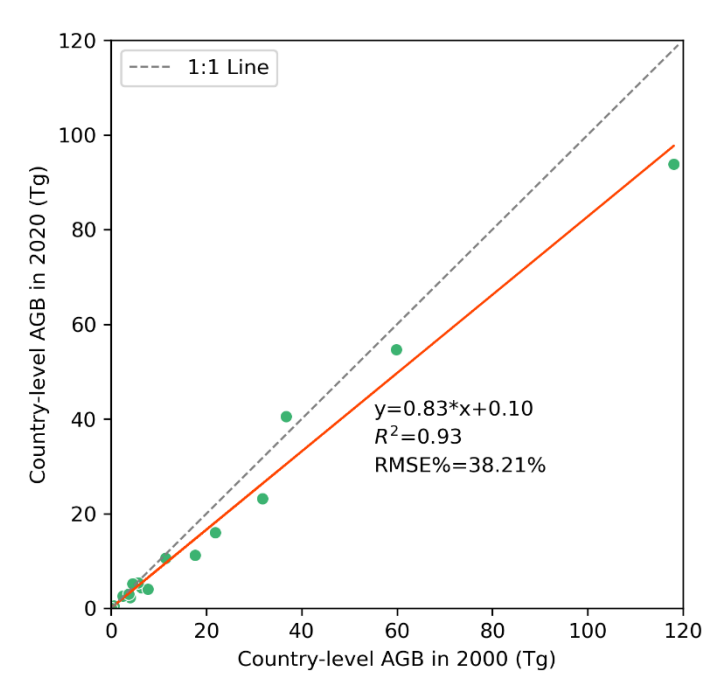


Figure 5-4. Country-level AGB estimates over undisturbed mangrove forests in 2020 versus 2000 (Tg).

5.4 Discussion

5.4.1 The variation of country-level mangrove regrowth areas

This study has revealed the pattern of AGB gains within mangrove regrowth areas as JRC TMF annual coverage products were employed to identify regrowing mangrove (new colonisation included). In the Americas, mangrove regrowth patterns vary significantly between countries, reflecting protection frameworks, human pressures, geomorphological setting, and extreme weather event-driven disturbance.

Mexico has exhibited the largest mangrove regrowth areas (> 85,000 ha), with hotspots around Laguna de Términos (**Figure 5-3**, **Figure 5-5A**). Numerous restoration projects have been implemented since 2016, particularly reforestation programs (Antúnez, 2024). Government reports indicate >5,000 ha of mangroves

were restored across several states between 2013 – 2016 (SEMARNAT, 2016), and ~56 ha of degraded mangroves were restored around Laguna de Términos by 2020 (CONANP, 2020), reflecting a mix of hydrologic rehabilitation and planting within protected areas. However, regrowth coexists with localised losses in Natural Protection Areas (NPAs), driven by human pressures in Términos (Osorio-Olvera et al., 2023), shrimp aquaculture in Marismas Nacionales (Lithgow et al., 2019), urban/tourism expansion in La Paz (Giovanni Ávila-Flores et al., 2017), and hydrologic alteration (Kumagai et al., 2020). Overall, the mangrove regrowth pattern in Mexico is that net recovery concentrated in protected sites with concurrent losses in development-exposed frontiers.

Brazil boasts the second largest mangrove coverage in the world, with nearly 85 – 87% of its mangroves legally designated within protected areas, such as marine extractive reserves and conservation units (de Lacerda et al., 2022; ICMBio, 2018). A total of 25,631 ha mangroves were found regrowing within these reserves, such as the Caeté-Taperaçu marine extractive reserve (**Figure 5-5B**), where there is a designated mangrove recovery area (Partelow et al., 2018). The high level of legal protection facilitates natural regeneration, however localised losses persist driven by coastal erosion in northern Brazil, shrimp aquaculture and salt ponds development on the Semiarid Equatorial Coast (SAE) (Vanin et al., 2025), and urbanisation in Espírito Santo (ETC) and South Granitic Coast (SGC) (de Lacerda et al., 2022).

Mangroves in Cuba are largely protected through national conservation frameworks, resulting in relatively stable or expanding mangrove areas. Regrowth has been supported by effective regulation and limited large-scale conversion (Goulart et al., 2018). But meanwhile, the disturbance driven by extreme weather events can lead to severe mangrove losses. For example, Hurricane Irma (2017) caused widespread mangrove damage along the northern coast with a staggering 78% of mangrove and wetlands showing damage (Turner et al., 2023).

Caribbean small-island states (e.g., Aruba, Cayman Islands, Guadeloupe, Trinidad & Tobago) exhibit regrowth largely confined to protected areas, consistent with natural recovery in low-disturbance settings but constrained by limited land and development pressure at the coast. In Trinidad & Tobago, mangrove conservation and restoration have been implemented within key sites, but industrial/urban expansion and sea level rise create localised vulnerabilities (Hassanali, 2017; Juman and Hassanali, 2013).

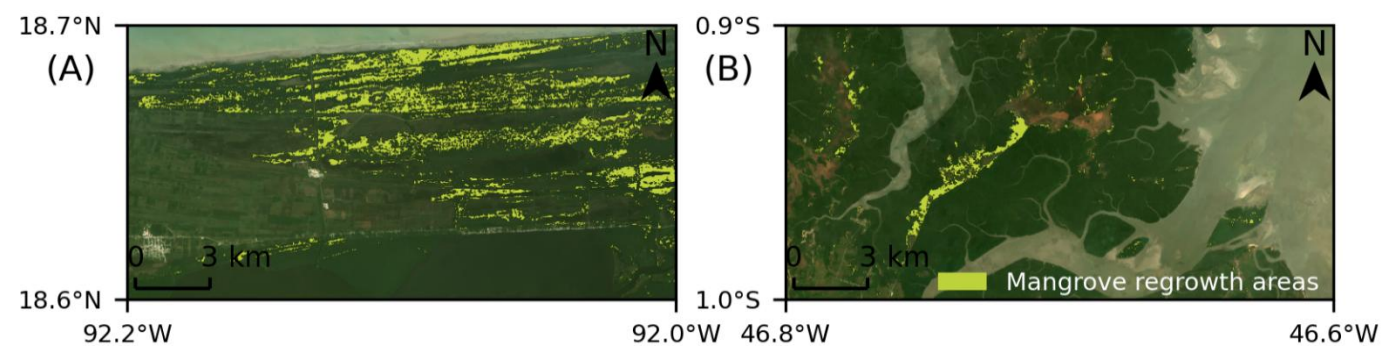


Figure 5-5. Zoom-in on intensive mangrove regrowth areas highlighted with red rectangles in Figure 5-1. (A) Laguna de Términos protected area, Mexico; (B) Caeté-Taperaçu marine extractive reserve, Brazil.

5.4.2 Comparability of AGB estimation methodologies

In this study, two approaches were developed for mangrove AGB estimation for the year 2000 and 2020, respectively. AGB is assumed to be stable across undisturbed, well-established and intact mangrove forests over time (Lagomasino et al., 2021). However, country-level AGB estimates in 2020 was lower than the ones in 2000 using the proposed methodologies over undisturbed mangrove forests (**Table 5-3**). Different resolutions of spaceborne datasets and regression limitation of RF algorithm may be the causes for these discrepancies. Mangrove AGB in 2020 was estimated and mapped on a 4.77 m resolution Planet mosaic, while in 2000 mangrove AGB was estimated and mapped on 30 m resolution SRTM DEM due to the availability of spaceborne datasets at that time. High resolution spaceborne imagery provides great potentials for investigating AGB distribution of mangrove regrowth at finer scales, however, AGB estimation for a specific region is more fragmented as the area covered by a 30 m pixel is covered by nearly 40 pixels of 4.77 m.

Unlike the approach for the AGB estimation in 2000, the biomass-height allometry (Equation 4.2) was applied to discrete GEDI footprints over 2020 instead of wall-to-wall DEM datasets, which were then utilised in the RF regression model to map on wall-to-wall Planet mosaic and environmental variables for mangrove AGB estimation of 2020. RF model works in a way that regression outcomes are derived from average prediction results from all the decision trees, which means RF regression model can extrapolate from input datasets. Also, mangrove AGB in 2000 is expected to be higher as using plot top heights in biomass-height allometry can lead to the overestimation of mangrove AGB (Rahman et al., 2021). However, except for the significant disagreement in Brazil (118 Tg in 2000 vs. 94 Tg in 2020), other countries represent comparable AGB estimates over undisturbed mangrove forests between 2000 and 2020. High agreements are therefore found in the comparisons of country-level AGB estimates across undisturbed mangrove forests between 2000 and 2020, demonstrating the compatibility of the proposed approaches (Figure 5-4).

5.4.3 Intercomparisons of AGB estimates on mangrove regrowth areas

Maximum canopy height was valued as a proxy in mangrove AGB estimation across the Americas as taller trees typically dominate higher AGB. Spaceborne DEM products show significant potentials for correlations with mangrove canopy height, under the assumption that mangroves are situated in low-lying, flat areas with negligible topographic variability (Fatoyinbo and Simard, 2013; Simard et al., 2006). Simard et al. (2019) utilized ICESat GLAS LiDAR altimetry data as true canopy height to calibrate SRTM DEM for the retrieval of pixel-wise maximum canopy height estimates across the world's mangrove forests as spaceborne LiDAR metrics demonstrate smaller measuring error than field measurements. This methodology was adopted to determine the distribution of maximum canopy height across mangrove forests in the Americas in 2000. However, since no follow-up DEMs have been developed in SRTM since 2000, i.e., the inconsistency in spaceborne ground elevation data between 2000 and 2020, it is challenging to estimate long-term mangrove AGB changes through consistent datasets. Ali and Rahman (2025) employed interpolated GEDI LiDAR observations to make spatiotemporal comparisons of canopy height and AGB with the ones derived from calibrated SRTM DEM. Instead, this study deployed discrete GEDI LiDAR observations as intermediate datasets in RF regression model with predictor variables of high-resolution spectral information and environmental variables to yield mangrove AGB estimates in 2020. Until now, there are GEDI L4B gridded AGB estimates and ESA CCI Biomass products freely available for global AGB estimation in 2020. Detailed descriptions of these two data products are in Section 4.2.8. Over mangrove regrowth areas, country-level AGB estimates from the approach are much higher than GEDI L4B AGB products which are average AGB values over 1×1 km grid (Figure 5-6). Higher agreements are found between the results and ESA biomass products as this dataset has a finer resolution of 100 m.

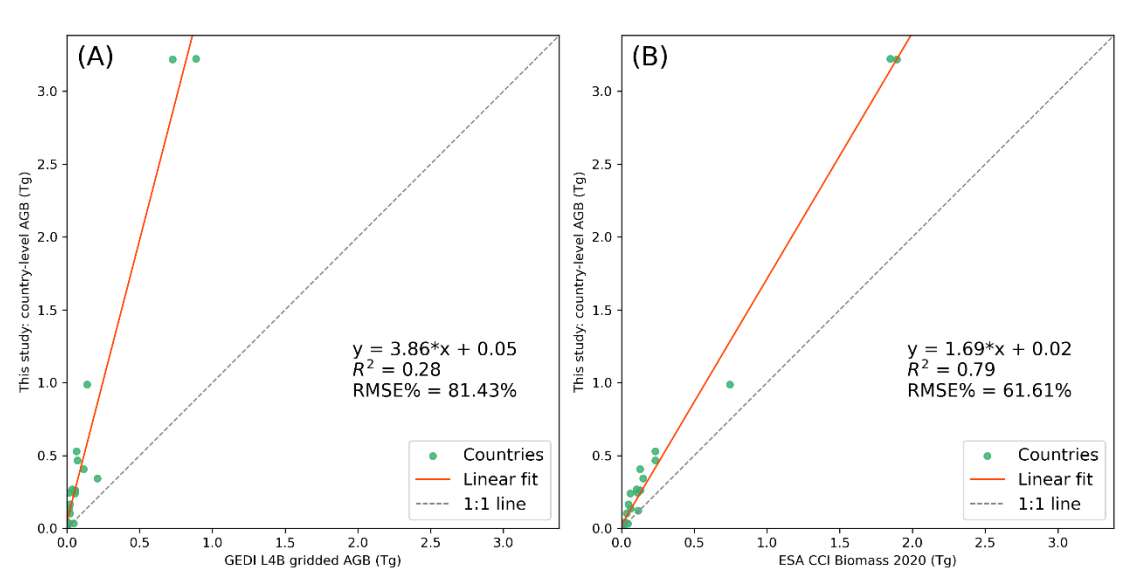


Figure 5-6. Country-level AGB estimates across mangrove regrowth areas using the proposed approach versus (A) GEDI L4B gridded AGB estimates and (B) ESA CCI Biomass 2020 product.

5.4.4 Research uncertainties and limitations

Compared to mangrove loss rates in the 20th century, the rates of mangrove loss have significantly decelerated since the beginning of the 21st century as mangrove conservation and restoration polices have been in place plus alternative coastal developments (Friess et al., 2024). Recent syntheses and global products provide consistent 2000-2020 indicators of mangrove extent and change (e.g., FAO 2023; GMW v3.0; JRC TMF), but few studies explicitly separate regrowth typologies (Type I vs. Type II) while also examining AGB dynamics, which is the contribution of this study. JRC TMF annual dataset (2000 and 2020) were used here to detect land cover transitions and a 2020 mangrove mask (Jia et al., 2023) to delimit mangrove areas; regrowth includes reforestation/afforestation and natural regeneration.

Formal confidence intervals are not computed for areas or AGB estimates in this study. Instead, the published validation of the input products is reported as indicative bounds. The JRC TMF dataset reports rigorous and independently validated change mapping for tropical moist forests with 91.4% overall accuracy (Vancutsem et al., 2021); likewise, the 2020 global mangrove mask from Jia et al., (2023) reports high overall accuracy of 95.2%. Therefore, area totals and fractions derived from these layers should be interpreted in light of the published accuracies of the input products, rather than as point-precise values. This caveat does not alter the direction of the main findings in this study, e.g., regrowth is more frequent on previously forested mangrove areas than non-forested lands; and a large proportion of regrowth occurs within protected areas. However, based on these indicative bounds, fine-grained country rankings should not be overinterpreted where differences are comparable in magnitude to the underlying product accuracies.

Due to remote sensing data availability, period-specific methodologies were employed for year 2000 and 2020 to investigate AGB dynamics. Error propagation for each AGB estimation methodology have been discussed in Section 3.9.1 and Section 4.4.3, respectively. The comparability between period-specific was assessed by comparing AGB estimates across undisturbed mangrove areas, which are assumed to be stable over time (**Figure 5-4**). However, methodological differences and associated errors among AGB estimates in regrowth areas between 2000 and 2020 remain unquantified and need to be well investigated in future study. As the analysis of AGB dynamics is conducted at country and continental levels, the results are still considered reliable to show broad trends, although the local and regional estimates should be interpreted with caution.

The results of this study showed that mangrove AGB was similarly gained from Type I and Type II regrowth across the Americas for two decades, but Type II regrowth represented higher AGB gains per hectare than Type I regrowth, as Type II regrowth can refer to a more long-term mangrove regrowth.

According to the report of FAO (2023), mangrove gains across the Americas were primarily driven by natural expansion between 2000 and 2020. The results demonstrate that mangroves have a significant capacity for resilience in terms of AGB gains, relevant to climate change adaptation and ongoing conservation efforts, however the intensity of mangrove regrowth, i.e., the timing of regrowth, remains unquantified. Additionally, AGB gains are linked to mangrove regrowth and does not include a companion workflow for AGB losses. Interpretation of net AGB accumulation therefore requires combining the present regrowth-linked gains with independent estimates of loss-linked reductions in the future study.

5.5 Conclusions

This study put forward the first comprehensive investigation into mangrove regrowth areas (new colonisation included) with AGB gains across the Americas for the first twenty years in the 21st century (2000-2020). Mangrove regrowth was categorised into two types delimited within mangrove coverage in 2020, identified using JRC TMF annual datasets; Type I regrowth refers to regrowing forests in 2020 from the undisturbed, degraded forests or deforested lands in 2000, while Type II regrowth includes forest regrowth in 2020 from water or other land cover in 2000. It is found that between 2000 and 2020 there was a total of 0.22 Mha mangrove regrowth over the Americas, including 0.17 Mha of Type I regrowth and 0.05 Mha of Type II regrowth. The annual datasets demonstrate great applicability for recognising mangrove regrowth across the Americas, revealing that Mexico, Brazil and Cuba are top three countries exhibiting significant regrowing areas and mangroves are more likely to regrow in previous forest areas than non-forest areas. Meanwhile, AGB dynamics over mangrove regrowth areas were computed using multisource remote sensing data, incorporated with biomass-height allometry developed from a compilation of field inventory data. Although different remote sensing data were introduced to estimate mangrove AGB between 2000 and 2020 due to data availability, the proposed methodology represents high agreements on country-level AGB summations across undistributed mangrove forests, which are considered well-established, intact without any disturbances. Over mangrove regrowth areas, AGB gains totalled 5.10 Tg comprising 2.71 Tg led by Type I regrowth and 2.39 Tg from Type II regrowth. However, given Type I regrowth areas three times as large as Type II regrowth areas, Type II regrowth demonstrates a significantly higher AGB per hectare, with a value of 52 Mg/ha compared to Type I regrowth's 16 Mg/ha as Type II regrowth can refer to a more long-term regrowth. Nonetheless, both types of regrowth signal the significant resilience of mangroves in terms of AGB regeneration and expansion relevant to climate change adaption and ongoing conservation efforts. This study provides an insight into mangrove regrowth against AGB dynamics, expected to help better understand scientific management of mangroves.

References

- Ali, Y., Rahman, M.M., 2025. Quantifying forest stocking changes in Sundarbans mangrove using remote sensing data. Science of Remote Sensing 11, 100181. https://doi.org/10.1016/j.srs.2024.100181
- Baccini, A., Goetz, S.J., Walker, W.S., et al., 2012. Estimated carbon dioxide emissions from tropical deforestation improved by carbon-density maps. Nature Clim Change 2, 182–185. https://doi.org/10.1038/nclimate1354
- Basyuni, M., Wirasatriya, A., Iryanthony, S.B., et al., 2023. Aboveground biomass and carbon stock estimation using UAV photogrammetry in Indonesian mangroves and other competing land uses. Ecological Informatics 77, 102227. https://doi.org/10.1016/j.ecoinf.2023.102227
- Bourgeois, C.F., MacKenzie, R.A., Sharma, S., et al., 2024. Four decades of data indicate that planted mangroves stored up to 75% of the carbon stocks found in intact mature stands. Science Advances 10, eadk5430. https://doi.org/10.1126/sciadv.adk5430
- Bunting, P., Rosenqvist, A., Hilarides, L., Lucas, R.M., Thomas, N., Tadono, T., Worthington, T.A., Spalding, M., Murray, N.J., Rebelo, L.-M., 2022. Global Mangrove Extent Change 1996–2020: Global Mangrove Watch Version 3.0. Remote Sensing 14, 3657. https://doi.org/10.3390/rs14153657
- CONANP, 2020. Restauración de manglares, una medida de adaptación al cambio climático [WWW Document]. URL http://www.gob.mx/conanp/es/articulos/restauracion-de-manglares-una-medida-de-adaptacion-al-cambio-climatico?idiom=es (accessed 25.02.2025).
- de Lacerda, L.D., Ferreira, A.C., Borges, R., et al., 2022. Mangroves of Brazil, in: Das, S.C., Pullaiah, Ashton, E.C. (Eds.), Mangroves: Biodiversity, Livelihoods and Conservation. Springer, Singapore. https://doi.org/10.1007/978-981-19-0519-3 20
- Dubayah, R., Blair, J.B., Goetz, S., et al., 2020. The Global Ecosystem Dynamics Investigation: High-resolution laser ranging of the Earth's forests and topography. Science of Remote Sensing 1, 100002. https://doi.org/10.1016/j.srs.2020.100002
- Duncanson, L., Kellner, J.R., Armston, J., et al., 2022. Aboveground biomass density models for NASA's Global Ecosystem Dynamics Investigation (GEDI) lidar mission. Remote Sensing of Environment 270, 112845. https://doi.org/10.1016/j.rse.2021.112845
- Ellison, A.M., 2000. Mangrove Restoration: Do We Know Enough? Restoration Ecology 8, 219–229. https://doi.org/10.1046/j.1526-100x.2000.80033.x
- FAO, 2023. The world's mangroves 2000–2020. FAO, Rome. https://doi.org/10.4060/cc7044en
- Farr, T.G., Rosen, P.A., Caro, E., et al., 2007. The Shuttle Radar Topography Mission. Reviews of Geophysics 45. https://doi.org/10.1029/2005RG000183

- Fatoyinbo, T., Feliciano, E.A., Lagomasino, D., et al., 2018. Estimating mangrove aboveground biomass from airborne LiDAR data: a case study from the Zambezi River delta. Environ. Res. Lett. 13, 025012. https://doi.org/10.1088/1748-9326/aa9f03
- Fatoyinbo, T.E., Simard, M., 2013. Height and biomass of mangroves in Africa from ICESat/GLAS and SRTM. International Journal of Remote Sensing 34, 668–681. https://doi.org/10.1080/01431161.2012.712224
- Friess, D.A., Adams, J., Andradi-Brown, D.A., et al., 2024. Mangrove forests: their status, threats, conservation and restoration, in: Reference Module in Earth Systems and Environmental Sciences. Elsevier, p. B9780323907989000317. https://doi.org/10.1016/B978-0-323-90798-9.00031-7
- Gardon, F.R., Santos, R.F. dos, Rodrigues, R.R., 2020. Brazil's forest restoration, biomass and carbon stocks: A critical review of the knowledge gaps. Forest Ecology and Management 462, 117972. https://doi.org/10.1016/j.foreco.2020.117972
- Giovanni Ávila-Flores, Gustavo Hinojosa-Arango, Judith Juárez-Mancilla, et al., 2017. The Use of the DSPIR Framework to Estimate Impacts of Urbanization on Mangroves: A Case Study From La Paz, Baja California Sur, Mexico, in: WIT Transactions on Ecology and The Environment. pp. 459–469.
- Goldberg, L., Lagomasino, D., Thomas, N., Fatoyinbo, T., 2020. Global declines in human-driven mangrove loss. Global Change Biology 26, 5844–5855. https://doi.org/10.1111/gcb.15275
- Goulart, F., Galán, Á.L., Nelson, E., et al., 2018. Conservation lessons from Cuba: Connecting science and policy. Biological Conservation 217, 280–288. https://doi.org/10.1016/j.biocon.2017.10.033
- Hassanali, K., 2017. Challenges in mainstreaming climate change into productive coastal sectors in a Small Island State The case of Trinidad and Tobago. Ocean & Coastal Management 142, 136–142. https://doi.org/10.1016/j.ocecoaman.2017.04.001
- Hu, T., Zhang, Y., Su, Y., et al., 2020. Mapping the Global Mangrove Forest Aboveground Biomass Using Multisource Remote Sensing Data. Remote Sensing 12, 1690. https://doi.org/10.3390/rs12101690
- ICMBio, 2018. Atlas dos Manguezais do Brasil. Instituto Chico Mendes de Conservação da Biodiversidade, Brasília, Brazil.
- Jia, M., Wang, Z., Mao, D., et al., 2023. Mapping global distribution of mangrove forests at 10-m resolution. Science Bulletin 68, 1306–1316. https://doi.org/10.1016/j.scib.2023.05.004
- JRC, 2023a. Tropical Forest Monitoring [WWW Document]. URL https://forobs.jrc.ec.europa.eu/TMF/data (accessed 10.28.24).
- JRC, 2023b. Joint Research Centre Tropical Moist Forest Data Users Guide (v1).
- Juman, R.A., Hassanali, K., 2013. Mangrove Conservation in Trinidad and Tobago, West Indies, in: Gerard Gleason, Thomas R. Victor (Eds.), Mangrove Ecosystems. Nova Science Publishers, Inc.

- Kauffman, J.B., Donato, D.C., 2012. Protocols for the measurement, monitoring and reporting of structure, biomass, and carbon stocks in mangrove forests. Center for International Forestry Research, Bogor, Indonesia.
- Komiyama, A., Ong, J.E., Poungparn, S., 2008. Allometry, biomass, and productivity of mangrove forests:

 A review. Aquatic Botany, Mangrove Ecology Applications in Forestry and Coastal Zone

 Management 89, 128–137. https://doi.org/10.1016/j.aquabot.2007.12.006
- Kumagai, J.A., Costa, M.T., Ezcurra, E., et al., 2020. Prioritizing mangrove conservation across Mexico to facilitate 2020 NDC ambition. Ambio 49, 1992–2002. https://doi.org/10.1007/s13280-020-01334-8
- Lagomasino, D., Fatoyinbo, T., Lee, S., et al., 2016. A Comparison of Mangrove Canopy Height Using Multiple Independent Measurements from Land, Air, and Space. Remote Sensing 8, 327. https://doi.org/10.3390/rs8040327
- Lang, N., Jetz, W., Schindler, K., et al., 2023. A high-resolution canopy height model of the Earth. Nat Ecol Evol 7, 1778–1789. https://doi.org/10.1038/s41559-023-02206-6
- Lithgow, D., de la Lanza, G., Silva, R., 2019. Ecosystem-Based Management strategies to improve aquaculture in developing countries: Case study of Marismas Nacionales. Ecological Engineering 130, 296–305. https://doi.org/10.1016/j.ecoleng.2017.06.039
- Lucas, R., Van De Kerchove, R., Otero, V., et al., 2020. Structural characterisation of mangrove forests achieved through combining multiple sources of remote sensing data. Remote Sensing of Environment 237. https://doi.org/10.1016/j.rse.2019.111543
- Osorio-Olvera, L., Rioja-Nieto, R., Torres-Irineo, E., et al., 2023. Natural Protected Areas effect on the cover change rate of mangrove forests in the Yucatan Peninsula, Mexico. Wetlands 43, 1–10. https://doi.org/10.1007/s13157-023-01697-0
- Partelow, S., Glaser, M., Solano Arce, S., Barboza, R.S.L., Schlüter, A., 2018. Mangroves, fishers, and the struggle for adaptive comanagement: applying the social-ecological systems framework to a marine extractive reserve (RESEX) in Brazil. E&S 23, art19. https://doi.org/10.5751/ES-10269-230319
- Prakash, A.J., Behera, M.D., Ghosh, S.M., et al., 2022. A new synergistic approach for Sentinel-1 and PALSAR-2 in a machine learning framework to predict aboveground biomass of a dense mangrove forest. Ecological Informatics 72, 101900. https://doi.org/10.1016/j.ecoinf.2022.101900
- Rahman, M.S., Donoghue, D.N.M., Bracken, L.J., et al., 2021. Biomass estimation in mangrove forests: a comparison of allometric models incorporating species and structural information. Environ. Res. Lett. 16, 124002. https://doi.org/10.1088/1748-9326/ac31ee

- Ram, M., Sheaves, M., Waltham, N.J., 2024. Tracking the long-term vegetation and soil characteristics of restored mangroves: a case study from Guyana's coast. Restoration Ecology 32, e14170. https://doi.org/10.1111/rec.14170
- Rodríguez-Veiga, P., Wheeler, J., Louis, V., et al., 2017. Quantifying Forest Biomass Carbon Stocks From Space. Curr Forestry Rep 3, 1–18. https://doi.org/10.1007/s40725-017-0052-5
- Shendryk, Y., 2022. Fusing GEDI with earth observation data for large area aboveground biomass mapping.

 International Journal of Applied Earth Observation and Geoinformation 115, 103108.

 https://doi.org/10.1016/j.jag.2022.103108
- SEMARNAT, 2016. Los manglares mexicanos [WWW Document]. URL http://www.gob.mx/semarnat/articulos/manglares-mexicanos (accessed 25.02.2025).
- Simard, M., Fatoyinbo, L., Smetanka, C., et al., 2019. Mangrove canopy height globally related to precipitation, temperature and cyclone frequency. Nature Geoscience 12, 40–45. https://doi.org/10.1038/s41561-018-0279-1
- Simard, M., Rivera-Monroy, V.H., Mancera-Pineda, J.E., et al., 2008. A systematic method for 3D mapping of mangrove forests based on Shuttle Radar Topography Mission elevation data, ICEsat/GLAS waveforms and field data: Application to Ciénaga Grande de Santa Marta, Colombia. Remote Sensing of Environment, Earth Observations for Terrestrial Biodiversity and Ecosystems Special Issue 112, 2131–2144. https://doi.org/10.1016/j.rse.2007.10.012
- Simard, M., Zhang, K., Rivera-Monroy, V.H., et al., 2006. Mapping height and biomass of mangrove forests in Everglades National Park with SRTM elevation data. Photogrammetric Engineering & Remote Sensing 72, 299–311.
- Turner, H.C., Galford, G.L., Hernandez Lopez, N., et al., 2023. Extent, Severity, and Temporal Patterns of Damage to Cuba's Ecosystems following Hurricane Irma: MODIS and Sentinel-2 Hurricane Disturbance Vegetation Anomaly (HDVA). Remote Sensing 15, 2495. https://doi.org/10.3390/rs15102495
- Vancutsem, C., Achard, F., Pekel, J.-F., et al., 2021. Long-term (1990–2019) monitoring of forest cover changes in the humid tropics. Science Advances 7, eabe1603. https://doi.org/10.1126/sciadv.abe1603
- Vanin, G.T., Lacerda, E.R., Mori, G.M., 2025. Drivers of mangrove area change and suppression in Brazil from 2000 to 2020. Conservation Biology 39, e14426. https://doi.org/10.1111/cobi.14426
- Wang, D., Wan, B., Liu, J., et al., 2020. Estimating aboveground biomass of the mangrove forests on northeast Hainan Island in China using an upscaling method from field plots, UAV-LiDAR data and Sentinel-2 imagery. International Journal of Applied Earth Observation and Geoinformation 85, 101986. https://doi.org/10.1016/j.jag.2019.101986

- Wang, L., Jia, M., Yin, D., et al., 2019. A review of remote sensing for mangrove forests: 1956–2018. Remote Sensing of Environment 231, 111223. https://doi.org/10.1016/j.rse.2019.111223
- Worthington, T.A., Andradi-Brown, D.A., Bhargava, R., et al., 2020. Harnessing Big Data to Support the Conservation and Rehabilitation of Mangrove Forests Globally. One Earth 2, 429–443. https://doi.org/10.1016/j.oneear.2020.04.018
- Zhu, Y., Liu, K., Liu, L., et al., 2020. Estimating and Mapping Mangrove Biomass Dynamic Change Using WorldView-2 Images and Digital Surface Models. IEEE Journal of Selected Topics in Applied Earth Observations and Remote Sensing 13, 2123–2134. https://doi.org/10.1109/jstars.2020.2989500

Chapter 6 Discussion

6.1 Methodological context and contributions

The accurate estimation of mangrove AGB using remote sensing data remains a critical challenge in global carbon cycle research, as direct measurements are time-consuming, destructive and spatially limited. Therefore, recent studies on mangrove AGB estimation have focused on integrating mangrove forest inventory, remote sensing data and modelling efforts (e.g., Simard et al., 2006, 2008, 2019; Aslan et al., 2016; Pham et al., 2020; Wang et al., 2020; Rovai et al., 2021; Vaghela et al., 2021). Remote sensing data used in mangrove AGB estimation include optical spaceborne imagery, SAR imagery, and airborne and spaceborne LiDAR data at various scales. Each of these data has associated strengths and weaknesses, making them naturally synergetic.

A key methodological contribution of this thesis is in demonstrating the viability and performance of employing global DEMs to estimate AGB of local mangrove forests. Though the SRTM has been employed for canopy height and AGB estimation in the USA, Colombia and Indonesia (Simard et al., 2006, 2008; Aslan et al., 2016), the studies on the comparison between open access global DEMs are limited. Additionally, compared with global mangrove AGB estimates using SRTM from Simard et al. (2019), the findings reveal the significant discrepancies between local and global estimates and underscore the importance of using local estimates to further validate global estimates, as the global allometry captures the overall trend but systematically underestimate the local AGB values.

Another key methodological contribution is in upscaling localised field inventory data to a continental level and integrating with high-resolution spaceborne imagery. Previous studies have relied on optical imagery (e.g., Landsat, WorldView, Pleiades) and SAR data (e.g., ALOS PALSAR, Sentinel-1) coupled with statistical or machine learning algorithms such as SVR (Jachowski et al., 2013; Pham et al. 2018; Navarro et al., 2019), RF (Pham & Brabyn, 2017; Wang et al., 2020) and ANN (Zhu et al., 2015; Ghosh & Behera, 2021). While these studies have demonstrated varying levels of accuracy (R² ranging from 0.45 to 0.93), their study areas normally cover local or regional mangrove forests with performance assessed using high-resolution data. The methodology proposed in this thesis deployed the first vegetation-specific spaceborne LiDAR mission (GEDI) to upscale limited localised mangrove tree measurements and characterise structural attributes across the Americas. Extensive GEDI-derived AGB estimates were generated by applying biomass-height allometry to GEDI observations, providing a reliable dataset to train and validate a RF model integrated with high-resolution Planet mosaics and rasterised environmental variables, which enables wall-to-wall mangrove AGB mapping at a continental scale.

The methodological contributions of this thesis therefore lie not only in performance evaluation of open access global DEMs on local mangrove forests but also in the introduction of spaceborne LiDAR data to upscale limited field inventory data to a continental scale. The synergistic use of global DEMs (broad coverage), spaceborne LiDAR (structural characteristics calibration), and high-resolution optical imagery (fine-scale variability) represents a methodological innovation that bridges the gap between local accuracy and continental applicability.

6.2 Transferability across regions and scales

The methodologies developed in this thesis demonstrate clear potential for application beyond the study areas in Mexico and the Americas. Through the integration of field inventory data, open access DEMs, spaceborne LiDAR measurements, high-resolution optical imagery, and rasterised environmental variables, the methodologies provide flexible templates that can be adapted to diverse mangrove areas in the world. Nonetheless, the transferability requires careful consideration of regional geomorphology, data availability, and ecosystem dynamics.

Mangroves exhibit diversity according to their geomorphic and sedimentary setting, which can be categorised as deltaic, estuarine, open coast, and lagoonal; among these, lagoonal mangroves are prominent in North and Central America and the Caribbean, accounting for about 79.4% (1,190,500 ha) of the global lagoonal mangrove extent (Worthington et al., 2020). The DEM-based approach for AGB estimation, developed and validated in lagoonal mangrove forests in Mexico, therefore holds significant potential for application to other extensive lagoonal mangrove systems in the Americas. However, in Southeast Asia, where the largest and most carbon-rich mangrove forests are located, and 1,352,200 ha mangroves (~31%) of whole mangrove extent in Indonesia) are tide dominated (Worthington et al., 2020; Jia et al., 2023), the feasibility of DEM-based canopy height retrieval requires further studies due to complex topography and strong tidal influence (Darmawan et al., 2015; Chaudhuri et al., 2019), as the DEM-based approach is implemented under the assumption that mangroves are situated in low and flat coastal areas. Relying on spaceborne LiDAR observations and dense time-series optical imagery may be necessary to capture biomass variations at fine scales. Also, in regions such as Indonesia and Malaysia, where the mangrove conversion and fragmentation are still intense (Bryan-Brown et al., 2020; Goldberg et al., 2020; Friess et al., 2024), VHR spaceborne imagery such as Planet mosaics enables the detection and quantification of biomass changes in small patches of regrowing or degraded mangroves, complementing coarser global biomass products.

In Africa, many mangrove regions are characterised by relatively sparse field data and limited monitoring (Naidoo, 2023). Here, the multisource methodology offers a practical solution to bridge data gaps. Spaceborne LiDAR data such as GEDI canopy height metrics provide reliable vegetation structural characteristics at 25 m circular footprints, which can be considered ground truths in field data-scarce regions for model calibration (Liu et al., 2021). Coupling these datasets with freely available Sentinel-2 or Landsat imagery could deliver cost-effective AGB mapping for countries with fewer resources to support high-resolution mangrove monitoring. Moreover, this methodology is adaptable with ICESat-2 LiDAR data and emerging missions such as NASA–ISRO SAR (NISAR) and ESA's Biomass satellite. Integrating the forthcoming spaceborne LiDAR data will enhance applicability of the methodology at the global scale.

Overall, the transferability of the proposed methodologies is found in the modular design: DEMs can be used where mangroves are located in low and flat coastal areas, spaceborne LiDAR missions such as GEDI and ICESat-2 can provide canopy height benchmarks across varied biogeographic regions, and high-resolution optical imagery can refine local spatial estimates. Future studies benefit from the application of the proposed methodologies across regions to improve global carbon accounting, and reveal regional comparisons in mangrove resilience, thereby strengthening the evidence base for targeted conservation and restoration efforts.

6.3 Implications for conservation, restoration, and carbon accounting

The improved estimation of mangrove AGB presented in this thesis carries significant implications for conservation, restoration, and carbon accounting at multiple scales. As mangrove are recognised as one of the most carbon-rich ecosystems (Alongi, 2020), accurate and spatially explicit biomass data are necessary to put mangroves into climate policy and management frameworks. This thesis produces reliable and high-resolution mangrove AGB estimates, addressing methodological challenges and strengthening the scientific foundations for both national and international decision-making.

In the context of conservation, spatially explicit AGB estimation maps can be straightforward sources to recognise priority mangrove areas for protection. Mangroves with high AGB stocks represent not only critical carbon sinks but the hotspots of biodiversity and ecosystem services (Bai et al., 2021; Liu et al., 2025). Through pinpointing these areas, governments and conservation organisations can target resources more efficiently to the most valuable mangrove forests against deforestation and degradation. The results in Chapter 5 underscore the resilience of regrowing mangroves, demonstrating substantial AGB gains

achieved over two decades of regrowth. This finding reinforces the ecological value of secondary forests and supports arguments for including them in mangrove conservation planning.

From a restoration perspective, the proposed methodologies offer alternative means to monitor and evaluate the effectiveness of mangrove rehabilitation projects. High-resolution AGB estimates enable the quantification of regrowth dynamics at finer scales (<10 m), providing more detailed metrics for assessing restoration success over time. This is particularly effective for regions where large-scale mangrove planting projects are underway, as managers can be equipped to assess the actual AGB accumulation and ecosystem recovery achieved rather than simply measuring survival rates.

For carbon accounting, countries with extensive mangrove cover can incorporate the results of this thesis into their national carbon emission inventories, supporting their commitments under the Paris Agreement and informing the participation in mechanisms such as REDD+ and voluntary carbon markets. Additionally, the capacity to detect and quantify mangrove AGB dynamics at finer scales improves the transparency and credibility of carbon accounting, which is important to attract international financial supports for conservation and restoration initiatives.

Overall, this thesis ensures that conservation and restoration of mangroves can be better aligned with climate mitigation strategies through scalable, accurate and transferable AGB estimation. At a broader level, the methodological advances developed in this thesis contribute to ongoing efforts to mainstream mangrove carbon stock into global assessments of nature-based climate solutions (Macreadie et al., 2021).

6.4 Research limitations and recommendations

This thesis proposes methodologies for accurately estimating mangrove AGB by integrating field inventory data with multisource remote sensing data. However, further investigation is needed to refine and validate the proposed approaches from multiple perspectives. A primary limitation of this research is the limited field inventory data of mangroves to develop more comprehensive biomass-height allometry and validate the resulting AGB estimates across three experimental chapters, which does not adequately examine the consistency between the estimation and ground truth. As it is typically difficult to carry out large-scale field campaigns in mangrove forests, the field inventory data was compiled from different sources in this research. Chapter 3 examined the feasibility and reliability of using historical and recent field data with temporal discrepancies up to 20 years for mangrove AGB estimation, but it is still necessary to account for temporal discrepancies of more than 20 years between field inventory data, when introducing them for rapidly regrowing mangrove species. In Chapter 4, GEDI LiDAR data were introduced to upscale the

limited localised measurements to a continental level under the assumption that LiDAR measurements are considered ground truth measurements of canopy heights with higher accuracy. GEDI canopy height metrics were obtained within circular footprints of 25 m in diameter, covering ~25 pixels of Planet mosaics. The median of the pixel values from Planet mosaics was used to represent optical characteristics of corresponding GEDI canopy height metrics. High agreements were found between predicted and observed AGB using the hold-out GEDI-based AGB estimates in the RF regression algorithm (**Figure 4-6**). While the trained RF algorithm applied to high-resolution Planet imagery produced the finer-scale estimation that are valuable for investigating spatiotemporal changes of mangrove AGB, this approach also introduced greater heterogeneity and uncertainty in AGB distribution patterns.

Mangrove forests are generally well-protected in the Americas, with 72% of mangroves in South America and 67% of mangroves in North and Central America and the Caribbean located within formally designated protected areas (Spalding and Leal, 2022). Additionally, FAO (2023) has reported mangrove gains between 2000 and 2020 were primarily driven by natural expansion. Given the situations of mangrove forests in the Americas, this region serves as an appropriate study area for investigating mangrove resilience relevant to climate change adaptation and ongoing conservation efforts. The JRC TMF dataset was introduced to identify mangrove regrowth areas and found that AGB gains related to the regrowth from non-forested areas are higher than those from previous forested areas. However, Chapter 5 did not specify the intensity of regrowth, i.e., the starting time of regrowth, which is critical for a detailed analysis of mangrove AGB dynamics driven by regrowth.

Future studies should focus on refining the correlation between plot-level AGB and canopy height metrics by incorporating more field inventory data across mangrove forests in varied ecological and geographical conditions, thereby improving model generalisability. When using remote sensing data to scale localised AGB estimates to broader areas, careful consideration must be given to temporal alignment with field inventory data and the spatial resolution requirements for accurate AGB estimation. Beyond investigating AGB dynamics in relation to mangrove areas and biomass gain and losses, future research should also equally prioritise investigating mangrove degradation impacts on AGB dynamics. Currently, mangroves are facing the challenge of being degraded by anthropogenic activities and extreme weather events. Degraded mangroves still maintain some ecosystem services at lower levels, generally prioritised to deploy restoration efforts which requires little more than a restriction or cessation of detrimental activities such as wastewater from adjoining aquaculture ponds and timber harvesting. The investigation of AGB dynamics across degraded mangroves can be an assessment to the level of degradation, beneficial to implement the restoration strategies. The ultimate goal of future studies is to refine AGB estimation methodologies to contribute valuable knowledge to supporting effective mangrove conservation and rehabilitation strategies.

References

- Alongi, D.M., 2020. Global Significance of Mangrove Blue Carbon in Climate Change Mitigation. Sci 2, 67. https://doi.org/10.3390/sci2030067
- Aslan, A., Rahman, A.F., Warren, M.W., et al., 2016. Mapping spatial distribution and biomass of coastal wetland vegetation in Indonesian Papua by combining active and passive remotely sensed data. Remote Sensing of Environment 183, 65–81. https://doi.org/10.1016/j.rse.2016.04.026
- Bai, J., Meng, Y., Gou, R., et al., 2021. Mangrove diversity enhances plant biomass production and carbon storage in Hainan Island, China. Functional Ecology 35, 774–786. https://doi.org/10.1111/1365-2435.13753
- Bryan-Brown, D.N., Connolly, R.M., Richards, D.R., et al., 2020. Global trends in mangrove forest fragmentation. Scientific Reports 10. https://doi.org/10.1038/s41598-020-63880-1
- Chacón Abarca, S., Chávez, V., Silva, R., et al., 2021. Understanding the Dynamics of a Coastal Lagoon:
 Drivers, Exchanges, State of the Environment, Consequences and Responses. Geosciences 11.
 https://doi.org/10.3390/geosciences11080301
- Chaudhuri, P., Chaudhuri, S., Ghosh, R., et al., 2019. The Role of Mangroves in Coastal and Estuarine Sedimentary Accretion in Southeast Asia, in: Sedimentary Processes Examples from Asia, Turkey and Nigeria. IntechOpen. https://doi.org/10.5772/intechopen.85591
- Chávez-Cerón, V., Mendoza-Baldwin, E., Ramírez-Méndez, E., et al., 2016. Response of Empirically Managed Sites to Winter Storms. Case Study: La Mancha, Veracruz, Mexico. Coast. Eng. Proc. 1(35), p. management.15. https://doi.org/10.9753/icce.v35.management.15
- Darmawan, S., Takeuchi, W., Vetrita, Y., et al., 2015. Impact of Topography and Tidal Height on ALOS PALSAR Polarimetric Measurements to Estimate Aboveground Biomass of Mangrove Forest in Indonesia. Journal of Sensors 2015, 641798. https://doi.org/10.1155/2015/641798
- Friess, D.A., Adams, J., Andradi-Brown, D.A., et al., 2024. Mangrove forests: their status, threats, conservation and restoration, in: Reference Module in Earth Systems and Environmental Sciences. Elsevier, p. B9780323907989000317. https://doi.org/10.1016/B978-0-323-90798-9.00031-7
- Ghosh, S.M., Behera, M.D., 2021. Aboveground biomass estimates of tropical mangrove forest using Sentinel-1 SAR coherence data The superiority of deep learning over a semi-empirical model. Computers & Geosciences 150, 104737. https://doi.org/10.1016/j.cageo.2021.104737
- Goldberg, L., Lagomasino, D., Thomas, N., et al., 2020. Global declines in human-driven mangrove loss. Global Change Biology 26, 5844–5855. https://doi.org/10.1111/gcb.15275
- Jachowski, N.R.A., Quak, M.S.Y., Friess, D.A., et al., 2013. Mangrove biomass estimation in Southwest Thailand using machine learning. Applied Geography 45, 311–321. https://doi.org/10.1016/j.apgeog.2013.09.024

- Jia, M., Wang, Z., Mao, D., et al., 2023. Mapping global distribution of mangrove forests at 10-m resolution. Science Bulletin 68, 1306–1316. https://doi.org/10.1016/j.scib.2023.05.004
- Liu, A., Cheng, X., Chen, Z., 2021. Performance evaluation of GEDI and ICESat-2 laser altimeter data for terrain and canopy height retrievals. Remote Sensing of Environment 264, 112571. https://doi.org/10.1016/j.rse.2021.112571
- Liu, S., He, S., Chen, S., 2025. Potential carbon stock distribution of mangrove and synergistic effect of ecosystem services in China. Ecological Indicators 178, 113931. https://doi.org/10.1016/j.ecolind.2025.113931
- Macreadie, P.I., Costa, M.D.P., Atwood, T.B., et al., 2021. Blue carbon as a natural climate solution. Nat Rev Earth Environ 2, 826–839. https://doi.org/10.1038/s43017-021-00224-1
- Naidoo, G., 2023. The mangroves of Africa: A review. Marine Pollution Bulletin 190, 114859. https://doi.org/10.1016/j.marpolbul.2023.114859
- Navarro, J.A., Algeet, N., Fernández-Landa, A., et al., 2019. Integration of UAV, Sentinel-1, and Sentinel-2 Data for Mangrove Plantation Aboveground Biomass Monitoring in Senegal. Remote Sensing 11. https://doi.org/10.3390/rs11010077
- Pham, M.H., Do, T.H., Pham, V.-M., et al., 2020. Mangrove forest classification and aboveground biomass estimation using an atom search algorithm and adaptive neuro-fuzzy inference system. PLOS ONE 15, e0233110. https://doi.org/10.1371/journal.pone.0233110
- Pham, T.D., Yoshino, K., 2017. Aboveground biomass estimation of mangrove species using ALOS-2 PALSAR imagery in Hai Phong City, Vietnam. Journal of Applied Remote Sensing 11, 026010. https://doi.org/10.1117/1.JRS.11.026010
- Pham, T.D., Yoshino, K., Le, N.N., et al., 2018. Estimating aboveground biomass of a mangrove plantation on the Northern coast of Vietnam using machine learning techniques with an integration of ALOS-2 PALSAR-2 and Sentinel-2A data. International Journal of Remote Sensing 39, 7761–7788. https://doi.org/10.1080/01431161.2018.1471544
- Rovai, A.S., Twilley, R.R., Castañeda-Moya, E., et al., 2021. Macroecological patterns of forest structure and allometric scaling in mangrove forests. Global Ecology and Biogeography 30, 1000–1013. https://doi.org/10.1111/geb.13268
- Simard, M., Fatoyinbo, L., Smetanka, C., et al., 2019. Mangrove canopy height globally related to precipitation, temperature and cyclone frequency. Nature Geoscience 12, 40–45. https://doi.org/10.1038/s41561-018-0279-1
- Simard, M., Rivera-Monroy, V.H., Mancera-Pineda, J.E., et al., 2008. A systematic method for 3D mapping of mangrove forests based on Shuttle Radar Topography Mission elevation data, ICEsat/GLAS waveforms and field data: Application to Ciénaga Grande de Santa Marta, Colombia. Remote

- Sensing of Environment, Earth Observations for Terrestrial Biodiversity and Ecosystems Special Issue 112, 2131–2144. https://doi.org/10.1016/j.rse.2007.10.012
- Simard, M., Zhang, K., Rivera-Monroy, V.H., et al., 2006. Mapping height and biomass of mangrove forests in Everglades National Park with SRTM elevation data. Photogrammetric Engineering & Remote Sensing 72, 299–311.
- Vaghela, B., Chirakkal, S., Putrevu, D., et al., 2021. Modelling above ground biomass of Indian mangrove forest using dual-pol SAR data. Remote Sensing Applications: Society and Environment 21, 100457. https://doi.org/10.1016/j.rsase.2020.100457
- Wang, D., Wan, B., Liu, J., et al., 2020. Estimating aboveground biomass of the mangrove forests on northeast Hainan Island in China using an upscaling method from field plots, UAV-LiDAR data and Sentinel-2 imagery. International Journal of Applied Earth Observation and Geoinformation 85, 101986. https://doi.org/10.1016/j.jag.2019.101986
- Worthington, T.A., zu Ermgassen, P.S.E., Friess, D.A., et al., 2020. A global biophysical typology of mangroves and its relevance for ecosystem structure and deforestation. Sci Rep 10, 14652. https://doi.org/10.1038/s41598-020-71194-5
- Zhu, Y., Liu, K., Liu, L., et al., 2015. Retrieval of Mangrove Aboveground Biomass at the Individual Species Level with WorldView-2 Images. Remote Sensing 7, 12192–12214. https://doi.org/10.3390/rs70912192

Chapter 7 Conclusions

This thesis presents improved mangrove AGB estimation methodologies integrated with compiled field inventory data and multisource remote sensing datasets, and quantifies AGB dynamics in mangrove regrowth areas. As outlined in Section 1.4, the research objectives focus on regional and continental mangrove AGB mapping and spatiotemporal analysis of AGB dynamics. Therefore, the objectives are achieved as follows:

Objective 1 – to develop the methodology of mangrove AGB estimation in the mangrove forests around La Mancha and El Llano lagoons in Mexico using freely accessible DEMs (Chapter 3)

Chapter 3 develops a mangrove AGB estimation approach through the integration of field inventory data of mangrove forests around La Mancha and El Llano lagoons in Mexico and open-access DEMs. Three 30 m global DEMs were introduced and evaluated to assess their feasibility and performance in estimating mangrove canopy height and AGB. DEM biases were calibrated using ICESat-2 ATL08 data. Field plot canopy heights showed high agreements with the calibrated DEMs ($R^2 = 0.73-0.82$). As a power-law parametric model was introduced to establish the relationship between plot-level AGB and mean canopy height, mangrove AGB across the study area was estimated by applying regressed parametric model to calibrated DEMs. The results demonstrated comparable AGB estimates and consistent spatial heterogeneity. Error analysis showed σ_{AGB} ranging between \pm 151.78 - 154.95 Mg/ha ($H_{mean} = 15$ m). Overall, this chapter presents the viability of using freely accessible DEMs for local mangrove canopy height and AGB estimation, supporting validation of global-scale AGB assessments.

Objective 2 – to develop a novel approach for mangrove AGB estimation across the Americas using compiled field inventory data and multisource remote sensing data (Chapter 4)

Chapter 4 presents a comprehensive account of mangrove AGB estimation across the Americas through the development of a novel approach that incorporates field inventory data and multisource datasets including spaceborne LiDAR data, optical imagery and environmental variables, rendering AGB estimates at a fine scale (<5 m) with an R² of 0.72 and an RMSE of 37.24 Mg/ha. The power-law parametric model was introduced to determine the relationship between field plot-level AGB and maximum canopy height, regressed by OLS with an R² of 0.36 and the RMSE of 92.86 Mg/ha. Due to a huge amount of spaceborne LiDAR data over mangrove forests in the Americas, LiDAR-derived AGB estimates from regressed power-law model demonstrated a significant capacity in RF algorithm training and validation with predictor variables of surface reflectance and vegetation indices from spaceborne optical imagery and environmental

variables. Precipitation and temperature worked better in explaining mangrove AGB variability than spectral information in terms of the performance of predictor variable selection. Mangrove AGB has been estimated across the Americas through the trained RF model with optimal hyperparameters and best selected predictor variables. Although environmental variables were found to contribute most to improving the performance of RF model, the introduction of high-resolution optical imagery helps investigate fine-scale mangrove regrowth, compared to existing global AGB estimation products for the same period.

Objective 3 – to quantify AGB dynamics of mangrove regrowth areas across the Americas between 2000 and 2020, reflecting mangrove resilience relevant to climate change adaptation and conservation efforts (Chapter 5)

Chapter 5 introduced annual TMF coverage maps for identifying mangrove regrowth areas in previously forested and non-forested areas between 2000 and 2020. The period-specific methodologies of AGB estimation were adopted due to the availability of remote sensing datasets. The methodology illustrated in Chapter 4 was utilised for the year of 2020, while the regressed power-law parametric model between field plot AGB and maximum canopy height was applied to a mangrove CHM derived from the calibrated SRTM DEM for AGB estimation in 2000. Country-level AGB estimates across undisturbed mangrove forests between 2000 and 2020 exhibited high agreements and comparable results. The analysis revealed that mangrove regrowth areas across the Americas totalled 0.17 Mha, contributing an estimated AGB gain of 5.10 Tg. Regrowing mangroves from previously forested and non-forested areas represented high AGB gains per hectare at 16 Mg/ha and 52 Mg/ha, respectively. These findings demonstrate the exceptional resilience of mangrove forests across the Americas with AGB gains occurring in mangrove regrowth areas, relevant to climate change adaptation and conservation efforts.

In summary, this thesis explores improved mangrove AGB estimation methodologies integrating field inventory data and multisource remote sensing datasets, including open-access DEMs, GEDI canopy height metrics, Planet continental mosaics, and rasterised environmental variables, and quantified AGB dynamics in regrowing mangrove areas across the Americas for two decades (2000-2020). To further refine mangrove AGB estimation, future research should: (i) incorporate more field inventory data through expanded field campaigns across various geographical settings to improve the relationship between field plot AGB and canopy height for generalisability; (ii) utilise temporally and spatially aligned remote sensing datasets with field measurements to reduce the uncertainty of AGB estimation, such as harmonising GEDI acquisitions with field survey dates to minimize biases in rapidly changing mangrove forests; and (iii) investigate AGB dynamics in regrowing, degraded, and dead mangroves in relation to the intensity of disturbances, using the JRC TMF transition dataset to achieve a more comprehensive understanding of mangrove resilience.

Overall, addressing these priorities will require coordinated efforts between remote sensing specialists and mangrove ecologists, but help better understand mangrove AGB distribution patterns and mangrove resilience regarding AGB gains and losses.